Structural Basis of Amyloid Oligomer Toxicity and Inhibition by Small Molecules and Molecular Chaperones

By Rashik Ahmed, Honours B.Sc.

A Thesis Submitted to the School of Graduate Studies in Partial Fulfilment

of the Requirements for the Degree

Doctor of Philosophy

Doctor of Philosophy (2020) **McMaster University**

(Biochemistry) **Hamilton, Ontario**

Thesis Title: Structural Basis of Amyloid Oligomer Toxicity and Inhibition by Small Molecules and Molecular Chaperones

Author: Rashik Ahmed, Honours B.Sc. (McMaster University)

Supervisor: Professor Giuseppe Melacini

Number of Pages: CLXXIII**,** 173

Thesis Abstract

Protein misfolding and the accumulation of insoluble aggregates is a hallmark of several neurodegenerative disorders, including Alzheimer's (AD) and Parkinson's disease (PD). In AD and PD patients, extracellular protein deposits consisting of amyloid beta (Aβ) and intraneuronal inclusions composed of alpha synuclein (αS) are observed, respectively. Notably, the spatiotemporal patterning of soluble protein oligomers of αS and Aβ closely follow disease progression, giving support to an emerging role of soluble oligomers in PD and AD pathogenesis. However, the structural features underlying the toxicity of Aβ and αS oligomers remain elusive. This doctoral dissertation aims at elucidating the structural determinants of oligomer toxicity by focusing on the development and application of multidisciplinary approaches based primarily on solution NMR in combination with electron microscopy, multi-angle light scattering, fluorescence microscopy, wide-angle x-ray diffraction and cellular biophysics. Using this interdisciplinary approach, in chapters 2 and 3, we identify at atomic resolution the key structural elements that facilitate the colocalization, interaction and subsequent insertion of soluble Aβ oligomers into membranes, which ultimately result in the loss of membrane integrity. Notably, we show that small molecules, such as green tea catechins, remodel these structural features and effectively perturb the interactions with membranes. In chapter 4, we extend these analyses to αS and identify how the chaperone, Human Serum Albumin (HSA), remodels toxic αS oligomers into non-toxic species and breaks the catalytic cycle that generates new toxic oligomers. Lastly, in chapter 5, we describe a novel solution NMR approach to map at atomic resolution the sites of early self-association, with minimal bias from monomer dynamics, an effect that frequently dominates residue-dependent variations in solution NMR measurements. Overall, given that Aβ and αS are archetypical amyloidogenic proteins, we anticipate that the structure – toxicity relationships established herein, and the related experimental approaches may be transferrable to other amyloidogenic systems.

Acknowledgements:

This dissertation is truly the amalgamation of the efforts of many people, whom during the past four years have supported, guided, and encouraged my work. First and foremost, I would like to thank my supervisor, Professor Giuseppe Melacini. Your continued patience, understanding and encouragement over the years has propelled me to reach heights that I never imagined I could. I am truly grateful for all the opportunities you have created for me, and the amount of time and dedication you have placed in my learning. It is uncanny that I am often told that I "sound just like Dr. Melacini", but I cannot take more pride in hearing this, as it is the greatest form of flattery to be told that you remind others of your role model. Thank you for inspiring me and teaching me what it means to be a scientist. I will continue to follow along the path that you have paved, and live by the wisdom that you have imparted through your many proverbs. I will continue to "go after the low hanging fruit", "hope for the best and prepare for the worst" and most importantly "not let perfect be the enemy of the good". I believe it is only appropriate that I should also share one of my favourite quotes: "a truly great mentor is hard to find, difficult to part with, and impossible to forget."

I would also like to thank the past and present members of the Melacini lab that I have had the privilege of working with. To my students, Michael, Jimmy and Tiffany, thank you for your patience and understanding. Through our trials and hurdles, I have learned how to be a good mentor. To Jinfeng, my "knight in shining armour", thank you for your unparalleled and genuine efforts in support of my research. I would not have been nearly as productive without your help. I sincerely appreciate your friendship and accompaniment over this journey. To Karla and Heba, though our time together has been short, thank you for all the good memories and "memes". I believe I have learned more from you than you have from me. To Naeimeh (*Namnam*), thank you for your utmost patience, encouragement and guidance over the years. I still recall all the heartache I gave you during my undergraduate thesis. Your words of reassurance and support have taught me the importance of persistence in the face of defeat. To my mentor in the lab, Dr. Madoka Akimoto, thank you for passing down your wealth of knowledge. I was relieved to know that I could always count on you to help me troubleshoot my experiments. To Dr. Bryan VanSchouwen, thank you for the laughs over the years and always helping me find the right words to use. I am often reminded of you saying, "Do you mean …", whenever I ask for help in formulating a sentence. To Olivia, thank you for your friendship and the good times, both in and out of the lab. You were always there whenever I needed to vent or required advice. My time in the Melacini lab has truly been an enjoyable experience because of you. Lastly, to my friend Dr. Stephen Boulton, thank you for all your support over the years. You have motivated me when I was down, guided me when I was lost and challenged me when I was complacent. I await with bated breath to hear about your successes in the future.

To my committee members Dr. Ray Truant and Dr. Yu Lu, thank you for teaching me the importance of framing a story, and finding the big picture. I have been able to expand the breadth of my research thanks to your guidance. To Dr. Maikel Rheinstadter, Dr. Richard Epand, Dr. Ryan Wylie and Dr. Gianluigi Veglia, thank you all for your continued support in my research projects. Dr. Veglia thank you for hosting me in your lab and teaching me the importance of reproducibility. Dr. Ryan Wylie, thank you for your continued mentorship over the years. I have thoroughly enjoyed our scientific conversations and have learned and developed in many ways.

To Mouhanad Babi and Vincent Huynh, thank you for the countless coffee breaks and lunches. You have made the last four years very memorable and have given me the encouragement I needed to push forward. To my other friends who have encouraged and supported me along the way, you know who you are.

I would also like to thank the staff at the NMR facility, Megan Fair, Dr. Hilary Jenkins and Dr. Bob Berno, for all your assistance. You went above and beyond to make the process of learning and using the NMR instrumentation easy and comfortable. To Dr. Bob Berno, thank you for introducing me to the world of NMR and for your continued guidance, both personally and professionally.

Last but most importantly, to my family, thank you for your unparalleled trust, support and encouragement from beginning to end, both in good times and in bad. I could not have done this without you - the comforts I have had over the years are the result of the many sacrifices that you have all made. I am grateful to my sister for always being there for me as a friend. I am forever indebted to my parents for giving me the opportunities and experiences that have made me who I am. This journey would not have been possible if not for you all, and I dedicate this milestone to you. Thank you for believing in me.

Table of Contents

List of Main Figures:

Chapter 1

Chapter 2

Chapter 3

Chapter 4

Chapter 5

Chapter 6

List of Supplementary Figures:

Chapter 2

Chapter 3

Chapter 4

Chapter 5

List of Tables:

List of Abbreviations:

Alzheimer's disease (AD)
Parkinson's disease (PD)
Amyloid beta (Aβ)
Alpha synuclein (αS)
Nuclear Magnetic Resonance (NMR)
Transmission electron microscopy (TEM)
Dynamic light scattering (DLS)
Size exclusion chromatography (SEC)
Size exclusion chromatography coupled with multi-angle light scattering (SEC-MALS)
Wide-angle X-ray diffraction (WAXD)
Human Serum Albumin (HSA)
Fatty acid and globulin free human serum albumin (rHSA)
Globulin free human serum albumin (gHSA)
Lewy Body (LB)
Huntington's disease (HD)
Neurofibrillary tangle (NFT)
Huntingtin protein (HTT)
Cerebrospinal fluid (CSF)
Soluble NSF attachment protein receptors (SNARE)
Amyloid precursor protein (APP)
Soluble amyloid precursor protein α/β (sAPPα/β)
83-amino acid C-terminal fragment (C83)
APP intracellular domain (AICD)
99-amino acid C-terminal fragment (C99)
Cerebral amyloid angiopathy (CAA)
Central hydrophobic core (CHC)
C-terminal region (CTR)
N-terminal region (NTR)
Non-amyloid β component of AD plaques (NAC)
(-)-epigallocatechin-3-gallate (EGCG)
(-)-epicatechin (EC)
(-)-gallocatechin-3-gallate (GCG)
(-)-catechin-3-gallate (CG)
(-)-epigallocatechin (EGC)
(-)-epicatechin-3-gallate (ECG)
Methyl-3,4,5-trihidroxybenzoate (MG)
Solid state NMR (ssNMR)
Dipolar assisted rotational resonance (DARR)
Insensitive nuclei enhanced polarization transfer (INEPT)
Reactive oxygen species (ROS)
Fatty acid (FA)
Saturation transfer difference/reference (STD/R)
Surface plasmon resonance (SPR)
Hexafluoroisopropanol (HFIP)
Heteronuclear single quantum coherence (HSQC)
Heteronuclear multiple quantum coherence (HMQC)
Methyl saturation transfer difference heteronuclear single quantum coherence (MeSTDHSQC)
Water saturation transfer difference heteronuclear single quantum (wSTDHSQC)
Dark state exchange saturation transfer (DEST)

Molecular weight (MW)
Low molecular weight (LMW)
High molecular weight (HMW)
Off-resonance rotating-frame Overhauser effect spectroscopy (OR-ROESY)
Transfer Nuclear Overhauser effect spectroscopy (TrNOESY)
8-anilinonaphthalene-1-sulfonate (ANS)
Compounded chemical shift (CCS)
Shared hierarchical academic research computing network (SHARCNET)
Particle mesh ewald (PME)
Molecular dynamics (MD)
Retinal pigment epithelial (RPE1)
Propidium iodide (PI)
Thioflavin T (ThT)
Small unilamellar vesicle (SUV)
Large unilamellar vesicle (LUV)
Continuous wave (CW)
Principal component (PC)
Singular value decomposition (SVD)
1,2-dioleoyl-sn-glycero-3-phosphoethanolamine (DOPE)
1,2-dioleoyl-sn-glycero-3-phospho-L-serine (DOPS)
1,2-dioleoyl-sn-glycero-3-phosphocholine (DOPC)
Dulbecco's modified eagle's medium (DMEM)
Phosphate buffered saline (PBS
Non-binding surface (NBS)
Biological large angle diffraction experiment (BLADE)
Solvent accessible surface area (SASA)
Oleic acid (OA)
Dansyl phenylalanine (Dan F)
Biolayer interferometry (BLI)
^{13}C-Oleic acid for the NMR-based assessment of albumin-bound Long Chain Fatty Acid Concentration (CONFA)
T2* weighted deconvolution (TIDE)
Self-association by temperature-induced relaxation enhancement (SATIRE)
Paramagnetic relaxation enhancement (PRE)
Intrinsically disordered protein (IDP)
Root mean square deviation (RMSD)
Post translational modification (PTM)

Chapter 1. Introduction

1.1 Protein Aggregation Underlies the Pathogenesis of Several Neurodegenerative Disorders Including Alzheimer's and Parkinson's Disease

The accumulation of insoluble protein inclusions is a key histopathological hallmark of multiple neurodegenerative disorders. In Parkinson's disease (PD), Lewy bodies (LBs) composed of aggregated alpha synuclein (αS) are found in the cytoplasm of neurons [1]. In Huntington's disease (HD), intraneuronal inclusions composed of the polyglutamine-rich huntingtin protein are observed[2]. In Alzheimer's disease (AD), both intra- and extra-cellular protein deposits, namely neurofibrillary tangles (NFTs) containing phosphorylated tau and amyloid plaques consisting of amyloid beta (Aβ), are detected[3].

The critical role of these amyloidogenic proteins in disease pathogenesis is supported by genetic mutations. Mutations found in the genes encoding the amyloid precursor protein (APP), from which Aβ is derived, or in the APP processing enzyme (presenilin 1 and 2 genes) are sufficient to cause AD[4]. Moreover, familial mutations in the SNCA gene encoding alpha synuclein invariably causes PD[5,6] and SNCA gene multiplications reduce the age of PD onset[7–9]. Similarly, expansion of the CAG repeat in exon 1 of the gene encoding the huntingtin protein (HTT) regulates the onset and severity of HD[10]. In all such cases, elevated levels of insoluble protein inclusions are observed. Therefore, concurrent lines of genetic evidence suggest a role of protein aggregates in disease pathogenesis.

Notably, the spatiotemporal patterning of these protein aggregates closely follows disease progression. Indeed, patients who died at earlier clinical stages of PD exhibited LBs confined to the lower brainstem, whereas patients at later stages of PD had LBs also in the upper brainstem and cortex[11,12]. In AD, the spread of NFTs from the transentorhinal region to the limbic system and finally the isocortical areas explains the characteristic impairment of episodic memory in the initial stages, semantic memory and other cognitive domains in the mid stages and the sparing of motor, sensory and primary visual functions up until the late phases[13–15]. Indeed, numerous clinical studies have established that the patterning of NFTs correlates with the severity and progression of AD[16–20].

However, unlike NFT accumulation, the patterning of amyloid plaques does not directly correlate with cognitive decline[21,22]. Moreover, cognitive deficits in transgenic mice manifest well before plaque deposition or detection of insoluble aggregates[23,24]. Such observations in conjunction with numerous failed clinical trials targeting Aβ plaque burden increase the ambiguity of a pathogenic role of insoluble Aβ aggregates. Nonetheless, emerging evidence suggests that soluble oligomeric Aβ species that precede the formation of amyloid plaques likely underlie memory impairment in these transgenic mice,

giving support to an emerging role of soluble protein oligomers in AD pathogenesis and other neurodegenerative disorders.

1.2 Pathological Relevance of Aβ and αS Oligomers

Seminal studies in the late 1990s demonstrated that in addition to mature fibrils, Aβ spontaneously forms soluble oligomers[25–27]. Notably, these oligomers are neurotoxic in the absence of amyloid fibrils[28]. Such soluble Aβ oligomers accumulate in the brains and CSF of AD patients[29,30] and directly correlate with cognitive impairment in AD mouse models[31]. Moreover, Aβ oligomers have been shown to promote tau hyperphosphorylation and NFT accumulation both *in vitro*[32,33] and *in vivo*[34,35], suggesting an early pathogenic role of soluble Aβ species.

Akin to Aβ, numerous lines of evidence suggest a pathological role of αS oligomers in PD. Although the spreading mechanism of LBs is consistent with disease progression and development of neurological symptoms in PD, presence of LBs in neurologically normal individuals[36,37] and weak correlation of LBs with very early stage PD symptoms[38,39] substantiate the relevance of alternative toxic agents in PD *i.e.* αS oligomers. Indeed, αS oligomers have been shown to be neurotoxic both *in vitro*[40] and *in vivo*[41] and present in PD patient brains[42]. Moreover, αS oligomers have been shown to dysregulate SNARE-complex formation[43] and induce extensive synaptic and dendritic loss[44], which occur in early stage PD prior to the degeneration of dopaminergic neurons. Therefore, soluble oligomers are implicated in both PD and AD pathogenesis, albeit αS is primarily intracellular whereas Aβ is primarily extracellular.

1.3 Prion-like Cell-to-Cell Transmission of αS: Implication of Extracellular αS in Parkinson's Disease Pathology

While LBs observed in PD are intracellular, emerging evidence suggests that trace amounts of αS is found extracellularly and may contribute to PD pathology *via* a prion-like cell-to-cell transmission mechanism.[45,46] Early *in vitro* and animal model investigations have shown that exogenously introduced αS aggregates are able to recruit and convert soluble αS into insoluble assemblies when internalized into cells.[47,48] Interestingly, small amounts of preformed aggregates are sufficient to initiate the seeding process, suggesting that the templating effect is self-perpetuating and can enable propagation between cells. Indeed, the expansion of LBs through anatomically connected regions of the brain from the peripheral tissues of the olfactory bulb to the cerebral cortex[49] is consistent with such a spreading hypothesis.

An increasing body of *in vivo* data in support of a prion-like spreading of αS is now available. Notably, fetal mesencephalic neurons grafted in the neostriatum of PD patient brains developed intracellular LBs years after original transplantation.[50,51] Such host-to-graft propagation has also been described in several animal model studies.[52–54] Moreover, monomeric and oligomeric forms of αS have been detected in the blood plasma[55] and cerebrospinal fluid (CSF)[56], supporting the hypothesis that αS can be secreted into the extracellular space.

Cell culture and mouse model studies aimed at understanding the mechanism of propagation collectively show that αS is secreted from cells *via* an unconventional exocytosis pathway independent of the endoplasmic reticulum and Golgi apparatus.[53,57] The extracellular αS can subsequently enter recipient cells, with αS aggregates exhibiting enhanced propensity to internalize compared to monomeric forms.[58] This emerging body of evidence implicates a possible role of extracellular αS in PD pathology and warrants a detailed high-resolution investigation of the structural and biophysical properties that enable the toxicity and spreading potential of these extracellular aggregates. In addition, αS may also serve as a model system for other amyloidogenic IDPs.

1.4 Processing and Molecular Architecture of Aβ and αS

1.4.1 Processing of the Amyloid Precursor Protein Generates Two Major Aβ Isoforms: Aβ40 and Aβ42

Aβ is generated from the enzymatic cleavage of the transmembrane amyloid precursor protein (APP). APP processing proceeds via two pathways: non-amyloidogenic and amyloidogenic. In the non-amyloidogenic pathway, α-secretase cleaves APP between residues 612 and 613 (*i.e.* K16 – K17 of Aβ).[59] This prevents the formation of Aβ and results in the release of an N-terminal extracellular fragment (sAPPα) and retention of an 83 amino acid C-terminal fragment (C83) in the membrane (Figure 1, *left*). C83 is then further processed by γ-secretase producing the APP intracellular domain (AICD) and the short 3kDa peptide p3.

In the amyloidogenic pathway, APP is first cleaved by β-secretase between residues 671 and 672, resulting in the release of the extracellular sAPPβ fragment (Figure 1, *right*).[59] The remaining 99 amino acid C-terminal fragment (C99) is subsequently cleaved by γ-secretase resulting in the release of AICD and Aβ into the intracellular and extracellular spaces, respectively. Given the imprecise selectivity of γ-secretase, several Aβ isoforms of varying C-terminal length (between residues 38 – 43) are generated. The predominant cleavage product is 40 residues in length (Aβ40), whereas a smaller proportion (approximately 10%) is composed of 42 residues (Aβ42).[59] Aβ42 is more hydrophobic and prone to self-association than Aβ40, and is also the predominant isoform found in AD amyloid plaques[60]. Notably, in

the amyloid deposits found in cerebral amyloid angiopathy (CAA), Aβ40 is the predominant form.[61] CAA has been implicated in the early steps of AD pathogenesis and an increasing body of literature suggests that cognitive impairment in the aging brain is driven by overlapping neurodegenerative and cerebrovascular pathologies. Therefore, both Aβ isoforms are of pathological significance.

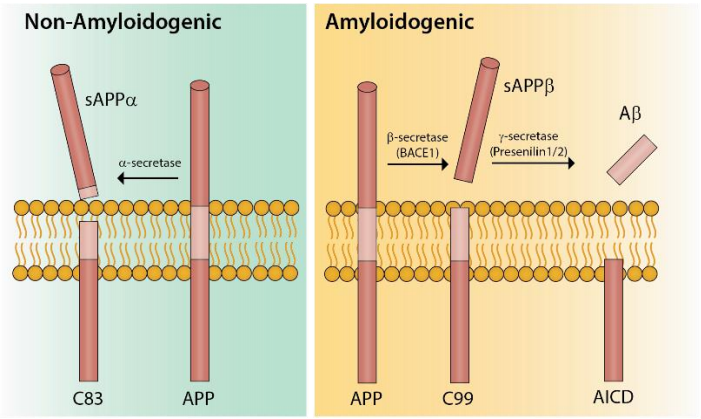

Figure 1. Enzymatic processing of the amyloid precursor protein (APP)[59].

1.4.2 Molecular Architecture of Aβ

Given the pathogenicity of soluble Aβ aggregates, research efforts have been focused on identifying the molecular motifs responsible for the aggregation propensity of Aβ. Aβ contains two hydrophobic clusters *i.e.* the central hydrophobic core (CHC) spanning residues 17 – 21 and the C-terminal region (CTR) spanning residues 30 – 40. The CHC (L17 - V18 - F19 - F20 - A21) has been suggested to be the predominant motif responsible for Aβ aggregation. Indeed, substitution of two or more CHC residues is sufficient to retard Aβ aggregation[62] and the short seven residue fragment KLVFFAE is sufficient for amyloid fibril formation[63]. Moreover, the CHC and CTR are involved in fibril formation as the two segments form parallel, in-register β-strands that are connected by a β-hairpin loop.[64] In addition to forming β-sheet structures, the two hydrophobic segments are also involved in membrane binding and typically adopt α-helical conformation when bound to membranes prior to eventual conversion into β-sheets.[65] Membrane interactions are one of the primary mechanisms of Aβ toxicity[66], and therefore the CHC and CTR are of significant pathological interest.

Unlike the CHC and CTR, the Aβ N-terminal region (NTR) is primarily disordered both in the monomeric and fibrillar forms.[64] Two key histidine residues *i.e.* His6 and His13, coordinate numerous divalent metal cations and metal binding significantly alters the kinetic pathways of Aβ aggregation.[67] Notably, several familial AD mutations have been identified in the NTR, including the English (H6R) and the Tottori (D7N)[68]. These mutations enhance Aβ aggregation propensity, increase the stability of higher order Aβ aggregates

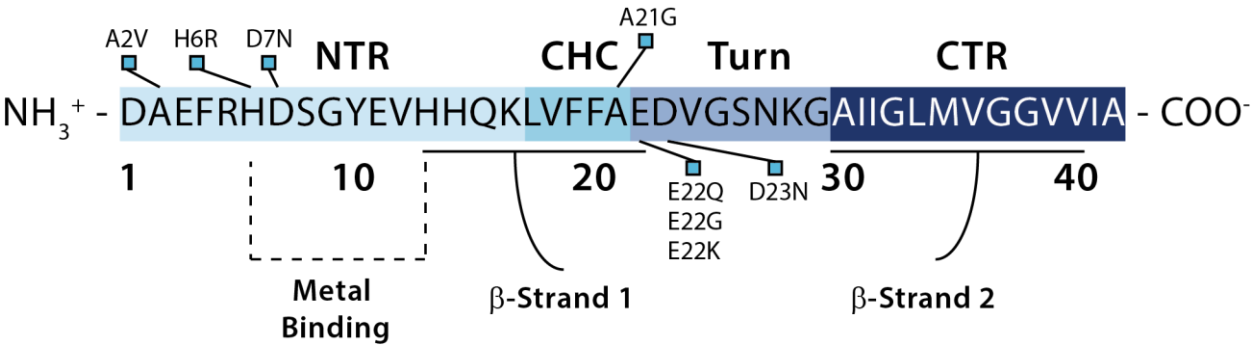

Figure 2. Amino acid sequence of Aβ42. The N-terminal region (NTR), central hydrophobic core (CHC), β-turn region (Turn) and C-terminal region (CTR) are distinctly colour-coded and the metal binding sites, β-strand positions[69] and selected familial mutation sites are annotated.

and enhance Aβ cell toxicity. However, it is still unclear at the molecular level how these segments *i.e.* the NTR, CHC and CTR, influence soluble oligomer toxicity. Such investigations have thus far remained difficult due to the transient nature of these oligomer intermediates and their intrinsic dynamics, which preclude their detection by conventional high-resolution spectroscopic techniques.

1.4.3 Molecular Architecture of αS

Alpha synuclein is a 140 amino acid (14 kDa) protein that consists of an amphipathic, lysine-rich N-terminus, a disordered, acidic C-terminus and a highly hydrophobic central motif spanning residues 61-95. The N-terminal segment contains seven imperfect repeats of a hexameric KTKEGV motif, similar to that found in apolipoproteins, suggesting a possible role of these segments in the association of αS with lipids through formation of an α-helix[70]. Indeed, i*n vitro* characterization of the interaction of αS with lipid membranes have shown that αS adopts an N-terminal kinked α-helix when associated with lipid bilayers[71], SDS micelles[72,73] and synaptic vesicles[74] and that membrane binding precedes the formation of β-sheet rich oligomers[75]. Interestingly, all of the familial SNCA mutations are found in the N-terminal region and such mutations alter the capacity of αS to interact with lipid membranes and aggregate[76]. The C-terminus, on the other hand, is involved in the interaction of αS with metals and proteins.[77]

Unlike the N- and C- termini, the αS central hydrophobic region known as the non-amyloid-β component of AD plaques (NAC), is shielded from the solvent.[78] This occlusion in monomeric αS is facilitated by transient interactions between the N- and C-termini[79] and is proposed to impede spontaneous aggregation[78]. Notably, 11 out of the 35 residues within the NAC region drive the aggregation of αS[80,81] and deletion of residues 71-82 completely suppresses αS aggregation *in vitro* and eliminates neurotoxicity in PD drosophila models.[82] Moreover, the αS homolog β-synuclein, which differs from αS by lacking residues 74-84 in the NAC region, does not aggregate.[83] Nonetheless, introduction of the 11 residue NACore segment into β-synuclein only mildly alters its aggregation propensity, suggesting that

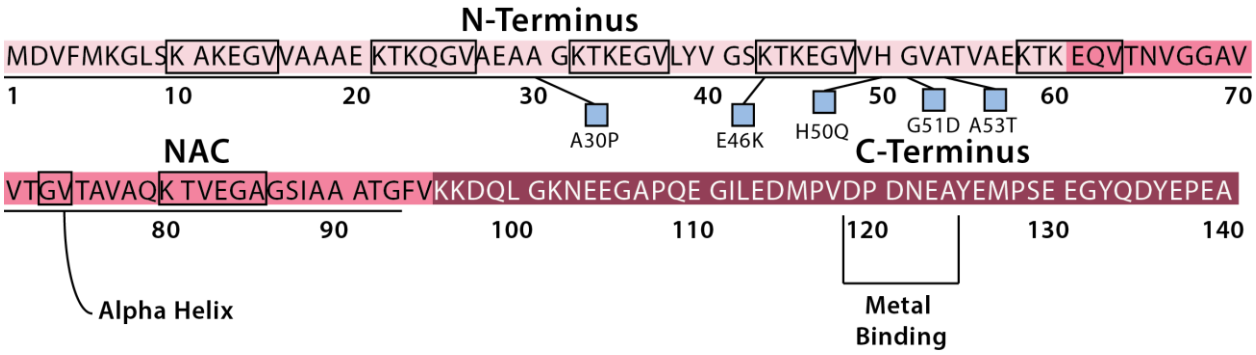

Figure 3. Amino acid sequence of alpha synuclein. The N-terminus, Non-amyloid β component (NAC), and C-terminus are distinctly colour-coded and the metal binding sites, α-helix position[71], "KTKEGV" imperfect repeats and selected familial mutation sites are annotated.

sensitive positioning of charged and hydrophobic residues underlies the aggregation behaviour of αS.[84] These results are consistent with segments outside the NAC region influencing aggregation behaviour, as exemplified by the N-terminal familial mutations.

While collectively these results show that distinct segments of αS regulate aggregation propensity and toxicity, it is not well understood how these regions facilitate oligomer toxicity. For such understanding, high-resolution characterization of oligomer structures is required. In the following section, efforts towards to this end for both Aβ and αS are described.

1.5 Structural and Biophysical Properties of Toxic Amyloid Oligomers

1.5.1 Aβ Oligomer Structures and Mechanisms of Toxicity

Despite the challenges associated with stabilizing and characterizing Aβ intermediates, it has been possible to delay the growth of aggregation intermediates to an extent sufficient to enable structural elucidation. For example, Ahmed et al. have shown that toxic Aβ42 oligomers stabilized through low temperature and salt conditions are largely disordered, but exhibit a turn conformation reminiscent of protofibrils and fibrils.[85] In contrast, for the other major isoform of Aβ, *i.e.* Aβ40, toxic oligomers adopt parallel, in-register β-sheets.[86] Although these studies have provided an initial framework to define structural features of toxic Aβoligomers, it remains unclear how these structural elements enable toxicity.

Numerous mechanisms of toxicity have been proposed for Aβ oligomers, including interactions with multiple cellular components, such as membranes.[4,66,87,88] In fact, extracellular Aβ oligomers are known to perturb biological and biomimetic membranes at multiple levels. The oligomers can (i) bind to membranes causing local perturbations[89,90], (ii) form annular structures that insert into the membrane and affect ion homeostasis[90–92] and (iii) bind to membrane receptors altering signal transduction pathways[93]. Similar hypotheses have been proposed to explain the neurotoxicity of Aβ protofibrils, although the latter

have been shown to act also through detergent-like permeabilization and eventual fragmentation of the membrane[90]. While these results highlight critical aspects of Aβ–membrane interactions, the structural elements that enable key interactions with the membranes remain elusive.

To improve the currently ill-defined relationship between structure and mechanisms of toxicity it is critical that studies investigating structures of oligomeric intermediates also elucidate the mechanisms by which the oligomers induce toxicity and *vice versa*. Both approaches need to combine within the same investigation, because the polymorphic nature of the oligomeric intermediates makes it is difficult to establish connections between different oligomer studies. Therefore, there is a critical need for investigations that can implement both to establish structure – toxicity relationships.

1.5.2 αS Oligomer Structures and Mechanisms of Toxicity

Characterizing the structural attributes of αS oligomers species presents similar challenges as for Aβ. Nevertheless, recently Chen et al. described a method for isolating metastable toxic αS oligomers accumulated during the self-association cascade.[94] Through lyophilization, the authors enriched the populations of low molecular weight αS oligomers and subsequently isolated these species through filtration. Two distinct oligomer variants consisting on average of 18 and 29 monomers were formed through this protocol. Both oligomer types adopt spherical conformations with ~35% residual anti-parallel β-sheet content. Cryo-EM analysis of these oligomers demonstrated that both variants exist as cylindrical or doughnut-shaped conformers with a hollow core enriched in solvent-exposed hydrophobic residues.[94] The oligomer variants interact favourably with negatively charged membranes and induce significant mitochondrial stress.

Fusco et al. further characterized these oligomers (called 'type B') at higher resolution using both solution and solid-state NMR (ssNMR).[75] Through comparison with a non-toxic oligomeric intermediate (called 'type A') prepared in the presence of (-)-epigallocatechin-3-gallate (EGCG), they revealed key structural attributes unique to toxic oligomers. Complementary dipolar assisted rotational resonance (DARR) and insensitive nuclei enhanced by polarization transfer (INEPT) ssNMR experiments revealed that toxic type B oligomers contain a rigid β-sheet core spanning residues 70 – 88 and a disordered N- and C-termini. In contrast, type A oligomers have a rigid N-terminus and a disordered NAC and C-terminus. These structural differences modulate the interactions with membranes. Whereas type B oligomers embed into the membrane, type A oligomers remain on the membrane surface. These *in vitro* observations are recapitulated *ex vivo* with type B oligomers significantly enhancing release of calcein and formation of reactive oxygen species (ROS), whereas no significant change is observed for type A oligomers.[75]

Overall, these findings begin to identify structural attributes that enable oligomer toxicity. However, further investigations elucidating other toxic oligomers populated during the self-association cascade are necessary to identify whether these structural motifs are common among toxic oligomers, and such concepts will inform the rational design of drug candidates for PD.

1.6 Thesis Outlook and Key Questions Addressed

A common theme stemming from the previous sections is that no single mechanism accounts for all the pathways of toxicity observed in PD and AD. Moreover, no single amyloid specie can account for all the mechanisms of toxicity observed. Toxicity therefore seems to be a universal effect arising from the nucleation-dependent aggregation process, which gives rise to varying oligomeric intermediates with different mechanisms of toxicity.[95] Indeed, this model reconciles the large body of literature reporting different oligomer structures and mechanisms of toxicity. An emerging theme within this conceptual framework is that although different toxic oligomer structures exist, these oligomers share common structural motifs.[4] These shared motifs are collectively termed "toxic surfaces" and the exposure of such surfaces is associated with the observed toxicity. However, these toxic surfaces are still unknown.

Therefore, one of the central questions addressed by this thesis is: what is the structural basis of amyloid oligomer toxicity? To this end, this dissertation focuses on two amyloidogenic proteins, namely Aβ and αS, and the structures of their oligomeric intermediates and associated mechanisms of extracellular toxicity. On-pathway oligomers of both αS and Aβ were stabilized through low temperature and salt conditions and characterized through a combination of biophysical techniques, which are explained in greater detail in section 1.6.1. of this thesis. Subsequently, these approaches were utilized to map the interactions of Aβ and αS oligomeric species with membranes, a key driver of AD and PD pathogenesis[66] (Chapters 3 and 4) . Moreover, potent inhibitors of oligomer toxicity were employed to assess the validity of the structure – toxicity relationships established, and jointly to determine inhibitory mechanisms of action (Chapters 2 and 4). Last but not least, we propose new approaches to map at residue resolution sites critical for the early steps of self-association (Chapter 5). An overview of the different chapters is provided in the next paragraphs.

Chapter 2: Molecular Mechanism for the (-)-Epigallocatechin gallate-induced Toxic to Non-toxic Remodeling of Aβ Oligomers (Ahmed et al., J. Am. Chem. Soc., 2017)

Chapter two describes the molecular mechanism by which the catechin, EGCG, remodels toxic Aβ oligomers into non-toxic assemblies. Our results show that EGCG binds Aβ oligomers with μM affinity at solvent-exposed hydrophobic sites and occludes the oligomer surface from monomer recognition. Notably, whereas toxic oligomers exhibit significant monomer – oligomer contacts at the CHC and CTR,

upon EGCG remodeling substantial loss of contacts is observed at these two sites and a concomitant enhancement of contacts is observed at the N-terminus. These findings explain the loss of seeding potential upon EGCG remodeling, as the two hydrophobic segments form the β-sheet layers in mature Aβ fibrils, but also rationalize the lack of monomer loss during EGCG-remodeling. Through the binary comparison of toxic, canonical and non-toxic, EGCG-remodeled oligomers, our investigation establishes that surface hydrophobicity and accessibility of the two hydrophobic segments enable oligomer cytotoxicity.

Chapter 3: Atomic Resolution Map of the Soluble Amyloid Beta Assembly Toxic Surfaces (Ahmed et al., Chemical Science, 2019)

In chapter three, we extend our structural analyses to a library of Aβ oligomers with varying degrees of cytotoxicity. These oligomers are chemically induced through non-covalent interactions with six EGCG analogs. Biophysical and *ex vivo* toxicity assays reveal that the oligomers enhance the permeability of mammalian cell membranes and alter the reductive potential of the cytosol to different extents, and that such functional differences stem from differences in the morphology and structural arrangement of the oligomeric species. Covariance analyses of the toxicity and structural observables allowed the identification of key structural determinants underlying oligomer toxicity. Notably, surface hydrophobicity, size, and exposure of the CHC and concomitant occlusion of the N-terminus from monomers/membranes is strongly correlated with loss of cell membrane integrity and mitochondrial function. Moreover, the CTR is shown to be ancillary for toxicity, explaining why oligomers, which lack the cross-β-sheet motif characteristic of mature fibrils, is the primary pathogenic species.

Chapter 4: Molecular Mechanism for the Suppression of Alpha Synuclein Membrane Toxicity by an Unconventional Extracellular Chaperone (Ahmed et al., J. Am. Chem. Soc., 2020)

In chapter four, we extend our structural investigations of toxic oligomers to the PD-associated αS protein. Through the comparison of toxic αS oligomers in the absence and presence of the potent molecular chaperone human serum albumin (HSA), we reveal key structural features unique to toxic oligomers and the HSA mechanism of action. We show that endogenous HSA binds solvent-exposed hydrophobic sites in αS oligomers with sub-μM affinity, in a manner independent of fatty-acid (FA) binding to the high-affinity FA loci in HSA. The occlusion of the oligomer surface in turn prevents the addition of monomers and breaks the catalytic cycle that promotes αS self-association. Moreover, HSA binding remodels αS oligomer and high molecular weight (HMW) fibrils into chimeric intermediates with reduced toxicity. Specifically, in the absence of HSA, residues within the NAC adopt a rigid β-sheet core, as indicated by the exclusive presence of NAC resonances in ssNMR DARR spectra. However, upon HSA addition, the

population of αS oligomers shifts towards more fibril-like states, as indicated by the appearance of new resonances that overlay with fibrils and the loss of resonances unique to oligomers. These characteristic HSA-induced changes in αS structure reduce the capacity of αS oligomers to interact with and embed into the membrane. Unexpectedly, HSA also directly interacts with the membrane and such interactions may additionally compete out αS binding. The chaperoning effect of HSA is not just limited to αS oligomers, as HSA also binds αS monomers at the N- and C-termini with sub mM affinity. However, unlike the interactions with αS oligomers, fatty acid binding to HSA competes out the interactions with the C-terminus of αS monomers.

Chapter 5: Mapping Early Oligomerization Sites at Atomic Resolution through Self-Association by Temperature-Induced Relaxation Enhancement (SATIRE) (Ahmed et al, *Manuscript in Preparation*)

While solution NMR techniques offer a means to access lowly populated oligomer species by taking advantage of the on – off exchange of NMR visible monomers from the surfaces of NMR-invisible oligomers (described in greater detail in section 1.6.1.3), they are often confounded by the complex intrinsic dynamics of the monomeric protein. In chapter six, we describe an approach to map early self-association sites in amyloidogenic proteins with minimal bias from monomer dynamics. We apply this approach to the archetypical intrinsically disordered protein, αS, for which self-association sites have been previously characterized by extensive mutations and shown to localize to the NAC region and the N-terminal segment spanning residues 30-53.

By monitoring the temperature-dependent changes in $^{15}N - R_2$ *i.e.* $\Delta R_2/\Delta T$, we show that residues involved in early self-association exhibit a characteristic switch from negative-to-positive $\Delta R_2/\Delta T$ *i.e.* non-linear dependency of R_2 with temperature. The non-linearly dependency strongly coincides with increases in the population of ThT-sensitive oligomers with aggregated MW < 1 MDa. In contrast, residues experiencing enhanced dynamics exhibit a distinctive linear and negative $\Delta R_2/\Delta T$. These features are systematically probed through the thermal R_2 correlation matrix and the network of residues involved in early self-association are identified through agglomerative clustering. Taken together, the SATIRE method offers a robust, label-free and sensitive approach to map early self-association sites in amyloidogenic proteins at atomic resolution and to probe the effect of aggregation inhibitors.

Chapter 6: Concluding Remarks and Future Directions

Chapter six summarizes the structure – toxicity relationships established for αS and Aβ oligomers and identifies possible modes of intervention as highlighted through elucidation of the mechanisms of action of potent oligomer inhibitors *e.g.* catechins and HSA. The final chapter also discusses the advantage of chemical exchanged-based solution NMR methods, such as the SATIRE approach, to identify early

oligomerization sites in amyloidogenic proteins. These findings are also contextualized in the framework of alternative hypotheses proposed for the etiology of Alzheimer's and Parkinson's diseases. Future directions regarding the extensibility of these findings to the crowded environments of *in situ* biofluids as well as the influence of age-related post-translational modifications are also discussed.

1.6.1 Solution NMR Toolset to Probe the Mechanisms of Amyloid Oligomer Toxicity and Inhibition by Small Molecules and Molecular Chaperones

The work presented in this section has been previously published and is reproduced here with permission from the Royal Society of Chemistry Chemical Communications. Full citation is as follows:

Ahmed, Rashik; Melacini, Giuseppe (2018): A solution NMR toolset to probe the molecular mechanisms of amyloid inhibitors. In *Chemical communications (Cambridge, England)* 54 (37), pp. 4644–4652. DOI: 10.1039/c8cc01380b.

1.6.1.1 Probing Oligomer – Inhibitor Interactions

While the mechanisms of amyloid inhibition are often complex and may include anti-inflammatory and anti-oxidants effects, one of the means by which amyloid inhibitors such as HSA can perturb Aβ oligomer toxicity is through binding Aβ oligomers and modulating their interactions with the extra-cellular and cellular environment.[97,98] Hence, the first question we sought to address through solution NMR was whether HSA interacts with Aβ oligomers. However, one caveat of solution NMR is its well-known size-limitation, which precludes the direct detection of soluble oligomers with aggregated MW often of the order of MDa. Nonetheless, we could take advantage of the notion that the monomers, which are NMR detectable, are in exchange with the NMR-invisible oligomeric species to indirectly probe the transient oligomers.[99,100]

A solution NMR experiment that capitalizes on the monomer-oligomer exchange is Saturation Transfer Difference (STD) NMR.[101,102] In STD NMR, we apply a weak radiofrequency (RF) pulse to selectively saturate the methyl protons of Aβ. The methyl saturation occurs in principle for both Aβ monomers and oligomers. However, the latter are typically more structured than the former and better diffuse the saturation from the methyl ''injection source''.[103] Thus, the primary effect of this weak RF pulse is preferential saturation of the oligomers. The saturation propagates through spin diffusion from the methyls to the rest of the Aβ oligomers as well as to any other molecules that are bound to them. A simplified version of this scheme is shown in Fig. 4, where saturation injection is schematically depicted as starting from the oligomers (Fig. 4, red). The oligomer saturation is then transferred to the protons of ligands bound to the oligomers, where the extent of saturation transfer to a specific ligand proton is dependent on the proximity to the

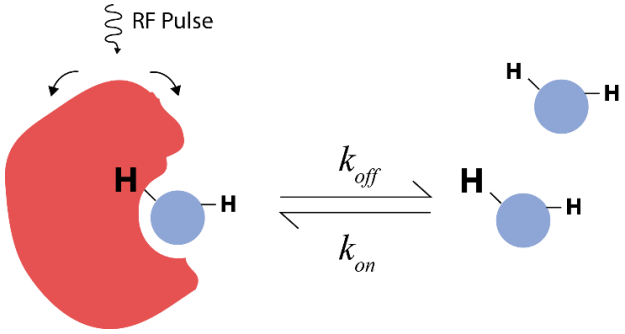

Figure 4. Schematic representation of the Saturation Transfer Difference (STD) NMR method.

oligomer (Fig. 4, black). Once the ligand dissociates from the oligomer surface, the loss in ligand proton signal in the spectra with on vs. off-resonance saturation is detected in the STD spectrum.

In case the saturation by the on-resonance RF field leaks through to the ligand signals resonating close to the saturation frequency, it is advisable to acquire a control STD spectrum for ligand only, in the absence of Aβ peptide. The control STD signal is then subtracted from the STD spectrum recorded for the ligand in the presence of Aβ oligomers. This double difference spectrum typically reflects saturation genuinely arising from oligomers as opposed to poor selectivity of the on-resonance RF field. Hence, the STD experiment probes the binding of ligands to Aβ oligomers and also provides a map of the oligomer-binding epitopes within the ligand.[104]

The STD NMR approach was applied to the interaction of HSA with Aβ(12–28) oligomers. The multi-domain protein HSA competes with Aβ monomers for the binding to Aβ oligomers.[105] This competition reduces the amount of saturation transfer from the monomers to the oligomers and we observe a dose-dependent decrease in the STD signal that saturates at high HSA concentrations.[106] The comparative analysis of STD-monitored binding isotherms for HSA and domain-deletion mutants in terms of a Scatchard-like model yielded an effective site-specific K_d of ~160 nM with multiple independent and equivalent binding sites in HSA for Aβ(12–28) oligomers.[106] These results are in agreement with an orthogonal study through surface plasmon resonance (SPR) which reported a K_d for the Aβ42 oligomers in the mM–nM range, which varies with the effective size of the oligomers.[107] These K_d values are comparable to the concentration of HSA within the cerebrospinal fluid (CSF), approximately 3μM,[108] and several orders of magnitude lower than the albumin concentration in plasma (0.5–0.7 mM),[108] suggesting that HSA binds Aβ oligomers both in the brain and plasma. Nonetheless, the interactions with the oligomers represent only a subset of the possible microscopic steps in the self-association pathway that are perturbed by inhibitors. Itis critical to also evaluate the binding affinities of inhibitors for Aβ monomers.

1.6.1.2 Selectively Probing Monomer – Inhibitor Interactions

Given that the Aβ monomers are the entry point of the self-association pathway and are essentially non-toxic, they serve as a clinically relevant target for AD preventative strategies. However, due to Aβ being notoriously aggregation prone, it is difficult to isolate purely monomeric species to examine inhibitor interactions. Most preparation protocols involve multiple treatments with hexafluoroisopropanol (HFIP), ammonium hydroxide (NH4OH) or sodium hydroxide (NaOH) and/or isolation of monomeric fractions through size exclusion chromatography.[109] While these preparations create an essentially monomeric solution, they do not prevent further aggregation during the acquisition time of the experiments used to characterize the monomer–inhibitor interactions. These limitations pose major experimental challenges in probing monomer–inhibitor interactions without bias from Aβ oligomers. Thus, an experiment that selectively probes the monomers within a heterogenous sample is essential. In this regard, solution NMR chemical shifts are of advantage as they report primarily on Aβ monomers.[110] A solution NMR experiment that is often used to measure chemical shift and intensity changes arising from protein–ligand interactions is the $^{1}H–^{15}N$ Heteronuclear Single Quantum Coherence (HSQC).[111,112] The HSQC experiment resolves most of the H–N correlations within the protein and provides a residue-resolution map of the ligand interactions (Fig. 5a).

A $^{1}H–^{15}N$ HSQC chemical shift-based approach was utilized to probe the interaction of Aβ monomers with inhibitory proteins such as HSA.[113] However, unlike the binding of low MW inhibitors (MW < 1 kDa) to Aβ monomers, the binding of HSA (MW ~66.6 kDa) significantly slows down the Brownian rotational diffusion of the HSA–Aβ monomer complex and broadens the NMR signals of Aβ monomers beyond detection, resulting in HSQC signal losses. Nonetheless, we can take advantage of the NMR intensity losses and use the magnitude of the residual Aβ monomer NMR signal to report on the fraction of Aβ monomers bound to HSA. In this manner, we can develop a binding isotherm for the HSA–Aβ monomer interaction by monitoring the loss in Aβ NMR signal as a function of HSA concentration (Fig. 5b).[113] The average Aβ monomer intensity losses were probed for the central hydrophobic core (CHC) region spanning residues 16–24 as well as the C-terminus spanning residues 36–40. Although both the CHC and C-terminus exhibit intensity losses upon HSA addition, we observe a significantly greater intensity loss at the C-terminus suggesting HSA preferentially binds Aβ monomers at the C-terminus.[113] Moreover, there appears to be an Aβ monomer isoform-specific binding preference for HSA, as we observe an appreciably larger intensity loss for Aβ40 compared to Aβ42. Based on the HSQC NMR intensity losses, we found that HSA binds Aβ monomers with a K_d in the 0.1–1 mM range, where the K_d variation is dependent on the number of Aβ monomers bound to HSA.[113] However, one limitation of this experimental approach is that we rely on the loss of intensity, which is a rather indirect measure of the extent of HSA binding to Aβ monomers.

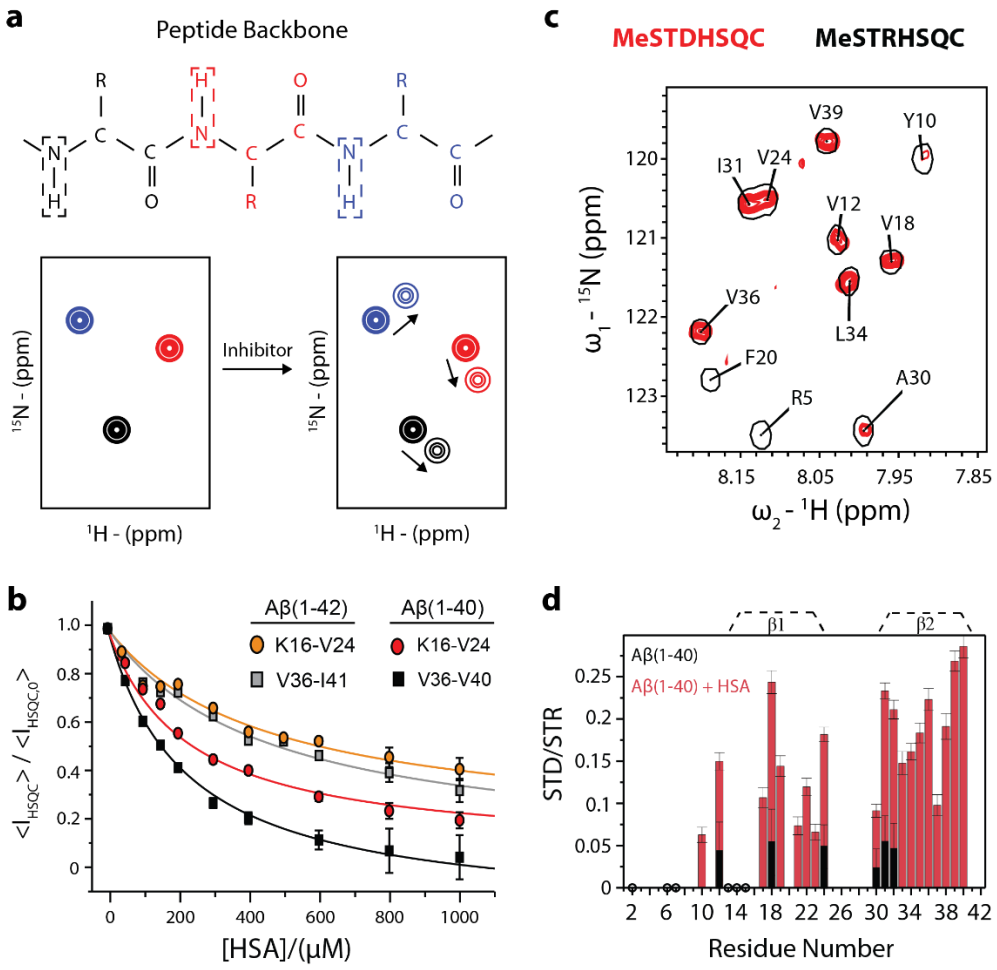

Figure 5. Proving the interactions of Aβ monomers with amyloid inhibitors, such as HSA. (a) Schematic representation of the bonds probed by ^{1}H-^{15}N HSQC NMR spectra. The dashed boxes indicate the protein backbone NHs detected by ^{1}H-^{15}N HSQC, which result in cross-peaks in the ^{1}H-^{15}N HSQC NMR spectra, and are colour coded to represent distinct amino acids. Inhibitor binding leads to change in chemical shifts and/or intensity losses within NMR spectra. (b) Average ^{1}H-^{15}N HSQC intensity losses of Aβ40 CHC (*red*) and C-terminal (*black*) residues and Aβ42 CHC (*orange*) and C-terminal (*grey*) residues as a function of HSA concentration. (c) Representative expansion of the MeSTDHSQC (*red*) spectrum superimposed onto the MeSTRHSQC (*black*) spectrum of Aβ40 in the presence of HSA. (d) Residue-specific STD: STR intensity ratios in the absence (*black*) and presence (*red*) of HSA.

To directly probe the binding of HSA to Aβ monomers, we combined the STD NMR experiment with the ^{1}H–^{15}N HSQC.[113,114] Briefly, we saturated the HSA methyl groups using a selective RF pulse and monitored the saturation transfer to uniformly labeled^{15}N–Aβ40 monomers which we detected using a ^{1}H–^{15}NHSQC read-out block. In this manner, the binding of HSA to Aβ monomers is detected as an HSA-induced enhancement in STD NMR signal of Aβ40 observed through the ^{1}H–^{15}N HSQC. The resultant MeSTDHSQC NMR experiment was used to map the binding site for HSA within Aβ40 monomers (Fig. 5c and d).[113] We observed a significant enhancement in Aβ40 monomer intensity in the CHC and C-terminus upon addition of HSA, consistent with the HSQC-intensity losses. Moreover, an MeSTDHSQC-based binding

isotherm was created as a control for the HSA–Aβ40 monomer interaction and provided an effective K_d in the sub-mM range, in agreement with the HSQC-based measurements.[113] It is important to note, that although weak, the affinity of HSA for Aβ monomers is

physiologically relevant as the concentration of HSA within blood plasma typically ranges between 0.5 and 0.7 mM.[108] Moving forward it will be important to evaluate how differences in monomer as well as oligomer binding affect the ability of amyloid inhibitors to reduces Aβ toxicity.

1.6.1.3 Probing the Surface Shielding of Aβ Oligomers

To probe the degree to which the oligomer surface is shielded from the environment, we quantified the on-off exchange of Aβ monomers from the oligomer surface (Fig. 6a).[113] For this purpose, we measured the ^{15}N-transverse relaxation rates (^{15}N-R_2) for both a dilute Aβ40 sample (monomer) and a concentrated Aβ40 sample (oligomer). The maximal difference in ^{15}N-R_2 between the monomeric and concentrated Aβ oligomer samples offers an approximation of the first-order association constant $k_{on,app}$ for the monomer–oligomer recognition.[100] We next measured the ^{15}N-R_2 for an oligomer sample in the presence of HSA and evaluated the change in $k_{on,\,app}$ due to HSA.[113] Notably, contributions arising from the binding of HSA to Aβ40 monomers is corrected for, and the modified ΔR_2 plot is shown in Fig. 6b. As seen in Fig. 6b, the Δ^{15}N-R_2 of Aβ40 upon HSA addition is for the most part within the experimental error margin of our R_2 data. Therefore, no significant changes in the first order association constant, $k_{on,\,app}$, for the recognition of monomers on the surface of oligomers occurs upon HSA addition. Nonetheless, a significant ΔR_2 enhancement is observed for select residues in the C-terminal region *e.g.* residues 37-40. This effect is consistent with Aβ monomers interacting with oligomer-bound HSA. One possible scenario includes one HSA domain interacting with Aβ monomers and a separate domain interacting with Aβ oligomers. However, $k_{on,\,app}$ is just a global parameter and reports on the overall change in the kinetics of Aβ monomer–oligomer contacts.[100]

To probe the residue-specific changes in Aβ monomer – oligomer contacts induced by HSA, we used Dark-state Exchange Saturation Transfer (^{15}N-based DEST) NMR.[110,115] A primary challenge in the evaluation of HSA-induced changes in the DEST profiles arises from possible biases due to instabilities of Aβ oligomers. Hence, we reduced DEST acquisition time by implementing the ^{15}N-DEST experiment in a simplified form, which is analogous to the MeSTDHSQC except that the on and off-resonance saturating RF fields are for the ^{15}N nuclei of amides rather than for the ^{1}H nuclei of methyls.[106,114] Considering that only the Aβ peptide is ^{15}N labeled, the ^{15}N saturation targets only Aβ oligomers.[106,114] The ^{15}N saturation transfer in DEST experiments was quantified similarly to the STD/STR ratio utilized to measure the extent of ^{1}H saturation transfer in the MeSTDHSQC experiments.

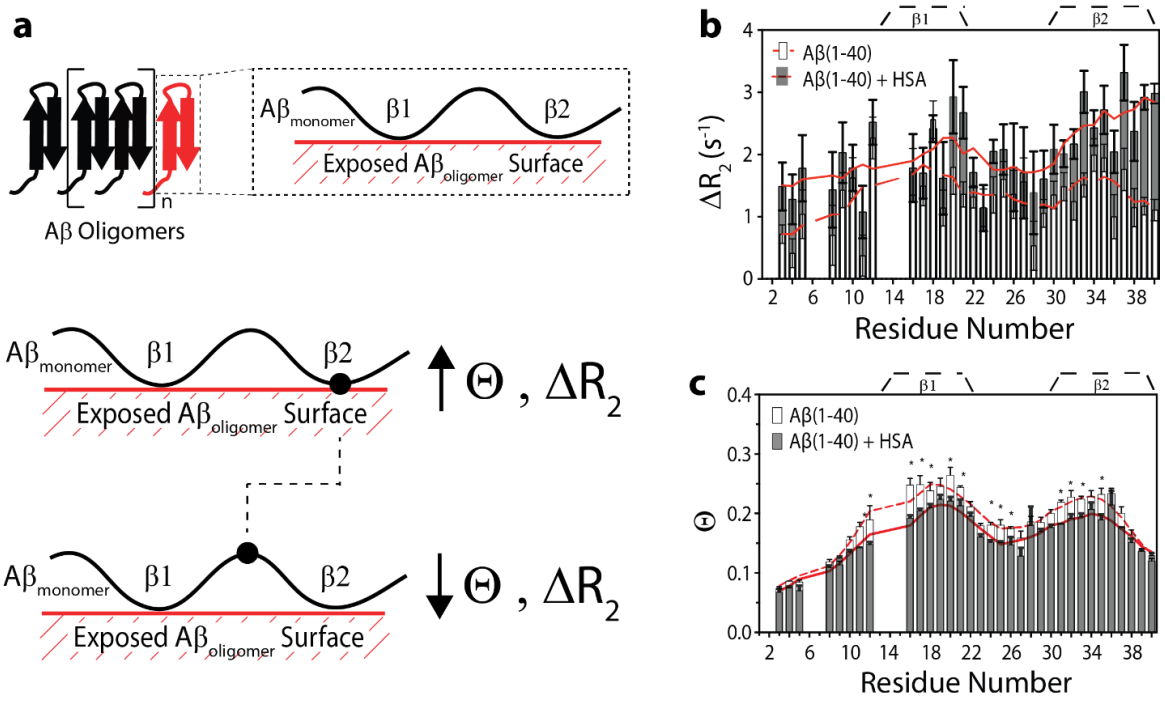

Figure 6. Probing surface shielding of Aβ oligomers in the presence of HSA. (a) Schematic representation of the probability of monomer – oligomer contacts as probed by ^{15}N Dark-state Exchange Saturation Transfer (DEST) (Θ) and ^{15}N transverse relaxation rate differences (ΔR_2) NMR. The red protomer in the oligomer represents a monomer exchanging with the oligomer surface, as represented in the dashed box. Black solid circles represent the amino acid of the monomer being probed by DEST and ΔR_2. Dashed line connecting black solid circles indicate change in perspective. (b) Differences in ^{15}N – R_2 values between dilute and concentrated Aβ40 samples, both samples either in the absence (*white*) or presence (*grey*) of HSA. Smoothed lines, calculated as the average ΔR_2 value for a given residue and the two residues directly adjacent to it, in the absence (*dashed red line*) and presence (*solid red line*) of HSA are displayed in front of the bars. (c) Θ values for a concentrated oligomeric Aβ40 sample in the absence (*white*) and presence (grey) of HSA. Smoothed lines are shown as in (b).

Specifically, the DEST difference, denoted here as Θ (Fig. 6a, *middle*), was calculated as:

$$\Theta = \frac{(I_{off} + I_{-off}) - (I_{on} + I_{-on})}{(I_{off} + I_{-off})} \quad (1)$$

where I_v denotes the peak height measured for a given residue at ^{15}N continuous wave offset of *v*kHz. The ^{15}N-DEST experiment measures the probability of a given Aβ monomer residue to be in contact with the Aβ oligomer surface (Fig. 6a).[110,114,115] The DEST Θ observable is expected to be higher for monomer residues in direct contact with the oligomer surface (Fig. 6a, *middle*) and lower for residues tethered to the oligomer surface (Fig. 6a, *bottom*). To probe the changes in the direct *vs.* tethered Aβ monomer – oligomer contact profile upon HSA addition, we performed the DEST experiment for a concentrated Aβ40 sample in the absence and presence of HSA (Fig. 6c). As seen in Fig. 6c, a global reduction in monomer –

oligomer contacts is observed upon HSA addition. Overall, our combined $^{15}N - R_2$ and ^{15}N – DEST NMR analyses indicate that HSA competes out monomer interactions and shields the β1 and β2 sites.

1.7 References

(1) Spillantini, M. G.; Schmidt, M. L.; Lee, V. M.; Trojanowski, J. Q.; Jakes, R.; Goedert, M. Alpha-synuclein in Lewy bodies. *Nature* **1997**, *388*, 839–840.

(2) DiFiglia, M.; Sapp, E.; Chase, K. O.; Davies, S. W.; Bates, G. P.; Vonsattel, J. P.; Aronin, N. Aggregation of huntingtin in neuronal intranuclear inclusions and dystrophic neurites in brain. *Science (New York, N.Y.)* **1997**, *277*, 1990–1993.

(3) John A. Hardy; Gerald A. Higgins. Alzheimer's disease: the amyloid cascade hypothesis. *Science* **1992**, *256*, 184–186.

(4) Benilova, I.; Karran, E.; Strooper, B. de. The toxic Aβ oligomer and Alzheimer's disease: an emperor in need of clothes. *Nature neuroscience* **2012**, *15*, 349–357.

(5) Polymeropoulos, M. H.; Lavedan, C.; Leroy, E.; Ide, S. E.; Dehejia, A.; Dutra, A.; Pike, B.; Root, H.; Rubenstein, J.; Boyer, R.*; et al.* Mutation in the alpha-synuclein gene identified in families with Parkinson's disease. *Science* **1997**, *276*, 2045–2047.

(6) Zarranz, J. J.; Alegre, J.; Gómez-Esteban, J. C.; Lezcano, E.; Ros, R.; Ampuero, I.; Vidal, L.; Hoenicka, J.; Rodriguez, O.; Atarés, B.*; et al.* The new mutation, E46K, of alpha-synuclein causes Parkinson and Lewy body dementia. *Annals of neurology* **2004**, *55*, 164–173.

(7) Farrer, M.; Kachergus, J.; Forno, L.; Lincoln, S.; Wang, D.-S.; Hulihan, M.; Maraganore, D.; Gwinn-Hardy, K.; Wszolek, Z.; Dickson, D.*; et al.* Comparison of kindreds with parkinsonism and alpha-synuclein genomic multiplications. *Annals of neurology* **2004**, *55*, 174–179.

(8) Chartier-Harlin, M.-C.; Kachergus, J.; Roumier, C.; Mouroux, V.; Douay, X.; Lincoln, S.; Levecque, C.; Larvor, L.; Andrieux, J.; Hulihan, M.*; et al.* α-synuclein locus duplication as a cause of familial Parkinson's disease. *The Lancet* **2004**, *364*, 1167–1169.

(9) Ibáñez, P.; Bonnet, A.-M.; Débarges, B.; Lohmann, E.; Tison, F.; Agid, Y.; Dürr, A.; Brice, A.; Pollak, P. Causal relation between α-synuclein locus duplication as a cause of familial Parkinson's disease. *The Lancet* **2004**, *364*, 1169–1171.

(10) MACDONALD, M. A novel gene containing a trinucleotide repeat that is expanded and unstable on Huntington's disease chromosomes. *Cell* **1993**, *72*, 971–983.

(11) Braak, H.; Rüb, U.; Gai, W. P.; Del Tredici, K. Idiopathic Parkinson's disease: possible routes by which vulnerable neuronal types may be subject to neuroinvasion by an unknown pathogen. *Journal of neural transmission (Vienna, Austria : 1996)* **2003**, *110*, 517–536.

(12) Braak, H.; Rüb, U.; Del Tredici, K. Cognitive decline correlates with neuropathological stage in Parkinson's disease. *Journal of the neurological sciences* **2006**, *248*, 255–258.

(13) Arnold, S. E.; Hyman, B. T.; Flory, J.; Damasio, A. R.; van Hoesen, G. W. The topographical and neuroanatomical distribution of neurofibrillary tangles and neuritic plaques in the cerebral cortex of patients with Alzheimer's disease. *Cerebral cortex (New York, N.Y. : 1991)* **1991**, *1*, 103–116.

(14) Braak, H.; Braak, E. Neuropathological stageing of Alzheimer-related changes. *Acta neuropathologica* **1991**, *82*, 239–259.

(15) Hyman, B. T.; van Hoesen, G. W.; Damasio, A. R.; Barnes, C. L. Alzheimer's disease: cell-specific pathology isolates the hippocampal formation. *Science* **1984**, *225*, 1168–1170.

(16) Arriagada, P. V.; Growdon, J. H.; Hedley-Whyte, E. T.; Hyman, B. T. Neurofibrillary tangles but not senile plaques parallel duration and severity of Alzheimer's disease. *Neurology* **1992**, *42*, 631–639.

(17) Bierer, L. M.; Hof, P. R.; Purohit, D. P.; Carlin, L.; Schmeidler, J.; Davis, K. L.; Perl, D. P. Neocortical neurofibrillary tangles correlate with dementia severity in Alzheimer's disease. *Archives of neurology* **1995**, *52*, 81–88.

(18) Giannakopoulos, P.; Herrmann, F. R.; Bussière, T.; Bouras, C.; Kövari, E.; Perl, D. P.; Morrison, J. H.; Gold, G.; Hof, P. R. Tangle and neuron numbers, but not amyloid load, predict cognitive status in Alzheimer's disease. *Neurology* **2003**, *60*, 1495–1500.
(19) Gómez-Isla, T.; Hollister, R.; West, H.; Mui, S.; Growdon, J. H.; Petersen, R. C.; Parisi, J. E.; Hyman, B. T. Neuronal loss correlates with but exceeds neurofibrillary tangles in Alzheimer's disease. *Annals of neurology* **1997**, *41*, 17–24.
(20) Ingelsson, M.; Fukumoto, H.; Newell, K. L.; Growdon, J. H.; Hedley-Whyte, E. T.; Frosch, M. P.; Albert, M. S.; Hyman, B. T.; Irizarry, M. C. Early Abeta accumulation and progressive synaptic loss, gliosis, and tangle formation in AD brain. *Neurology* **2004**, *62*, 925–931.
(21) Aizenstein, H. J.; Nebes, R. D.; Saxton, J. A.; Price, J. C.; Mathis, C. A.; Tsopelas, N. D.; Ziolko, S. K.; James, J. A.; Snitz, B. E.; Houck, P. R.; *et al*. Frequent amyloid deposition without significant cognitive impairment among the elderly. *Archives of neurology* **2008**, *65*, 1509–1517.
(22) Terry, R. D.; Masliah, E.; Salmon, D. P.; Butters, N.; DeTeresa, R.; Hill, R.; Hansen, L. A.; Katzman, R. Physical basis of cognitive alterations in Alzheimer's disease: synapse loss is the major correlate of cognitive impairment. *Annals of neurology* **1991**, *30*, 572–580.
(23) Hsia, A. Y.; Masliah, E.; McConlogue, L.; Yu, G. Q.; Tatsuno, G.; Hu, K.; Kholodenko, D.; Malenka, R. C.; Nicoll, R. A.; Mucke, L. Plaque-independent disruption of neural circuits in Alzheimer's disease mouse models. *Proceedings of the National Academy of Sciences of the United States of America* **1999**, *96*, 3228–3233.
(24) Westerman, M. A.; Cooper-Blacketer, D.; Mariash, A.; Kotilinek, L.; Kawarabayashi, T.; Younkin, L. H.; Carlson, G. A.; Younkin, S. G.; Ashe, K. H. The Relationship between Aβ and Memory in the Tg2576 Mouse Model of Alzheimer's Disease. *J. Neurosci.* **2002**, *22*, 1858–1867.
(25) Kuo, Y. M.; Emmerling, M. R.; Vigo-Pelfrey, C.; Kasunic, T. C.; Kirkpatrick, J. B.; Murdoch, G. H.; Ball, M. J.; Roher, A. E. Water-soluble Abeta (N-40, N-42) oligomers in normal and Alzheimer disease brains. *The Journal of biological chemistry* **1996**, *271*, 4077–4081.
(26) Podlisny, M. B.; Ostaszewski, B. L.; Squazzo, S. L.; Koo, E. H.; Rydell, R. E.; Teplow, D. B.; Selkoe, D. J. Aggregation of secreted amyloid beta-protein into sodium dodecyl sulfate-stable oligomers in cell culture. *The Journal of biological chemistry* **1995**, *270*, 9564–9570.
(27) Roher, A. E.; Chaney, M. O.; Kuo, Y. M.; Webster, S. D.; Stine, W. B.; Haverkamp, L. J.; Woods, A. S.; Cotter, R. J.; Tuohy, J. M.; Krafft, G. A.; *et al*. Morphology and toxicity of Abeta-(1-42) dimer derived from neuritic and vascular amyloid deposits of Alzheimer's disease. *The Journal of biological chemistry* **1996**, *271*, 20631–20635.
(28) Lambert, M. P.; Barlow, A. K.; Chromy, B. A.; Edwards, C.; Freed, R.; Liosatos, M.; Morgan, T. E.; Rozovsky, I.; Trommer, B.; Viola, K. L.; *et al*. Diffusible, nonfibrillar ligands derived from Abeta1-42 are potent central nervous system neurotoxins. *Proceedings of the National Academy of Sciences of the United States of America* **1998**, *95*, 6448–6453.
(29) Kayed, R.; Head, E.; Thompson, J. L.; McIntire, T. M.; Milton, S. C.; Cotman, C. W.; Glabe, C. G. Common structure of soluble amyloid oligomers implies common mechanism of pathogenesis. *Science (New York, N.Y.)* **2003**, *300*, 486–489.
(30) Georganopoulou, D. G.; Chang, L.; Nam, J.-M.; Thaxton, C. S.; Mufson, E. J.; Klein, W. L.; Mirkin, C. A. Nanoparticle-based detection in cerebral spinal fluid of a soluble pathogenic biomarker for Alzheimer's disease. *Proceedings of the National Academy of Sciences of the United States of America* **2005**, *102*, 2273–2276.
(31) Tomic, J. L.; Pensalfini, A.; Head, E.; Glabe, C. G. Soluble fibrillar oligomer levels are elevated in Alzheimer's disease brain and correlate with cognitive dysfunction. *Neurobiology of disease* **2009**, *35*, 352–358.
(32) Jin, M.; Shepardson, N.; Yang, T.; Chen, G.; Walsh, D.; Selkoe, D. J. Soluble amyloid beta-protein dimers isolated from Alzheimer cortex directly induce Tau hyperphosphorylation and neuritic degeneration. *Proceedings of the National Academy of Sciences of the United States of America* **2011**, *108*, 5819–5824.

(33) Felice, F. G. de; Wu, D.; Lambert, M. P.; Fernandez, S. J.; Velasco, P. T.; Lacor, P. N.; Bigio, E. H.; Jerecic, J.; Acton, P. J.; Shughrue, P. J.; *et al.* Alzheimer's disease-type neuronal tau hyperphosphorylation induced by A beta oligomers. *Neurobiology of aging* **2008**, *29*, 1334–1347.
(34) Serrano-Pozo, A.; William, C. M.; Ferrer, I.; Uro-Coste, E.; Delisle, M.-B.; Maurage, C.-A.; Hock, C.; Nitsch, R. M.; Masliah, E.; Growdon, J. H.; *et al.* Beneficial effect of human anti-amyloid-beta active immunization on neurite morphology and tau pathology. *Brain* **2010**, *133*, 1312–1327.
(35) Pooler, A. M.; Polydoro, M.; Maury, E. A.; Nicholls, S. B.; Reddy, S. M.; Wegmann, S.; William, C.; Saqran, L.; Cagsal-Getkin, O.; Pitstick, R.; *et al.* Amyloid accelerates tau propagation and toxicity in a model of early Alzheimer's disease. *Acta Neuropathologica Communications* **2015**, *3*, 14.
(36) Parkkinen, L.; Pirttilä, T.; Tervahauta, M.; Alafuzoff, I. Widespread and abundant alpha-synuclein pathology in a neurologically unimpaired subject. *Neuropathology : official journal of the Japanese Society of Neuropathology* **2005**, *25*, 304–314.
(37) Frigerio, R.; Fujishiro, H.; Ahn, T.-B.; Josephs, K. A.; Maraganore, D. M.; DelleDonne, A.; Parisi, J. E.; Klos, K. J.; Boeve, B. F.; Dickson, D. W.; *et al.* Incidental Lewy body disease: do some cases represent a preclinical stage of dementia with Lewy bodies? *Neurobiology of aging* **2011**, *32*, 857–863.
(38) Parkkinen, L.; Pirttilä, T.; Alafuzoff, I. Applicability of current staging/categorization of alpha-synuclein pathology and their clinical relevance. *Acta neuropathologica* **2008**, *115*, 399–407.
(39) Colosimo, C.; Hughes, A. J.; Kilford, L.; Lees, A. J. Lewy body cortical involvement may not always predict dementia in Parkinson's disease. *Journal of Neurology, Neurosurgery, and Psychiatry* **2003**, *74*, 852–856.
(40) Karpinar, D. P.; Balija, M. B. G.; Kügler, S.; Opazo, F.; Rezaei-Ghaleh, N.; Wender, N.; Kim, H.-Y.; Taschenberger, G.; Falkenburger, B. H.; Heise, H.; *et al.* Pre-fibrillar alpha-synuclein variants with impaired beta-structure increase neurotoxicity in Parkinson's disease models. *The EMBO Journal* **2009**, *28*, 3256–3268.
(41) Winner, B.; Jappelli, R.; Maji, S. K.; Desplats, P. A.; Boyer, L.; Aigner, S.; Hetzer, C.; Loher, T.; Vilar, M.; Campioni, S.; *et al.* In vivo demonstration that alpha-synuclein oligomers are toxic. *Proceedings of the National Academy of Sciences of the United States of America* **2011**, *108*, 4194–4199.
(42) Sharon, R.; Bar-Joseph, I.; Frosch, M. P.; Walsh, D. M.; Hamilton, J. A.; Selkoe, D. J. The Formation of Highly Soluble Oligomers of α-Synuclein Is Regulated by Fatty Acids and Enhanced in Parkinson's Disease. *Neuron* **2003**, *37*, 583–595.
(43) Choi, B.-K.; Choi, M.-G.; Kim, J.-Y.; Yang, Y.; Lai, Y.; Kweon, D.-H.; Lee, N. K.; Shin, Y.-K. Large α-synuclein oligomers inhibit neuronal SNARE-mediated vesicle docking. *Proceedings of the National Academy of Sciences of the United States of America* **2013**, *110*, 4087–4092.
(44) Rockenstein, E.; Nuber, S.; Overk, C. R.; Ubhi, K.; Mante, M.; Patrick, C.; Adame, A.; Trejo-Morales, M.; Gerez, J.; Picotti, P.; *et al.* Accumulation of oligomer-prone α-synuclein exacerbates synaptic and neuronal degeneration in vivo. *Brain* **2014**, *137*, 1496–1513.
(45) Lee, H.-J.; Bae, E.-J.; Lee, S.-J. Extracellular α--synuclein-a novel and crucial factor in Lewy body diseases. *Nature reviews. Neurology* **2014**, *10*, 92–98.
(46) Ma, J.; Gao, J.; Wang, J.; Xie, A. Prion-Like Mechanisms in Parkinson's Disease. *Frontiers in neuroscience* **2019**, *13*, 552.
(47) Luk, K. C.; Kehm, V.; Carroll, J.; Zhang, B.; O'Brien, P.; Trojanowski, J. Q.; Lee, V. M.-Y. Pathological α-Synuclein Transmission Initiates Parkinson-like Neurodegeneration in Non-transgenic Mice. *Science (New York, N.Y.)* **2012**, *338*, 949–953.
(48) Volpicelli-Daley, L. A.; Luk, K. C.; Patel, T. P.; Tanik, S. A.; Riddle, D. M.; Stieber, A.; Meaney, D. F.; Trojanowski, J. Q.; Lee, V. M.-Y. Exogenous α-synuclein fibrils induce Lewy body pathology leading to synaptic dysfunction and neuron death. *Neuron* **2011**, *72*, 57–71.
(49) Braak, H.; Tredici, K. D.; Rüb, U.; Vos, R. A.I. de; Jansen Steur, E. N.H.; Braak, E. Staging of brain pathology related to sporadic Parkinson's disease. *Neurobiology of aging* **2003**, *24*, 197–211.

(50) Li, J.-Y.; Englund, E.; Holton, J. L.; Soulet, D.; Hagell, P.; Lees, A. J.; Lashley, T.; Quinn, N. P.; Rehncrona, S.; Björklund, A.; *et al*. Lewy bodies in grafted neurons in subjects with Parkinson's disease suggest host-to-graft disease propagation. *Nature medicine* **2008**, *14*, 501–503.
(51) Kordower, J. H.; Chu, Y.; Hauser, R. A.; Olanow, C. W.; Freeman, T. B. Transplanted dopaminergic neurons develop PD pathologic changes: a second case report. *Movement disorders : official journal of the Movement Disorder Society* **2008**, *23*, 2303–2306.
(52) Angot, E.; Steiner, J. A.; Lema Tomé, C. M.; Ekström, P.; Mattsson, B.; Björklund, A.; Brundin, P. Alpha-synuclein cell-to-cell transfer and seeding in grafted dopaminergic neurons in vivo. *PloS one* **2012**, *7*, e39465.
(53) Hansen, C.; Angot, E.; Bergström, A.-L.; Steiner, J. A.; Pieri, L.; Paul, G.; Outeiro, T. F.; Melki, R.; Kallunki, P.; Fog, K.; *et al*. α-Synuclein propagates from mouse brain to grafted dopaminergic neurons and seeds aggregation in cultured human cells. *The Journal of clinical investigation* **2011**, *121*, 715–725.
(54) Bernis, M. E.; Babila, J. T.; Breid, S.; Wüsten, K. A.; Wüllner, U.; Tamgüney, G. Prion-like propagation of human brain-derived alpha-synuclein in transgenic mice expressing human wild-type alpha-synuclein. *Acta Neuropathologica Communications* **2015**, *3*, 75.
(55) El-Agnaf, O. M. A.; Salem, S. A.; Paleologou, K. E.; Curran, M. D.; Gibson, M. J.; Court, J. A.; Schlossmacher, M. G.; Allsop, D. Detection of oligomeric forms of alpha-synuclein protein in human plasma as a potential biomarker for Parkinson's disease. *FASEB journal : official publication of the Federation of American Societies for Experimental Biology* **2006**, *20*, 419–425.
(56) Borghi, R.; Marchese, R.; Negro, A.; Marinelli, L.; Forloni, G.; Zaccheo, D.; Abbruzzese, G.; Tabaton, M. Full length α-synuclein is present in cerebrospinal fluid from Parkinson's disease and normal subjects. *Neuroscience Letters* **2000**, *287*, 65–67.
(57) Lee, H.-J.; Patel, S.; Lee, S.-J. Intravesicular localization and exocytosis of alpha-synuclein and its aggregates. *J. Neurosci.* **2005**, *25*, 6016–6024.
(58) Danzer, K. M.; Kranich, L. R.; Ruf, W. P.; Cagsal-Getkin, O.; Winslow, A. R.; Zhu, L.; Vanderburg, C. R.; McLean, P. J. Exosomal cell-to-cell transmission of alpha synuclein oligomers. *Molecular neurodegeneration* **2012**, *7*, 42.
(59) LaFerla, F. M.; Green, K. N.; Oddo, S. Intracellular amyloid-beta in Alzheimer's disease. *Nature reviews. Neuroscience* **2007**, *8*, 499–509.
(60) Younkin, S. G. The role of Aβ42 in Alzheimer's disease. *Journal of Physiology-Paris* **1998**, *92*, 289–292.
(61) Greenberg, S. M.; Bacskai, B. J.; Hernandez-Guillamon, M.; Pruzin, J.; Sperling, R.; van Veluw, S. J. Cerebral amyloid angiopathy and Alzheimer disease - one peptide, two pathways. *Nature reviews. Neurology* **2020**, *16*, 30–42.
(62) Hilbich, C.; Kisters-Woike, B.; Reed, J.; Masters, C. L.; Beyreuther, K. Substitutions of hydrophobic amino acids reduce the amyloidogenicity of Alzheimer's disease βA4 peptides. *Journal of Molecular Biology* **1992**, *228*, 460–473.
(63) Ma, B.; Nussinov, R. Stabilities and conformations of Alzheimer's beta -amyloid peptide oligomers (Abeta 16-22, Abeta 16-35, and Abeta 10-35): Sequence effects. *Proceedings of the National Academy of Sciences of the United States of America* **2002**, *99*, 14126–14131.
(64) Lührs, T.; Ritter, C.; Adrian, M.; Riek-Loher, D.; Bohrmann, B.; Döbeli, H.; Schubert, D.; Riek, R. 3D structure of Alzheimer's amyloid-beta(1-42) fibrils. *Proceedings of the National Academy of Sciences of the United States of America* **2005**, *102*, 17342–17347.
(65) Coles, M.; Bicknell, W.; Watson, A. A.; Fairlie, D. P.; Craik, D. J. Solution structure of amyloid beta-peptide(1-40) in a water-micelle environment. Is the membrane-spanning domain where we think it is? *Biochemistry* **1998**, *37*, 11064–11077.
(66) Lee, S. J. C.; Nam, E.; Lee, H. J.; Savelieff, M. G.; Lim, M. H. Towards an understanding of amyloid-β oligomers: characterization, toxicity mechanisms, and inhibitors. *Chemical Society reviews* **2017**, *46*, 310–323.
(67) Faller, P.; Hureau, C.; Berthoumieu, O. Role of metal ions in the self-assembly of the Alzheimer's amyloid-β peptide. *Inorganic chemistry* **2013**, *52*, 12193–12206.

(68) Ono, K.; Condron, M. M.; Teplow, D. B. Effects of the English (H6R) and Tottori (D7N) familial Alzheimer disease mutations on amyloid beta-protein assembly and toxicity. *The Journal of biological chemistry* **2010**, *285*, 23186–23197.
(69) Paravastu, A. K.; Leapman, R. D.; Yau, W.-M.; Tycko, R. Molecular structural basis for polymorphism in Alzheimer's beta-amyloid fibrils. *Proceedings of the National Academy of Sciences of the United States of America* **2008**, *105*, 18349–18354.
(70) Davidson, W. S.; Jonas, A.; Clayton, D. F.; George, J. M. Stabilization of alpha-synuclein secondary structure upon binding to synthetic membranes. *The Journal of biological chemistry* **1998**, *273*, 9443–9449.
(71) Fusco, G.; Simone, A. de; Gopinath, T.; Vostrikov, V.; Vendruscolo, M.; Dobson, C. M.; Veglia, G. Direct observation of the three regions in α-synuclein that determine its membrane-bound behaviour. *Nature communications* **2014**, *5*, 3827.
(72) Ulmer, T. S.; Bax, A.; Cole, N. B.; Nussbaum, R. L. Structure and dynamics of micelle-bound human alpha-synuclein. *The Journal of biological chemistry* **2005**, *280*, 9595–9603.
(73) Bussell, R.; Eliezer, D. A Structural and Functional Role for 11-mer Repeats in α-Synuclein and Other Exchangeable Lipid Binding Proteins. *Journal of Molecular Biology* **2003**, *329*, 763–778.
(74) Giuliana Fusco; Tillmann Pape; Amberley D. Stephens; Pierre Mahou; Ana Rita Costa; Clemens F. Kaminski; Gabriele S. Kaminski Schierle; Michele Vendruscolo; Gianluigi Veglia; Christopher M. Dobson; *et al.* Structural basis of synaptic vesicle assembly promoted by α-synuclein. *Nat Commun* **2016**, *7*, 1–12.
(75) Fusco, G.; Chen, S. W.; Williamson, P. T. F.; Cascella, R.; Perni, M.; Jarvis, J. A.; Cecchi, C.; Vendruscolo, M.; Chiti, F.; Cremades, N.; *et al.* Structural basis of membrane disruption and cellular toxicity by α-synuclein oligomers. *Science (New York, N.Y.)* **2017**, *358*, 1440–1443.
(76) Bodner, C. R.; Maltsev, A. S.; Dobson, C. M.; Bax, A. Differential Phospholipid Binding of α-Synuclein Variants Implicated in Parkinson's Disease Revealed by Solution NMR Spectroscopy†. *Biochemistry* **2009**, *49*, 862–871.
(77) Bisaglia, M.; Tessari, I.; Mammi, S.; Bubacco, L. Interaction between alpha-synuclein and metal ions, still looking for a role in the pathogenesis of Parkinson's disease. *Neuromolecular medicine* **2009**, *11*, 239–251.
(78) Francois-Xavier Theillet; Andres Binolfi; Beata Bekei; Andrea Martorana; Honor May Rose; Marchel Stuiver; Silvia Verzini; Dorothea Lorenz; Marleen van Rossum; Daniella Goldfarb; *et al.* Structural disorder of monomeric α-synuclein persists in mammalian cells. *Nature* **2016**, *530*, 45–50.
(79) Dedmon, M. M.; Lindorff-Larsen, K.; Christodoulou, J.; Vendruscolo, M.; Dobson, C. M. Mapping long-range interactions in alpha-synuclein using spin-label NMR and ensemble molecular dynamics simulations. *Journal of the American Chemical Society* **2005**, *127*, 476–477.
(80) Du, H.-N.; Tang, L.; Luo, X.-Y.; Li, H.-T.; Hu, J.; Zhou, J.-W.; Hu, H.-Y. A peptide motif consisting of glycine, alanine, and valine is required for the fibrillization and cytotoxicity of human alpha-synuclein. *Biochemistry* **2003**, *42*, 8870–8878.
(81) Giasson, B. I.; Murray, I. V.; Trojanowski, J. Q.; Lee, V. M. A hydrophobic stretch of 12 amino acid residues in the middle of alpha-synuclein is essential for filament assembly. *The Journal of biological chemistry* **2001**, *276*, 2380–2386.
(82) Periquet, M.; Fulga, T.; Myllykangas, L.; Schlossmacher, M. G.; Feany, M. B. Aggregated α-Synuclein Mediates Dopaminergic Neurotoxicity In Vivo. *J. Neurosci.* **2007**, *27*, 3338–3346.
(83) Biere, A. L.; Wood, S. J.; Wypych, J.; Steavenson, S.; Jiang, Y.; Anafi, D.; Jacobsen, F. W.; Jarosinski, M. A.; Wu, G. M.; Louis, J. C.; *et al.* Parkinson's disease-associated alpha-synuclein is more fibrillogenic than beta- and gamma-synuclein and cannot cross-seed its homologs. *The Journal of biological chemistry* **2000**, *275*, 34574–34579.
(84) Rivers, R. C.; Kumita, J. R.; Tartaglia, G. G.; Dedmon, M. M.; Pawar, A.; Vendruscolo, M.; Dobson, C. M.; Christodoulou, J. Molecular determinants of the aggregation behavior of alpha- and beta-synuclein. *Protein science : a publication of the Protein Society* **2008**, *17*, 887–898.

(85) Ahmed, M.; Davis, J.; Aucoin, D.; Sato, T.; Ahuja, S.; Aimoto, S.; Elliott, J. I.; van Nostrand, W. E.; Smith, S. O. Structural conversion of neurotoxic amyloid-beta(1-42) oligomers to fibrils. *Nature structural & molecular biology* **2010**, *17*, 561–567.
(86) Chimon, S.; Shaibat, M. A.; Jones, C. R.; Calero, D. C.; Aizezi, B.; Ishii, Y. Evidence of fibril-like β-sheet structures in a neurotoxic amyloid intermediate of Alzheimer's β-amyloid. *Nature structural & molecular biology* **2007**, *14*, 1157–1164.
(87) Kotler, S. A.; Walsh, P.; Brender, J. R.; Ramamoorthy, A. Differences between amyloid-β aggregation in solution and on the membrane: insights into elucidation of the mechanistic details of Alzheimer's disease. *Chemical Society reviews* **2014**, *43*, 6692–6700.
(88) Chiti, F.; Dobson, C. M. Protein Misfolding, Amyloid Formation, and Human Disease: A Summary of Progress Over the Last Decade. *Annual review of biochemistry* **2017**, *86*, 27–68.
(89) Ambroggio, E. E.; Kim, D. H.; Separovic, F.; Barrow, C. J.; Barnham, K. J.; Bagatolli, L. A.; Fidelio, G. D. Surface behavior and lipid interaction of Alzheimer beta-amyloid peptide 1-42: a membrane-disrupting peptide. *Biophysical Journal* **2005**, *88*, 2706–2713.
(90) Sciacca, M. F. M.; Kotler, S. A.; Brender, J. R.; Chen, J.; Lee, D.-k.; Ramamoorthy, A. Two-step mechanism of membrane disruption by Aβ through membrane fragmentation and pore formation. *Biophysical Journal* **2012**, *103*, 702–710.
(91) Miller, Y.; Ma, B.; Tsai, C.-J.; Nussinov, R. Hollow core of Alzheimer's Abeta42 amyloid observed by cryoEM is relevant at physiological pH. *Proceedings of the National Academy of Sciences of the United States of America* **2010**, *107*, 14128–14133.
(92) Quist, A.; Doudevski, I.; Lin, H.; Azimova, R.; Ng, D.; Frangione, B.; Kagan, B.; Ghiso, J.; Lal, R. Amyloid ion channels: a common structural link for protein-misfolding disease. *Proceedings of the National Academy of Sciences of the United States of America* **2005**, *102*, 10427–10432.
(93) Um, J. W.; Nygaard, H. B.; Heiss, J. K.; Kostylev, M. A.; Stagi, M.; Vortmeyer, A.; Wisniewski, T.; Gunther, E. C.; Strittmatter, S. M. Alzheimer amyloid-β oligomer bound to postsynaptic prion protein activates Fyn to impair neurons. *Nature neuroscience* **2012**, *15*, 1227–1235.
(94) Chen, S. W.; Drakulic, S.; Deas, E.; Ouberai, M.; Aprile, F. A.; Arranz, R.; Ness, S.; Roodveldt, C.; Guilliams, T.; De-Genst, E. J.; *et al.* Structural characterization of toxic oligomers that are kinetically trapped during α-synuclein fibril formation. *Proceedings of the National Academy of Sciences of the United States of America* **2015**, *112*, E1994-2003.
(95) Linse, S. Monomer-dependent secondary nucleation in amyloid formation. *Biophysical Reviews* **2017**, *9*, 329–338.
(96) Sun, Y.; Hung, W.-C.; Chen, F.-Y.; Lee, C.-C.; Huang, H. W. Interaction of tea catechin (-)-epigallocatechin gallate with lipid bilayers. *Biophysical Journal* **2009**, *96*, 1026–1035.
(97) Cascella, M.; Bimonte, S.; Muzio, M. R.; Schiavone, V.; Cuomo, A. The efficacy of Epigallocatechin-3-gallate (green tea) in the treatment of Alzheimer's disease: an overview of pre-clinical studies and translational perspectives in clinical practice. *Infectious agents and cancer* **2017**, *12*, 36.
(98) Mannini, B.; Cascella, R.; Zampagni, M.; van Waarde-Verhagen, M.; Meehan, S.; Roodveldt, C.; Campioni, S.; Boninsegna, M.; Penco, A.; Relini, A.; *et al.* Molecular mechanisms used by chaperones to reduce the toxicity of aberrant protein oligomers. *Proceedings of the National Academy of Sciences of the United States of America* **2012**, *109*, 12479–12484.
(99) Vallurupalli, P.; Bouvignies, G.; Kay, L. E. Studying "invisible" excited protein states in slow exchange with a major state conformation. *Journal of the American Chemical Society* **2012**, *134*, 8148–8161.
(100) Fawzi, N. L.; Ying, J.; Torchia, D. A.; Clore, G. M. Kinetics of amyloid beta monomer-to-oligomer exchange by NMR relaxation. *Journal of the American Chemical Society* **2010**, *132*, 9948–9951.
(101) Bhunia, A.; Bhattacharjya, S.; Chatterjee, S. Applications of saturation transfer difference NMR in biological systems. *Drug discovery today* **2012**, *17*, 505–513.
(102) Mayer, M.; Meyer, B. Characterization of Ligand Binding by Saturation Transfer Difference NMR Spectroscopy. *Angew. Chem. Int. Ed.* **1999**, *38*, 1784–1788.

(103) Huang, H.; Milojevic, J.; Melacini, G. Analysis and optimization of saturation transfer difference NMR experiments designed to map early self-association events in amyloidogenic peptides. *The journal of physical chemistry. B* **2008**, *112*, 5795–5802.
(104) Mayer, M.; Meyer, B. Group epitope mapping by saturation transfer difference NMR to identify segments of a ligand in direct contact with a protein receptor. *Journal of the American Chemical Society* **2001**, *123*, 6108–6117.
(105) Milojevic, J.; Raditsis, A.; Melacini, G. Human serum albumin inhibits Abeta fibrillization through a "monomer-competitor" mechanism. *Biophysical Journal* **2009**, *97*, 2585–2594.
(106) Milojevic, J.; Melacini, G. Stoichiometry and affinity of the human serum albumin-Alzheimer's Aβ peptide interactions. *Biophysical Journal* **2011**, *100*, 183–192.
(107) Wang, C.; Cheng, F.; Xu, L.; Jia, L. HSA targets multiple Aβ42 species and inhibits the seeding-mediated aggregation and cytotoxicity of Aβ42 aggregates. *RSC Adv.* **2016**, *6*, 71165–71175.
(108) Bohrmann, B.; Tjernberg, L.; Kuner, P.; Poli, S.; Levet-Trafit, B.; Näslund, J.; Richards, G.; Huber, W.; Döbeli, H.; Nordstedt, C. Endogenous proteins controlling amyloid beta-peptide polymerization. Possible implications for beta-amyloid formation in the central nervous system and in peripheral tissues. *The Journal of biological chemistry* **1999**, *274*, 15990–15995.
(109) Ryan, T. M.; Caine, J.; Mertens, H. D. T.; Kirby, N.; Nigro, J.; Breheney, K.; Waddington, L. J.; Streltsov, V. A.; Curtain, C.; Masters, C. L.; *et al.* Ammonium hydroxide treatment of Aβ produces an aggregate free solution suitable for biophysical and cell culture characterization. *PeerJ* **2013**, *1*, e73.
(110) Fawzi, N. L.; Ying, J.; Ghirlando, R.; Torchia, D. A.; Clore, G. M. Atomic-resolution dynamics on the surface of amyloid-β protofibrils probed by solution NMR. *Nature* **2011**, *480*, 268–272.
(111) Boulton, S.; Melacini, G. Advances in NMR Methods To Map Allosteric Sites: From Models to Translation. *Chemical reviews* **2016**, *116*, 6267–6304.
(112) Williamson, M. P. Using chemical shift perturbation to characterise ligand binding. *Progress in nuclear magnetic resonance spectroscopy* **2013**, *73*, 1–16.
(113) Algamal, M.; Ahmed, R.; Jafari, N.; Ahsan, B.; Ortega, J.; Melacini, G. Atomic-resolution map of the interactions between an amyloid inhibitor protein and amyloid β (Aβ) peptides in the monomer and protofibril states. *The Journal of biological chemistry* **2017**, *292*, 17158–17168.
(114) Milojevic, J.; Esposito, V.; Das, R.; Melacini, G. Understanding the molecular basis for the inhibition of the Alzheimer's Abeta-peptide oligomerization by human serum albumin using saturation transfer difference and off-resonance relaxation NMR spectroscopy. *Journal of the American Chemical Society* **2007**, *129*, 4282–4290.
(115) Fawzi, N. L.; Ying, J.; Torchia, D. A.; Clore, G. M. Probing exchange kinetics and atomic resolution dynamics in high-molecular-weight complexes using dark-state exchange saturation transfer NMR spectroscopy. *Nature protocols* **2012**, *7*, 1523–1533.

Chapter 2. Molecular Mechanism for the (-)-Epigallocatechin gallate-induced Toxic to Non-toxic Remodeling of Aβ Oligomers

2.1 Author's Preface

The work presented in this chapter has previously been published and is reproduced here with permission from the Journal of the American Chemical Society. Full citation is as follows:

Ahmed, R.; VanSchouwen, B.; Jafari, N.; Ni, X.; Ortega, J.; Melacini, G. Molecular Mechanism for the (-)-Epigallocatechin Gallate-Induced Toxic to Nontoxic Remodeling of Aβ Oligomers. *J. Am. Chem. Soc.* **2017**, *139*, 13720–13734.

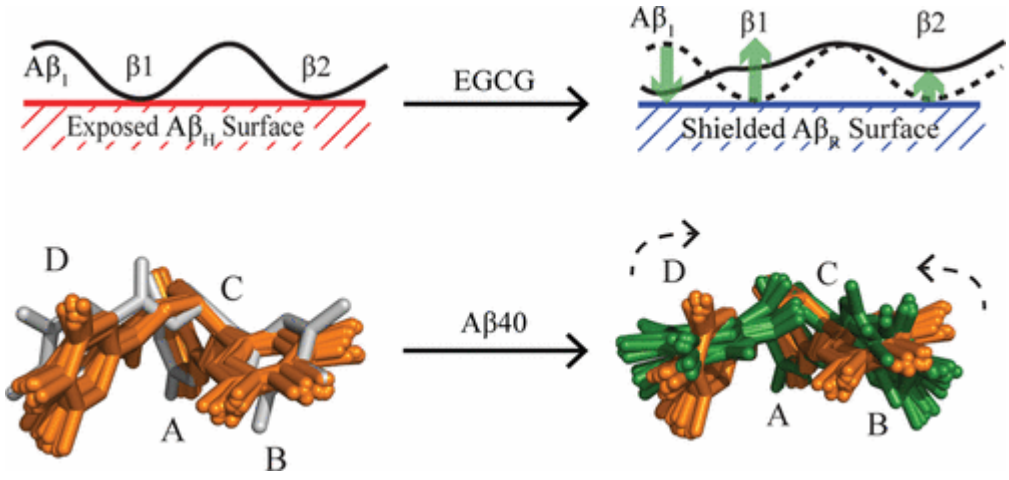

I conducted most of the experiments necessary for the manuscript and analyzed the data. Dr. Bryan VanSchouwen performed the MD simulations and grid search for the free and bound EGCG structures. Naeimeh Jafari provided helpful discussions. Dr. Xiaodan Ni acquired and analyzed the transmission electron microscopy data with support from Dr. Joaquin Ortega. I co-wrote the manuscript and designed the research with Dr. Giuseppe Melacini.

2.2 Abstract

(−)-Epigallocatechin gallate (EGCG) effectively reduces the cytotoxicity of the Alzheimer's disease β-amyloid peptide (Aβ) by remodeling seeding-competent Aβ oligomers into off-pathway seeding-incompetent Aβ assemblies. However, the mechanism of EGCG-induced remodeling is not fully understood. Here we combine ^{15}N and ^{1}H dark-state exchange saturation transfer (DEST), relaxation, and chemical shift projection NMR analyses with fluorescence, dynamic light scattering, and electron microscopy to elucidate how EGCG remodels Aβ oligomers. We show that the remodeling adheres to a Hill−Scatchard model whereby the Aβ(1−40) self-association occurs cooperatively and generates Aβ(1−40) oligomers with multiple independent binding sites for EGCG with a Kd∼10-fold lower than that for the Aβ(1−40) monomers. Upon binding to EGCG, the Aβ(1−40) oligomers become less solvent exposed, and the β-regions, which are involved in direct monomer−protofibril contacts in the absence of EGCG, undergo a direct-to-tethered contact shift. This switch toward less engaged monomer−protofibril contacts explains the seeding incompetency observed upon EGCG remodeling and suggests that EGCG interferes with secondary nucleation events known to generate toxic Aβ assemblies. Unexpectedly, the N-terminal residues experience an opposite EGCG-induced shift from tethered to direct contacts, explaining why EGCG remodeling occurs without release of Aβ(1−40) monomers. We also show that upon binding Aβ(1−40) oligomers the relative positions of the EGCG B and D rings change with respect to that of ring A. These distinct structural changes occurring in both Aβ(1−40) oligomers and EGCG during remodeling offer a foundation for understanding the molecular mechanism of EGCG as a neurotoxicity inhibitor. Furthermore, the results reported here illustrate the effectiveness of DEST-based NMR approaches in investigating the mechanism of low-molecular-weight amyloid inhibitors.

2.3 Introduction

Protein misfolding and the consequent self-association into toxic oligomers and amyloid deposits are central elements of the etiology of a wide range of disorders, from type II diabetes to neurodegenerative conditions such as Alzheimer's disease.[1–7] Understanding how small molecules modulate the self-association pathways of amyloidogenic polypeptides is therefore of pathological and pharmacological relevance.[8–21] Among the small molecules with the most promising therapeutic potential is the polyphenol (–)-epigallocatechin gallate (EGCG) extracted from green tea.[8,9,12,16,17] EGCG inhibits the formation of toxic, seeding-competent, on-pathway intermediates arising from the self-association of amyloidogenic peptides and stabilizes nontoxic, seeding-incompetent, off-pathway oligomers.[9–11,13–15,18] This reduction in cellular toxicity is observed also in the presence of preformed, mature amyloid fibrils and oligomers, which are bound by EGCG and are effectively remodeled into smaller and less toxic off-pathwayassemblies.[8]

The ability of EGCG to bind and redirect amyloidogenic peptides in either the early or late stages of self-association into non-neurotoxic assemblies (Figure 1) has prompted intense scrutiny of the complexes formed by EGCG and amyloidogenicpeptides.[8,9,12] Solid-state NMR (ssNMR) has provided an important initial picture of how EGCG remodels the oligomers formed by the prototypical amyloidogenic peptide Aβ(1−40) linked to Alzheimer's disease, denoted here as Aβ40. On the basis of the ssNMR data, it is clear that the EGCG-induced Aβ40 oligomers preserve a β-sheet structure for residues 29−36 and an intact salt bridge between D23 and K28. The latter stabilizes a hairpin spanning residues ∼23−28,[12] similar to what has been observed for mature cross-β fibrils and toxic Aβ oligomers in the absence of EGCG.[22,23] These observations indicate that the effect of EGCG on the structure of the C-terminal Aβ40 residues alone is insufficient to fully explain how EGCG remodels Aβ40 into nontoxic assemblies; *i.e.* the toxicity reduction elicited by EGCG arises from perturbations of other aspects of Aβ40 oligomers. For example, EGCG may perturb the dynamic contacts of Aβ40 monomers with the surface of Aβ40 protofibrils and/or affect regions that are invisible to ssNMR. These include the N-terminal Aβ40 region spanning residues 1−21, which could not be identified by ssNMR in the presence of EGCG due to broadening caused by static disorder.[12]

A further clue supporting the hypothesis that EGCG perturbs the N-terminal Aβ40 residues is provided by preliminary solution NMR studies[12,16] on monomeric Aβ40, which revealed that some of the most significant EGCG-induced chemical shift changes occur in the Aβ central hydrophobic core spanning residues 10−20.[12,16] These results are in agreement with the notion that changes in Aβ residues <∼20 may account for the reduced toxicity exhibited by EGCG-induced Aβ40 oligomers. However, beyond this preliminary clue, the molecular basis of the EGCG-induced remodeling from toxic to nontoxic Aβ40

oligomers has remained so far largely elusive. Furthermore, fundamental features of the complexes formed by EGCG and amyloidogenic peptides are currently unknown. For example, itis unclear what the relative affinities of EGCG for monomers *vs.* oligomers are and how EGCG perturbs the recognition of monomers by protofibrils (Figure 1), two aspects critical for understanding seeding competency and secondary nucleation.[24] Addressing these questions is essential to elucidate the mechanism of action of EGCG as an amyloid-remodeling agent.

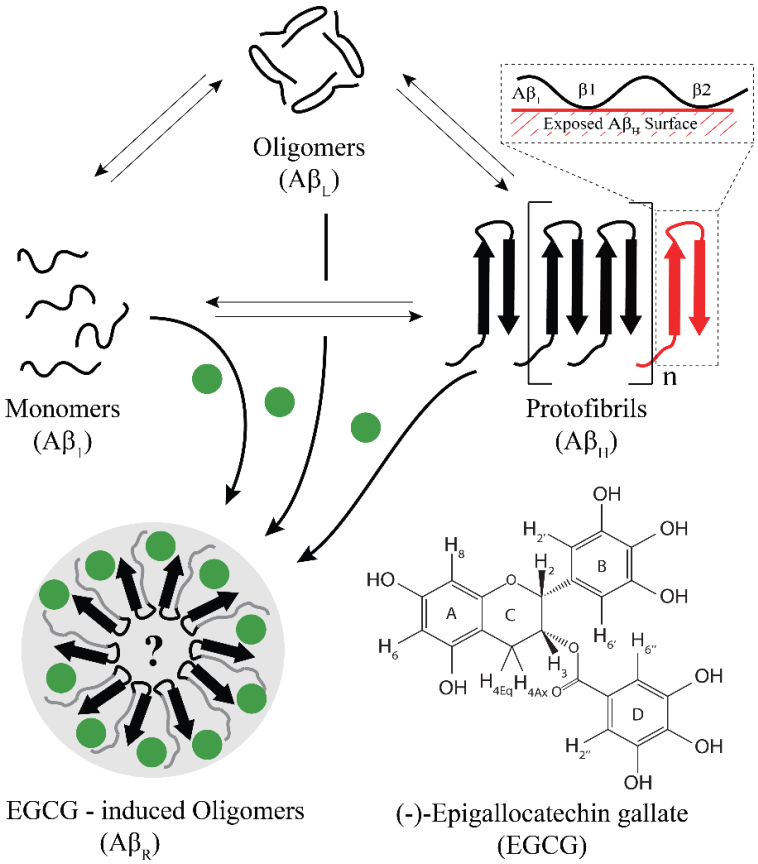

Figure 1. *Schematic representation of the Aβ peptide aggregation pathways and their remodeling by EGCG.* Under pathogenic conditions, NMR-detectable Aβmonomers ($A\beta_1$) self-associate into a distribution of soluble oligomers, referred to here as $A\beta_L$. The $A\beta_L$ oligomers eventually grow into high molecular weight oligomeric protofibrils ($A\beta_H$), which are too large to be directly detectable through conventional NMR techniques, but can be probed through DEST NMR. The red polypeptide chain illustrates a representative protofibril edge with surface-exposed sites available for recognizing $A\beta_1$, as shown in the inset (dashed rectangle). The two β-strands are the regions most likely involved in direct contacts with the protofibril surface, while the N-terminal region is more likely subject to primarily tethered contacts. Although not explicitly shown, it is possible that more than a single protofibril edge is involved in contacts with $A\beta_1$. In the presence of EGCG, Aβ monomers aggregate through an off-pathway mechanism leading to the formation of EGCG-induced oligomers ($A\beta_R$).[9,12] EGCG also remodels pre-existing Aβoligomers and protofibrils into off-pathway oligomers ($A\beta_R$).[8] While the structure of the EGCG-induced oligomers has not been fully characterized, solid-state NMR data suggest the presence of a hairpin turn followed by a C-termina lβ-strand.[12] Less is known about the structure in the region preceding the turn region (*shown in gray*). EGCG is shown as green circles. The actual number of protomers comprising the Aβ40 oligomers and the EGCG: Aβ stoichiometry may deviate from what is shown here for illustrative purposes only.

Here we investigate the mechanism of action of EGCG through apo *vs.* holo comparative NMR analyses of dilute and concentrated Aβ40 solutions, in which Aβ40 is respectively in the ~monomeric state or in a pseudoequilibrium between monomers and soluble high molecular weight oligomeric protofibrils. The latter species, although NMR-invisible ("dark"), are effectively probed through dark-state exchange saturation transfer (DEST) NMR spectroscopy[25,26] with either ^{1}H or ^{15}N saturation. Specifically, using ^{1}H-based DEST in which saturation is introduced through water, in combination with fluorescence, we probed how EGCG affects the solvent exposure of the Aβ40 oligomers. Using ^{15}N-based DEST NMR, in combination with ^{15}N-T_2 relaxation measurements, we mapped at residue resolution how EGCG perturbs the contacts between the surface of Aβ40 protofibrils and the Aβ40 monomers. The interactions of the latter with EGCG were analyzed through chemical shift projection analyses. In addition, we complemented the Aβ40-based DEST NMR with ligand-based NMR. Specifically, saturation transfer difference (STD), off-resonance rotating-frame Overhauser effect (ROE), and transfer nuclear Overhauser effect (NOE) measurements were acquired to measure the affinity of EGCG for Aβ40 oligomers and model how the EGCG conformation changes upon Aβ40 oligomer binding. On the basis of the combined peptide and ligand-based NMR data as well as morphology control data (*i.e.* DLS and EM), we propose a molecular mechanism for the EGCG-induced remodeling of the Aβ40 oligomers.

2.4 Results

2.4.1 EGCG Selectively Binds Multiple Equivalent and Independent Sites within Aβ Oligomers, Conforming to a "Hill-Scatchard-like" Model with a Per-Site Effective Affinity in the Sub 200 μM Range.

The ability of EGCG to bind Aβ oligomers is one of the key determinants of its detoxifying function.[8,9,12,27] Hence, as a first step towards understanding the mechanism of action of EGCG, we sought to measure the affinity of EGCG for Aβ oligomers through saturation transfer difference (STD) NMR spectra[17,28–32] measured at different EGCG concentrations, as shown in Figure 2a. The resulting STD amplification factors were utilized to build the isotherm (Figure 2b) for EGCG binding to Aβ oligomers. The STD-based binding isotherm (Figure 2b) exhibits a typical dose–response pattern and was analyzed in terms of a Scatchard-like model, which accounts for the possibility of multiple EGCG binding sites in Aβ oligomers under the assumption that such sites are independent and equivalent. Scatchard-like binding isotherms are in excellent agreement with the experimental data (Figure 2b), resulting in an effective affinity of ~140 ± 50 μM per EGCG binding site within Aβ oligomers. This result appears to be largely independent of the effective Aβ40 oligomer concentration (*i.e.* $[A\beta_n]_{eff}$), as shown in Figure 2b, confirming the 100–200 μM affinity of EGCG for Aβ oligomers.

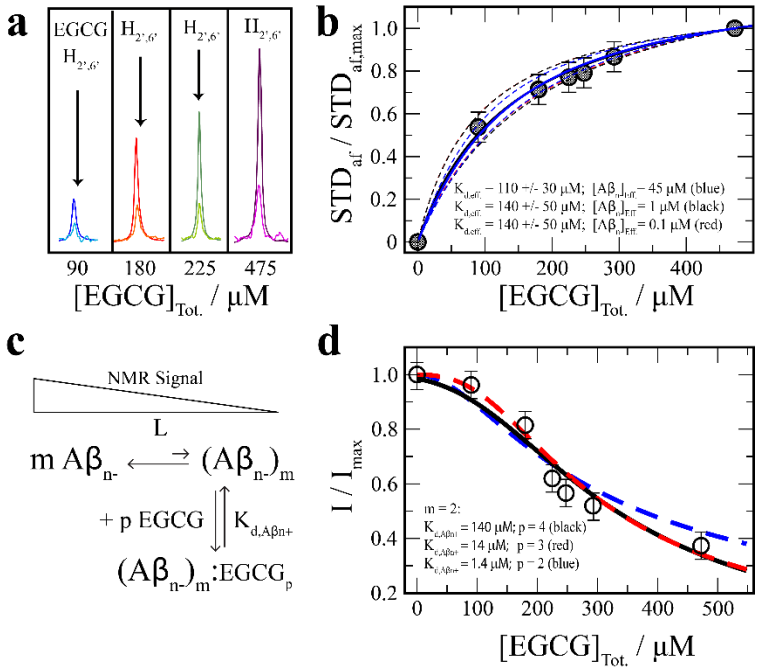

Figure 2. *Binding of EGCG to Aβ40 oligomers.* The affinity of EGCG for the Aβ(1−40) oligomers was probed through saturation transfer difference (STD) and reference (STR) NMR spectra (a), acquired with a total Aβ(1−40) concentration of 90 μM at a temperature of 283K and a pH of 6.8 in 20 mM sodium phosphate buffer. The STR spectra (darker shade) in (a) have been uniformly scaled down with respect to the STD spectra (lighter shade) at all concentrations to avoid off-scale truncation. The resulting STD amplification factor (STDaf) was utilized to measure the affinity of EGCG for Aβ(1−40) oligomers (b). For this purpose, the STDaf values were normalized to the highest measured value (*i.e.*, at $[EGCG]_{tot}$= 475 μM). The normalized $STD_{af}/STD_{af,max}$ ratios are shown as shaded circles in (b).The effective Aβ(1−40) oligomer concentration (i.e., $[A\beta_n]_{eff}$)is unknown, and therefore, $K_{d,eff}$ values were evaluated for representative $[A\beta_n]_{eff}$ values, as shown in the figure. (c) The EGCG-dependent Aβ40 monomer vs oligomer equilibrium was probed by measuring the 1D NMR methyl intensity losses as a function of increasing $[EGCG]_{tot}$, as shown by the empty circles in (d). The data in (d) were modeled according to a Hill−Scatchard mechanism as outlined in(c), where $A\beta_n$ denotes NMR-detectable low-MW Aβ(1−40) species, L is the equilibrium constant for the $mA\beta_n$ *vs.* $(A\beta_{n-})m$ self-association equilibrium, and $K_{d,A\beta n+}$ is the site-specific dissociation constant of the $(A\beta_{n-})m/EGCG_p$ complex. Further details are available in the Supporting Information. The legend at the bottom left of (d) reports possible sets of parameters of the Hill−Scatchard model in (c) that account for the observed 1D intensity losses vs $[EGCG]_{tot}$ data, while keeping the m and p values minimal. However, it should be noted that higher values of m and p are also consistent with the experimental data in (d). For each set of K_d, $A\beta_{n+}$, m, and p values, the self-association equilibrium constant L was selected for optimal fit.

Further insight into the binding of EGCG to Aβoligomers is provided by the loss of the 1D NMR Aβ signal observed at increasing concentrations of EGCG (Figure 2d, empty circles).The data in Figure 2d were acquired after allowing Aβ to equilibrate upon addition of each EGCG titration aliquot (Figure S1a, Supporting Information). Hence, the 1D intensity losses reported in Figure 2d reflect Aβ states at thermodynamic equilibrium. One of the simplest thermodynamic models to account for the EGCG-induced NMR signal losses assumes a cooperative "Hill-like" self-association of m NMR-detectable Aβ species, denoted as $A\beta_{n-}$, resulting in the formation of NMR-undetectable $(A\beta_{n-})m$ oligomers (Figure 2c). The $A\beta_{n-}$ species include primarily monomers, but it is possible that low-MW Aβ oligomers contribute to

the detected NMR signal as well. According to the model of Figure 2c, association of $A\beta_{n-}$ into larger $(A\beta_{n-})m$ oligomers is the primary mechanism to account for the observed 1D signal losses (Figure 2d).[25,33] In the absence of EGCG, the $A\beta_{n-}$ *vs.* $(A\beta_{n-})m$ equilibrium is skewed toward the NMR-detectable low MW species. However, EGCG promotes the self-association of $A\beta_{n-}$ into $(A\beta_{n-})m$ by selectively binding to the latter, resulting in NMR intensity losses (Figure 2d). The binding of EGCG to $(A\beta_{n-})m$ is assumed to be "Scatchard-like", whereby p molecules of EGCG bind the $(A\beta_{n-})m$ oligomers at independent and equivalent binding sites, consistent with the analysis of the STD data in Figure 2b. Since the $A\beta_{n-}$ self-association is modeled according to a Hill-like scheme, while EGCG binding is modeled according to a Scatchard-like mechanism, the model of Figure 2c is referred to here as a "Hill–Scatchard-like" model.

The Hill–Scatchard-like model of Figure 2c provides a simple framework to quantitatively rationalize the 1D NMR intensity losses reported in Figure 2d. For this purpose, we first assumed that the affinity of EGCG for the $(A\beta_{n-})m$ oligomers is comparable to the K_d value obtained through the STD_{af} analysis (Figure 2b), *i.e.* $K_{d,A\beta n+} \approx 140$ μM. We then computed through binding polynomials the relative fraction of $A\beta_{n-}$ species as a function of $[EGCG]_{tot}$ (Supporting Information) and compared it to the normalized 1D NMR intensity losses. While a good fit was obtained already with $K_{d,A\beta n+} \approx 140$ μM (Figure 2d, black line), lower $K_{d,A\beta n+}$ values should be taken into consideration as well because the STD experiments of Figure2a, b preferentially sense weak binding events.[28–32] To account for this possibility, the analysis of the 1D signal loss data was repeated with $K_{d,A\beta n+}$ values reduced by 1 and 2 orders of magnitude (Figure 2d, red and blue lines). The analyses of Figure 2d reveal that, irrespective of the exact $K_{d,A\beta n+}$ values used in the fitting, each self-association event of the low-MW $A\beta_{n-}$ species requires the binding of more than one EGCG molecule (*i.e.* $p \geq m$). In conclusion, the STD (Figure 2a, b) and 1D intensity loss (Figure 2c, d) data are both consistent with EGCG binding Aβ oligomers at multiple independent and equivalent sites, conforming to a Scatchard-like model, with per-site affinity in the sub 200 μM range.

2.4.2 EGCG Binding Markedly Perturbs the Distribution of Direct *vs.* Tethered Dynamic Contacts between Aβ40 Monomers and the Surface of Aβ40 Protofibrils.

To test if and how EGCG binding affects the recognition of Aβ40 monomers by Aβ40 protofibrils, a process critical for seeding and secondary nucleation, we utilized dark-state exchange saturation transfer (^{15}N-based DEST) spectroscopy.[25,26,33–35] For this purpose, we first prepared a solution with Aβ40 in a pseudoequilibrium between monomers and soluble protofibrillar oligomers with a size distribution centered at ≤∼100 nm, as previously described[25,26,33] and confirmed by DLS for our sample (Figure 3a). The DLS data also show that addition of EGCG to this sample results in a narrower size distribution more polarized toward Aβ40 oligomers with sizes close to 100 nm (Figure 3b). The DLS changes observed upon EGCG addition (Figure 3a, b) are consistent with the previously reported ability of EGCG to stabilize Aβ40

oligomers starting from either Aβ40 monomers or large protofibrils[8] and indicate that EGCG-induced remodeling takes place under the experimental conditions suitable for NMR DEST data acquisition. This conclusion was further confirmed through negative stain electron microscopy (EM) (Figure 3c). The EM images acquired in the absence of EGCG detect wormlike protofibrils of varying sizes, corroborating the wide size distribution observed by DLS (Figure 3a). On the contrary, in the presence of 300 μM EGCG, the majority of the protofibrils were remodeled into smaller spherical oligomers that appear more uniform in size, consistent with the narrower DLS-based size distribution observed after EGCG addition (Figure 3b).

The EGCG-induced remodeling confirmed by DLS and EM (Figure 3a–c) at the level of morphological changes was then investigated at residue resolution through DEST experiments acquired before and after addition of EGCG (Figure 3d, e). Figure 3d shows the residue-specific Θ parameter, which quantifies the relative on-resonance *vs.* off-resonance DEST saturation averaged over positive and negative offsets (see the Experimental Section). The Θ observable is a sensitive indicator of direct contacts between Aβ40 monomers and the surface of Aβ40 protofibrils.[25,26,33] In the absence of EGCG, two local maxima are observed in the residue distribution of the Θ parameter, and as expected,[25,26] they fall within the two β-strands typically observed in Aβ40 protofibrils (Figure 3d). The DEST experiment was then repeated in the presence of EGCG at a concentration sufficiently high to induce significant populations of EGCG-remodeled Aβ40 oligomers, but sufficiently low to preserve enough Aβ40 monomers to be detectable by solution NMR.

A compromise between these two opposite requirements is typically obtained at $[EGCG]_{tot}$: $[A\beta40]_{tot}$ ratios in the 1–2 range, which falls just before the midpoint for the transition from NMR-detectable species to EGCG-remodeled Aβ40 oligomers, as illustrated by Figure 2d. This 1–2 stoichiometric ratio range defines the "window of opportunity" to probe through solution NMR the initial changes in Aβ40 as it undergoes EGCG-induced remodeling. Addition of EGCG results in a redistribution of Θ values remarkably different from that arising from self-association in the absence of EGCG (Figure 3d–f). EGCG causes a decrease of the average Θ values observed for the two β-strands, with a more pronounced Θ loss close to β1, while a concurrent significant net increase is detected for the N-terminal Θ values (Figure 3f). This result provides valuable clues as to how EGCG remodels the Aβ40 protofibrils, and it is in agreement with the comparative analysis of the ^{15}N R_2 relaxation rates (Figure 3g–i), which are also sensitive indicators of monomer–protofibrils contacts.[25,26,33,36] In the absence of EGCG, local maxima are observed for the dark *vs*. dilute ΔR_2 profile in the vicinity of the two β-strands (Figure 3g), as expected,[25,26] while, in the presence of EGCG, the most significant ΔR_2 losses are observed near the β-strand regions (Figure 3h, i), pointing to less direct local contacts and/or a reduction in the global $k_{on,app}$ for the recognition of Aβ40 monomers by the Aβ40 protofibrils. Although the errors in the measured ΔR values (Figure 3g–i) are larger than those

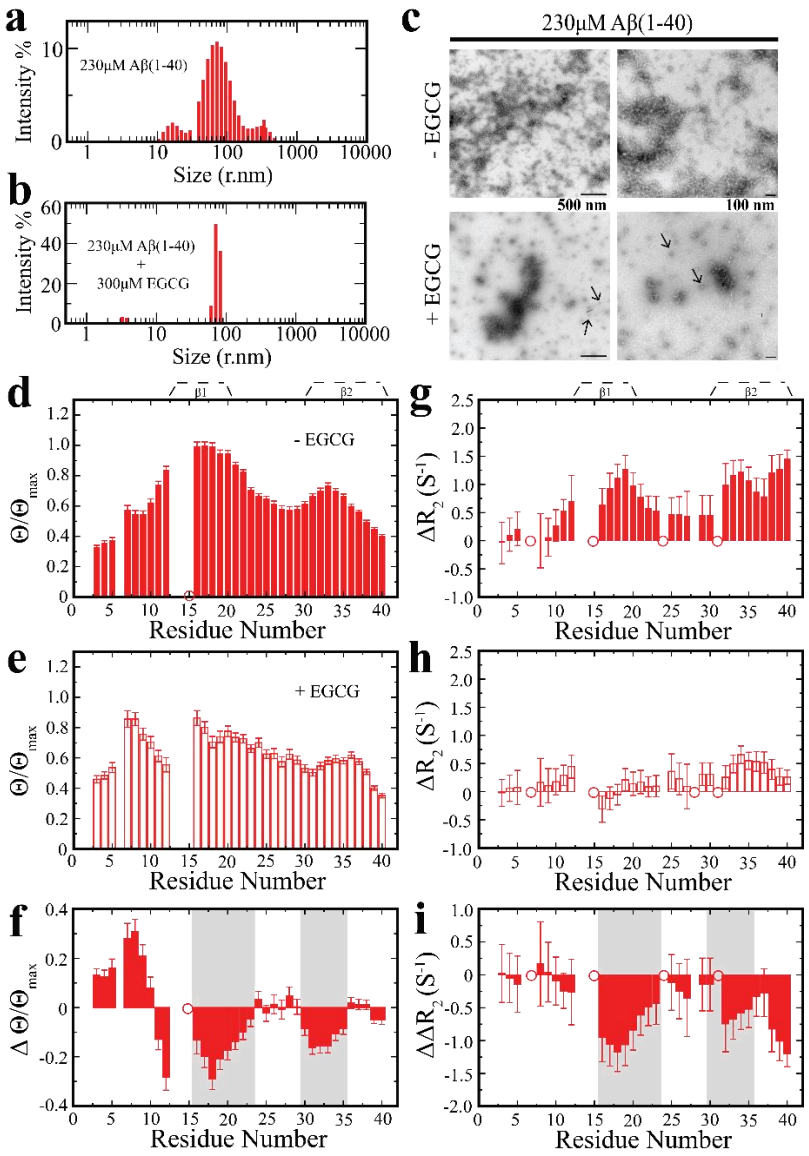

Figure 3. *EGCG-dependent changes in Aβcontacts at the surface of Aβ40 protofibrils.* (a) Size distribution of Aβ species in a 230 μM Aβ40 sample as probed by dynamic light scattering (DLS). (b) As (a), except in the presence of 300 μM EGCG. (c) Electron microscopy negative stain images of the samples used in (a) and (b). Black arrows indicate representative oligomers consistent with a quasi-spherical morphology observed in the presence of EGCG. Left and right panels are images at different magnification scales (i.e. 50K vs 100K). (d) Residue-specific dark exchange saturation transfer (DEST) differences (Θ) measured for the sample used in (a). The DEST profile was smoothened by averaging the Θ values for each residue and the two residues directly adjacent to it, when available. The resulting smoothened profile was then normalized to the maximum Θ value (*i.e.* that observed for apo L17). Residues affected by overlap are indicated by open circles. (e) As (d), but for the sample used in (b). (f) Differences between the Θ/Θ_{max} ratios for the apo and holo samples reported in (d) and (e). (g) Residue-specific differences in ^{15}N transverse relaxation rates, ΔR_2, between the sample used in (a) and the monomeric reference sample (30 μM), smoothened as in (d). Residues affected by overlap are flagged with open circles. (h) As (g), except the ΔR_2 reported is between those for the sample used in (b) and the monomeric reference sample. (i) Difference between the ΔR_2 values for the apo and holo samples reported in (g) and (h). In panels(f) and (i), the regions with negative $\Delta\Theta/\Theta_{max}$ and $\Delta\Delta R2$, respectively, that partially overlap with the β-strands found in cross-β structures are highlighted in gray.

estimated for the ΔΘ values (Figure 3d–f), both approaches are consistent with a consensus pattern in which EGCG elicits a dual effect on the recognition of Aβ40 monomers by protofibrils. For the 15–22 region near the β1 strand, EGCG results in a net inhibition of direct Aβ40 monomer–protofibril contacts (Figure 3f,i), while, for the preceding N-terminal segment, EGCG leads to the opposite effect, *i.e.* a net induction of more engaged direct Aβ40 monomer – protofibril contacts (Figure 3f).

2.4.3 EGCG Binding Decreases the Solvent Exposure of Aβ40 Oligomers.

To further explore how EGCG affects the ability of Aβ40 oligomers to recognize Aβ40 monomers, we probed the solvent accessibility of Aβ40 oligomers through water-saturation transfer difference heteronuclear single-quantum coherence (WSTDHSQC) experiments. For this purpose, water was selectively inverted in alternate scans through radiation damping,[37] and polarization was transferred from water to Aβ40 either through chemical exchange with labile protons (k_{ex}, Figure S2b, Supporting Information) or through intermolecular cross-relaxation from bound water molecules (σ, Figure S2b). Once saturation has been transferred from water to Aβ40 protons (XH, Figure S2b) through either k_{ex} or σ, further propagation of saturation to other Aβ protons occurs through spin diffusion, which relies on cross-relaxation (Figure S2b). The propagated saturation is then monitored by a $^{15}N–^{1}H$ HSQC experiment, which provides a high-resolution readout of the WSTDHSQC experiment (Figure S2b). The extent of WSTDHSQC propagation to a specific amide is quantified by normalizing the WSTDHSQC cross-peak intensities to those of a control HSQC experiment and to the residue-specific intrinsic exchange rates computed for unstructured peptides,[38] as captured by the Γ ratio (further details available in the Experimental Section). The Γ values were initially measured in the absence of EGCG for a "dark" Aβ40 sample similar to that utilized for the DEST experiments, in which soluble Aβ40 oligomers are present, as well as for a more dilute Aβ40 sample, in which the concentration of Aβ40 oligomers is significantly decreased (Figure 4a, b). The respective Γ profiles show that most residues are subject to a Γ increase in going from the dilute to the concentrated Aβ40 sample (Figure 4a, b, f, blue bars), referred to as $\Delta\Gamma_{-EGCG}$. The positive $\Delta\Gamma_{-EGCG}$ values are due primarily to the more efficient spin diffusion in the Aβ40 oligomers vs monomers (Figure S2b). The oligomer *vs.* monomer increase in spin-diffusion efficiency is independently confirmed by introducing saturation through methyl groups as opposed to water (MeSTDHSQC) (Figure S2a). The normalized MeSTDHSQC values for all detectable Aβ40 residues exhibit a marked enhancement in going from the dilute to the concentrated sample (Figure S3a, b, Supporting Information, and Figure 4i, blue bars). These concentrated (dark) vs dilute changes in WSTDHSQC and MeSTDHSQC provide a useful benchmark to evaluate the WSTDHSQC and MeSTDHSQC variations occurring upon EGCG addition.

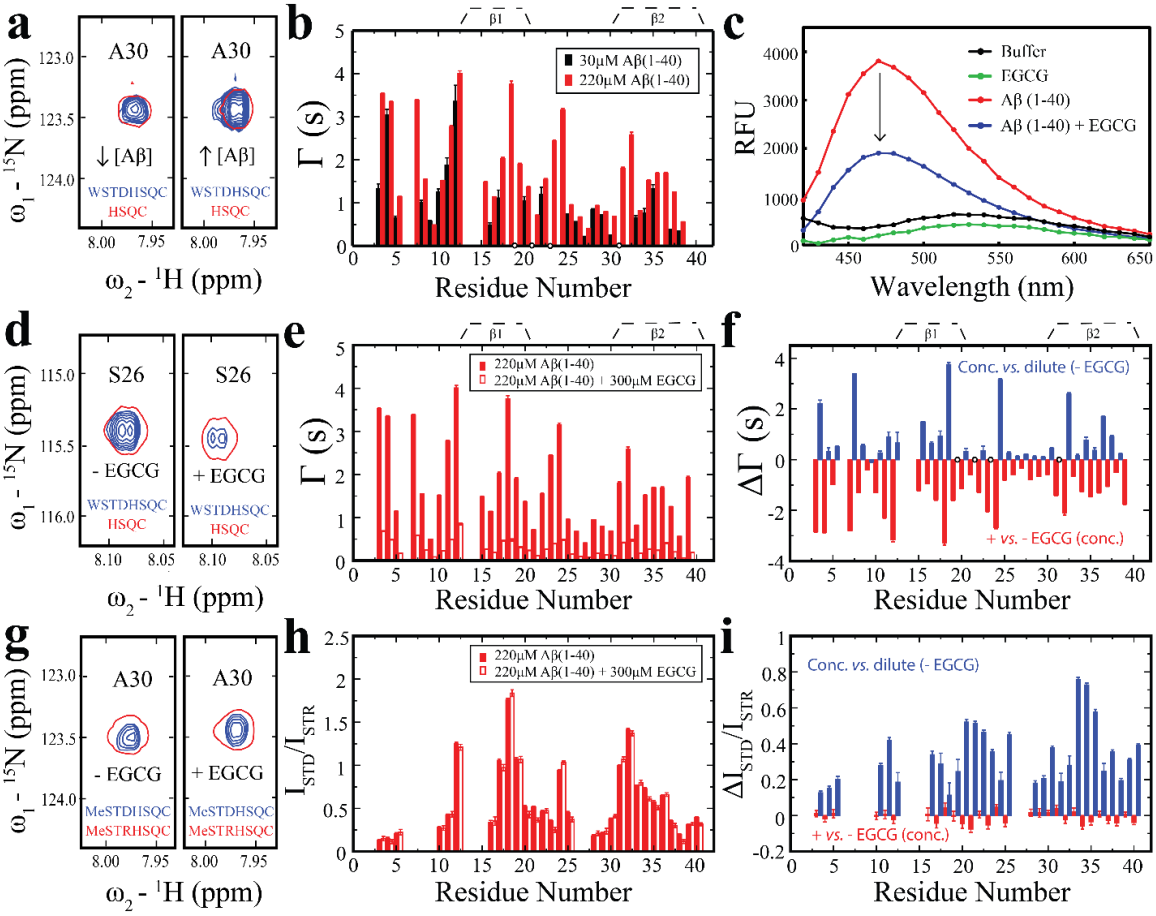

Figure 4. *EGCG-dependent changes in the solvent exposure of Aβ40 oligomers.* (a) Representative expansions of WSTDHSQC (blue) and reference HSQC (red) spectra of low- and high-concentration Aβ40 samples (i.e., 30 vs 220 μM). (b) WSTDHSQC profiles of the samples shown in (a), normalized to the reference HSQC intensities and corrected for residue-specific intrinsic exchange rates with water (see the Experimental Section). Residues that could not be resolved due to overlap are indicated by open circles. (c) Relative ANS fluorescence intensities of 180 M EGCG (green), buffer control (black), and 90 μM Aβ40 in the absence (red) and presence (blue) of 180 μM EGCG. (d) Representative expansions of the WSTDHSQC (blue) and HSQC (red) spectra of "dark" 220 μM Aβ40 in the absence and presence of EGCG. The reference spectra (red) were scaled to the same intensity. (e) WSTDHSQC profiles of the samples shown in (d) and computed as in (b). (f) Difference in the WSTDHSQC profiles shown in (e) (red). For convenience, the difference in WSTDHSQC profiles shown in (b) is also included (blue). (g) As (d), except for the MeSTDHSQC (blue) and MeSTRHSQC (red) spectra, where the on-resonance saturation is on the methyls. (h) MeSTDHSQC profiles of the samples shown in (g). (i) Difference in the MeSTDHSQC profiles shown in (h) (red). For convenience, the difference in MeSTDHSQC profiles shown in Figure S3b (Supporting Information) is also included (blue).

Upon addition of EGCG to the concentrated Aβ40 sample, a striking and pervasive decrease in Γ values is observed, referred to as $\Delta\Gamma_{+EGCG}$, with a magnitude comparable to the $\Delta\Gamma_{-EGCG}$ values although of opposite sign (Figure 4d–f). Since addition of EGCG does not appreciably affect the radiation-damping driven

inversion–recovery profile (Figure S2c), a negative $\Delta\Gamma_{+EGCG}$ may primarily arise from a reduced efficiency in the spin diffusion (Figure S2b) and/or in the intermolecular polarization transfer from water to Aβ40 protons (k_{ex} and/or $\sigma_{H2O-solute}$, Figure S2b). The former option is unlikely as the changes in normalized MeSTDHSQC upon EGCG addition are marginal and overall negligible comparable to those observed in going from dilute to concentrated Aβ40 samples in the absence of EGCG (Figure 4g–i). This observation suggests that the observed negative $\Delta\Gamma_{+EGCG}$ values reflect mainly a less efficient intermolecular polarization transfer from water to Aβ40 protons (k_{ex} and/or $\sigma_{H2O-solute}$, Figure S2b), suggesting that EGCG binding decreases the solvent exposure of Aβ40 oligomers and/or monomers. A significant contribution from the latter species is unlikely considering the Aβ40 oligomer *vs.* monomer binding selectivity of EGCG and was definitively ruled out through a control experiment on a dilute (30 μM) Aβ40 solution containing primarily monomers (Figure S3d–f). EGCG was added to the dilute Aβ40 solution in minimal amounts (70 μM) to limit the formation of EGCG-induced Aβ40 oligomers, as proven by the minimal changes in the MeSTDHSQC profiles relative to those observed between concentrated and dilute samples (Figure S3g–i). In this case, the markedly negative $\Delta\Gamma_{+EGCG}$ values observed for the dark sample (Figure 4f, red bars) were absent (Figure S3f), confirming that EGCG–Aβ40 monomer interactions do not significantly contribute to the EGCG-induced decrease in solvent exposure. Overall, the combined WSTDHSQC and MeSTDHSQC data of Figures 4d–i and S3a,b,d–f consistently point to an EGCG-induced decrease in the solvent accessibility of the Aβ40 oligomer surface.

To independently corroborate the EGCG-induced solvent shielding of Aβ40 oligomers emerging from the WSTDHSQC analysis, we turned to 8-anilinonaphthalene-1-sulfonate (ANS) fluorescence. ANS is a well-known fluorescent probe that reports on solvent-exposed hydrophobic sites, as the maximum ANS fluorescence emission intensity is known to increase and be subject to a blue wavelength shift upon ANS binding to such sites.[39,40] As a result, the ANS fluorescence dramatically increases in the presence of an Aβ40 solution containing oligomers (Figure 4c). However, upon addition of EGCG to the Aβ40 oligomer solution, a major loss in the ANS fluorescence is observed (Figure 4c), indicating that EGCG leads to a significant decrease in solvent-exposed hydrophobic sites. Furthermore, the ANS *vs.* EGCG competition for binding to Aβ40 oligomers was also independently confirmed through 1D STD experiments on ANS–EGCG mixtures (Figure S3c). Overall, the ANS fluorescence and STD results are in full agreement with the WSTDHSQC-based conclusions on the solvent shielding of the EGCG-remodeled Aβ40 oligomers. To gain further insight into the mechanism underlying the EGCG-induced remodeling of Aβ40 oligomers, we complemented our protein-based NMR investigations (Figures 3 and 4) with ligand-based NMR experiments, including saturation transfer for group epitope mapping, off-resonance ROE, and transfer NOE measurements (Figure 5).

2.4.4 EGCG Primarily Interacts with Aβ40 Oligomers through Rings A and D and is Subject to a Conformational Change upon Aβ40 Oligomer Binding.

The group epitope mapping by 1D STD (Figure 5a, b) reveals distinct differences in the extent of saturation among the four rings of EGCG, with the extent of saturation transfer from the Aβ40 oligomers to EGCG decreasing in the order A > D > B ≥ C (Figure 5a, b). This observation suggests that rings A and D are the primary contact sites with the Aβ40 assemblies. To investigate if the relative orientation of the EGCG rings is altered by the binding of EGCG to Aβ40 oligomers, we acquired off-resonance rotating-frame nuclear Overhauser effect correlation spectroscopy (ROESY) data for EGCG in the absence of Aβ40 (Figure 5c, e, g) and transfer nuclear Overhauser effect spectroscopy (NOESY) data for EGCG in the presence of EGCG-induced Aβ40 oligomers (Figure 5d, f, h). As shown in Figure 5c, e, g, for free EGCG, the only observed cross-peaks pertain to contacts within ring C or between rings C and B. However, in the presence of EGCG-induced Aβ40 oligomers, several additional cross-peaks involving contacts between EGCG rings B–D are detected (Figure 5d, f, h). The absence of these cross-peaks for free EGCG is not due to poor signal-to-noise ratios (Figure 5e, inset), suggesting that the additional cross-peaks observed in the presence of Aβ40 reflect a genuine conformational change of EGCG occurring upon binding the EGCG-Aβ40 oligomers.

The transfer NOEs are accounted for by two major clusters of Aβ40 oligomer-bound EGCG structures (Figure 5j, k). In one cluster (Figure 5j), the EGCG ester bond adopts a trans configuration and the planes of rings B and D rotate relative to their orientation in apo EGCG (Figure 5i), while still preserving an overall topology for the four rings similar to that of unbound EGCG (Figure 5i). In the other cluster (Figure 5k), the EGCG ester bond adopts a cis configuration, resulting in a ring center-of-mass topology clearly different from that of apo EGCG (Figure 5k). Here, ring D flips over toward rings B and C due to the cis ester bond, and ring B rotates relative to its orientation in apo EGCG, as in the trans configuration (Figure 5k). While the cis configuration for the ester bond is typically less stable than the trans configuration,[41] on the basis of our data alone, we cannot currently rule out the possibility that Aβ40 oligomer binding preferentially stabilizes EGCG structures with cis ester bonds. On the contrary, EGCG structures with a cis ester bond could be ruled out for the apo samples on the basis of the observed ROEs.

Irrespective of whether the Aβ40 oligomers select for the trans or cis ester bond isomers, the combined STD and transfer NOESY analyses indicate that the primary Aβ40 oligomer contact sites within EGCG are rings A and D and that rings B and D undergo significant reorientations upon binding the Aβ40 assemblies (Figure 5). However, Figure 5 or the previous experiments of Figures 3 and 4 do not probe the EGCG interactions with Aβ40 monomers. To fill this gap and investigate at residue resolution how EGCG binds to Aβ40 monomers, we analyzed the apo vs holo comparative chemical shift changes for a highly diluted (30 μM) Aβ40 solution, as shown in Figure 6.

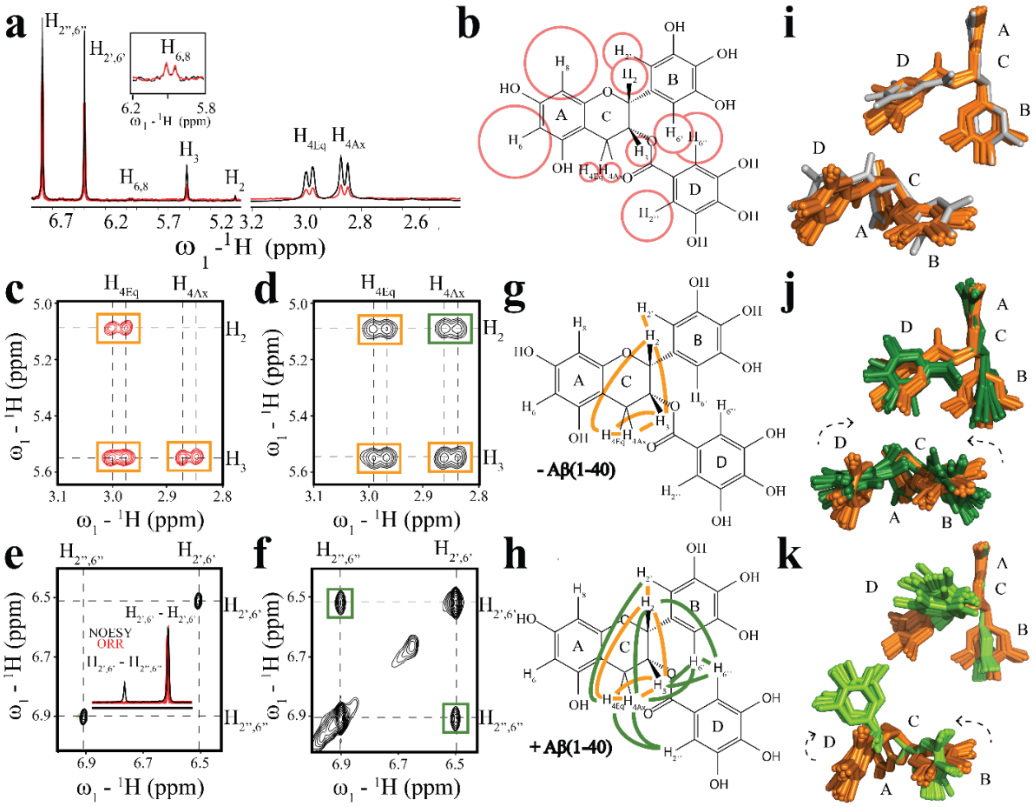

Figure 5. *Conformational switch of EGCG upon binding Aβ40 oligomers and EGCG epitope mapping.* (a) STD (red) and STR (black) spectra of 475 μM EGCG in the presence of 90 μM Aβ40. The STR spectrum is scaled down to match the intensity of EGCG proton peaks 6 and 8 of ring A (inset). (b) Schematic representation of the binding epitope of EGCG bound to Aβ40 oligomers, as derived from the STD:STR ratios seen in (a). The sizes of the red circles are interpreted as an approximate indicator of the proximity of the EGCG protons to the surface of the Aβ40 oligomers. All circles are scaled logarithmically to the EGCG ring A 6 and 8 protons, which were arbitrarily set to 100%. (c, e) Selected expansions of off-resonance ROESY spectra of 180 μM EGCG (158 ms mixing time). The diagonal is phased positive and shown in black, and the negative cross-peaks are indicated in red. (d, f) Selected expansion of Tr-NOESY spectra of 90 μM Aβ(1–40) in the presence of 720 μM EGCG (60 ms mixing time). Orange boxes highlight EGCG intramolecular cross-peaks common to the free and Aβ40-bound samples, and green boxes label additional cross-peaks observed only in the Aβ40-bound sample. The inset in (e) displays the overlap of the extracted rows from the Tr-NOESY (black) and off-resonance ROESY (red) spectra. (g) Schematic summary of ROEs observed for unbound EGCG mapped onto the structure of EGCG. (h) As (g), but with the Tr-NOEs detected for the Aβ40-bound EGCG. The color code is the same as that in (c)–(f). (i) Overlay of apo EGCG structures in two different orientations. The starting EGCG structure, which was derived from PDB ID 3NG5 (gray), is overlapped with the apo EGCG structures obtained from a grid search and selected on the basis of the 1H–1H off-resonance ROESY cross-peaks reported in (g) (orange). (j) Apo EGCG structures as in (i) (orange), superimposed to holo EGCG structures from a grid search filtered on the basis of the ^{1}H–^{1}H Tr-NOEs reported in (h) (dark green). The ester bond was kept in a trans configuration in these EGCG structures. The black dashed arrows highlight possible changes in conformation between apo and holo EGCG. (k) As (j), except with the holo EGCG structures in a cis ester bond configuration (light green). The arrows illustrate the rotations that occur during the apo–holo transition, assuming that the D ring rotation is coupled to the isomerization of the ester bond.

2.4.5 EGCG Binds Aβ40 Monomers Weakly and Non-specifically.

Figure 6a shows the residue-specific compounded chemical shift changes (ΔCCS) observed for 30 μM Aβ40 upon addition of EGCG at concentrations ranging from 40 to 300 μM. Considering that this EGCG concentration range is comparable to the $K_{d,eff}$ for the binding of EGCG to Aβ40 oligomers (Figure 2b, d), the ΔCCS values reported in Figure 6a may arise from early low-MW EGCG-induced Aβ40 oligomers in fast exchange with Aβ40 monomers and/or from direct EGCG interactions with Aβ40 monomers. The former scenario is unlikely on the basis of the absence of significant concentrated vs dilute parts per million (ppm) differences (Figure S6a, b, Supporting Information). The absence of appreciable contributions to the ΔCCS values reported in Figure 6a from EGCG-induced Aβ40 self-association is also supported by the marginal difference in the MeSTDHSQC profiles measured for dilute Aβ40 in the absence and presence of EGCG (Figure S3h). Hence, we conclude that the chemical shift changes shown in Figure 6a report primarily on the direct interaction between EGCG and Aβ40 monomers ($Aβ40_1$).

Since the chemical shifts of Figure 6a report primarily on Aβ40 monomers,[33,43] a ppm-based isotherm for the binding of EGCG to Aβ40 monomers was built assuming that the apo−holo exchange is fast on the chemical shift time scale; *i.e.* ppm changes are linear averages of the ppm values in the pure apo and holo states (Figure 6b). Figure 6b shows that the chemical shifts scale linearly with the EGCG concentration even in the presence of a 10-fold excess of EGCG, as expected in the case of weak binding, *i.e.* $K_d \geq 1$ mM (Figure 6b). A similar affinity of EGCG for $Aβ40_1$ in the >1 mM range is obtained also when EGCG concentrations are limited to the 0−60 μM window (Figure S6c, d). This concentration range is below the 140 μM Kd for EGCG binding to Aβ40 oligomers and hence is less likely to induce the formation of Aβ40 oligomers compared to the 0−300 μM EGCG concentration window. This further confirms that the EGCG-induced chemical shift changes shown in Figure 6a report primarily on the EGCG−$Aβ40_1$ interactions. Overall, these observations suggest that the Aβ40 oligomer vs Aβ40 monomer selectivity of EGCG as sensed by STD and ppm changes, respectively, amounts to a K_d ratio of at least ∼1 order of magnitude.

Another key implication of the chemical shift changes shown in Figure 6a is that the majority of the most pronounced EGCG-induced CCS changes are observed for residues within the two β-strands seen in the Aβ40 protofibrils (Figure 6a). However, unlike the CCS variations, which quantify the magnitude of the EGCG-dependent chemical shift changes, the directions of the EGCG-dependent chemical shift variations are only marginally residue dependent (Figure 6c). For example, EGCG shifts upfield the ^{15}N and ^{1}H ppm values of both L17 and F19 (Figure 6c). To check to what extent these "parallel" shifts occur for other residue pairs, we systematically measured the θ angle, which quantifies the relative direction of chemical shift changes, as illustrated in Figure 6d. Figure 6e shows the matrix of residue pairs with cos θ values >0.95 computed for both the highest and lowest EGCG concentrations utilized in Figure 6a. On the basis

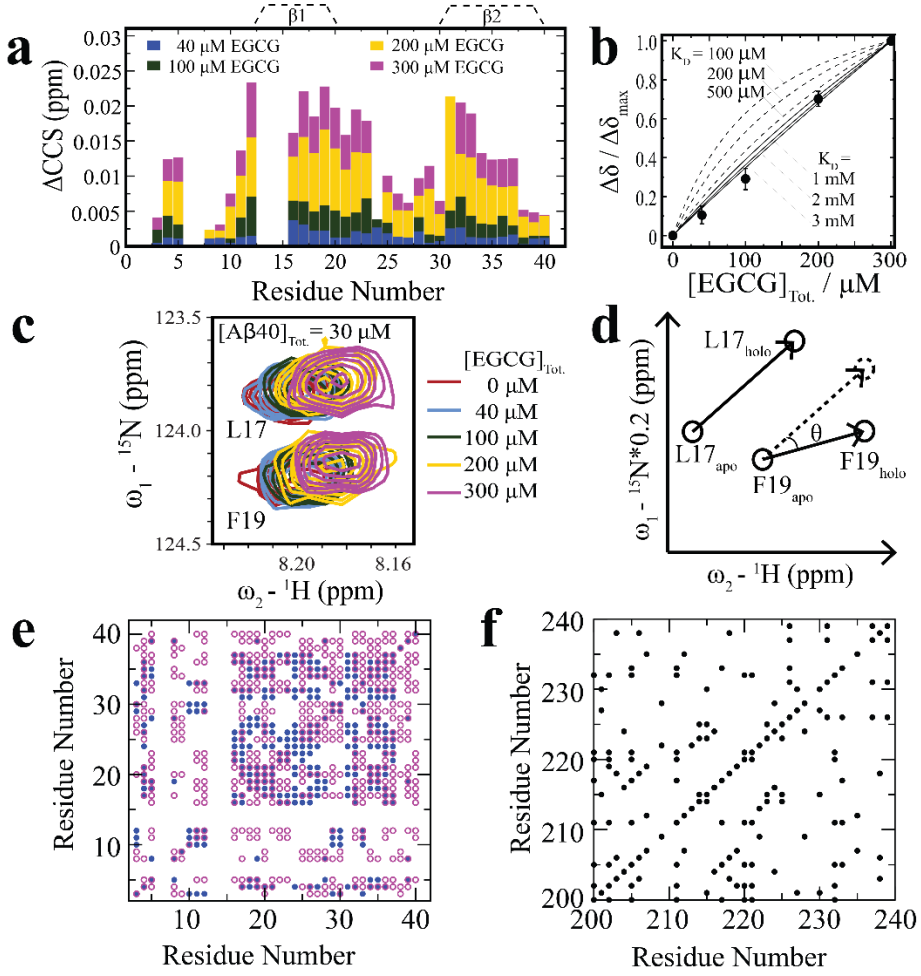

Figure 6. *EGCG–Aβ40 monomer interactions as mapped by compounded and projection chemical shift analyses.* (a) Compounded chemical shift differences (ΔCCS) derived from ^{1}H–^{15}N HSQC spectra of 30 μM Aβ40 acquired in the absence and presence of 40 μM (blue), 100 μM (green), 200 μM (yellow), and 300 μM (purple) EGCG. The position of the β-strands found in Aβ40 protofibrils is marked by dashed trapezoids. (b) Measurement of the affinity of EGCG for Aβ40 monomers. The combined chemical shift changes (ΔCCS) for residues with ΔCCS at 300 μM EGCG of >0.014 ppm[42] were normalized to the ΔCCS value measured at $[EGCG]_{tot}$ = 300 μM, averaged and plotted against $[EGCG]_{tot}$, as shown by the filled circles. Dashed (solid) binding isotherms were then computed for K_d values <(>)1 mM, as shown in the figure. The experimental data are accounted for by K_d values >1 mM. (c) HSQC expansions illustrating representative EGCG-induced chemical shift changes observed for dilute (30 μM) Aβ40. (d) Schematic representation of the pairwise chemical shift projection analysis and definition of the θ angle for a representative residue pair. The two black vectors illustrate the direction of change in the (^{15}N, ^{1}H) plane. (e) cos θ matrix of 30 μM Aβ40 for the 40 μM (solid blue circles) and 300 μM (open purple circles) EGCG concentrations. (f) cos θ matrix for apo *vs.* cAMP-bound PKA RIα (96–244) (solid black circles), used as a model system for specific binding. A cut-off of cos θ > 0.95 was used to display the cross-peaks in both (e) and (f).

of Figure 6e, it is clear that most residue pairs in Aβ40 are subject to EGCG-induced chemical shift changes along the same direction in the ^{15}N and ^{1}H plane, in marked contrast to what is typically observed for specific ligand-binding interactions for which the likelihood of parallel shifts is significantly lower (Figure

6f; Figure S7, Supporting Information). The similar upfield direction observed for the EGCG-induced HSQC peak shifts is in agreement with the $A\beta40_1$ NH groups being generally located above or below the plane of the aromatic rings of EGCG, whereas, if these NH amides were involved in specific hydrogen bonds with EGCG, the HSQC peak shifts of different residues would not be expected to be parallel to the extent observed here.[9,44] Overall, the chemical shift projection analyses consistently point to the EGCG–Aβ40 monomer binding being most likely nonspecific.

2.5 Discussion

We have investigated both dilute and concentrated ("dark") Aβ40 solutions in the absence and presence of EGCG through the comparative analysis of NMR (i.e., peptide-based NMR, such as ^{1}H and ^{15}N DEST, ^{15}N T_2, and chemical shift projections, as well as ligand-based NMR, such as STD, off-resonance ROEs, and transfer NOEs) and non-NMR (DLS, EM, and ANS fluorescence) data. The key new results emerging from these integrated analyses are summarized in Figure 7 (blue shaded boxes), which provides a foundation to explain how EGCG remodels the pathways of Aβ40 self-association. Specifically, we have shown that EGCG binds Aβ40 oligomers and monomers with sub 200 μM and >1 mM affinities, respectively (Figures 2b, 6b, and S6d). These results are consistent with previous isothermal titration calorimetry (ITC) studies reporting overall affinities of EGCG for Aβ42 in the ~50–700 μM range.[45] However, on the basis of ITC data alone, the distinct contributions from Aβ monomers *vs.* oligomers could not be fully separated.[46] On the contrary, this separation is possible by solution NMR, as chemical shifts (Figure 6a,b) and STD (Figure 2a,b) report primarily on the binding of EGCG to monomers and oligomers, respectively.

The Aβ40 oligomer *vs.* monomer binding selectivity of EGCG drives the remodeling of Aβ40 self-association according to a Hill–Scatchard model (Figure 2c, d), whereby Aβ40 oligomerization occurs cooperatively (Hill-like equilibrium), creating multiple equivalent and independent binding sites for EGCG (Scatchard-like binding). While the exact stoichiometry of the complex formed by Aβ40 oligomers and EGCG is currently unknown, fitting of the proposed Hill–Scatchard model suggests that multiple EGCG molecules are bound per Aβ40 oligomer (Figure 2c, d). This result is consistent with the range of stoichiometries previously proposed on the basis of ITC data for EGCG binding to Aβ40, although, as mentioned above, the separation of monomer *vs.* oligomer contributions is challenging in ITC experiments.[45]

The exact location of the EGCG binding sites within the Aβ40 oligomers is currently not fully defined, although the competitive binding between ANS and EGCG, as revealed by our fluorescence (Figure 4c) and STD (Figure S3c, Supporting Information) data, is consistent with EGCG preferentially interacting with exposed hydrophobic residues.[9,12] Another possible mode of interaction between EGCG and

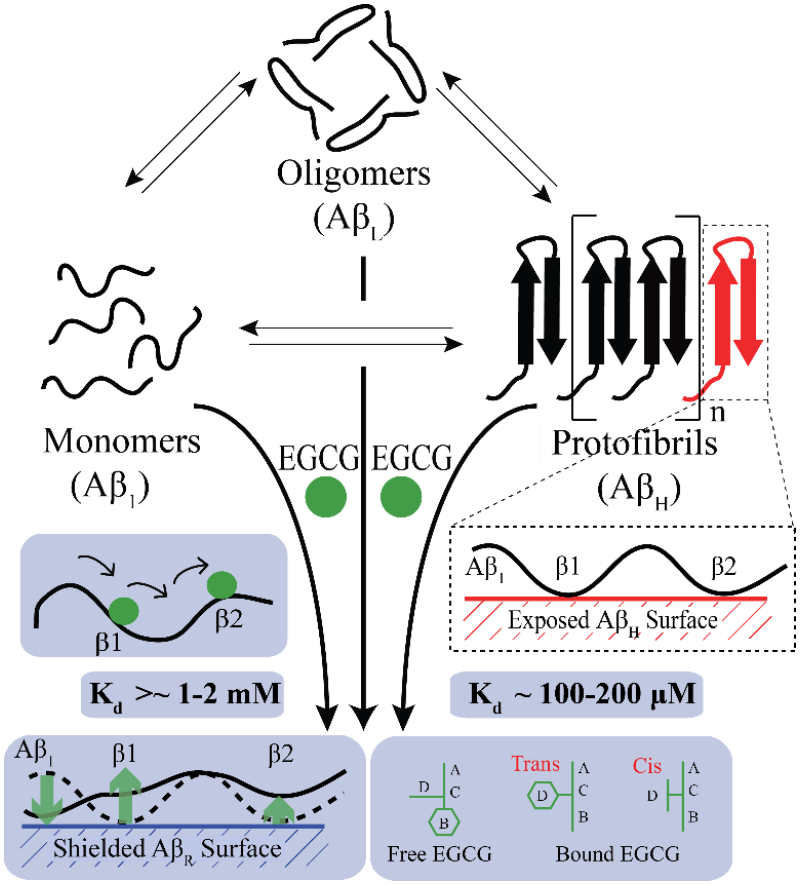

Figure 7. Proposed mechanism for the EGCG-induced remodeling of Aβ40 into nontoxic oligomers. The proposed mechanism builds upon the scheme shown in Figure 1 and highlights the novel features revealed in this study for the interactions of EGCG with Aβ40 monomers and oligomers (light blue background). The exact stoichiometry for the binding of EGCG to Aβ40 monomers is not known, but it is possible that two molecules of EGCG bind at regions spanning the two β-strands observed in the Aβ40 protofibrils. Alternatively, a single EGCG molecule could bind an Aβ40 polypeptide chain that forms a loop whereby EGCG interacts with both β-strand regions. However, the latter possibility is less likely given the low affinity and specificity observed for the EGCG interactions with Aβ40 monomers. Similarly, the exact stoichiometry for the binding of EGCG to Aβ40 oligomers is not known, but on the basis of the Hill–Scatchard model of Figure 2c, d, multiple EGCG molecules are predicted to bind each Aβ40 oligomer. The binding of EGCG results in an overall reduction of solvent exposure (blue AβR surface *vs.* red AβH surface) and perturbs the partitioning of direct *vs.* tethered contacts of Aβ40 monomers with the surface of the Aβ40 protofibrils. The two β-strand regions that exhibit predominantly direct contacts in the absence of EGCG (expanded dashed rectangle) are subject to a shift toward more tethered contacts (upward-pointing green arrow), while the N-terminal region becomes more engaged in direct contacts (downward-pointing green arrow). The dashed and solid $A\beta_1$ lines in the light blue rectangle at the bottom left represent approximate direct *vs.* tethered contact profiles before and after EGCG binding. The variations in solvent shielding and in the distribution of surface contacts illustrated here define distinct molecular differences between toxic and nontoxic EGCG-remodeled Aβ40 oligomers. Coupled to these changes in Aβ40 oligomers upon binding EGCG are the modulations in the conformation of EGCG. Upon Aβ40 oligomer binding, EGCG rings B and D reorient with respect to the plane formed by rings A and C (trans conformation) or EGCG undergoes ester bond isomerization to bring ring D closer to rings A–C while still reorienting ring B with respect to rings A and C (cis conformation).

amyloidogenic peptides is through covalent linkages, *e.g.* formation of a Schiff base with the primary amine of lysine side chains, as previously reported for the SEVI peptide.[47] However, this type of covalent interaction is ruled out for the binding of EGCG to Aβ40 under our experimental conditions, as it would suppress the saturation transfer observed in Figure 2a and the transfer NOEs (Figure 5d, f), which rely on the dynamic exchange between bound and unbound forms of EGCG.

Our data show that the binding of EGCG to the Aβ40 oligomers is coupled to marked changes in both EGCG (Figure 5) and the Aβ40 assemblies (Figure 7). EGCG primarily associates with the Aβ40 oligomers through rings A and D and undergoes a conformational change upon binding whereby rings D and B reorient with respect to rings A and C (Figure 5). This conformational change observed in the presence of Aβ40 oligomers is in full agreement with previous results from Airoldi et al. showing that EGCG analogues lacking the gallate moiety (i.e., ring D) are less effective in binding and remodeling preformed Aβ fibrils.[17] Upon binding to multiple EGCG molecules, the Aβ40 oligomers are subject to an overall decrease in solvent exposure (Figures 4 and S3). The EGCG-induced surface shielding effect may arise from EGCG coating the surface of the remodeled Aβ40 oligomers, but possibly also from Aβ40 structural changes driven by EGCG binding at other sites. In either case, EGCG induces losses in overall solvent exposure of the Aβ40 oligomers, including hydrophobic surface sites targeted by the ANS fluorophore (Figures 4 and S3). Considering that increased surface hydrophobicity has been previously proposed as one of the key cytotoxicity determinants of protein oligomers,[40] the EGCG-induced shielding of Aβ40 oligomers (Figures 4 and S3) provides an initial explanation for the reduced cellular toxicity exhibited by the EGCG-remodeled Aβ40 assemblies.

Another major implication of the enhanced surface shielding observed upon EGCG binding is a distinct change in how Aβ40 protofibrils recognize Aβ40 monomers, *i.e.* in the probability distribution of direct *vs.* tethered contacts between monomers and the surface of protofibrils as probed by DEST and T_2 variations (Figures 3d–i and 7). The two sites most likely to be involved in direct Aβ40 monomer–protofibril contacts in the absence of EGCG, *i.e.* β1 and β2, experience a net shift toward more tethered contacts (Figures 3d–i and 7). On the contrary, most of the N-terminal region preceding β1, which is primarily tethered before addition of EGCG, becomes more engaged in direct contacts with the Aβ40 protofibril surface after EGCG addition (Figures 3d–i and 7).

The direct-to-tethered contact shift observed for the β1 and β2 regions explains the loss of seeding competency observed for the EGCG-remodeled Aβ40 oligomers and suggests that EGCG interferes with the mechanism that generates toxic Aβ oligomers through surface-catalyzed secondary nucleation.[24,48,49] The direct-to-tethered contact switch detected for the β-segments is likely the result of the interactions of EGCG with both Aβ40 oligomers and monomers. EGCG binding to the Aβ40 oligomers results in solvent

shielding and hence reduced surface availability for direct contacts (Figure 7), whereas the interactions of EGCG with the Aβ40 monomers, although weak, may compete with the Aβ40 oligomers, since they cluster around similar β-regions as indicated by the chemical shift analyses (Figures 6a and 7). Interestingly, the dual effect of EGCG, with a direct-to-tethered contact shift in the β1 and β2 segments and a concurrent but opposite tethered-to-direct contact shift in the N-terminal region (Figures 3d–i and 7), explains the ability of EGCG to remodel Aβ40 assemblies without first releasing Aβ40 monomers.[8]

2.6 Conclusion

We have shown that the EGCG-induced remodeling of Aβ40 assemblies conforms to a Hill–Scatchard model and is driven by an oligomer vs monomer selective multisite binding of EGCG (*i.e.* K_d values of ~<200 μM and >1 mM for Aβ40 oligomers and monomers, respectively), resulting in reduced solvent exposure of the EGCG-remodeled Aβ40 oligomers and in a perturbed distribution of direct *vs.* tethered contacts between the Aβ40 monomers and the protofibril surface. The residues most involved in direct protofibril–monomer contacts in the absence of EGCG, *i.e.* the β1 and β2 regions, are subject to a direct-to-tethered switch upon EGCG binding, explaining the reduced seeding competency of the EGCG-remodeled Aβ40 oligomers and suggesting that EGCG may break the catalytic cycle that leads to neurotoxic Aβ40 assemblies through surface-catalyzed secondary nucleation. In addition, our data also show that the N-terminal residues, which are primarily tethered in the absence of EGCG, undergo a reversed switch toward more direct contacts. This observation explains why the EGCG-induced remodeling of Aβ40 oligomers occurs without transient release of Aβ40 monomers, thus further suppressing possible secondary nucleation events. Overall, the previously unanticipated differences between non-remodeled and EGCG-remodeled Aβ40 oligomers revealed by our data define an initial, but critical, step toward understanding the molecular basis for the reduced cytotoxicity displayed by Aβ40 oligomers in the presence of EGCG.

We also show that, upon binding the Aβ40 oligomers, EGCG undergoes a conformational change whereby rings B and D reorient with respect to the plane defined by rings A and C. The conformation of Aβ40 oligomer-bound EGCG may inform the design of EGCG analogues with enhanced anti-amyloidogenic potencies. Last, but not least, the results presented here illustrate a versatile experimental strategy based on combining peptide-based NMR (*i.e.* ^{15}N DEST, ^{15}N T_2, ^{1}H DEST, including WSTDHSQC and MeSTDHSQC, and chemical shift projection analyses), ligand-based spectroscopies (i.e., 1D STD, off-resonance ROEs and transfer NOEs, competitive ANS fluorescence, and STD), and morphological control data (*i.e.* DLS and EM) to dissect the mechanism of action of low-MW amyloid inhibitors in general.

2.7 Experimental Section

Sample Preparation

Uniformly ^{15}N-labeled Aβ40 was purchased from rPeptide Inc. with purity greater than 97%, while unlabeled Aβ40 was purchased from EZBiolab Inc. with purity greater than 95%. The stock solutions for both labeled and unlabeled peptides were prepared in the same manner by dissolving 1 mg of the peptides in 1 mL of 10 mM NaOH. The resulting mixture was sonicated twice for 2 min with a 2 min incubation period on ice in between. After sonication, the samples were divided into 100 μL aliquots, lyophilized, and frozen at −20 °C. After this point, the preparation protocols for the labeled and unlabeled Aβ40 samples diverged. The ^{15}N-labeled peptides were dissolved in metal-free buffer solutions prepared through the chelating agent Chelex 100 (Sigma-Aldrich, C7901) and were also desalted, as follows. The aliquots of lyophilized 15N-labeled Aβ were each dissolved in either 225 or 250 μL of 3 mM Tris (pH 8) for dilute or concentrated samples, respectively. The solutions were then run through a Zeba column pretreated with 3 mM Tris (pH 8) and centrifuged at 1000g for 1 min, and the flow-through containing the peptide was collected. The flow-through was then combined with either 225 or 250 μL of 100 mM HEPES (pH 6.6), 20% D2O, for dilute or concentrated samples, respectively. Preparation of the 30 μM dilute ^{15}N-Aβ40 solution required one lyophilized aliquot dissolved in 450 μL of NMR buffer whereas that of the concentrated (220−230 μM) ^{15}N-Aβ40 solution required ten aliquots dissolved in 500 μL of NMR buffer to account for peptide losses during the Zeba column treatment. The concentrations of the peptide solutions were checked by absorbance measurements at 280 nm. While the dilute sample was not subject to further treatment, the concentrated samples were incubated for at least 7 days prior to NMR data acquisition.[25,26] The incubation was monitored through the losses in 2D ^{1}H−^{15}N HSQC Aβ cross-peak intensities (Figure S1d) to ensure that equilibration was reached prior to the acquisition of other data. A timeline for the equilibration and data acquisition of the dilute and concentrated NMR samples is provided in Figure S1e. At the end of the concentrated sample equilibration, a heterogeneous mixture consisting of monomers, low molecular weight oligomers, and protofibrils was produced, as confirmed by DLS and EM (Figure 3a−c). Samples of the unlabeled peptides, used for ligand-based experiments (Figures 2 and 5), were prepared by dissolving two aliquots in 500 μL of 20 mM sodium phosphate buffer (pH 6.8), 100% D2O, 0.05% NaN3. The resulting mixture was sonicated twice for 2 min with a 2 min incubation period on ice in between. The final concentration, assessed by absorbance measurements at 280 nm, was approximately 90 μM. (−)-Epigallocatechin gallate (EGCG) was purchased from Sigma-Aldrich (E4143), with purity greater than 95%. A 2.8 mM stock solution was prepared by dissolving the EGCG powder in either 50 mM HEPES, 1.5 mM Tris, 10% D2O (pH 6.8), or 20 mM sodium phosphate buffer, 100% D2O, 0.05% NaN_3, as necessary to match the peptide conditions.

Negative Stain Electron Microscopy (EM)

Aliquots were obtained from the concentrated (230 μM) ^{15}N-Aβ40 peptide sample used for NMR experiments at 13.5 and 15.5 days after initial preparation. The first aliquot containing the protein alone before EGCG addition is representative of the NMR sample at the end of all apo NMR experiments, whereas the second aliquot, collected after EGCG addition, is representative of the NMR sample at the end of all holo NMR experiments. The aliquots were applied onto copper EM grids (400-mesh) freshly coated with a continuous layer of amorphous carbon. For this purpose, grids were floated on a 5 μL drop of the aliquots for 2 min immediately after a glow discharge treatment of the grid with 5 mA for 15 s. Excess sample was blotted with filter paper, and the grids were stained with 1% uranyl acetate for 1 min. The grids were loaded into a room temperature holder and introduced into a JEOL 1200-EX electron microscope operated at 80 kV. All images were acquired on an AMT XR-41 side-mount cooled 4 megapixel format charge-coupled device (CCD) camera.

Dynamic Light Scattering (DLS)

The samples used for DLS were from the same aliquots utilized for EM imaging. DLS measurements were performed using a Zetasizer Nano S instrument (Malvern Instruments, Malvern, U.K.). Autocorrelation functions were accumulated for 2 min at 10 °C and with an angle θ of 173° with a 4 mW He–Ne laser operating at a wavelength of 633 nm. All measurements were performed using a 12 μL (ZEN2112) quartz cell. The particle diameter detection limit was 0.6–6 μm. The viscosity value for water was used in the analysis of all measurements. All the samples were centrifuged for 10 min at 13000 rpm prior to DLS measurements.

ANS Fluorescence

Two 500 μL aliquots of 100 μM unlabeled Aβ40 in 50 mM HEPES, 1.5 mM Tris (pH 6.8), were preincubated at 37 °C overnight. Following incubation, ANS was added to each sample to a final concentration of 200 μM and EGCG was added to one sample to a final concentration of 180 μM. The dilution factor was approximately 10%, bringing the final concentration of Aβ to 90 μM. Additional control samples of 200 μM ANS in the absence or presence of 180 μM EGCG were also prepared. The samples were allowed to settle on ice for 1 h and then loaded onto a black 96-well plate and scanned using a BioTek Synergy plate reader. All data were acquired at 10 °C in spectral scanning mode with excitation at 380 nm and emission read between 420 and 650 nm.

NMR Spectroscopy

All NMR spectra were recorded at 10 °C, unless otherwise specified, using either a Bruker AV 700 spectrometer equipped with a TCI cryoprobe or a Bruker 850 HD spectrometer equipped with a TXI probe. All spectra were analyzed with TopSpin 3.2.1 and Sparky.[50] Additional details are discussed below.

Measurement of ^{1}H NMR Intensity Losses as a Function of the EGCG Concentration

Unlabeled 90 μM Aβ40, prepared as described above, was titrated with increasing concentrations of EGCG up to 475 μM, and after each addition of EGCG, ^{1}H NMR spectra were acquired with 256 scans, 32K complex points, and a spectral width of 15.98 ppm. The ^{1}H NMR intensity losses, as determined by relative changes in the intensity of the Aβ methyl peaks, were modeled according to a Hill–Scatchard mechanism as outlined in Figure 2c, where $A\beta_{n-}$ denotes NMR-detectable low-MW Aβ(1–40) species, L is the equilibrium constant for the $mA\beta_{n-}$ *vs.* $(A\beta_{n-})m$ self-association equilibrium, and $K_{d,A\beta n+}$ is the site-specific dissociation constant of the $(A\beta_{n-})m$: $EGCG_p$ complex. Further details are available in the Supporting Information. The modeled curves shown in Figure 2d were computed using the minimal values of m and p that recapitulate the experimental 1D NMR intensity losses. For each set of $K_{d,A\beta n+}$, m, and p values, the L parameter was varied to optimize the fit to the experimental intensity data.

Ligand-Based 1D Saturation Transfer Difference (STD) NMR Experiments to Measure the EGCG Binding Affinity to Aβ40 Oligomers and Map the Binding Epitopes within EGCG

The titration of unlabeled 90 μM Aβ40 was also monitored by acquiring 1D STD NMR spectra.[28–31] STD spectra were recorded with 1024 scans, 32K complex points, and a spectral width of 15.98 ppm. Selective saturation of Aβ40 oligomers was implemented through methyl irradiation, using a train of 20 Gaussian-shaped pulses of 50 ms, separated by a 1 ms interpulse delay. A 30 ms spin lock was also employed to suppress peptide signals that overlap EGCG resonances. Subtraction of on-resonance vs off-resonance intensities was completed through phase cycling. Saturation transfer reference (STR) spectra were recorded with 256 scans, 32K complex points, and a spectral width of 15.98 ppm. A binding isotherm was created through modeling the STD amplification factors[30] (STD_{af}) at each

EGCG concentration using the 2′ and 6′ EGCG proton peaks. The STD_{af} was calculated as:

$$STD_{af} \propto \frac{I_0 - I_{sat}}{I_0} L_{tot} \quad (1)$$

where $I_0 - I_{sat}$ represents the signal intensity in the STD spectrum, I_0 is the intensity in the STR spectrum, and L_{tot} is the total EGCG concentration. The EGCG epitopes for binding to the Aβ40 oligomers were determined through the STD *vs.* STR ratio of each EGCG proton resonance at ligand concentrations where

the protein is nearly saturated ([EGCG] ≈ 475 μM). For the purpose of epitope mapping, the STD *vs.* STR ratios were then normalized to the highest ratio, in this case for the 6 and 8 protons of ring A, which was set to 100%.

$^{1}H–^{15}N$ Heteronuclear Single Quantum Coherence (HSQC) Experiments to Measure the EGCG Binding Affinity to Aβ40 Monomers

Uniformly ^{15}N-labeled 30 μM Aβ40, prepared as described above, was titrated with EGCG up to 300 μM and monitored by sensitivity-enhanced $^{1}H–^{15}N$ HSQC spectra. The HSQC spectra were recorded with 64 scans, a recycle delay of 1.0 s, 256 (t1) and 2048 (t2) complex points, and spectral widths of 31.82 and 14.06 ppm for the ^{15}N and ^{1}H dimensions, respectively. The ^{1}H and ^{15}N carrier frequencies were set at the water resonance and at the center of the amide region, respectively.

Binding Data Analysis

The STD_{af} measured by selectively saturating the Aβ(1–40) oligomers through methyl irradiation were modeled through a Scatchard-like binding isotherm:

$$STD_{af} / STD_{af,max} \propto [EGCG]/([EGCG] + K_{d,eff}) \quad (2)$$

where [EGCG] is the concentration of free EGCG and $K_{d,eff}$ is an effective site-specific dissociation constant for the binding of EGCG to the Aβ(1–40) oligomers. A similar binding isotherm was utilized to model the $\Delta\delta/\Delta\delta_{max}$ *vs.* $[EGCG]_{tot}$ plots utilized to measure the affinity of EGCG for Aβ(1–40) monomers at 30 μM, as shown in Figures 6b and S6d. For this purpose, we first calculated the EGCG-induced combined chemical shift changes (ΔCCS) as:

$$\Delta CCS = \sqrt{(0.2\Delta\delta_{Nh})^2 + \Delta\delta_{Hn}{}^2} \quad (3)$$

To build the binding isotherm at higher EGCG concentrations (*i.e.* 0–300 μM), as shown in Figure 6b, the residues with CCS changes larger than the 0.014 ppm cutoff[42] were selected, normalized with respect to the corresponding CCS change at 300 μM, and averaged, resulting in the plot of Figure 6d. To build the binding isotherm at low EGCG concentrations (*i.e.* 0–60 μM), as shown in Figure S6d, the residues with the 10 highest ΔCCS values were selected (*i.e.* 7, 12, 13, 16–20, 27, and 31), and for each of them, the ΔCCS values were normalized to the respective values measured at $[EGCG]_{tot}$ = 60 μM. The average normalized ΔCCS across the 10 selected residues was calculated to obtain the Δδ/Δδmax values reported in Figure S6d.

Pairwise Chemical Shift Projection Analyses

To evaluate the relative direction of the EGCG-induced displacements of ^{1}H,^{15}N HSQC cross-peaks, a displacement vector was defined for each residue as:

$$\Delta\vec{v}_i = (\delta_{Hn,holo,i} - \delta_{Hn,apo,i}\ ,\ 0.2\delta_{Nh,holo,i} - 0.2\delta_{Nh,apo,i}) \quad (4)$$

where $\delta_{Hn,holo,i}$ and $\delta_{Hn,apo,i}$ denote the amide ^{1}H chemical shift values measured in parts per million for residue *i* in the presence and absence of EGCG, respectively, while $\delta_{Nh,holo,i}$ and $\delta_{Nh,apo,i}$ are the respective amide ^{15}N chemical shift values in parts per million. The angle ϑij between the displacement vectors of two generic residues i and j is then computed through the renormalized dot product:[42,51–54,54,54]

$$\cos(\vartheta_{ij}) = \frac{\Delta\vec{V}_i \cdot \Delta\vec{V}_j}{|\Delta\vec{V}_i||\Delta\vec{V}_j|} \quad (5)$$

The residue pairs with cos(ϑij) > 0.95 were then visualized in a 40 × 40 matrix as shown in Figure 6e. This process was repeated for two different concentrations of EGCG (*i.e.* 40 and 300 μM), as well as for the case of a representative ligand binding specifically to a folded globular protein (i.e., cAMP binding to RIα (96–244)[52,55]).

^{15}N Dark-State Exchange Saturation Transfer (DEST) and ^{15}N Transverse Relaxation NMR To Probe the Exchange Dynamics at the Surface of Aβ40 Protofibrils

DEST and ^{15}N transverse relaxation NMR data were acquired in the absence and presence of 300 μM EGCG for a uniformly ^{15}N-labeled 230 μM Aβ40 sample, prepared as described above. The DEST and transverse relaxation rates were measured after sample equilibration (*i.e.* 11.5 days since initial preparation) and immediately following EGCG addition (*i.e.* at 13.5 days). The timeline of data acquisition is provided in Figure S1e. The DEST was implemented with a 900 ms ^{15}N continuous wave (CW) saturation pulse at four different radiofrequency offsets (+35, +2, −2, and −35 kHz) and a field strength of 350 Hz. Two-dimensional DEST data were collected as four interleaved data sets, corresponding to the four frequency offsets recorded with 32 scans, 128 dummy scans, a recycle delay of 1.50 s, 256 (t1) and 4K (t2) complex points, and spectral widths of 14.28 ppm (^{1}H) and 31.82 ppm (^{15}N). All spectral processing was completed with TopSpin 3.2.1, including the addition and subtraction of DEST data sets, and the spectra were transferred to Sparky for peak intensity measurements. The Gaussian line fitting function of Sparky was used to determine the fitted peak heights, and the signal-to-noise ratio was used as a measure of error for the fitted peak heights. The DEST difference, denoted here as Θ, was calculated as follows:

$$\Theta = \frac{(I_{+35} + I_{-35}) - (I_{+2} + I_{-2})}{(I_{+35} + I_{-35})} \quad (6)$$

where I_v denotes the peak height measured for a given residue at a ^{15}N CW offset of *v* kHz. The ^{15}N transverse relaxation rates were measured using a pseudo-3D pulse sequence containing water flip back and sensitivity enhancement. The spectra were recorded with 16 scans, 128 dummy scans, a recycle delay of 1.50 s, 4K complex points for a spectral width of 14.28 ppm in the t2 dimension, and 170 complex points for a spectral width of 31.82 ppm in the t1 dimension. The total CPMG lengths were 8.48, 16.96, 25.44, 33.92, 42.4, 50.88, 59.36, and 76.32 ms. The pseudo-3D spectra were processed with TopSpin 3.2.1, and the peak height decays were fitted to an exponential in Sparky.

WSTDHSQC and MeSTDHSQC

Unlike the 1D STD experiments outlined above, the STDHSQC pulse sequences described here aim at probing the saturation transferred to the amides of ^{15}N-labeled solutes (*i.e.* Aβ40) rather than to the EGCG ligand. Hence, these STD experiments utilize a ^{15}N,^{1}H HSQC readout block. The STDHSQC data were acquired for uniformly ^{15}N-labeled 30 and 220 μM Aβ40 samples, prepared as described above, in the absence and presence of 70 and 300 μM EGCG, respectively. Saturation was introduced either through methyl irradiation (MeSTDHSQC) or through water (WSTDHSQC) via a radiation-damping-driven selective inversion of the water polarization controlled by bipolar gradient pulses in alternate scans.[37] The WSTDHSQC pulse sequence was implemented using an HSQC detection block with 128 scans, a recycle delay of 1.20 s, 4K (t2) and 200 (t1) complex points, and spectral widths of 14.28 ppm (^{1}H) and 31.82 ppm (^{15}N). A reference ^{1}H,^{15}N HSQC spectrum was also recorded to normalize the WSTDHSQC intensities. The spectra were processed on TopSpin 3.2.1 and transferred to Sparky for intensity measurements using the Gaussian fitting function. The normalized WSTDHSQC intensities were further corrected for the residue-specific intrinsic exchange rates of amide protons with water ($k_{ex\ intr}$) calculated using the CIntX tool[38] to result in the Γ value defined as:

$$\Gamma = I_{WSTDHSQC}/(I_{HSQC}k_{ex\ intr}) \quad (7)$$

The MeSTDHSQC pulse sequence was obtained by replacing the spin-lock and water-gate modules of the 1D STD experiment optimized for ligand-based detection[28,29] with a sensitivity-enhanced HSQC block. Selective irradiation of the Aβ40 oligomers was achieved using methyl irradiation. The spectra were recorded with 128 scans and 4K (t2) and 200 (t1) complex points for spectral widths of 14.28 ppm (^{1}H) and 31.82 ppm (^{15}N), respectively. Reference sensitivity enhanced MeSTRHSQC spectra were also recorded to normalize the MeSTDHSQC intensities.

Ligand-Based Off-Resonance Rotational (ORR) Overhauser Effect Spectroscopy and Transfer Nuclear Overhauser Effect Spectroscopy (TrNOESY) To Probe the EGCG Conformation in the Apo and Aβ40 Oligomer-Bound States

Unlabeled 90 μM Aβ40, prepared as described above, was incubated with 720 μM EGCG and probed by TrNOESY NMR with a WATERGATE suppression scheme. The TrNOESY spectrum was recorded with 64 scans, a recycle delay of 1.20 s, 512 (t1) and 2048 (t2) complex points, and spectral widths of 11.98 ppm for each ^{1}H dimension. An NOE buildup was generated using NOESY mixing times ranging from 60 to 300 ms. The shortest mixing of 60 ms was used to measure the NOEs reported in Figure 5b, d. Similarly, an ORR NMR spectrum of 180 μM EGCG in the same buffer conditions used for the TrNOESY NMR was recorded with 48 scans, a recycle delay of 1.20 s, 700 (t1) and 2048 (t2) complex points, and spectral widths of 11.98 ppm for each ^{1}H dimension. The ORR mixing time was 158 ms, including two 4 ms adiabatic ramps, and the effective field angle was 54.7°. The TrNOEs and ROEs were utilized as experimental restraints in the modeling of EGCG holo and apo conformations, respectively.

Overall Protocol for Modeling the EGCG Conformations

As a starting point, we utilized EGCG conformations found in structures solved by X-ray crystallography and deposited in the Protein Data Bank (PDB), resulting in a total of seven EGCG structures. Each of these seven EGCG structures was isolated from the respective original PDB file, energy-minimized, and utilized as starting points for a 50 ns unrestrained MD simulation. Out of the seven MD simulations, two exhibited no significant violations of the ROEs observed for unbound EGCG (Figure S4) and were selected as starting points for a systematic grid search of the four rotatable bonds present in EGCG (Figure 1). These two grid-search EGCG conformational ensembles were then filtered on the basis of either the ROEs observed for unbound EGCG or the TrNOEs observed for bound EGCG, as shown in Figure 5i–k and Figure S5a–c (Supporting Information). Further details are provided below.

Initial Structure Preparation for Molecular Dynamics (MD) Simulations

EGCG structures were obtained from three PDB structures: three from 3NG5, two from 3OOB, and two from 4AWM. Molecular structures with hydrogen atoms were generated (as mol2 structure files) from each of the seven initial EGCG structures using the UCSF Chimera 1.10.1 molecular visualization software.[56] PDB coordinate files and molecular structure topology and parameter data formatted for use with the CHARMM all-atom force field were then generated from the mol2 structure files using the SwissParam software.[57] The topology and parameter data were then inserted into the respective parameter files for the CHARMM27 force field[58–61] in preparation for subsequent MD simulation setup.

MD Simulation Protocol

All MD simulations were performed using the NAMD 2.9 software[62] on the Shared Hierarchical Academic Research Computing Network (SHARCNET).[63] The CHARMM27 force field with CMAP correction,[58–61] supplemented with the molecular structure topology and parameter data computed for the EGCG molecule (as described above), was implemented for all simulations. Molecular structure coordinate and parameter files for the EGCG structures were constructed using the "Psfgen" module of VMD 1.8.6.64 The structures were then immersed in a cubic box of TIP3P water molecules (with box dimensions of 30 Å) using the Solvate module of VMD 1.8.6,64 such that there was a minimum distance of 8 Å between the EGCG molecule and the edge of the solvent box.

Initial energy minimizations were performed using the conjugate gradient algorithm of NAMD. Minimization was performed for 2000 steps, using a cut-off of 12 Å for all nonbonded energy calculations. Electrostatic interactions beyond the cut-off distance were computed using the particle mesh Ewald (PME) algorithm,[65] with a tolerance of 10−6 and a maximum grid spacing of 1.0 Å. Molecular dynamics simulations were then performed under cubic periodic boundary conditions, beginning from the energy-minimized initial structures. A time step of 1.0 fs was implemented throughout the simulations. All water molecules were constrained to their equilibrium geometries using the SETTLE algorithm,[66] and all covalent bonds to hydrogen were constrained using the SHAKE algorithm.[67] A cut-off of 9 Å with PME implementation was utilized for nonbonded energy calculations during the simulations. Short-range nonbonded and long-range electrostatic interactions were evaluated every 2.0 and 4.0 fs, respectively, using the RESPA multiple time step integrator.[68] All minimizations and simulations were executed on a 2.2 GHz Opteron cluster, using 64 CPUs per run.

The structures were heated linearly from −273 to +34 °C over 200 ps at constant volume, using the velocity reassignment protocol of NAMD. The heated structures were then simulated at 34 °C and constant volume (NVE ensemble) for another 1.0 ns to allow a period of temperature equilibration prior to introduction of pressure regulation. Finally, the structures were simulated at a constant temperature and pressure (NPT ensemble) for 50.0 ns, saving structures every 10000 time steps (*i.e.* every 10.0 ps) for subsequent analysis. A constant temperature of 34 °C was maintained using the Langevin dynamics algorithm,[69] with a Langevin damping coefficient of 1.0 ps^{-1}. A constant pressure of 1 atm (1.01325 bar) was maintained using the Nosé–Hoover Langevin piston method,[62] with a barostat oscillation period of 200.0 fs and a barostat damping time scale of 100.0 fs.

Conversion of ROEs/NOEs into Distance Restraints

Upper limits for distances between pairs of 1H nuclei were computed from the intensities of the $^{1}H–^{1}H$ ROE/NOE cross-peaks observed for unbound or Aβ-bound EGCG, respectively, as follows:[70]

$$r_{ij} = \sqrt[6]{\frac{I_{ref}}{I_{ij}}} \tag{8}$$

where I_{ij} is the intensity of the ROE/NOE cross-peak observed for ^{1}H nuclei *i* and *j*, r_{ij} is the computed distance between ^{1}H nuclei *i* and *j*, and I_{ref} is the ROE/NOE cross-peak intensity for a pair of ^{1}H nuclei separated by a known distance r_{ref}. The distances were calculated using the known distance between the two ^{1}H nuclei of the C-ring methylene group of EGCG (Figure 1), and errors in the calculated distances were computed using error propagation. On the basis of the computed distances, it was determined that the ^{1}H nuclei pairs with observed ROEs/NOEs all fell within a $^{1}H–^{1}H$ distance range of 1.9–2.8 Å (*i.e.* the range considered to represent "strong" ROEs/NOEs). To account for potential errors in the ROE/NOE measurements, a margin of 1.0 additional Å was applied to the calculated distances. Therefore, a more conservative $^{1}H–^{1}H$ distance cutoff of 3.8 Å was selected for screening the EGCG simulation trajectories for structures whose $^{1}H–^{1}H$ distances were in agreement with the observed $^{1}H–^{1}H$ ROEs/NOEs.

Screening of EGCG MD Simulation Trajectories against the Observed 1H–1H ROEs

For each EGCG structure from the MD simulation trajectories, the distances between pairs of hydrogen atoms with observed $^{1}H–^{1}H$ ROEs were computed and utilized to compute a violation energy score ($E_{violation}$) defined as:

$$E_{violation} = \begin{cases} \left(r_{obsd} - r_{cutoff}\right)^2 & if\ r_{obsd} > r_{cutoff} \\ 0 & if\ r_{obsd} > r_{cutoff} \end{cases} \tag{9}$$

where r_{obsd} is the computed distance between the hydrogen atoms and r_{cutoff} is the selected distance cut-off of 3.8 Å. If a hydrogen atom pair involved a C–H group from the B or D ring of EGCG (Figure 1), then distances were calculated for both C–H hydrogen atoms of that ring, and the smaller of the two calculated distances was used to determine the violation energy score for the hydrogen atom pair in question. This is because the closer C–H hydrogen atom is expected to dominate the observed $^{1}H–^{1}H$ ROE. The computed violation energy scores for all examined hydrogen atom pairs were then added to obtain a total violation energy score for each EGCG structure from a given MD trajectory. The total violation energy scores for each MD simulation trajectory were then plotted as boxplots (Figure S4) to assess the overall

extent of agreement of the structures with the observed ^{1}H–^{1}H ROEs, whereby low total violation energy scores indicate good agreement of the structures with the observed ^{1}H–1H ROEs.

Grid Search for EGCG Conformations Consistent with the Experimental ROEs or NOEs

Using the two EGCG structures with minimal ROE violations (*i.e.* the first EGCG ligand from PDB ID 3NG5 and the second EGCG ligand from PDB ID 3OOB, Figure S4) as starting points, potential conformers of the EGCG molecule were generated by performing bond rotations around the four rotatable bonds that link the rings of the EGCG molecule to one another (Figure 1): the bond linking the B and C rings, the ester bond situated between the C and D rings, and the bonds that link the ester moiety to the C and D rings. All rotations were performed using Fortran scripts, implementing a bond rotation subroutine available online. The ester bond was rotated in increments of 180° to allow exploration of its cis and trans conformations, while the other three bonds were rotated in increments of 20°. To relax potential steric clashes in the generated structures, energy minimizations were performed for the structures using the conjugate gradient algorithm of NAMD. Minimization was performed for 1000 steps, with no cut-off implemented for the nonbonded energy calculations.

Screening of EGCG Structures from the Grid Search against the Observed 1H–1H ROEs or NOEs.

Total violation energy scores for the energy-minimized grid-search structures were computed as follows. Upper limit distance cut-offs were computed as described above for all proton pairs with an observed ROE or NOE, while a 3.8 Å lower limit distance cutoff was applied to proton pairs for which an ROE or NOE was not observed. The 10 structures with the lowest total violation energy scores were then selected. To filter out structures with violations of covalent geometry or nonbonded contacts, the total bonded and nonbonded potential energies were computed:[62]

$$E_{bonded} = E_{bond} + E_{angle} + E_{dihedral} + E_{improper} \quad (10)$$

$$E_{non\text{-}bonded} = E_{electrostatic} + E_{VDW} \quad (11)$$

where E_{bond}, E_{angle}, $E_{dihedral}$, and $E_{improper}$ are the total bond-stretching, bond-angle-bending, dihedral rotation, and improper dihedral potential energies, respectively, and $E_{electrostatic}$ and E_{VDW} are the total electrostatic and van der Waals nonbonded potential energies. Structures with bonded and nonbonded potential energies greater than 50 kcal/mol were excluded from analysis.

2.8 References

(1) Bodner, C. R.; Maltsev, A. S.; Dobson, C. M.; Bax, A. Biochemistry **2010**, *49*, 862–871.
(2) Roche, J.; Shen, Y.; Lee, J. H.; Ying, J.; Bax, A. Biochemistry **2016**, *55*, 762–775.
(3) Bodner, C. R.; Dobson, C. M.; Bax, A. J. Mol. Biol. **2009**, *390*, 775–790.
(4) Baias, M.; Smith, P. E. S.; Shen, K.; Joachimiak, L. A.; Zerko, S.; Kozminski, W.; Frydman, J.; Frydman, L. J. Am. Chem. Soc. **2017**, *139*, 1168–1176.
(5) Cantarutti, C.; Raimondi, S.; Brancolini, G.; Corazza, A.; Giorgetti, S.; Ballico, M.; Zanini, S.; Palmisano, G.; Bertoncin, P.; Marchese, L.; Mangione, P. P.; Bellotti, V.; Corni, S.; Fogolari, F.; Esposito, G. Nanoscale **2017**, *9*, 3941–3951.
(6) Temussi, P. A.; Masino, L.; Pastore, A. EMBO J. **2003**, *22*, 355–361.
(7) Masino, L.; Nicastro, G.; Menon, R. P.; Piaz, F. D.; Calder, L.; Pastore, A. J. Mol. Biol. **2004**, *344*, 1021–1035.
(8) Bieschke, J.; Russ, J.; Friedrich, R. P.; Ehrnhoefer, D. E.; Wobst, H.; Neugebauer, K.; Wanker, E. E. Proc. Natl. Acad. Sci. U. S. A. **2010**, *107*, 7710–7715.
(9) Ehrnhoefer, D. E.; Bieschke, J.; Boeddrich, A.; Herbst, M.; Masino, L.; Lurz, R.; Engemann, S.; Pastore, A.; Wanker, E. E. Nat. Struct. Mol. Biol. **2008**, *15*, 558–566.
(10) Ehrnhoefer, D. E.; Duennwald, M.; Markovic, P.; Wacker, J. L.; Engemann, S.; Roark, M.; Legleiter, J.; Marsh, J. L.; Thompson, L. M.; Lindquist, S.; Muchowski, P. J.; Wanker, E. E. Hum. Mol. Genet. **2006**, *15*, 2743–2751.
(11) Hauber, I.; Hohenberg, H.; Holstermann, B.; Hunstein, W.; Hauber, J. Proc. Natl. Acad. Sci. U. S. A. **2009**, *106*, 9033–9038.
(12) Lopez del Amo, J. M.; Fink, U.; Dasari, M.; Grelle, G.; Wanker, E. E.; Bieschke, J.; Reif, B. J. Mol. Biol. **2012**, *421*, 517–524.
(13) Meng, X.; Munishkina, L. A.; Fink, A. L.; Uversky, V. N. Biochemistry **2009**, *48*, 8206–8224.
(14) Rambold, A. S.; Miesbauer, M.; Olschewski, D.; Seidel, R.; Riemer, C.; Smale, L.; Brumm, L.; Levy, M.; Gazit, E.; Oesterhelt, D.; Baier, M.; Becker, C. F.; Engelhard, M.; Winklhofer, K. F.; Tatzelt, J. J. Neurochem. **2008**, *107*, 218–229.
(15) Roberts, B. E.; Duennwald, M. L.; Wang, H.; Chung, C.; Lopreiato, N. P.; Sweeny, E. A.; Knight, M. N.; Shorter, J. Nat. Chem. Biol. **2009**, *5*, 936–946.
(16) Sinha, S.; Du, Z.; Maiti, P.; Klarner, F.-G.; Schrader, T.; Wang, C.; Bitan, G. ACS Chem. Neurosci. **2012**, *3*, 451–458.
(17) Sironi, E.; Colombo, L.; Lompo, A.; Messa, M.; Bonanomi, M.; Regonesi, M. E.; Salmona, M.; Airoldi, C. Chem. - Eur. J. **2014**, *20*, 13793–13800.
(18) Zhu, M.; Rajamani, S.; Kaylor, J.; Han, S.; Zhou, F.; Fink, A. L. J. Biol. Chem. 2004, 279, 26846–26857.
(19) Bonanomi, M.; Visentin, C.; Natalello, A.; Spinelli, M.; Vanoni, M.; Airoldi, C.; Regonesi, M. E.; Tortora, P. Chem. - Eur. J. **2015**, *21*, 18383–18393.
(20) Guzzi, C.; Colombo, L.; Luigi, A. D.; Salmona, M.; Nicotra, F.; Airoldi, C. Chem. - Asian J. **2017**, *12*, 67–75.
(21) Jang, H.; Connelly, L.; Arce, F. T.; Ramachandran, S.; Lal, R.; Kagan, B. L.; Nussinov, R. Phys. Chem. Chem. Phys. **2013**, *15*, 8868–8877.
(22) Ma, B.; Nussinov, R. Proc. Natl. Acad. Sci. U. S. A. **2002**, *99*, 14126–14131.
(23) Petkova, A. T.; Ishii, Y.; Balbach, J. J.; Antzutkin, O. N.; Leapman, R. D.; Delaglio, F.; Tycko, R. Proc. Natl. Acad. Sci. U. S. A. **2002**, *99*, 16742–16747.
(24) Meisl, G.; Yang, X.; Frohm, B.; Knowles, T. P. J.; Linse, S. Sci. Rep. **2016**, *6*, 18728.
(25) Fawzi, N. L.; Ying, J.; Ghirlando, R.; Torchia, D. A.; Clore, G. M. Nature **2011**, *480*, 268–272.
(26) Fawzi, N. L.; Ying, J.; Torchia, D. A.; Clore, G. M. Nat. Protoc. **2012**, *7*, 1523–1533.
(27) Hyung, S.-J.; DeToma, A. S.; Brender, J. R.; Lee, S.; Vivekanandan, S.; Kochi, A.; Choi, J.-S.; Ramamoorthy, A.; Ruotolo, B. T.; Lim, M. H. Proc. Natl. Acad. Sci. U. S. A. **2013**, *110*, 3743–3748.
(28) Huang, H.; Milojevic, J.; Melacini, G. J. Phys. Chem. B **2008**, *112*, 5795–5802.

(29) Milojevic, J.; Esposito, V.; Das, R.; Melacini, G. J. Am. Chem. Soc. **2007**, *129*, 4282−4290.
(30) Mayer, M.; Meyer, B. J. Am. Chem. Soc. **2001**, *123*, 6108−6117.
(31) DALVIT, C. Prog. Nucl. Magn. Reson. Spectrosc. **2007**, *51*, 243−271.
(32) Dalvit, C.; Fogliatto, G.; Stewart, A.; Veronesi, M.; Stockman, B. J. Biomol. NMR **2001**, *21*, 349−359.
(33) Fawzi, N. L.; Ying, J.; Torchia, D. A.; Clore, G. M. J. Am. Chem. Soc. **2010**, *132*, 9948−9951.
(34) Vallurupalli, P.; Sekhar, A.; Yuwen, T.; Kay, L. E. J. Biomol. NMR **2017**, *67*, 243−271.
(35) Fusco, G.; Pape, T.; Stephens, A. D.; Mahou, P.; Costa, A. R.; Kaminski, C. F.; Kaminski Schierle, G. S.; Vendruscolo, M.; Veglia, G.; Dobson, C. M.; De Simone, A. Nat. Commun. **2016**, *7*, 12563.
(36) Ceccon, A.; Tugarinov, V.; Bax, A.; Clore, G. M. J. Am. Chem. Soc. **2016**, *138*, 5789−5792.
(37) Fan, J.-S.; Lim, J.; Yu, B.; Yang, D. J. Biomol. NMR **2011**, *51*, 151−162.
(38) Richa, T.; Sivaraman, T. J. Pharm. Sci. Res. 2012, 4, 1852−1858. (39) Cardamone, M.; Puri, N. K. Biochem. J. **1992**, *282*, 589−593.
(40) Mannini, B.; Mulvihill, E.; Sgromo, C.; Cascella, R.; Khodarahmi, R.; Ramazzotti, M.; Dobson, C. M.; Cecchi, C.; Chiti, F. ACS Chem. Biol. **2014**, *9*, 2309−2317.
(41) Pawar, D. M.; Khalil, A. A.; Hooks, D. R.; Collins, K.; Elliott, T.; Stafford, J.; Smith, L.; Noe, E. A. J. Am. Chem. Soc. **1998**, *120*, 2108−2112.
(42) Selvaratnam, R.; Chowdhury, S.; VanSchouwen, B.; Melacini, G. Proc. Natl. Acad. Sci. U. S. A. **2011**, *108*, 6133−6138.
(43) Camilloni, C.; De Simone, A.; Vranken, W. F.; Vendruscolo, M. Biochemistry **2012**, *51*, 2224−2231.
(44) Williamson, M. P. Prog. Nucl. Magn. Reson. Spectrosc. **2013**, *73*, 1−16.
(45) Wang, S.-H.; Liu, F.-F.; Dong, X.-Y.; Sun, Y. J. Phys. Chem. B **2010**, *114*, 11576−11583.
(46) Natural Compounds as Therapeutic Agents for Amyloidogenic Diseases; Vassallo, N., Ed.; Advances in Experimental Medicine and Biology 863; Springer International Publishing: Cham, Switzerland, **2015**.
(47) Popovych, N.; Brender, J. R.; Soong, R.; Vivekanandan, S.; Hartman, K.; Basrur, V.; Macdonald, P. M.; Ramamoorthy, A. J. Phys. Chem. B **2012**, *116*, 3650−3658.
(48) Cohen, S. I. A.; Arosio, P.; Presto, J.; Kurudenkandy, F. R.; Biverstal, H.; Dolfe, L.; Dunning, C.; Yang, X.; Frohm, B.;
Vendruscolo, M.; Johansson, J.; Dobson, C. M.; Fisahn, A.; Knowles, T. P. J.; Linse, S. Nat. Struct. Mol. Biol. **2015**, *22*, 207−213.
(49) Liu, H.; Yu, L.; Dong, X.; Sun, Y. J. Colloid Interface Sci. **2017**, *491*, 305−312.
(50) Goddard, T. D.; Kneller, D. G. Sparky3; University of California: San Francisco.
(51) Selvaratnam, R.; VanSchouwen, B.; Fogolari, F.; Mazhab-Jafari, M. T.; Das, R.; Melacini, G. Biophys. J. **2012**, *102*, 630−639.
(52) Akimoto, M.; Selvaratnam, R.; McNicholl, E. T.; Verma, G.; Taylor, S. S.; Melacini, G. Proc. Natl. Acad. Sci. U. S. A. **2013**, *110*, 14231−14236.
(53) Selvaratnam, R.; Mazhab-Jafari, M. T.; Das, R.; Melacini, G. PLoS One **2012**, *7*, e48707.
(54) Ruschak, A. M.; Kay, L. E. Proc. Natl. Acad. Sci. U. S. A. **2012**, *109*, E3454−62.
(55) Moleschi, K. J.; Akimoto, M.; Melacini, G. J. Am. Chem. Soc. **2015**, *137*, 10777−10785.
(56) Pettersen, E. F.; Goddard, T. D.; Huang, C. C.; Couch, G. S.; Greenblatt, D. M.; Meng, E. C.; Ferrin, T. E. J. Comput. Chem. **2004**, *25*, 1605−1612.
(57) Zoete, V.; Cuendet, M. A.; Grosdidier, A.; Michielin, O. J. Comput. Chem. **2011**, *32*, 2359−2368.
(58) MacKerell, A. D.; Bashford, D.; Bellott, M.; Dunbrack, R. L.; Evanseck, J. D.; Field, M. J.; Fischer, S.; Gao, J.; Guo, H.; Ha, S.; Joseph-McCarthy, D.; Kuchnir, L.; Kuczera, K.; Lau, F. T.; Mattos, C.; Michnick, S.; Ngo, T.; Nguyen, D. T.; Prodhom, B.; Reiher, W. E.; Roux, B.; Schlenkrich, M.; Smith, J. C.; Stote, R.; Straub, J.; Watanabe, M.; Wiorkiewicz-Kuczera, J.; Yin, D.; Karplus, M. J. Phys. Chem. B **1998**, *102*, 3586−3616.
(59) Mackerell, A. D., JR; Feig, M.; Brooks, C. L. J. Comput. Chem. **2004**, *25*, 1400−1415.
(60) Foloppe, N.; MacKerell, A. D., Jr. J. Comput. Chem. **2000**, *21*, 86−104.
(61) MacKerell, A. D.; Banavali, N. K. J. Comput. Chem. **2000**, *21*, 105−120.

(62) Phillips, J. C.; Braun, R.; Wang, W.; Gumbart, J.; Tajkhorshid, E.; Villa, E.; Chipot, C.; Skeel, R. D.; Kale, L.; Schulten, K. J. Comput. Chem. **2005**, *26*, 1781−1802.
(63) The Shared Hierarchical Academic Research Computing Network (SHARCNET).
(64) Visual Molecular Dynamics (VMD); Theoretical and Computational Biophysics Group, Beckman Institute: Urbana, IL, **2007**.
(65) Darden, T.; York, D.; Pedersen, L. J. Chem. Phys. **1993**, *98*, 10089−10092.
(66) Miyamoto, S.; Kollman, P. A. J. Comput. Chem. **1992**, *13*, 952−962.
(67) Ryckaert, J.-P.; Ciccotti, G.; Berendsen, H. J. J. Comput. Phys. **1977**, *23*, 327−341.
(68) Tuckerman, M.; Berne, B. J.; Martyna, G. J. J. Chem. Phys. **1992**, *97*, 1990−2001.
(69) Izaguirre, J. A.; Catarello, D. P.; Wozniak, J. M.; Skeel, R. D. J. Chem. Phys. **2001**, *114*, 2090−2098.
(70) Butts, C. P.; Jones, C. R.; Towers, E. C.; Flynn, J. L.; Appleby, L.; Barron, N. J. Org. Biomol. Chem. **2011**, *9*, 177−184.

2.9 Supplementary Information

Analysis of the "Hill-Scatchard-like" model (Figure 2c,d)

Assuming that mAβ40$_{n-}$ low-MW oligomers or monomers associate cooperatively in a Hill-like manner and that p molecules of EGCG bind the (Aβ40$_{n-}$)m oligomers at sites that are independent and equivalent ("Scatchard-like" model), the binding polynomial for the model depicted in Figure 2e is:

$$Q = [P] + [P_m]\{1 + ([A]/ K_{d,A\beta n+})\}^p \quad \text{(S1)}$$

where P and A stand for Aβ40$_{n-}$ and EGCG, respectively, while $K_{d,A\beta n+}$ is the per-site dissociation constant for EGCG binding to the (Aβ40$_{n-}$) m oligomers. Hence, the fraction of low-MW oligomers or monomers (P) is:

$$x_P = [P] / Q \quad \text{(S2)}$$

or, considering that $L = [P_m]/[P]^m$:

$$x_P = 1 / \{1 + L[P]^{m-1}\{1 + ([A]/ K_{d,A\beta n+})\}^p\} \quad \text{(S3)}$$

By incrementing the [A] values from 0 to 500 μM in steps of 2 μM, this equation was utilized to compute the x_P vs. [EGCG] functions shown in Figure 2d to model the 1D NMR signal losses occurring as the [EGCG] concentration increases. For this purpose the [P] value at each [A] value was computed as $x_{P,i-1}$ $[P]_{Tot}$, where $x_{P,i-1}$ is the x_P value computed for the preceding [A] value. The first value of [P] was assumed to be $[P]_{Tot}$. Furthermore, the effective concentration of (Aβ40$_{n-}$)m oligomers was assumed to be sufficiently low to assume that $[A]_{Tot.} \sim [A]$ and the effect on x_P of EGCG binding to Aβ40$_{n-}$ was hypothesized to be negligible.

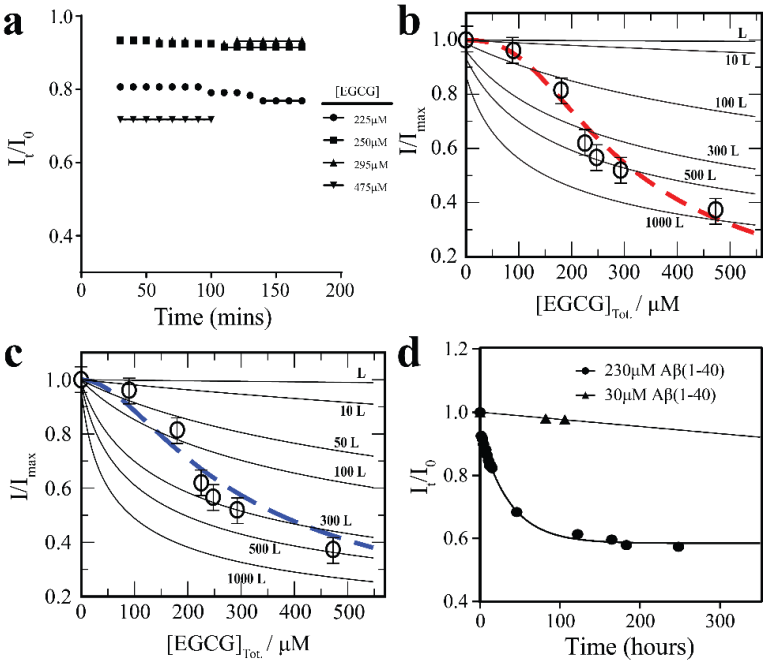

Figure S1. *Control data for Figures 2 and 3.* (a) Time dependent monitoring of relative Aβ40 methyl intensities after each EGCG addition in the titration shown in Figure 2b, d. The intensities reported are relative to the intensity at the last time point of the previous EGCG concentration. Equilibration plots are shown for representative EGCG concentrations. (b, c) Additional simulations to show that the experimental data of Fig. 2d cannot be accounted for by p = 1, irrespective of the L values chosen. The thick dashed red curve is as in Fig. 2d ($K_{d,A\beta n+}$=14 μM, m=2, p=3) and is reported here for comparison purposes, while the thin solid black curves were computed setting p = 1, *i.e.* using $K_{d,A\beta n+}$=14 μM, m=2, p=1 and L values scaled up by a factor of 1, 10, 10^2, $3*10^2$, $5*10^2$ and 10^3. In(c) the thick dashed blue curve is as in Fig. 2d ($K_{d,A\beta n+}$=1.4 μM, m=2, p=2) and is reported here for comparison purposes, while the thin solid black curves were computed using p = 1, i.e. $K_{d,A\beta n+}$=1.4 μM, m=2, p=1 and L values scaled up by a factor of 1, 10, 50, 10^2, $3*10^2$, $5*10^2$ and 10^3. These simulations show that with a value of p = 1 it would be challenging to fit the model in Fig. 2c to the data in Fig. 2d, further confirming that p > 1, *i.e.* multiple EGCG molecule bound per Aβ oligomer. (d) Relative NMR Intensity *vs.* time profiles of 230 μM ^{15}N Aβ40 (red) and 30 μM ^{15}N Aβ40 (blue). NMR intensity measurements are based on the average peak intensities in the 2D ^{15}N-^{1}H HSQC spectra and reported relative to the intensities at t = 0. (e) Timeline of the equilibration and data acquisition of the dilute (30 μM) and concentrated (220 μM and 230 μM) ^{15}N labeled samples. The red dashed line indicates the time of EGCG addition. The black arrows indicate either the times during which ^{15}N-^{1}H HSQCs were acquired to monitor sample equilibration or aliquots were removed from the 230 μM Aβ40 sample for DLS and EM measurements.

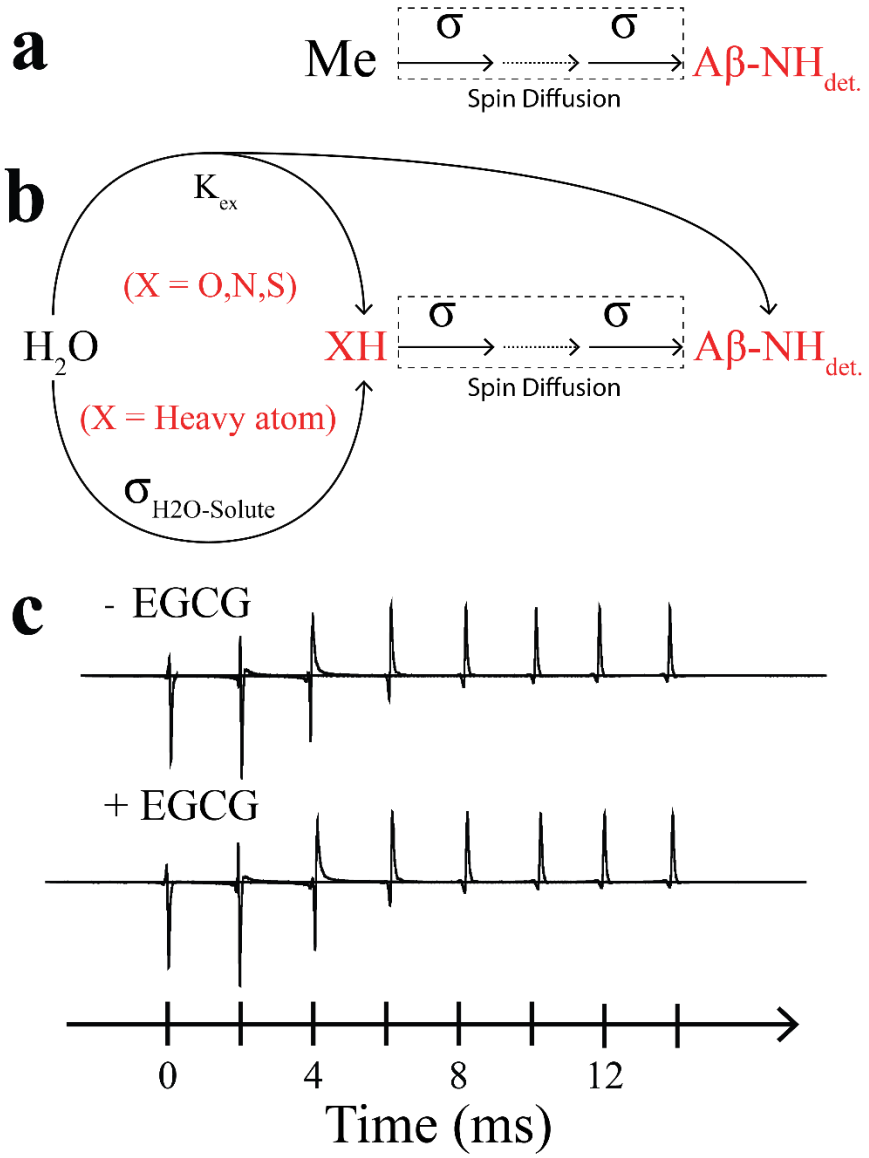

Figure S2. Magnetization transfer pathways in MeSTDHSQC (a) and wSTDHSQC experiments (b). (a) In the MeSTDHSQC experiment saturation is introduced through the methyl ^{1}H spins and transferred through multiple relayed dipolar-dipolar cross-relaxation steps (σ), *i.e.* spin-diffusion, to the amides of Aβ (red), which are then frequency labeled in the HSQC experiment providing an effective read-out. (b) In the wSTDHSQC experiment saturation is introduced through the water ^{1}H spins and transferred to the solute through either proton exchange ($K_{ex.}$) with labile XH protons (including the Aβ amides) and/or intermolecular cross-relaxation ($\sigma_{H2O\text{-}Solute}$). The subsequent steps resemble the spin-diffusion pathway shown in panel (a). In (a) and (b), the exchange of Aβ polypeptide chains between the monomeric and oligomeric states is not explicitly shown for the sake of simplicity, although it is clear that cross-relaxation is most efficient in the oligomeric state, while NMR detection occurs in the monomeric state. Water magnetization was selectively inverted through radiation damping. The efficiency of radiation damping-driven water inversion did not change appreciably upon addition of EGCG, as shown in the water magnetization inversion recovery profiles of panel (c).

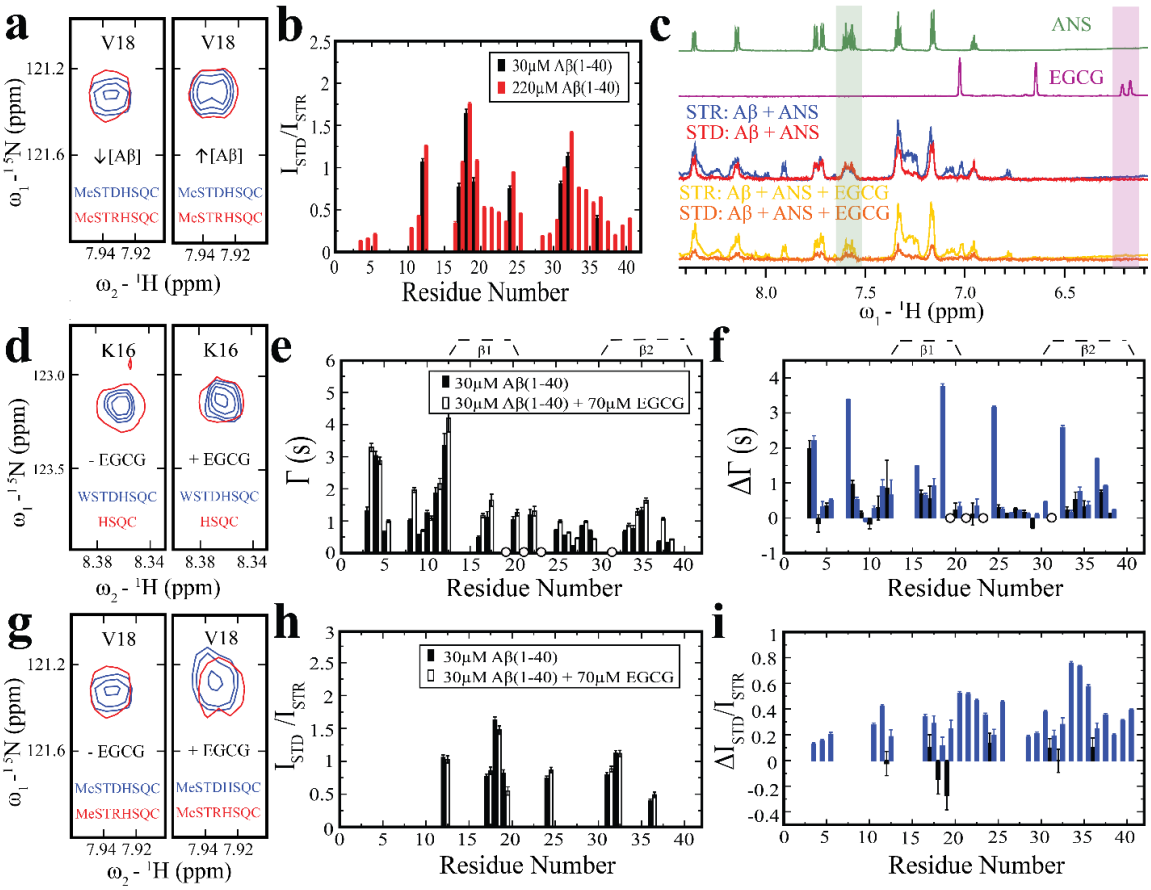

Figure S3. *Additional control experiments for Figure 4 on the solvent exposure of the Aβ40 oligomers.* (a) Representative expansion from MeSTDHSQC (blue) and MeSTRHSQC (red) spectra of dilute (30 μM) and concentrated (220 μM) Aβ40. (b) Residue-specific MeSTDHSQC/MeSTRHSQC profiles for the Aβ40 samples shown in (a). Color codes are shown in the panel. (c) ^{1}H NMR spectrum of 200 μM ANS (green) and 180 μM EGCG (purple). 1D-STR (blue) and 1D-STD (red) spectra of 90 μM Aβ40 in the presence of 200 μM ANS. 1D-STR (yellow) and 1D-STD (orange) spectra of 90 μM Aβ40 in the presence of 200 μM ANS and 180 μM EGCG. The green and purple shaded areas highlight peaks unique to ANS and EGCG, respectively. The STR spectra were scaled down such that the STD:STR ratio for the unique ANS peak (green highlight) in the Aβ-ANS mixture was equal to 1. (d) Representative expansion from the WSTDHSQC (blue) and reference HSQC (red) spectra of 30 μM Aβ40 in the absence and presence of 70 μM EGCG. (e) WSTDHSQC profiles of the samples shown in (d), normalized to the HSQC intensities and corrected for residue-specific intrinsic exchange rates with water (see Experimental Section). (f) Difference in the WSTDHSQC profiles shown in (e) (black) superimposed for the convenience of comparison to the difference in WSTDHSQC profiles shown in Fig. 4f (blue).(g) As (d), except of the MeSTDHSQC (blue) and MeSTRHSQC (red) spectra. (h) MeSTDHSQC/MeSTRHSQC profiles of the samples shown in (g). The profile in the absence of EGCG is as the dilute profile show in panel (b) and it is shown here again for the convenience of comparison. (i) Difference between the profiles shown in (h) (black)overlapped with the difference between the profiles shown in (b) (blue).

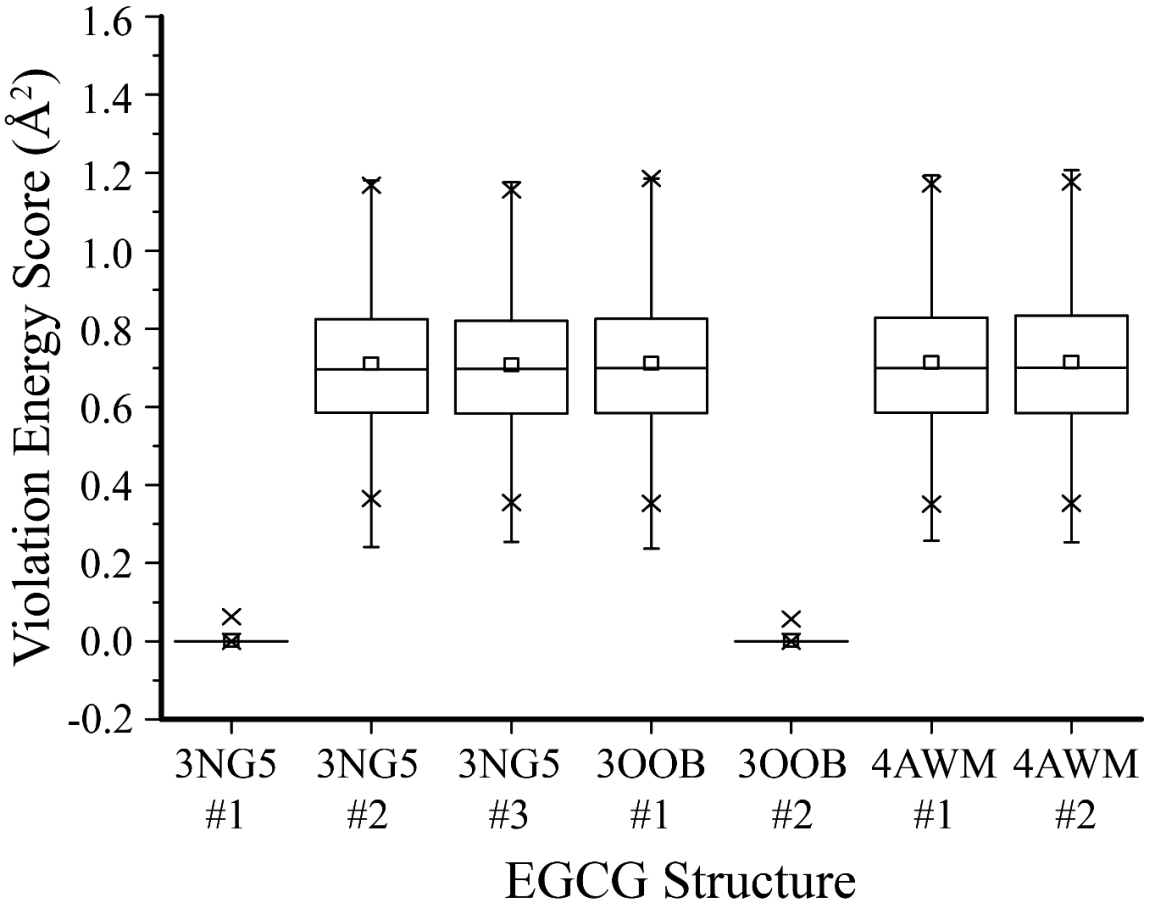

Figure S4. *Distributions of total violation energy scores computed for the EGCG structures from each MD simulation trajectory*. Violation energy scores computed as described in the Experimental Section based on the ^{1}H-^{1}H ROEs observed for unbound EGCG. The first EGCG ligand from PDB ID "3NG5" ("3NG5#1") and the second EGCG ligand from PDB ID "3OOB" ("3OOB#2") exhibited the best agreement of the respective MD trajectories with the ^{1}H-^{1}H ROEs observed for unbound EGCG (as indicated by near-zero violation energy scores), and were thus selected for grid-search analysis. All boxplots were constructed using Origin 9.1 (OriginLabCorporation), and the statistics reported in each boxplot are as follows: the middle, bottom and top lines of the central box represent the median, 25th percentile and 75th percentile of the data set, respectively; the whiskers represent additional data falling within 1.5*IQR above the 75th percentile or below the 25th percentile, where IQR is the difference between the 75th and 25th percentiles; the "□"symbol represents the mean of the data set; and the two "×"symbols represent the 1st and 99th percentiles of the MD data set.

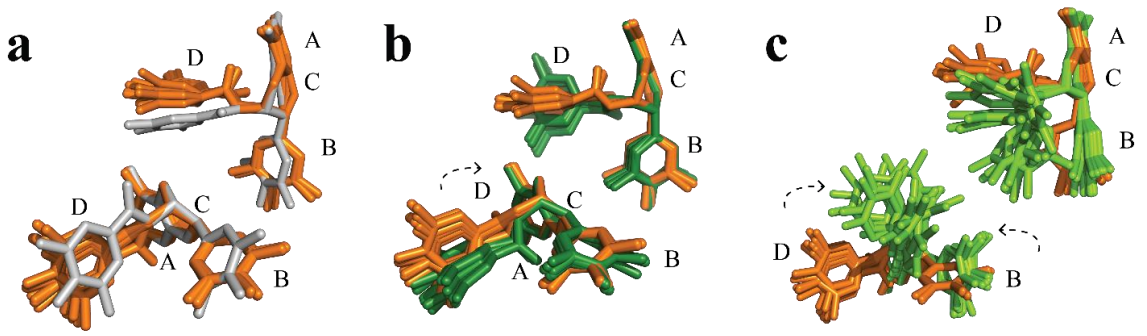

Figure S5. *Selected structures from the grid-search starting from the second EGCG ligand of PDB ID "3OOB".* (a) Overlap of the apo EGCG structure (gray) derived from PDB ID "3OOB" with the apo grid-search structures selected based on the observed $^{1}H - ^{1}H$ ROEs (orange). Two orientations are shown. (b) Apo structures from the grid-search in (a) superimposed to the holo grid-search structures selected based on the $^{1}H - ^{1}H$ NOEs (dark green). The EGCG ester bond was kept in a trans configuration. Black dashed arrow indicates apo *vs.* holo conformational changes. (c) As in panel (b), except with the EGCG ester bond isomerized to cis (light green). The black dashed arrows illustrate the rotations that occur in the apo –holo transition.

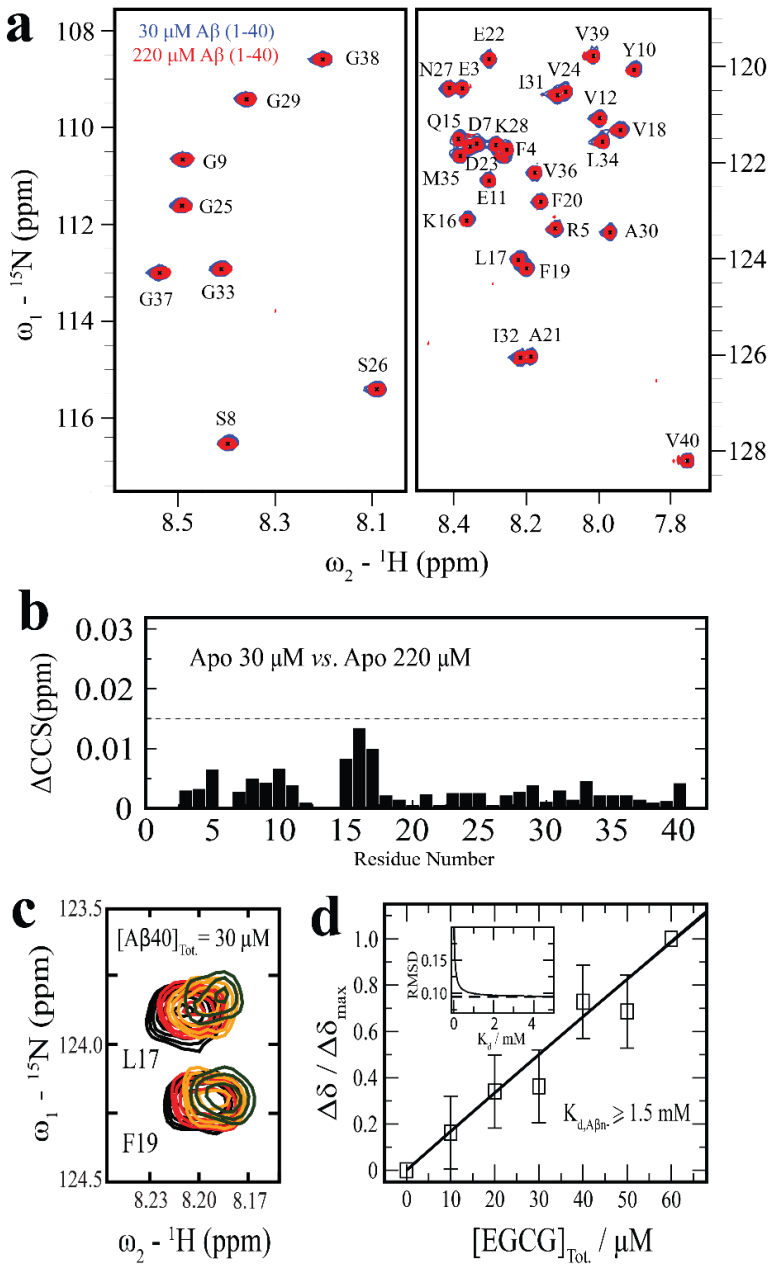

Figure S6. *Control chemical shift data.* No major chemical shift variations are observed between dilute (30 μM) and concentrated (220 μM) Aβ40, as shown by spectral overlap (a) and compounded chemical shift changes lower than the 0.014 ppm threshold value[46] (b). The affinity of EGCG for the Aβ(1-40) monomers was probed through combined chemical shift changes obtained from ^{1}H-^{15}N HSQC NMR spectra (c), acquired with a total Aβ(1-40) concentration of 30 μM and increasing EGCG concentrations, at a temperature of 283 K and a pH 6.8 in 50 mM HEPES, 1.5mM Tris 10% D_2O buffer. The combined chemical shifts were normalized to the value measured at $[EGCG]_{Tot.}$ 60 μM as explained in the Experimental Section and plotted against $[EGCG]_{Tot.}$, as shown by the empty squares in panel (d). The inset in panel (d) illustrates the RMSD *vs.* K_d plot, pointing to K_d values ≥1.5 mM, which result in the straight black line in the main panel (d).

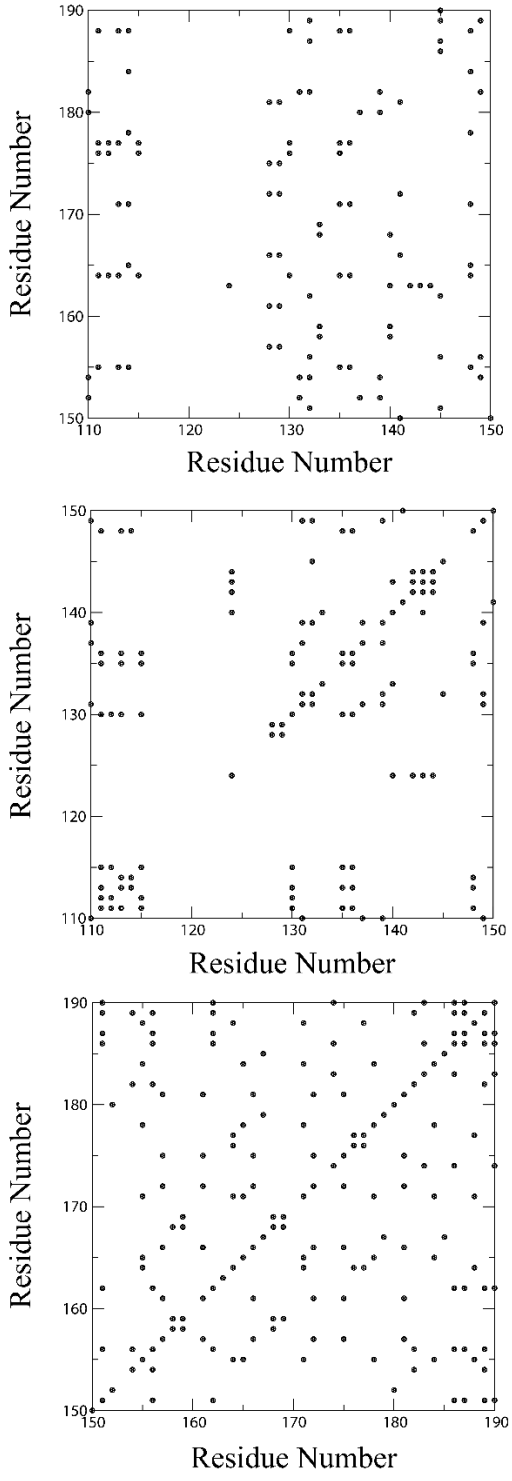

Figure S7. *Additional control cosθ matrix data.* Other representative 40 residue x 40 residue sections of the apo *vs.* cAMP-bound cos θ matrix for PKA RIα (96-244) (solid black circles). A cut-off of cos θ > 0.95 was used to display the cross-peaks in all panels.

Chapter 3. Atomic Resolution Map of the Soluble Amyloid Beta Assembly Toxic Surfaces

3.1 Author's Preface

The work presented in this chapter has previously been published and is reproduced here with permission from the Royal Society of Chemistry: Chemical Science. Full citation is as follows:

Ahmed, R.; Akcan, M.; Khondker, A.; Rheinstädter, M. C.; Bozelli, J. C.; Epand, R. M.; Huynh, V.; Wylie, R. G.; Boulton, S.; Huang, J.; *et al*. Atomic resolution map of the soluble amyloid beta assembly toxic surfaces. *Chemical science* **2019**, *10*, 6072–6082.

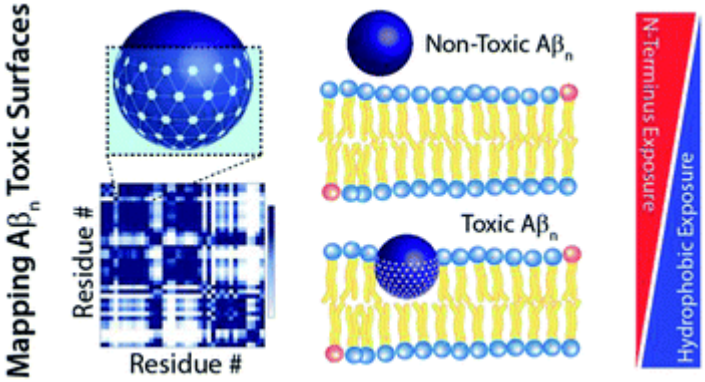

I conducted most of the experiments necessary for the manuscript and analyzed the data. Michael Akcan performed the ThT fluorescence experiments. Adree Khondker acquired and analyzed the Wide-Angle X-ray Diffraction (WAXD) data with support from Dr. Maikel Rheinstädter. Jose Carlos Bozelli Jr. made the liposomes and Dr. Richard Epand provided feedback regarding the membrane data. Vincent Huynh cultured the mammalian cell lines and provided feedback on the cell toxicity data with support from Dr. Ryan Wylie. Dr. Stephen Boulton provided support with the covariance and clustering analyses. Jinfeng Huang constructed the map of the toxic surfaces superimposed on the Aβ40 fibril structure. I co-wrote the manuscript and designed the research with Dr. Giuseppe Melacini.

3.2 Abstract

Soluble amyloid beta assemblies ($A\beta_n$) are neurotoxic and play a central role in the early phases of the pathogenesis cascade leading to Alzheimer's disease. However, the current knowledge about the molecular determinants of $A\beta_n$ toxicity is at best scant. Here, we comparatively analyze $A\beta_n$ prepared in the absence or presence of a catechin library that modulates cellular toxicity. By combining solution NMR with dynamic light scattering, fluorescence spectroscopy, electron microscopy, wide-angle X-ray diffraction and cell viability assays, we identify a cluster of unique molecular signatures that distinguish toxic *vs.* nontoxic Aβ assemblies. These include the exposure of a hydrophobic surface spanning residues 17–28 and the concurrent shielding of the highly charged N-terminus. We show that the combination of these two dichotomous structural transitions promotes the colocalization and insertion of β-sheet rich $A\beta_n$ into the membrane, compromising membrane integrity. These previously elusive toxic surfaces mapped here provide an unprecedented foundation to establish structure-toxicity relationships of Aβ assemblies.

3.3 Introduction

While the etiology of Alzheimer's disease (AD) is complex and not fully understood, genetic mutations provide compelling evidence that the amyloid beta (Aβ) peptide plays a critical role in AD pathogenesis.[1,2] Indeed, mutations in the genes encoding either the Aβ progenitor (*i.e.* the amyloid precursor protein or APP) or the APP processing enzyme (presenilin 1 and 2 genes) are sufficient to cause AD.[1] Moreover, none of the familial AD mutations involve genes encoding for the tau protein. Instead, tau mutations enhance the deposition of neurofibrillary tangles *i.e.* the other neuropathological hallmark of AD, but not amyloid plaques, and lead to different neuropathological disorders.[3] These genetic signatures coupled with the observation that Aβ deposition precedes other biochemical and histopathological changes, including neurofibrillary tangle formation,[4] provide evidence that tau aggregation occurs downstream to Aβ aggregation. In addition, Aβ clearance is controlled by one of the most significant risk factors for late onset AD, *i.e.* APOE4.[5] Given the genetic link between Aβ and AD, one of the main hypotheses proposed to explain AD pathogenesis is the amyloid cascade. The amyloid hypothesis posits that neuronal death in AD patients is associated with the increased production, self-association and accumulation of Aβ in the brain.[2]

Since it was originally postulated, the generality of the amyloid cascade hypothesis has been challenged because Aβ plaque burden correlates poorly with cognitive dysfunction.[6] However, this inconsistency has been reconciled by considering that soluble oligomers and protofibrils formed during the self-association cascade towards mature fibrils are neurotoxic[7] and better correlate with cognitive impairment in the early stages of AD.[8] Moreover, the neurotoxicity of Aβ oligomers has been linked to tau hyperphosphorylation,[9] providing further evidence in support of the upstream role of soluble Aβ assemblies in the AD pathogenesis cascade.[1]

The central role of soluble Aβ oligomers and protofibrils in AD has prompted substantial efforts to identify the molecular determinants of neurotoxicity in soluble Aβ assemblies ($A\beta_n$, where *n* represents the number of Aβ molecules comprising the assembly).[10–22] Unfortunately, given the transient and heterogeneous nature of Aβ intermediates, characterization of their structure and properties has been challenging. Despite these hurdles, it has been possible to delay the growth of aggregation intermediates to an extent sufficient to enable structural elucidation. For example, Ahmed *et al.* have shown that toxic $A\beta_{42}$ oligomers stabilized through low temperature and salt conditions are largely disordered, but exhibit a turn conformation reminiscent of protofibrils and fibrils.[20] In contrast, for the other major isoform of Aβ, *i.e.* $A\beta_{40}$, toxic oligomers adopt parallel, in-register β-sheets.[21] While these studies have provided an initial framework to define structural features of toxic $A\beta_n$, the location of the "toxic $A\beta_n$ surfaces" remains

unclear. Mapping such surface sites is critical as the exposure of toxic surfaces shared by multiple soluble $A\beta_n$ species has been hypothesized to be one of the main causes of $A\beta_n$ toxicity.[1,23]

Exposure of these toxic surfaces is thought to facilitate interactions with multiple cellular components, including membranes, which underlie key pathogenic steps in the progression of AD.[1,22,24–26] In fact, extracellular Aβ oligomers are known to perturb biological and biomimetic membranes at multiple levels. The oligomers can (i) bind to membranes causing local perturbations,[19,27] (ii) form annular structures that insert into the membrane and affect ion homeostasis[16,18,19] and (iii) bind to membrane receptors altering signal transduction pathways.[28] Similar hypotheses have been proposed to explain the neurotoxicity of Aβ protofibrils,[17] although the latter have been shown to act also through detergent-like permeabilization and eventual fragmentation of the membrane.[19] While these results highlight critical aspects of Aβ–membrane interactions, the "toxic surfaces" that enable key interactions with the membrane, as well as the underlying mechanism, remain elusive.

As a further step towards dissecting the molecular determinants of soluble $A\beta_n$ toxicity and mapping the toxic $A\beta_n$ surfaces, here we systematically investigate a library of $A\beta_{40}$ assemblies sampling different degrees of cellular toxicity. To this end, we first stabilized canonical, toxic $A\beta_{40}$ assemblies through desalting and low temperature[29] and then treated them with a diverse set of catechins, ranging from (–)-epigallocatechin-3-gallate (EGCG), which remodels Aβ into non-toxic structures,[30] to (–)-epicatechin (EC), which is expected to detoxify Aβ only partially. We then profiled our soluble Aβ library through multiple complementary techniques with different degrees of spatial resolution, including extrinsic fluorescence, electron microscopy, dynamic light scattering, wide-angle X-ray diffraction and NMR spectroscopy. Unlike previous attempts to dissect the toxicity determinants of Aβ assemblies,[20,21] here we characterize representative soluble Aβ assemblies from our library both in the absence and presence of model membranes.

The comparative analysis of our soluble $A\beta_{40}$ library reveals a cluster of key toxicity determinants and the associated mechanism of action. We discovered that toxicity scales proportionally to the enhanced hydrophobic exposure of $A\beta_{40}$ assemblies and their ability to interact with Aβ monomers and cell membranes. The hydrophobic region spanning residues 17–28 is more accessible to monomer recognition in toxic $A\beta_n$ relative to $A\beta_n$ with reduced cellular toxicity. Moreover, whereas increased exposure of hydrophobic residues is required for toxicity, we find that shielding of the highly charged N-terminus, *i.e.* residues < 12, from Aβ monomer recognition enhances the toxicity of $A\beta_n$. These toxic $A\beta_n$ surfaces are critical for the binding of $A\beta_n$ to lipid membranes and for forming membrane-embedded β-sheet structures, which compromise the integrity of the cell membrane. The resulting model provides a foundation to start defining structure-toxicity relationships of Aβ assemblies.

3.4 Results

3.4.1 An $A\beta_{40}$ Assembly Library that Samples a Cytotoxicity Gradient.

As a first step towards dissecting the determinants of $A\beta_{40}$ toxicity, we prepared a library of soluble $A\beta_n$ spanning a cytotoxicity gradient. For this purpose, we incubated canonical (non-treated) $A\beta_n$ with a collection of seven distinct catechins expected to remodel to varying extents the pre-existing soluble toxic $A\beta_n$ into less toxic species[30–32] (Fig. S1, Experimental Section). Out of this $A\beta_n$ library, we selected a sub-set of representative Aβ assemblies (*i.e.* those formed in the presence of the EC, (−)-epigallocatechin (EGC) and EGCG catechins) for toxicity profiling in a human retinal pigment epithelial (RPE1) cell line. The state of the RPE1 cells was first monitored by performing PrestoBlue assays, which rely on the reductive potential of the cell as a proxy of cellular viability.[33] Relative to mock (*i.e.* PBS delivery vehicle), canonical $A\beta_n$ significantly decrease cellular viability (Fig. 1a, *black vs. grey*). In contrast, $A\beta_n$ formed in the presence of catechins are less effective in reducing cellular viability, in the order EC (Fig. 1a, *green*), EGC (Fig. 1a, *yellow*) and EGCG (Fig. 1a, *maroon*), for which no significant difference is detected compared to mock (Table S1). Only negligible changes in cellular viability were observed for cells treated with catechins alone (Fig. 1a, *dark green*, *orange* and *brown*).

We also stained RPE1 cells with the necrotic cell marker propidium iodide (PI), which binds to DNA in cells with severely compromised membranes.[34] The RPE1 cells were also counterstained with the nuclear marker Hoechst 33342 [35] to show that non-specific PI-staining is negligible under our conditions, as indicated by the purple *vs.* red fluorescence for PI in merged *vs.* separate panels, respectively (Fig. 1b). Fluorescence microscopy images of RPE1 cells treated with canonical $A\beta_n$ indicate prominent staining with PI (Fig. 1b). In contrast, $A\beta_n$ formed in the presence of catechins exhibit remarkably less PI staining (Fig. 1b), following the same EC < EGC < EGCG ranking as the cellular viability assay (Fig. 1a). Overall, these results suggest that the Aβ assemblies in our library elicit different levels of cellular dysfunction and cell death. Hence, the comparative analysis of such Aβ aggregates is anticipated to reveal key molecular determinants of soluble Aβ toxicity.

3.4.2 The Aβ Assembly Library Spans a Wide Distribution of Sizes, Hydrophobic Solvent Exposures and Cross β-sheet Contents.

We first evaluated how our catechin library remodels the distribution of Aβ assemblies. For this purpose, the relative populations of the NMR visible low MW Aβ species (*e.g.* monomers) were gauged through residual ^{1}H NMR intensities (Fig. 1c), while the NMR invisible $A\beta_n$ were probed by dynamic light scattering (DLS) (Fig. 1d and e). While it is important to complement these data with size estimations through other

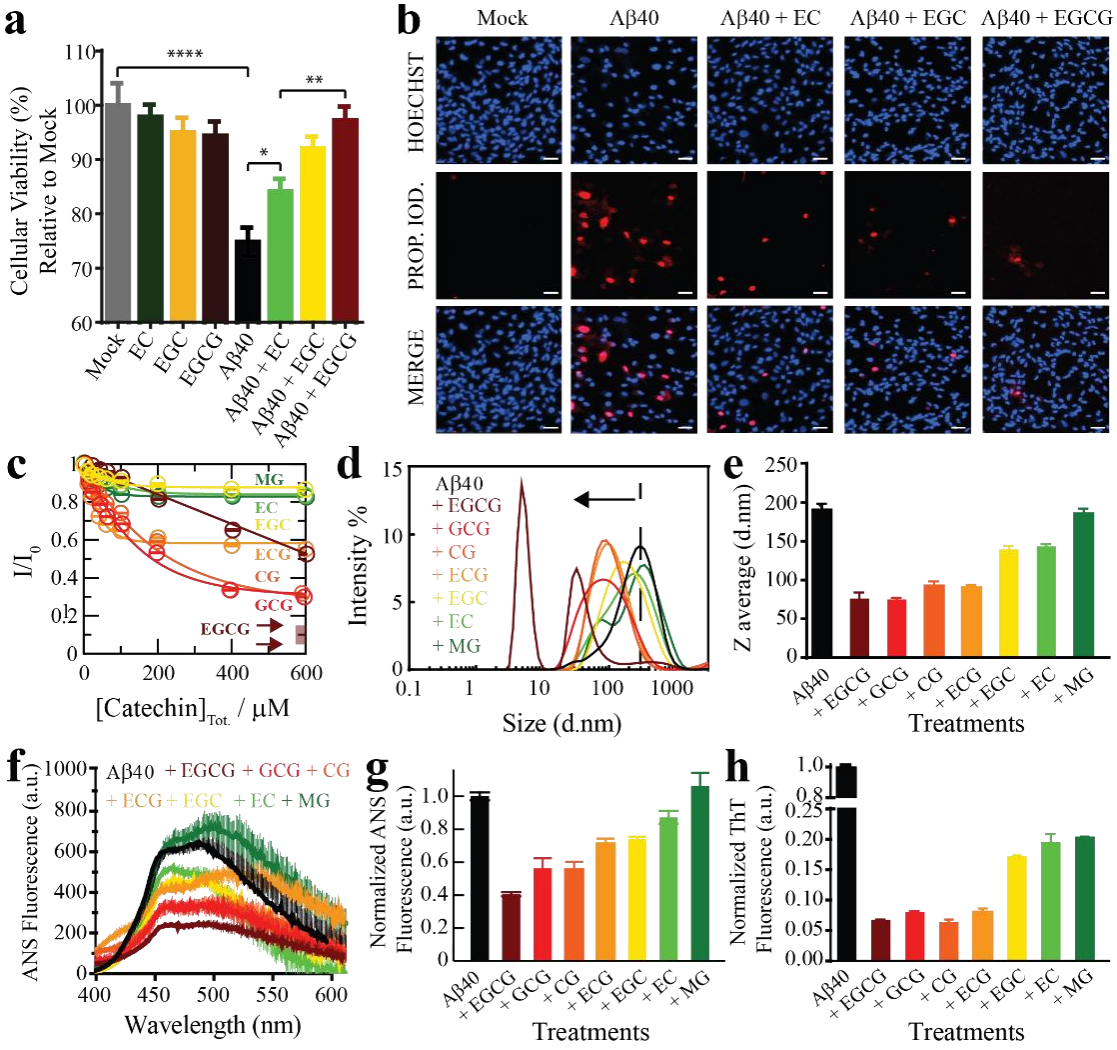

Figure 1. *The Aβ$_n$ library samples a wide-distribution of toxicity, hydrophobic exposure, cross β-sheet content and sizes.* (a) Mitochondrial activity of retinal pigment epithelial (RPE1) cells after treatment with representative Aβ$_{40}$ assemblies and associated controls, as monitored by the reduction of resazurin using the PrestoBlue assay.[33] The data reported show the mean and standard deviation of technical replicates. One-way ANOVA and subsequent Tukey's post-hoc test was used to determine statistical significance between treatments and mock (1X PBS delivery solution), with *, ** and **** representing *p*-values of 0.05, 0.01 and <0.0001, respectively. (b) Representative fluorescence microscopy images of RPE1 cells (scale bar, 50 μm), showing intracellular Hoechst 33342 and propidium iodide fluorescence after incubation with selected Aβ$_{40}$ assemblies. (c) Normalized Aβ$_{40}$ methyl intensity losses upon catechin addition relative to the state in the absence of catechins. (d) Size distribution of Aβ$_{40}$ assemblies in the absence (*black*) and presence of catechins (*coloured as per legend*) as determined by intensity measurements in dynamic light scattering experiments. (e) Z-average of the Aβ$_{40}$ assemblies in (d). (f) ANS fluorescence spectra of Aβ$_{40}$ assemblies in the absence (*black*) and presence of catechins (*colour coded as per the legend*). (g) ANS fluorescence intensities at 454 nm for the samples in (k), normalized to the intensity for Aβ$_{40}$ alone. (h) Thioflavin T fluorescence intensities at 485 nm of Aβ$_{40}$ assemblies in the absence (*black*) and presence of catechins (*coloured as per legend*) normalized to the intensity of canonical assemblies.

means, such as TEM (*vide infra*), interestingly, we observed that all catechins in our library reduce the populations of both the Aβ monomers (Fig. 1c) and the Aβ assemblies at the opposite end of the molecular weight (MW) distribution (Fig. 1d and e). These results suggest that the Aβ species at the extremes of the probability distribution are converted by the catechins into Aβ species with intermediate MW. However, the extent of this remodeling is markedly catechin-dependent with (–)-catechin-3-gallate (CG) leading to large reductions in both the monomer and high MW populations (Fig. 1c–e) and methyl-3,4,5-trihydroxybenzoate (MG) causing only marginal changes (Fig. 1c–e).

We also investigated the surface hydrophobicity of the Aβ assemblies formed under our conditions, as exposed hydrophobic surfaces have been associated with toxicity for another amyloidogenic system.[36] The surface hydrophobicity of $A\beta_n$ was probed through 8-anilino-1-naphthalenesulfonic acid (ANS) fluorescence, which exhibits a characteristic blueshift and enhancement in fluorescence intensity upon binding exposed hydrophobic sites. A substantial enhancement in ANS fluorescence was observed for canonical $A\beta_n$ (Fig. 1f and g, black), whereas the extent of such enhancement is significantly reduced for most catechin-treated $A\beta_n$ (Fig. 1f and g, coloured). Notably, the measurements of the catechin-treated $A\beta_n$ surface hydrophobicity (Fig. 1f and g) rank in the same order as the cell toxicities (Fig. 1a), suggesting that exposed hydrophobic surfaces are a key determinant of $A\beta_n$ toxicity.

Another unique signature of amyloids is the formation of extensive cross β-sheets, as reported by the fluorescent dye Thioflavin T (ThT). Canonical, toxic $A\beta_n$ exhibit significant ThT fluorescence in comparison to catechin-remodeled $A\beta_n$ (Fig. 1h). While the decreased ThT fluorescence in the presence of EGCG is in agreement with previous observations,[30,37,38] our data on the extended catechin library reveal that other catechins also preserve the ability to destabilize intermolecular β-sheets and/or outcompete ThT. Hence, ThT-responsive β-amyloids do not appear to correlate with cytotoxicity as well as the observables reported above *i.e.* size and hydrophobic exposure. Indeed, solvent accessible hydrophobic moieties are one of the main drivers for Aβ–membrane interactions, which in turn have been proposed as a key determinant of the cytotoxicity associated with Aβ.[39] This hypothesis is supported by our propidium iodide results, which indicate that toxic $A\beta_n$ severely compromise the integrity of cell membranes (Fig. 1b). To further corroborate this hypothesis, we evaluated the interactions between a representative subset of our $A\beta_n$ library and biomimetic membranes (small unilamellar vesicles, SUVs).

3.4.3 Toxic Aβ Assemblies Co-localize, Bind and Insert into Biomimetic Membranes.

We profiled the membrane interactions of selected Aβ assemblies from our library that report on representative regions of our toxicity scale, *i.e.* the canonical as well as the EC- and EGCG-remodeled $A\beta_n$ (Fig. 1a). For this purpose, SUVs composed of a mixture of DOPE : DOPS : DOPC lipids were prepared with

an effective size distribution ranging from ~10–100 nm and an average diameter of ~34 nm (Fig. 2a and b). Prior to the addition of the $A\beta_n$ library to the SUVs, we characterized the morphology of the $A\beta_n$ by TEM to ensure that significant catechin-induced remodeling occurs. Indeed, compared to canonical $A\beta_n$, which primarily adopt "worm-like" protofibrils (Fig. 2c, *top left panel*), we observed both spherical assemblies and amorphous aggregates in the presence of EGCG (Fig. 2c, *top right panel*). The latter of the two species has been reported to be an intermediate in the formation of the former.[23] In contrast, the EC-remodeled $A\beta_n$ displays features of both canonical and EGCG-remodeled $A\beta_n$, albeit more closely resembling the canonical $A\beta_n$ (Fig. 2c, *top center panel*). Having confirmed that catechin-induced remodeling of $A\beta_n$ occurs, we then evaluated to what extent the $A\beta_n$ library interacts with SUVs.

TEM images reveal that canonical $A\beta_n$ significantly colocalize with SUVs. For example, it is possible to observe select $A\beta_n$ co-positioned with the lipids (Fig. 2c, *bottom left panel*). Similar to the canonical $A\beta_n$, EC-remodeled $A\beta_n$ are also somewhat colocalized with the SUVs (Fig. 2c, *bottom center panel*). However, in stark contrast to both the canonical and EC-remodeled $A\beta_n$, the EGCG-remodeled $A\beta_n$ are on average spatially distinct from the SUVs (Fig. 2c, *bottom right panel*).

To complement the TEM data on canonical *vs.* catechin-remodeled $A\beta_n$–membrane interactions, we performed ^{15}N-transverse relaxation (R_2), ^{1}H-based saturation transfer difference (STD) as well as ^{15}N-Dark State Exchange Saturation Transfer (DEST) NMR experiments, which collectively probe the interactions of Aβ with high MW (HMW) species, including SUVs, $A\beta_n$ and their complexes, through the lens of the NMR visible Aβ monomers (Fig. 3a–g).[29,40–48] Upon addition of SUVs to the canonical $A\beta_n$, we observed marked enhancements in R_2 and STD (Fig. 3a and b), consistent with the $A\beta_n$–membrane interactions revealed by TEM (Fig. 2c). The SUV-induced changes in R_2 and ^{1}H-based saturation transfer are more pronounced for the residues in the β1 (residues 12–24) and β2 regions (residues 30–40) than for the N-terminal moiety (residues < 12), indicating that the β1 and β2 segments serve as key hot-spots of the SUV-Aβ interactions under our experimental conditions. This conclusion is independently confirmed by the comparative analysis of the ^{15}N-DEST data (Fig. 3g–m).

Residues in direct contact with the $A\beta_n$/SUV surface typically display an attenuation of the residual monomer DEST signal, leading to broadening of the residue-specific ^{15}N-DEST *vs.* offset profile relative to amino acids for which the monomer is disengaged from the $A\beta_n$/SUV surface.[31] Such broadening of the ^{15}N-DEST profile is quantitatively measured through the Θ parameter at intermediate ^{15}N-continuous wave (CW) offsets,[40,49,50] as explained in the Methods. Consistent with the R_2 and STD data (Fig. 3a and b), upon SUV addition to canonical $A\beta_n$, major DEST *vs.* offset profile broadening and corresponding Θ enhancements are observed for the β1 and β2 regions (Fig. 3c–g and k; Fig. S3). A similar observation

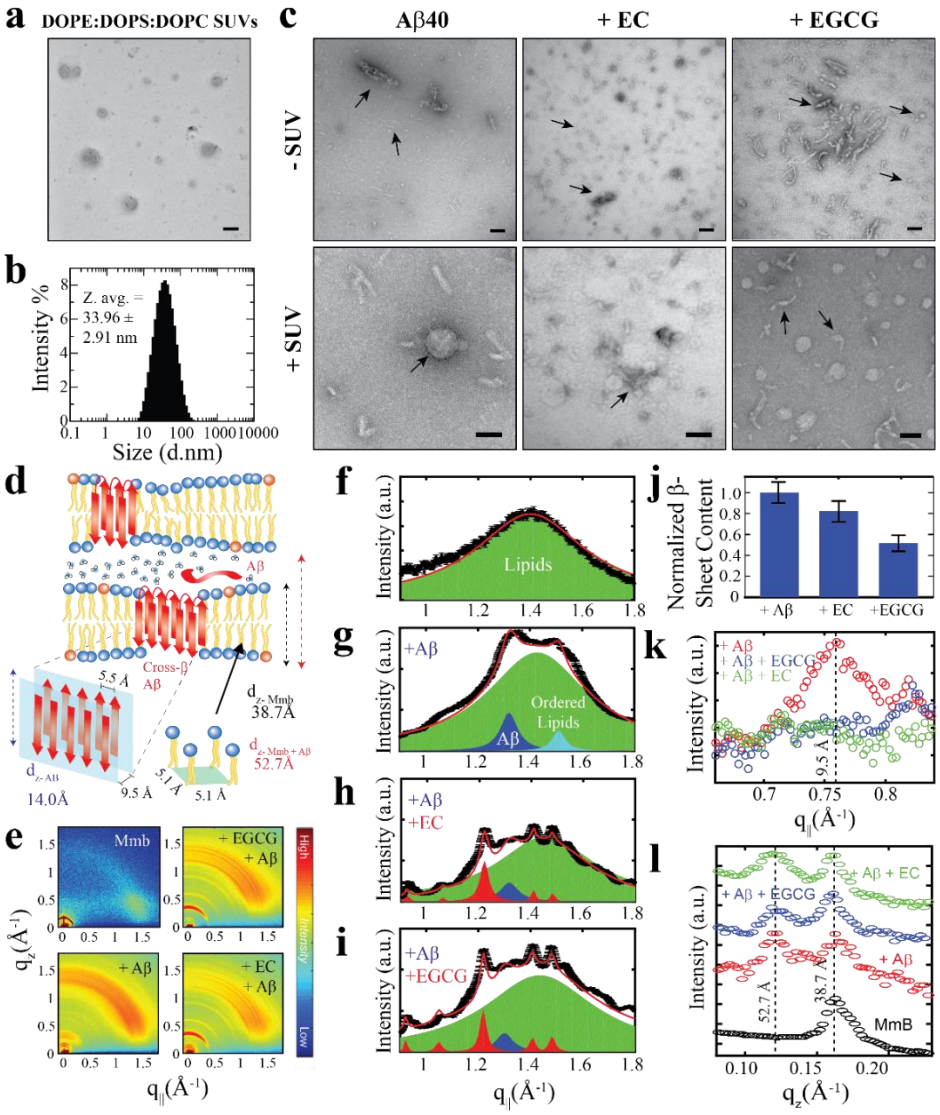

Figure 2. *Localization and insertion of $A\beta_{40}$ assemblies into model membranes.* (a) Negative-stain TEM image of 800 μM DOPE : DOPS : DOPC SUVs. (b) Size distribution of SUVs shown in (a) as determined through dynamic light scattering intensity measurements. (c) Negative-stain TEM images of $A\beta_{40}$ assemblies in the absence and presence of EC and EGCG and the same assemblies treated with the SUVs in (a) and (b). All scale bars correspond to 100 nm. (d) Schematic summary of the information extracted from wide-angle X-ray diffraction experiments. (e) Complete two-dimensional intensity maps of the X-ray diffraction data with both in-plane and out-of-plane features. (f–i) In-plane ($q_{\parallel}$) diffraction patterns (*black line*) and fitted Lorentzian peaks (*coloured peaks*) for DOPE : DOPS : DOPC lipids (*green peaks*) in the absence and presence of $A\beta_{40}$ assemblies (*blue peaks*) with and without catechins (*red peaks*). Red lines indicate total fits derived from the summation of component peaks. (j) Normalized population of membrane-embedded β-sheet assemblies relative to canonical $A\beta_{40}$ assemblies, derived through the integration of blue Aβ peaks in (f–i). (k) In-plane ($q_{\parallel}$) diffraction patterns highlighting the cross-β inter-sheet signal intensity, which correspond to the 9.5 Å spacing between β-sheets shown in (d). (l) Out-of-plane (q_z) diffraction patterns depicting the membrane lamellar spacing (panel d, dashed black and red lines corresponding to 38.7 and 52.7 Å, respectively) in the absence (*black*) and presence (*coloured as per legend*) of $A\beta_{40}$ assemblies.

applies to the addition of SUVs to EC-remodeled Aβ, which on average display a pattern comparable to canonical $Aβ_n$ (Fig. 3h and l *vs.* Fig. 3g and k; Fig. S4). Conversely, the EGCG-remodeled Aβ do not exhibit significant β1 and β2 enhancements as compared to canonical and EC-remodeled Aβ (Fig. 3i and m; Fig. S5), in excellent agreement with the TEM observations. While the combination of our TEM and ^{15}N-based NMR experiments reveal key differences in Aβ–membrane interactions between the less toxic EGCG-remodeled Aβ and the more toxic canonical and EC-remodeled Aβ, they do not provide direct insight about whether $Aβ_n$ inserts into the membrane and about the structural features of membrane-embedded $Aβ_n$. To this end, we conducted wide-angle X-ray diffraction (WAXD) experiments in the presence of model membranes for Aβ assemblies at representative regions of our toxicity scale (Fig. 2d–l).

The WAXD two-dimensional intensity maps (Fig. 2e) were modeled with a series of Lorentzian fits (Methods) to derive structural features both in-plane ($q_{||}$, Fig. 2f–k) and out-of-plane (q_z, Fig. 2l) of the membrane. For the lipid sample in the absence of $Aβ_n$, in-plane and out-of-plane Bragg peaks were observed at 1.41 $Å^{-1}$ (Fig. 2f) and 0.17 $Å^{-1}$ (Fig. 2l, *black*), respectively, corresponding to the formation of bilayer stacks with an effective bilayer width of 38.7 Å and a 5.1 Å spacing between individual lipids (Fig. 2d). Addition of canonical $Aβ_n$ to these lipid bilayers results in additional in-plane features at 1.32 $Å^{-1}$ (Fig. 2g, *blue*) and 0.76 $Å^{-1}$ (Fig. 2k, *red*), indicating the presence of membrane-embedded $Aβ_n$ adopting laminated β-sheets with 5.5 Å spacing between adjacent β-strands and 9.5 Å between β-sheet layers (Fig. 2d). Interestingly, we observe an additional peak at 1.51 $Å^{-1}$ (Fig. 2g, *cyan*) corresponding to highly ordered lipids likely in the regions interfacing with the embedded $Aβ_n$. Moreover, an out-of-plane diffraction pattern is observed at ~0.12 $Å^{-1}$ (Fig. 2l, *red*) consistent with the presence of Aβ not embedded into the bilayer (Fig. 2d).

Compared to canonical $Aβ_n$, the EC- and EGCG-remodeled $Aβ_n$ still preserve extended β-sheets in the membrane (Fig. 2h and i, *blue*), although the relative amounts are decreased in the presence of EC and EGCG, in that order (Fig. 2j). In contrast, neither of the catechin-remodelled $Aβ_n$ exhibit packing of β-sheet layers (Fig. 2k, green and blue), in agreement with our ThT data (Fig. 2h). Overall, these findings suggest that the toxic $Aβ_n$ formed under our conditions colocalize, interact and insert into lipid membranes wherein they adopt β-sheet structures. To identify the toxic $Aβ_n$ surfaces that facilitate these multivalent interactions with the membrane, we comparatively examined the ^{15}N-DEST differences between canonical, EC- and EGCG-remodeled $Aβ_n$ in the presence of model membranes (Fig. 3n, Fig. S2).

3.4.4 Toxic *vs.* Non-Toxic Aβ Assemblies in the Membrane Environment Exhibit Marked Differences in Aβ-Recognition profiles.

To focus on the effects of the catechins, the canonical $Aβ_n$ DEST profile (Fig. S2b) was subtracted from the catechin-remodeled $Aβ_n$ DEST profiles (Fig. S2c and d). Since all profiles in Fig. S2b–d were recorded in

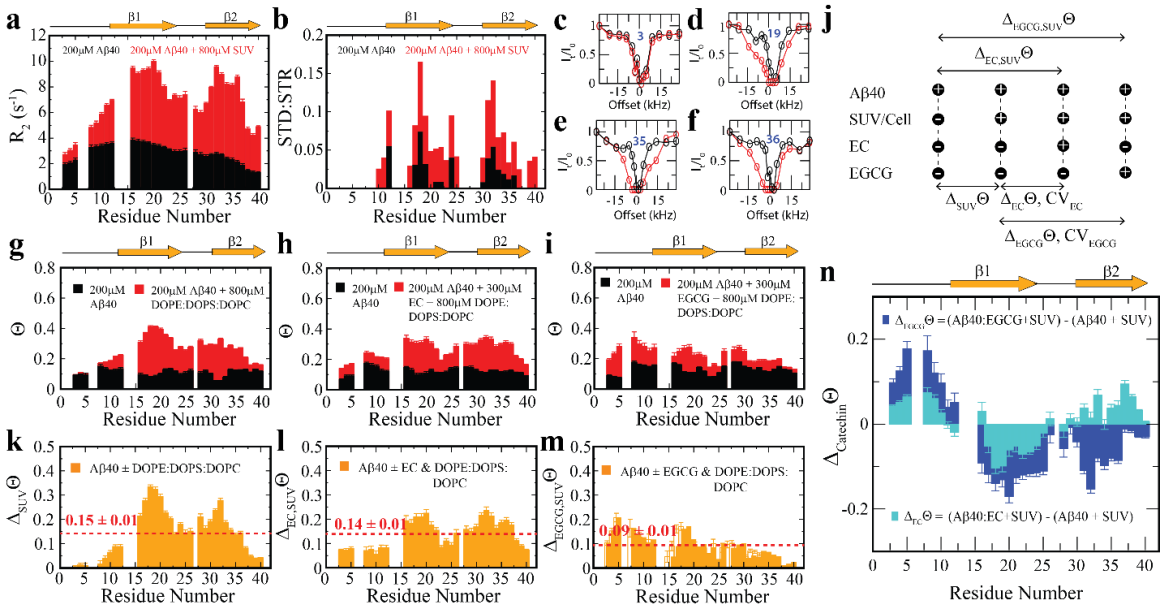

Figure 3. *Exchange dynamics of Aβ$_{40}$ monomers on the surface of soluble Aβ$_{40}$ assemblies and model membranes.* (a) ^{15}N-R$_2$ and (b) MeSTDHSQC for the canonical Aβ$_{40}$ assemblies in the absence (*black*) and presence (*red*) of DOPE : DOPS : DOPC SUVs. (c–f) Representative ^{15}N-DEST profiles for the samples shown in (a). (g) ^{15}N-Θ profiles for the samples shown in (a), colour coding is as per legend. (h) ^{15}N-Θ profiles for canonical Aβ$_{40}$ assemblies in the absence (*black*) and presence (*red*) of EC followed by DOPE : DOPS : DOPC SUV addition. (i) ^{15}N-Θ profiles for canonical Aβ$_{40}$ assemblies in the absence (*black*) and presence (*red*) of EGCG followed by DOPE : DOPS : DOPC SUV addition. (j) Definition of key differentials in the ^{15}N-DEST measurements and the corresponding normalized cellular viabilities. (k) Difference between the Θ profiles shown in (g). The dashed red line indicates the average Θ value. (l) Difference in the Θ profiles shown in (h). (m) Difference between the Θ profiles shown in (i). (n) ^{15}N-Θ difference profiles for (h, *red*) *vs.* (g, *red*) (*cyan*) and (i, red) *vs.* (g, *red*) (*blue*).

the presence of SUVs, the resulting DEST differences (Fig. 3n) report primarily on the catechin-induced remodeling of Aβ monomer–Aβ$_n$ contacts. Specifically, the EGCG-remodeled *vs.* canonical Aβ$_n$ ^{15}N-Θ profile differences ($\Delta_{EGCG}\Theta$) show significant decreases in Θ in the two β-strand regions typically observed in Aβ protofibrils (Fig. 3n, *dark blue*). These losses are consistent with the Aβ monomers being less engaged with the Aβ$_n$ surface at the two β-strand sites in the presence of EGCG. However, the EGCG-induced disengagement detected for the β1 and β2 regions does not extend to the N-terminal segment, for which a significant enhancement in direct contacts is observed (Fig. 3n, *dark blue*). A similar N-terminal Θ DEST enhancement is observed also upon EC addition (Fig. 3n, *light blue*), albeit with reduced magnitude (Fig. 3n, *light vs. dark blue*). Likewise, in the β1 region the EC-remodeled Aβ$_n$ show Θ losses with a reduced extent compared to the EGCG-remodeled Aβ$_n$ (Fig. 3n, *light vs. dark blue*). However, the DEST pattern observed for the N-terminal and β1 regions does not extend to the β2 segment, for which EC and EGCG result in opposite Θ changes (Fig. 3n, *light vs. dark blue*). These findings imply that exposure

of the hydrophobic β1-turn region and concomitant shielding of the N-terminus are two key structural transitions intimately linked to toxicity, as these toxic surfaces modulate interactions with the membrane.

3.4.5 Selection of Molecular Determinants of Aβ$_n$ Toxicity.

In order to systematically isolate the Aβ$_n$ features relevant for toxicity, we identified groups of coupled Aβ$_n$ observables by relying on the data correlation matrix (Fig. 4a), whose elements represent the absolute Pearson's correlation coefficients ($|r|$) between each pair of Aβ$_n$ observables (Supplementary Information). Through agglomerative clustering of the correlation matrix, we then built a dendrogram that partitions the Aβ$_n$ observables into five distinct clusters (Fig. 4b). The largest cluster, denoted as cluster 1, includes the $\Delta_{Cat}\Theta_i$ values for residues in the 3–28 region as well as three low resolution observables, *i.e.* the

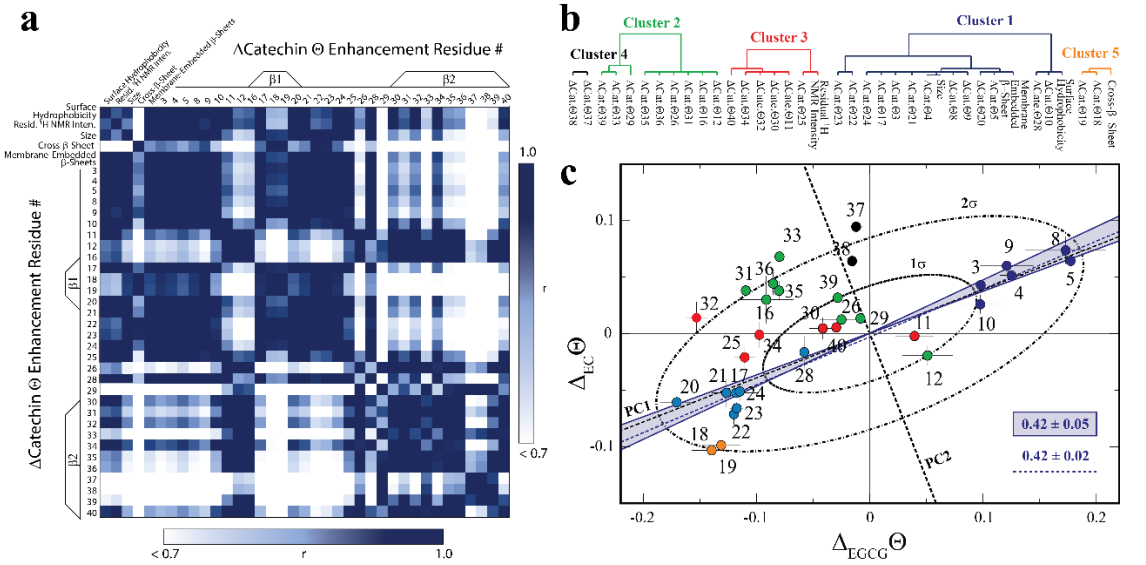

Fig. 4 *Identification of the determinants of Aβ assembly toxicity through agglomerative clustering and Singular Value Decomposition (SVD).* (a) Correlation matrix for the Aβ$_n$ observables from Fig. 1–3. Correlations with an absolute Pearson's correlation coefficient > 0.95 are indicated in dark blue. (b) Dendrogram displaying the clusters with an absolute Pearson's correlation coefficient > 0.9 obtained through complete linkage agglomerative clustering. (c) Singular Value Decomposition (SVD) of the ^{15}N-DEST data. The dashed black lines indicate the first and second principal components (PC1 and PC2) obtained through the SVD of the column-mean centered ($\Delta_{EC}\Theta_i$, $\Delta_{EGCG}\Theta_i$) matrix, where *i* is the residue number. The ellipsoids at one and two standard deviations for the residue scores along PC1 and PC2 are shown as black dot-dashed curves. Data for residues assigned to clusters 1, 2 and 3, 4 and 5 though agglomerative clustering are displayed as solid dark/light blue, green, red, black and orange circles, respectively, and the corresponding residue number is reported beside each circle. The solid blue lines define the region of the ($\Delta_{EC}\Theta_i$, $\Delta_{EGCG}\Theta_i$) plane that is expected to scale with the relative cellular viability (CV) defined as $(CV_{Aβ40+EC} - CV_{Aβ40})/(CV_{Aβ40+EGCG} - CV_{Aβ40}) = 0.42 \pm 0.05$, based on the data of Fig. 1. The dashed blue line (slope of 0.42 ± 0.02 and correlation coefficient of 0.98) was obtained from the linear regression of the DEST data in cluster 1 (blue) and confirms that cluster 1 correlates with cellular viability. PC1 (slope of 0.39) aligns with the residues for cluster 1.

membrane-embedded β-sheet, the size and the surface hydrophobicity. Since these measurables rank similarly to the relative toxicities (Fig. 1), we hypothesized that cluster 1 defines key molecular determinants of $A\beta_n$ toxicity. This hypothesis is confirmed by two independent lines of evidence.

First, if we re-compute the correlation matrix and agglomerative clustering after including the relative toxicities (Fig. 1a), we find that the toxicity partitions within cluster 1 (Fig. S6), confirming that the observables in this cluster scale with Aβn toxicity. Second, in the $\Delta_{EGCG}\Theta_i$ *vs.* $\Delta_{EC}\Theta_i$ plot (Fig. 4c), the cluster 1 residues fall at or near the region expected to scale with the relative EC vs. EGCG cell viability (CV) data, defined as $(CV_{A\beta40+EC} - CV_{A\beta40})/(CV_{A\beta40+EGCG} - CV_{A\beta40}) = 0.42 \pm 0.05$ (shaded blue area, Fig. 4c). The linear regression of $\Delta_{EGCG}\Theta_i$ *vs.* $\Delta_{EC}\Theta_i$ for cluster 1 is in fact in excellent agreement with the value expected based on the relative cellular viability (dashed blue line with slope of 0.42 ± 0.02 and correlation coefficient of 0.98; Fig. 4c). Hence, we conclude that cluster 1 (blue dendrogram in Fig. 4b and blue circles in Fig. 4c) is relevant for the toxicity of $A\beta_n$.

To gain further insight on the significance of the $\Delta_{EGCG}\Theta_i$ *vs.* $\Delta_{EC}\Theta_i$ plot and independently corroborate the residue clusters obtained through the agglomerative clustering analysis, we also performed Singular Value Decomposition (SVD) of the data in Fig. 4c. The SVD analysis reveals that the first principal component (dashed black line, Fig. 4c), which accounts for 88% of the total variance, not only resides within the range expected to scale with the relative cellular viability (i.e. within the shaded blue area in Fig. 4c), but also aligns with the residues for cluster 1. Interestingly, the SVD reveals that cluster 1 (blue circles, Fig. 4c) is composed of two distinct sub-sets that are mostly confined at opposite extremes of PC1, between the 1σ and 2σ ellipsoids (Fig. 4c). The sub-set with positive PC1 components (dark blue circles) represents the N-terminal residues that become engaged in monomer recognition, as probed by DEST, when cellular viability is enhanced. On the contrary, the cluster 1 sub-set with negative PC1 scores (light blue circles) arises from the β1-turn region residues that become engaged when cellular viability decreases.

In stark contrast to cluster 1, the other clusters obtained from the agglomerative clustering analysis (Fig. 4b, black, green, red and orange circles) fall outside the range expected to scale with cellular viability (blue shaded area, Fig. 4c) and exhibit components along PC2 that are overall higher than those observed for cluster 1 (Fig. 4c). In conclusion, the combined analyses of the correlation matrix, agglomerative clustering and SVD consistently identify the constituents of cluster 1, *i.e.* surface hydrophobicity, size, membrane-embedded β-sheets, N-terminal residue disengagement and β1-turn region engagement, as key molecular determinants of Aβn toxicity.

In order to verify the predictive power of the correlation between $A\beta_n$ toxicity and cluster 1, we measured the relative toxicities for the Aβ assemblies not included in Fig. 1a and we compared them to those predicted by our model (Fig. 4; Fig. S7). These $A\beta_n$ toxicities were not used to train our model and hence provide a critical test of its prognostic capacity. As seen in Fig. S7d, a strong linear correlation is observed between the predicted and observed toxicities ($r \geq 0.94$), with a slope within error to one, thus validating the predictive power of our model.

3.5 Discussion

In summary, our investigation of the $A\beta_n$ library through the comparative analysis of ^{15}N-R_2 and DEST NMR combined with WAXD, TEM, DLS and extrinsic fluorescence reveals key structural differences that distinguish toxic *vs.* non-toxic Aβ assemblies. The integrated analyses of our data through agglomerative clustering and SVD consistently identify a cluster of molecular attributes unique to toxic $A\beta_n$ (Fig. 4b, cluster 1), including surface hydrophobicity, size, membrane-embedded β-sheets, shielding of the N-terminus and simultaneous exposure of the β1-turn region to Aβ monomers, as probed through DEST NMR.

Our data shows that toxic $A\beta_n$ exhibit solvent exposed hydrophobic sites accessible to ANS binding. While the relationship between surface hydrophobicity and toxicity has been observed previously for several protein systems such as the Type A/B HypF-N assemblies,[51,52] the A^+/A^- $A\beta_{42}$ oligomer pair,[53] the sup35p oligomer pair,[54] and others,[55] here we not only systematically confirm this association for the Aβ system using a library of Aβ assemblies, but we also propose an unprecedented mechanism of $A\beta_n$ toxicity probed at multiple degrees of resolution. Such mechanism reveals how hydrophobic exposure relates to Aβ–membrane interactions and Aβ monomer recognition. The combination of our TEM, DLS and ^{15}N-DEST and R_2 data collectively shows that $A\beta_n$ with greater surface hydrophobicity *e.g.* canonical and EC-remodeled $A\beta_n$ colocalize and interact with the membrane surface more effectively than the less toxic $A\beta_n$ with less exposed hydrophobic sites *e.g.* the EGCG-remodeled $A\beta_n$ (Fig. 5a).

The surface hydrophobicity-mediated interactions with the membrane are not limited to the membrane surface, as our WAXD data show that canonical and EC-remodeled $A\beta_n$ exhibit significant populations of β-sheets embedded in the membrane compared to EGCG-remodeled $A\beta_n$. The functional effect of the membrane-embedded β-sheets is recapitulated by our propidium iodide-based assay, which indicates that canonical $A\beta_n$ significantly enhance the permeability of the cell membrane compared to the less toxic $A\beta_n$ formed in the presence of EGCG. Notably, we also found that cross-β-sheet structures are dispensable for membrane insertion, as only canonical $A\beta_n$ exhibit cross lamination of β-sheet layers, whereas EC-remodeled $A\beta_n$, with comparable levels of membrane-embedded β-sheets, exhibit considerably reduced

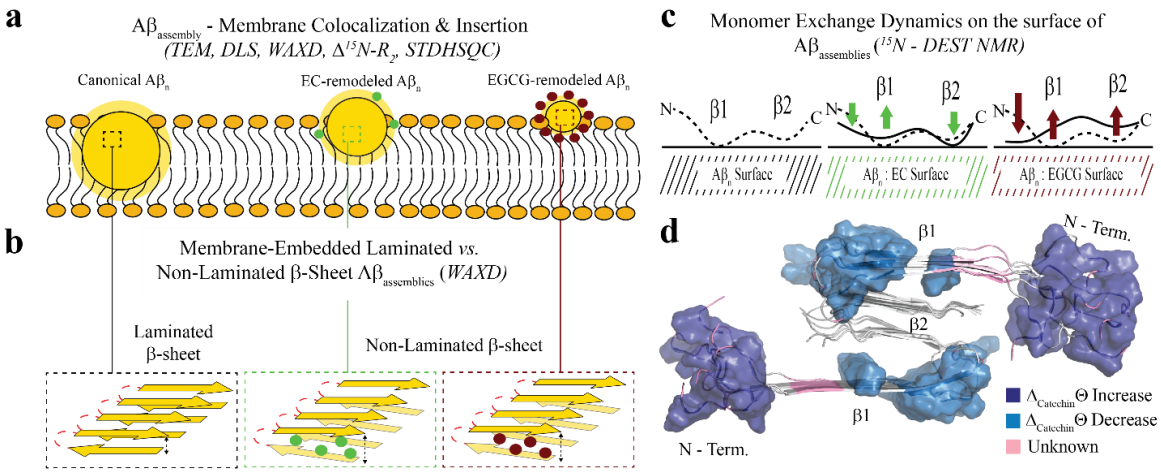

Fig. 5 *Proposed model for the molecular determinants of Aβ assembly toxicity.* (a) Toxic $Aβ_n$ (canonical $Aβ_n$) exhibit significant solvent exposure of hydrophobic surfaces (*yellow glow surrounding* $Aβ_n$). Exposed hydrophobic surfaces facilitate the colocalization, interaction and subsequent insertion of $Aβ_n$ into the membrane. (b) Membrane-embedded $Aβ_n$ adopt both laminated and non-laminated β-sheets, indicating that under our experimental conditions the non-laminated β-sheet signature is the minimum structural feature required for membrane insertion and induction of toxicity. (c) Toxic *vs.* non-toxic $Aβ_n$ exhibit unique regiospecific differences in the recognition of Aβ monomers within a membrane environment. Relative to canonical $Aβ_n$ (*black*), EC- (*green*) and EGCG-remodeled $Aβ_n$ (*maroon*) exhibit progressive engagement of contacts with Aβ monomers at the N-terminus and disengagement at the β1-turn region, following the same ranking as their measured toxicities. In contrast, for the β2 region no correlation is observed between toxicity and $Aβ_n$ monomer recognition. Relevant experimental techniques are indicated in parenthesis. (d) Mapping on the structure of $Aβ_{40}$ fibrils[57] (PDB code: 2LMN) the Aβ residues in cluster 1 (Fig. 4b and c). The N-terminal and β1-turn residues that correlate with toxicity (*blue*) are found in the external regions of the Aβ fibril structure. In contrast, β2 is involved in the lamination of multiple β-sheet layers and is largely inaccessible (Table S2), explaining its ancillary role in toxicity.

cross lamination, similar to EGCG remodeled $Aβ_n$ (Fig. 2k and 5b). The lack of correlation between toxicity and β-sheet cross-lamination is also consistent with the variability in sheet-to-sheet pairing angles reported for oligomers of model amyloidogenic sequences stabilized by macrocyclic peptides.[56]

The correlation and SVD analyses also identify a cluster of residues confined to the N-terminus and β1-loop region that are key to the regulation of $Aβ_n$ toxicity (Fig. 4b and c, cluster 1). The probability distribution of contacts between Aβ monomers and the $Aβ_n$/SUVs surface is markedly enhanced in the β1-loop region (residues 17–28) and concomitantly reduced at the N-terminal segment (residues 3–10) as the $Aβ_n$ toxicity increases (Fig. 3n and 5c, *green vs. maroon arrows*). Interestingly, an unexpected decorrelation with toxicity is observed at the β2 region (residues 30–40) (*clusters 2 and 4*), for which the EC-remodeled $Aβ_n$, with intermediate toxicity, exhibits a further enhancement in contacts relative to the canonical $Aβ_n$ (Fig. 3n and 5c, *green*), in stark contrast to the reduction observed for EGCG-remodeled $Aβ_n$ (Fig. 3n and 5c, *green vs. maroon arrows*).

Notably, the N-terminus and β1-loop Aβ regions identified by the correlation and SVD analyses to be toxicity determinants (Fig. 4c, cluster 1) are located at the external surface of the $A\beta_{40}$ fibril structure (Fig. 5d, *blue surfaces*). Furthermore, most familial AD mutations (English, Tottori, Iowa, Arctic, Dutch and Italian) that alter the biophysical properties of Aβ are observed in the N-terminal and β1 regions.[1,58] Conversely, the β2 region not identified by SVD as linked to toxicity, is inaccessible to the environment (Table S2) and is found embedded into the structural core of the fibril, where it is involved in the cross lamination of multiple β-sheet layers (Fig. 5d, *grey cartoon*). These observations agree with our WAXD and ThT data, consistently pointing to β-sheet lamination as accessory to toxicity induction.

3.6 Conclusion

Overall, our data indicate that $A\beta_n$ toxicity is regulated by the solvent exposure of hydrophobic surfaces, wherein the hydrophobic β1-turn region is more accessible to monomer/SUV recognition, while the highly charged N-terminus is shielded from such recognition. In comparison, the role of β2 appears to be largely ancillary. These toxic surfaces enhance the colocalization, contacts and subsequent insertion of β-sheet rich $A\beta_n$ into the membrane, leading to compromised membrane stability. Moreover, the proposed model is able to predict relative toxicities solely based on low-resolution measurements, such as size and surface hydrophobicity. Modulation of these properties through small-molecule treatment can be utilized as an effective strategy to reduce the toxicity associated with soluble Aβ assemblies. In addition, soluble oligomers of amyloidogenic peptides with different sequences have been suggested to share a common conformation,[59] and Aβ is not only relevant for dominantly inherited AD, but also serves as a model system for a broad-range of amyloid disorders. Hence, the cluster of molecular attributes identified here to correlate with toxicity may be transferrable to other amyloidogenic systems.

3.7 Experimental Section

Amyloid Beta Assembly Library Preparation

^{15}N uniformly labeled Aβ40 was purchased from rPeptide with purity greater than 97%. Similarly, non-labeled Aβ40 was purchased from EZBiolab Inc. with purity greater than 95 %. The commercial Aβ40 lyophilized powders, both labeled and non-labeled, were treated as described previously[50]. Briefly, 1 mg of peptide was temporarily dissolved in 80 µL of 1% NH_4OH/ddH2O then further diluted to a concentration of 1 mg/mL with ddH_2O. The solution was then lyophilized and resuspended in 10 mM NaOH at 1 mg/mL. The NaOH solution was then divided into aliquots, lyophilized and frozen at -20°C until use. The lyophilized powders were dissolved to form Aβ assemblies through three different methods that serve three distinct purposes, e.g. toxicity profiling, low-resolution characterization and high-resolution mapping of Aβ40 assembly-membrane interactions by NMR. Assemblies prepared for cellular viability and

membrane permeability assays were created as follows. Non-labeled lyophilized powder was resuspended in 1X Phosphate Buffer Saline (PBS) pH 7.4 with and without catechins to a final concentration of 30 μM Aβ40 and 150 μM catechin. The mixtures were then incubated at 37 °C for 16 hours to form Aβ assemblies. Assemblies prepared for the low-resolution characterization experiments different from cell viability assays were generated by resuspending non-labeled Aβ40 in 20 mM Sodium Phosphate Buffer pH 6.8 with and without catechins. The aqueous buffer was in 100% D2O for NMR samples, while H2O was utilized for other techniques. The final concentrations of Aβ40 and catechin were 30 μM and 300 μM, respectively. The mixtures were then incubated at 10 °C for 24 hours for assembly formation. Lastly, assemblies for the high-resolution assembly–membrane interaction experiments were prepared as previously described[50]. Briefly, ^{15}N-labeled or non-labeled lyophilized Aβ40 were resuspended in 3 mM Tris pH 8, desalted using a Zeba Column and mixed with 100 mM HEPES pH 6.6 and 20% D2O at a 1:1 ratio. The final concentration of Aβ40 was ~200μM, as determined by absorbance measurements at 280 nm using an extinction coefficient of 1490 cm^{-1}. The samples were then incubated at 10 °C for seven days until equilibration, as determined through stabilization of Aβ intensities in 2D ^{1}H-^{15}N HSQC spectra. Catechin-induced assemblies were created by the addition of catechins to the pre-incubated samples to a final catechin concentration of 300 μM. The mixtures were then incubated at 10 °C for another 24 hours to allow sufficient remodeling. Although different buffer conditions are required for different sets of experimental techniques, the library of assemblies created within each set was prepared following the same protocol.

Catechin Stock Preparation

(-)-epigallocatechin-3-gallate (EGCG), (-)-gallocatechin-3-gallate (GCG), (-)-catechin-3-gallate (CG), (-)-epicatechin-3-gallate (ECG), (-)-epigallocatechin (EGC), (-)-epicatechin (EC) and Methyl 3,4,5-trihydroxybenzoate (MG) were purchased from Sigma Aldrich, with a purity greater than 95%. A 2.8 mM stock solution was prepared in either 20 mM Sodium Phosphate buffer pH 6.8 and 100% D_2O, 0.05% NaN_3 or 50 mM HEPES, 1.5 mM Tris pH 6.8 and 10% D_2O, as needed to match protein conditions.

Preparation of DOPE:DOPS:DOPC Small Unilamellar Vesicles (SUVs)

1,2-dioleoyl-sn-glycero-3-phosphoethanolamine (DOPE), 1,2-dioleoylsn-glycero-3-phospho-L-serine (DOPS), and 1,2-dioleoyl-sn-glycero-3-phosphocholine (DOPC) were purchased from Avanti Polar Lipids. The lipids were stored at -20°C, under Argon. Solutions in chloroform were prepared from the lipids and were mixed to result in a 5:3:2 lipid molar ratio. The lipid mixture was then evaporated under a stream of nitrogen gas and dried thoroughly under vacuum to yield a thin lipid film on the wall of a glass test tube. The thin film was re-hydrated with 50 mM HEPES, 1.5 mM Tris pH 6.8 and 10% D_2O at a concentration of

15 mg/mL and subjected to vortex mixing and sonication until the solution became clear. The concentration of total phospholipids was confirmed by measuring the amount of inorganic phosphate released after digestion[60].

Cell Culturing

Non-transformed human epithelial cells immortalized with hTERT (RPE1) were originally purchased from A.T.C.C. (Manassas, Virginia). RPE1 cells were cultured in Dulbecco's modified Eagle's medium (DMEM): F-12 and supplemented with 10% FBS and 0.01 mg/mL hygromycin B. Cell cultures were maintained in a 5% CO_2 humidified atmosphere at 37 °C and grown until they reached confluence, up to a maximum of ten passages.

Cellular Viability Probed through Presto Blue Assay

RPE1 cells were seeded at 10,000 cells per well and grown for 24 hours prior to treatments. The cells were then treated with pre-formed Aβ40 assemblies (4 μM final concentration), mock (1X PBS delivery solution) and catechins (20 μM final concentration), and incubated for 48 hours at 37 °C and 5% CO_2. The presto blue reagent (resazurin) was added to each well and the plate was incubated for a further two hours at 37 °C, 5% CO_2. Fluorescence measurements were acquired using excitation and emission wavelengths of 560 and 590 nm, respectively, using a Biotek Cytation 5 plate reader. The error on these measurements was estimated through the standard deviation of five technical replicates.

Cell Membrane Permeability Probed through Propidium Iodide Assay

RPE1 cell membrane permeability measurements were conducted using the same cell growth and treatment protocol as in the cellular viability assays and were implemented in parallel with the cellular viability assay although on a different plate. The membrane diffusible and non-membrane diffusible nuclear dyes Hoechst and propidium iodide were added to wells to final concentrations of 5 μg/mL and 1 μg/mL, respectively. The plate was incubated at 37 °C and 5% CO_2 for two hours and then imaged using a Biotek Cytation 5 plate reader and the DAPI (377,447) and RFP (531,593) channels.

Negative Stain Electron Microscopy (EM)

Aliquots of the Aβ40 canonical assemblies devoid of catechins, EC-induced Aβ40 assembly and EGCG-induced Aβ40 assembly samples were taken at the end of each of the ^{15}N-DEST experiments, *i.e.* prior to catechin addition, after catechin addition but prior to SUV addition and finally after SUV addition, to ensure that the EM images are representative of the species probed in the ^{15}N-DEST experiments. The reaction mixtures were diluted 10-folds with ddH_2O. Copper EM grids (400-mesh), which had been freshly

coated with a continuous layer of amorphous carbon, were glow discharged with 5 mA current for 15 seconds and shortly afterward the grids were floated on 3 µL drops of the diluted assembly reaction mixtures for two 2 min. Excess of sample was blotted with filter paper and the grids were stained with 1 % uranyl acetate for 30 seconds. Grids were loaded in a room temperature holder and introduced into a JEOL 1200-EX electron microscope operated at 80 kV. All images were acquired with an AMT XR-41 Side-Mount Cooled 4 megapixel format CCD camera.

Dynamic Light Scattering (DLS)

The samples used for DLS matched those that were imaged by TEM and are therefore also representative of the species probed in the ^{15}N-DEST experiments. DLS measurements were performed using a Zetasizer Nano ZS Instrument (Malvern Instruments, Malvern UK). Autocorrelation functions were accumulated for two minutes at 10 °C with an angle θ of 173° and a 4 mW He-Ne laser operating at a wavelength of 633 nm. All measurements were performed using a 40 µL (ZEN0040) plastic cuvette. The particle diameter detection limit was 0.6 –6 µm. The viscosity value for water was used in the analysis of all measurements. All the samples were centrifuged for 10 min at 13,000 rpm prior to DLS measurements.

ANS Fluorescence

Aβ40 assemblies prepared as described above were treated with ANS to a final concentration of 200 µM and the mixtures were added to a Corning 96 half-area microwell plate with non-binding surface (NBS) treatment. Fluorescence measurements were implemented using a BioTek Cytation 5 plate reader in spectral scanning mode with excitation at 380 nm and emission reading in the 400-600 nm range. Minimal fluorescence contributions arising from buffer and catechins were subtracted from the respective assembly-containing wells. All measurements were performed with five technical replicates and the standard deviation between replicates was used as an estimation of the error.

Thioflavin T (ThT) Fluorescence

Aβ40 assemblies prepared as described above were treated with ThT to a final concentration of 50 µM and the mixtures were added to a Corning 96 half-area microwell plate with non-binding surface (NBS) treatment. Fluorescence measurements were implemented using a BioTek Cytation 5 plate reader in endpoint mode with excitation and emission wavelengths at 450 nm and 485 nm, respectively. All measurements were performed with five technical replicates and the standard deviation between replicates was used as an estimation of the error.

Wide-Angle X-ray Diffraction (WAXD)

The membranes were deposited on single-side 1 × 1 cm^2 polished silicon wafers. To create a hydrophilic surface, the wafers were immersed in Piranha solution (H_2SO4:H_2O_2, 7/3, vol/vol) for 30 min on a 3D orbital shaker (VWR). The wafers were then washed with ultrapure water (ddH_2O) before membrane deposition. Solutions of lipids, amyloids and catechins were mixed in the same ratios as for the ^{15}N-DEST NMR samples and 100 µL of the solution was applied on each wafer. Samples were slowly dried on an orbital incubating shaker to ensure that the solution spread evenly on the wafer. The resulting membranes were then hydrated in a closed chamber with a saturated salt solution of $Mg(NO_3)_2$[6 H2O] (Sigma) to result in a relative humidity of 50 % over 24 hours at 300 K.

Both out-of-plane (q_z) and in-plane ($q_{||}$) scattering data were obtained using the Biological Large Angle Diffraction Experiment (BLADE) at McMaster University. BLADE uses a 9 kW (45 kV, 200 mA) CuKα rotating anode at a wavelength of 1.5418 Å. Both source and detector were mounted on movable arms such that the membranes stay horizontal during measurements. Focusing, multi-layer optics provided a high intensity collimated 200 µm sized beam with monochromatic X-ray intensities up to 108 counts/s. Scattering was detected using a Rigaku HyPix-3000 2D semiconductor detector with an area of 3000 mm^2 and a 100 µm pixel size, as previously described[61]. All scans were carried out at 300 K. The result of such an X-ray experiment is a 2-dimensional intensity map with a large area (0.03 $Å^{-1} < q_z < 1.1$ $Å^{-1}$ and 0 $Å^{-1} < q_{||} <$ 3.1 $Å^{-1}$) in reciprocal space. The corresponding real-space length scales are determined by $d = 2\pi/|Q|$ and cover length scales from about 2.5 to 60 Å, incorporating typical molecular dimensions and distances. To determine the β-sheet signals, the background scattering was fit with an exponential decay. For lipid and protein signals along the in-plane axis, the chain-chain distance was determined from $a_c = 4\pi/(\sqrt{3} \times q_T)$, where q_T is the position of the tail or protein correlation peak. The intensity, $I(q_{||})$, was then modeled with a series of Lorentzian fits incorporating the lipid tail correlation peak, the β-sheet peak[62], and the catechin crystallite peaks[63].

General NMR Spectroscopy

All NMR spectra were recorded at 10 °C using either a Bruker AV 700 spectrometer equipped with a TCI cryo-probe or a Bruker 850 HD spectrometer equipped with a TXI probe. All spectra were analyzed with TopSpin 3.2.1 and Sparky using Gaussian line-fitting. Additional details are discussed below.

Measurement of ^{1}H NMR intensity losses as a function of catechin concentration

Samples of canonical Aβ40 assemblies, prepared as described above, were titrated with increasing concentrations of catechins up to 600 µM. The titration was monitored by ^{1}H NMR spectra acquired

immediately after the addition of each catechin aliquot with 128 scans, 32K complex points and a spectral width of 11.98 ppm. Dilution effects upon catechin addition are corrected for. The relative changes in the ^{1}H NMR intensity of the Aβ methyl peaks were modeled according to a single exponential decay model. The plateau intensity was derived through the fitting of the experimental points.

^{15}N Dark-state Exchange Saturation Transfer (DEST) and ^{15}N transverse relaxation NMR

The ^{15}N-DEST experiment was implemented with a 900 ms ^{15}N continuous wave (CW) saturation pulse at 16 different radiofrequency offsets (no saturation, -28, -21, -14, -9, -5, -3, -1.5, 0, 1.5, 3, 5, 9, 14, 21 and 28 kHz) and a field strength of 170 Hz. The experiment was recorded in interleaved mode with 24 scans, 128 dummy scans, a recycle delay of 1.20 s, 200 (t1) and 2K (t2) complex points and spectral widths of 14.28 ppm (^{1}H) and 31.82 ppm (^{15}N). All spectral processing was implemented in TopSpin 3.2.1. and transferred to Sparky for peak intensity measurements. The Gaussian line fitting function in Sparky was used to determine the fitted peak heights and the signal-to-noise ratio was used as a measure of error on the fitted peak heights. The DEST difference, denoted here as Θ, was calculated as follows:

$$\Theta = \frac{(I_{+28} + I_{-28}) - (I_{+14} + I_{-14})}{(I_{+28} + I_{-28})} \quad (1)$$

where I_{ν} denotes the peak height measured for a given residue at a ^{15}N CW offset of ν kHz.

The ^{15}N transverse relaxation rates were measured using a pseudo-3D pulse sequence with water flip back and sensitivity enhancement. The experiment was recorded with 32 scans, 128 dummy scans, a recycle delay of 1.20 s, 2K complex points for a spectral width of 14.28 ppm in the t2 dimension and 200 complex points for a spectral width of 31.82 ppm in the t1 dimension. The total CPMG lengths were 13.88, 27.76, 41.64, 55.52, 69.40, 83.28, 97.16, 124.92, and 152.68 ms. The CPMG pulse train includes ^{15}N spin-echos composed of ^{15}N 180° pulses within two 0.9 ms delays. The pseudo-3D spectra were processed with TopSpin 3.2.1. and the peak height decays were fitted to an exponential in Sparky.

Methyl STDHSQC

Saturation was introduced through methyl irradiation (MeSTD, 50ms Gaussian pulses at a carrier frequency of 417 Hz at 700 MHz) and recorded with a sensitivity enhanced ^{15}N, ^{1}H-(HSQC) read out block. Hence, the STDHSQC pulse sequence probes the saturation transferred to the amides of ^{15}N-labeled solutes (*i.e.* Aβ40). The spectra were recorded with 64 scans, 2K (t2) and 200 (t1) complex points for spectral widths of 14.1 ppm (^{1}H) and 31.8 ppm (^{15}N), respectively. Reference HSQC spectra were also recorded with the same acquisition parameters, but 16 scans. The spectra were processed on TopSpin 3.2.1 and transferred to Sparky for intensity measurements using the Gaussian fitting function.

Correlation matrix, Agglomerative Clustering and Singular Value Decomposition of Aβ$_n$ Observables

Correlation matrix: The low-resolution Aβ$_n$ observables *i.e.* surface hydrophobicity, cross-β-sheet content, size, residual ^{1}H NMR intensity and membrane-embedded β-sheet were normalized to canonical Aβ$_n$ and combined with the high-resolution $\Delta_{catechin}\Theta$ data to create a data matrix (**D**). The **D** matrix was organized with the 37 low-and high-resolution Aβ$_n$ observables arranged into rows measured for up to eight Aβ$_n$ states in our library, which were arranged into columns. The absolute Pearson's correlation coefficients ($|r|$) were computed between each set of Aβ$_n$ observables to generate the absolute correlation matrix of **D** transpose. A three-score gradient colouring system was applied to the correlation matrix, wherein any elements with $|r| \geq 0.95$ was denoted in dark blue, $|r| = 0.85$ in light blue and $|r| \leq 0.70$ in white.

Agglomerative Clustering: Complete-linkage agglomerative clustering based on the correlation matrix of the transposed D matrix was performed using the Cluster 3.0 program (http://bonsai.hgc.jp/~mdehoon/software/cluster/) and the dendrogram trees were generated using JavaTreeview (http://jtreeview.sourceforge.net/). Complete linkage is one of the most conservative criteria to assign members to a cluster. The clusters in Fig. 4b were identified using a cut-off value of 0.9 for the absolute Pearson's correlation coefficient.

Singular Value Decomposition: The $\Delta_{EC}\Theta$ and $\Delta_{EGCG}\Theta$ data for all assigned and resolved Aβ40 residues were compiled into a 32 x 2 matrix and column mean centered to result in a new matrix (**M'**). The matrix **M'** was then factorized as $\mathbf{UxSxV^T}$ through Singular Value Decomposition (SVD) through the Octave software (http://www.gnu.org/software/octave/). The slope of the first principal component was computed based on the V matrix as the V_{12}/V_{11} ratio, while the second principal component was assumed perpendicular to the first. The score matrix was computed as **UxS**. The percentage of the total variance accounted for by the first (second) principal component was computed as $S_1^2/(S_2^2+ S_2^2)$ $(S_2^2/(S_2^2+ S_2^2))$.

Computation of the Solvent Accessible Surface Area (SASA) of the Aβ40 Fibril Structure

The SASA was computed through the Getarea software based on the Aβ40 fibril structure (PDB ID: 2LMN)[57]. The missing N-terminal residues were inserted through alignment of the 2M4J structure[64] with residues 9 and 10 of the 2LMN structure. This process was repeated for all twelve protomers in 2LMN. Using AMBER 1665, the system was then charge neutralized by adding sodium ions and subsequently solvated in a rectangular box of TIP3P water molecules with a minimum solute–wall distance of 12 Å and box dimensions of 124, 112 and 88 Å. The topology and coordinate files were generated using the Amber force field 14SB. Energy minimizations were then carried out prior to gradually increasing the temperature from 0 K to 300 K for a total duration of 100 ps with the first 20 ps in the NVT ensemble and the following

80 ps in the NPT ensemble. Lastly, the system was equilibrated at 300 K with a weak coupling algorithm for 300 ns to generate the final structure. The whole optimization was conducted while restraining the core 2LMN structure *i.e.* the heavy atoms of residues 12-40 for each protomer using a 500 kcal/mol force constant. All simulations were performed on the Shared Hierarchical Academic Research Computing Network (SHARCNET).

3.8 References

1. I. Benilova , E. Karran and B. de Strooper , *Nat. Neurosci.*, 2012, **15** , 349 —357.
2. J. A. Hardy and G. A. Higgins , *Science*, 1992, **256** , 184 —185.
3. E. S. Musiek and D. M. Holtzman , *Nat. Neurosci.*, 2015, **18** , 800 —806.
4. C. R. Jack , D. S. Knopman , W. J. Jagust , R. C. Petersen , M. W. Weiner , P. S. Aisen , L. M. Shaw , P. Vemuri , H. J. Wiste , S. D. Weigand , T. G. Lesnick , V. S. Pankratz , M. C. Donohue and J. Q. Trojanowski , *Lancet Neurol.*, 2013, **12** , 207 —216.
5. J. M. Castellano , J. Kim , F. R. Stewart , H. Jiang , R. B. DeMattos , B. W. Patterson , A. M. Fagan , J. C. Morris , K. G. Mawuenyega , C. Cruchaga , A. M. Goate , K. R. Bales , S. M. Paul , R. J. Bateman and D. M. Holtzman , *Sci. Transl. Med.*, 2011, **3** , 89ra57.
6. R. D. Terry , E. Masliah , D. P. Salmon , N. Butters , R. DeTeresa , R. Hill , L. A. Hansen and R. Katzman , *Ann. Neurol.*, 1991, **30** , 572 —580.
7. W. L. Klein , G. A. Krafft and C. E. Finch , *Trends Neurosci.*, 2001, **24** , 219 —224.
8. J. L. Tomic , A. Pensalfini , E. Head and C. G. Glabe , *Neurobiol. Dis.*, 2009, **35** , 352 —358.
9. M. Jin , N. Shepardson , T. Yang , G. Chen , D. Walsh and D. J. Selkoe , *Proc. Natl. Acad. Sci. U. S. A.*, 2011, **108** , 5819 —5824.
10. Y. Miller , B. Ma and R. Nussinov , *Biophys. J.*, 2009, **97** , 1168 —1177.
11. K. Ono , M. M. Condron and D. B. Teplow , *Proc. Natl. Acad. Sci. U. S. A.*, 2009, **106** , 14745 —14750.
12. P.-N. Cheng , C. Liu , M. Zhao , D. Eisenberg and J. S. Nowick , *Nat. Chem.*, 2012, **4** , 927 —933.
13. R. Riek and D. S. Eisenberg , *Nature*, 2016, **539** , 227 —235.
14. M. Kinoshita , E. Kakimoto , M. S. Terakawa , Y. Lin , T. Ikenoue , M. So , T. Sugiki , A. Ramamoorthy , Y. Goto and Y.-H. Lee , *Phys. Chem. Chem. Phys.*, 2017, **19** , 16257 —16266.
15. J. D. Gehman , R. Verardi , A. K. Mehta , G. Veglia and F. Separovic , *Biophys. J.*, 2010, **98** , 176a.
16. Y. Miller , B. Ma , C.-J. Tsai and R. Nussinov , *Proc. Natl. Acad. Sci. U. S. A.*, 2010, **107** , 14128 —14133 .
17. H. A. Lashuel , D. Hartley , B. M. Petre , T. Walz and P. T. Lansbury , *Nature*, 2002, **418** , 291.
18. A. Quist , I. Doudevski , H. Lin , R. Azimova , D. Ng , B. Frangione , B. Kagan , J. Ghiso and R. Lal , *Proc. Natl. Acad. Sci. U. S. A.*, 2005, **102** , 10427 —10432.
19. M. F. M. Sciacca , S. A. Kotler , J. R. Brender , J. Chen , D.-k. Lee and A. Ramamoorthy , *Biophys. J.*, 2012, **103** , 702 —710.
20. M. Ahmed , J. Davis , D. Aucoin , T. Sato , S. Ahuja , S. Aimoto , J. I. Elliott , W. E. van Nostrand and S. O. Smith , *Nat. Struct. Mol. Biol.*, 2010, **17** , 561 —567.
21. S. Chimon , M. A. Shaibat , C. R. Jones , D. C. Calero , B. Aizezi and Y. Ishii , *Nat. Struct. Mol. Biol.*, 2007, **14** , 1157 —1164.
22. S. J. C. Lee , E. Nam , H. J. Lee , M. G. Savelieff and M. H. Lim , *Chem. Soc. Rev.*, 2017, **46** , 310 —323.
23. C. A. Ross and M. A. Poirier , *Nat. Rev. Mol. Cell Biol.*, 2005, **6** , 891 —898.
24. S. A. Kotler , P. Walsh , J. R. Brender and A. Ramamoorthy , *Chem. Soc. Rev.*, 2014, **43** , 6692 —6700.
25. F. Chiti and C. M. Dobson , *Annu. Rev. Biochem.*, 2017, **86** , 27 —68.
26. T. Kawarabayashi , M. Shoji , L. H. Younkin , L. Wen-Lang , D. W. Dickson , T. Murakami , E. Matsubara , K. Abe , K. H. Ashe and S. G. Younkin , *J. Neurosci.*, 2004, **24** , 3801 —3809.

27. E. E. Ambroggio , D. H. Kim , F. Separovic , C. J. Barrow , K. J. Barnham , L. A. Bagatolli and G. D. Fidelio , *Biophys. J.*, 2005, **88** , 2706 —2713.
28. J. W. Um , H. B. Nygaard , J. K. Heiss , M. A. Kostylev , M. Stagi , A. Vortmeyer , T. Wisniewski , E. C. Gunther and S. M. Strittmatter , *Nat. Neurosci.*, 2012, **15** , 1227 —1235.
29. N. L. Fawzi , J. Ying , R. Ghirlando , D. A. Torchia and G. M. Clore , *Nature*, 2011, **480** , 268 —272.
30. J. Bieschke , J. Russ , R. P. Friedrich , D. E. Ehrnhoefer , H. Wobst , K. Neugebauer and E. E. Wanker , *Proc. Natl. Acad. Sci. U. S. A.*, 2010, **107** , 7710 —7715.
31. E. Sironi , L. Colombo , A. Lompo , M. Messa , M. Bonanomi , M. E. Regonesi , M. Salmona and C. Airoldi , *Chemistry*, 2014, **20** , 13793 —13800.
32. C. Visentin , F. Pellistri , A. Natalello , J. Vertemara , M. Bonanomi , E. Gatta , A. Penco , A. Relini , L. de Gioia , C. Airoldi , M. E. Regonesi and P. Tortora , *Hum. Mol. Genet.*, 2017, **26** , 3271 —3284.
33. M. Xu , D. J. McCanna and J. G. Sivak , *J. Pharmacol. Toxicol. Methods*, 2015, **71** , 1 —7.
34. H. Lecoeur *Exp. Cell Res.*, 2002, **277** , 1 —14.
35. S. A. Latt and G. Stetten , *J. Histochem. Cytochem.*, 1976, **24** , 24 —33.
36. B. Mannini , E. Mulvihill , C. Sgromo , R. Cascella , R. Khodarahmi , M. Ramazzotti , C. M. Dobson , C. Cecchi and F. Chiti , *ACS Chem. Biol.*, 2014, **9** , 2309 —2317.
37. F. L. Palhano , J. Lee , N. P. Grimster and J. W. Kelly , *J. Am. Chem. Soc.*, 2013, **135** , 7503 —7510.
38. J. M. Lopez del Amo , U. Fink , M. Dasari , G. Grelle , E. E. Wanker , J. Bieschke and B. Reif , *J. Mol. Biol.*, 2012, **421** , 517 —524.
39. T. L. Williams and L. C. Serpell , *FEBS J.*, 2011, **278** , 3905 —3917.
40. R. Ahmed and G. Melacini , *Chem. Commun.*, 2018, **54** , 4644 —4652.
41. J. Milojevic , V. Esposito , R. Das and G. Melacini , *J. Am. Chem. Soc.*, 2007, **129** , 4282 —4290.
42. G. Fusco , S. W. Chen , P. T. F. Williamson , R. Cascella , M. Perni , J. A. Jarvis , C. Cecchi , M. Vendruscolo , F. Chiti , N. Cremades , L. Ying , C. M. Dobson and A. de Simone , *Science*, 2017, **358** , 1440 —1443.
43. G. Fusco , T. Pape , A. D. Stephens , P. Mahou , A. R. Costa , C. F. Kaminski , G. S. Kaminski Schierle , M. Vendruscolo , G. Veglia , C. M. Dobson and A. de Simone , *Nat. Commun.*, 2016, **7** , 12563.
44. G. Fusco , A. de Simone , T. Gopinath , V. Vostrikov , M. Vendruscolo , C. M. Dobson and G. Veglia , *Nat. Commun.*, 2014, **5** , 3827.
45. N. L. Fawzi , J. Ying , D. A. Torchia and G. M. Clore , *J. Am. Chem. Soc.*, 2010, **132** , 9948 —9951.
46. C. R. Bodner , C. M. Dobson and A. Bax , *J. Mol. Biol.*, 2009, **390** , 775 —790.
47. C. R. Bodner , A. S. Maltsev , C. M. Dobson and A. Bax , *Biochemistry*, 2010, **49** , 862 —871.
48. A. Ceccon , V. Tugarinov , A. Bax and G. M. Clore , *J. Am. Chem. Soc.*, 2016, **138** , 5789 —5792.
49. M. Algamal , R. Ahmed , N. Jafari , B. Ahsan , J. Ortega and G. Melacini , *J. Biol. Chem.*, 2017, **292** , 17158 —17168.
50. R. Ahmed , B. VanSchouwen , N. Jafari , X. Ni , J. Ortega and G. Melacini , *J. Am. Chem. Soc.*, 2017, **139** , 13720 —13734.
51. S. Campioni , B. Mannini , M. Zampagni , A. Pensalfini , C. Parrini , E. Evangelisti , A. Relini , M. Stefani , C. M. Dobson , C. Cecchi and F. Chiti , *Nat. Chem. Biol.*, 2010, **6** , 140 —147.
52. C. Capitini , J. R. Patel , A. Natalello , C. D'Andrea , A. Relini , J. A. Jarvis , L. Birolo , A. Peduzzo , M. Vendruscolo , P. Matteini , C. M. Dobson , A. de Simone and F. Chiti , *Chem. Commun.*, 2018, **54** , 8637 —8640.
53. A. R. A. Ladiwala , J. Litt , R. S. Kane , D. S. Aucoin , S. O. Smith , S. Ranjan , J. Davis , W. E. van Nostrand and P. M. Tessier , *J. Biol. Chem.*, 2012, **287** , 24765 —24773.
54. R. Krishnan , J. L. Goodman , S. Mukhopadhyay , C. D. Pacheco , E. A. Lemke , A. A. Deniz and S. Lindquist , *Proc. Natl. Acad. Sci. U. S. A.*, 2012, **109** , 11172 —11177.
55. B. Bolognesi , J. R. Kumita , T. P. Barros , E. K. Esbjorner , L. M. Luheshi , D. C. Crowther , M. R. Wilson , C. M. Dobson , G. Favrin and J. J. Yerbury , *ACS Chem. Biol.*, 2010, **5** , 735 —740.
56. J. Zheng , C. Liu , M. R. Sawaya , B. Vadla , S. Khan , R. J. Woods , D. Eisenberg , W. J. Goux and J. S. Nowick , *J. Am. Chem. Soc.*, 2011, **133** , 3144 —3157.

57. A. T. Petkova , Y. Ishii , J. J. Balbach , O. N. Antzutkin , R. D. Leapman , F. Delaglio and R. Tycko , *Proc. Natl. Acad. Sci. U. S. A.*, 2002, **99** , 16742 —16747.
58. C. de Jonghe *Hum. Mol. Genet.*, 2001, **10** , 1665 —1671.
59. R. Kayed , E. Head , J. L. Thompson , T. M. McIntire , S. C. Milton , C. W. Cotman and C. G. Glabe , *Science*, 2003, **300** , 486 —489.
60. B. N. Ames, *Methods in Enzymology*, 1966, **8**, 115-118.61
61. A. Khondker, R. J. Alsop, S. Himbert, J. Tang, A.-C. Shi, A. P. Hitchcock and M. C. Rheinstädter, *Scientific reports*, 2018, **8**, 12367.62J.
62. Tang, R. J. Alsop, M. Backholm, H. Dies, A.-C. Shi and M. C. Rheinstädter, *Soft matter*, 2016, **12**, 3165–3176.63A. 63. J. Smith, P. Kavuru, K. K. Arora, S. Kesani, J. Tan, M. J. Zaworotko and R. D. Shytle, *Molecular pharmaceutics*, 2013, **10**, 2948–2961.64J.
64. Lu, W. Qiang, S. C. Meredith, W. Yau, C. D. Schweiters and R. Tycko, *Cell*, 2013, **154**, 1257-1268.65
65. D.A. Case, R.M. Betz, D.S. Cerutti, T.E. Cheatham, III, T.A. Darden, R.E. Duke, T.J. Giese, H. Gohlke, A.W. Goetz, N. Homeyer, S. Izadi, P. Janowski, J. Kaus, A. Kovalenko, T.S. Lee, S. LeGrand, P. Li, C. Lin, T. Luchko, R. Luo, B. Madej, D. Mermelstein, K.M. Merz, G. Monard, H. Nguyen, H.T. Nguyen, I. Omelyan, A. Onufriev, D.R. Roe, A. Roitberg, C. Sagui, C.L. Simmerling, W.M. Botello-Smith, J. Swails, R.C. Walker, J. Wang, R.M. Wolf, X. Wu, L. Xiao and P.A. Kollman (2016), AMBER 2016, University of California, San Francisco.

3.9 Supplementary Information

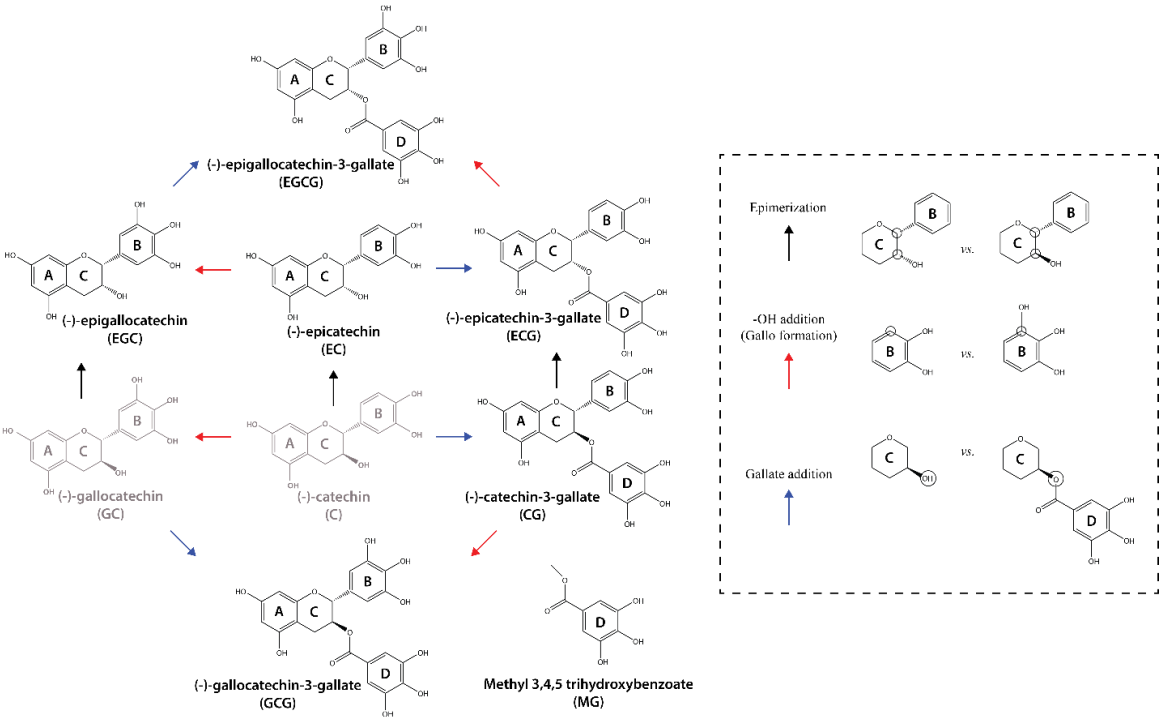

Figure S1. – *Catechin library utilized to modulate Aβ40 toxicity.* Arrows represent single substitutions and are categorized as epimerization (black), 3′-OH addition to ring B (gallo formation) (red), and esterification of the ring C –OH by gallate addition (blue). The (-)-catechin and (-)-gallocatechin compounds are shown here for comparative purposes only and were not included in the compound library (grey). The arrows are used for illustrative purposes only and do not reflect endogenous synthetic pathways.

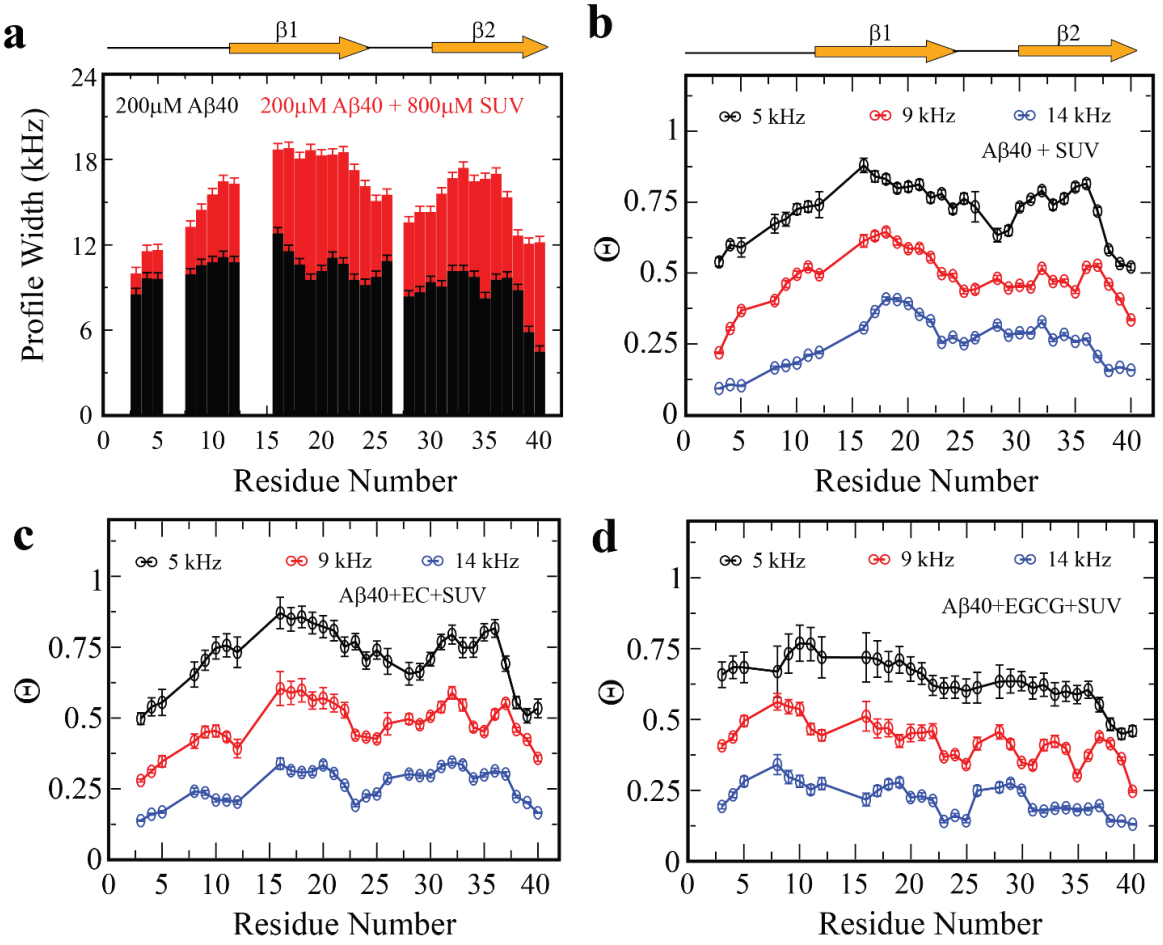

Figure S2. – *Atomic resolution map of the Aβ40 monomer exchange dynamics in the presence of DOPE:DOPS:DOPC SUVs.* (a) ^{15}N – DEST profile widths for Aβ40 assemblies in the absence (black) and presence (red) of SUVs. (b) ^{15}N – Θ DEST profiles of canonical Aβ40 assemblies at 5 (black), 9 (red) and 14 (blue) kHz offsets. The ^{15}N – Θ profiles were smoothened by averaging the Θ values for each residue and the two residues directly adjacent to it, when available. (c) As (b) except for the EC-remodeled Aβ40 assemblies in the presence of SUVs. (d) As (c) except for the EGCG-remodeled $A\beta_n$ in the presence of SUVs.

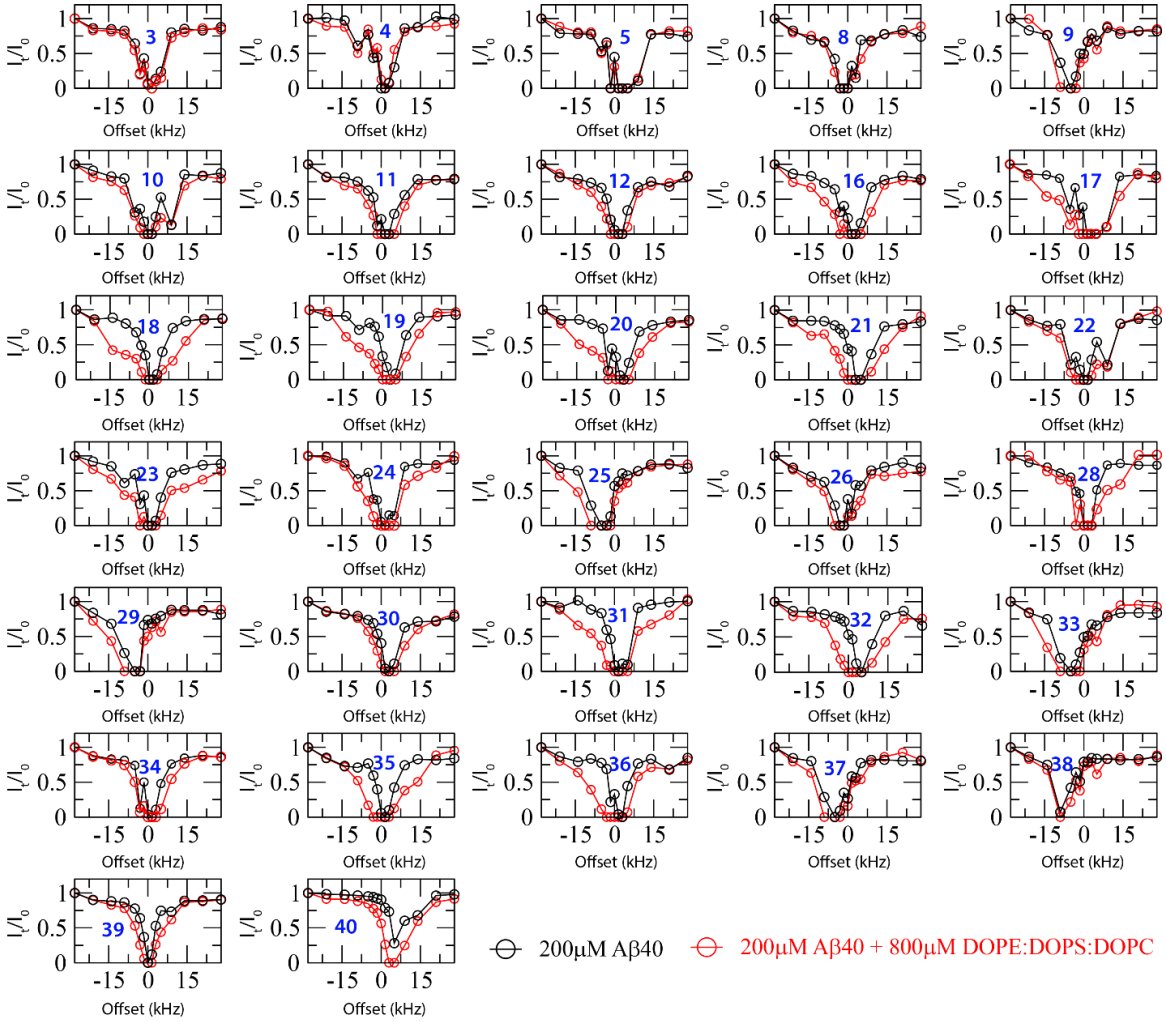

Figure S3. – Residue-specific ^{15}N –DEST profiles of canonical Aβ40 assemblies in the absence (black) and presence (red) of DOPE:DOPS:DOPC SUVs. The profiles for residues 3, 19, 35 and 36 from Fig. 3c-f are shown here as well for convenience of comparison.

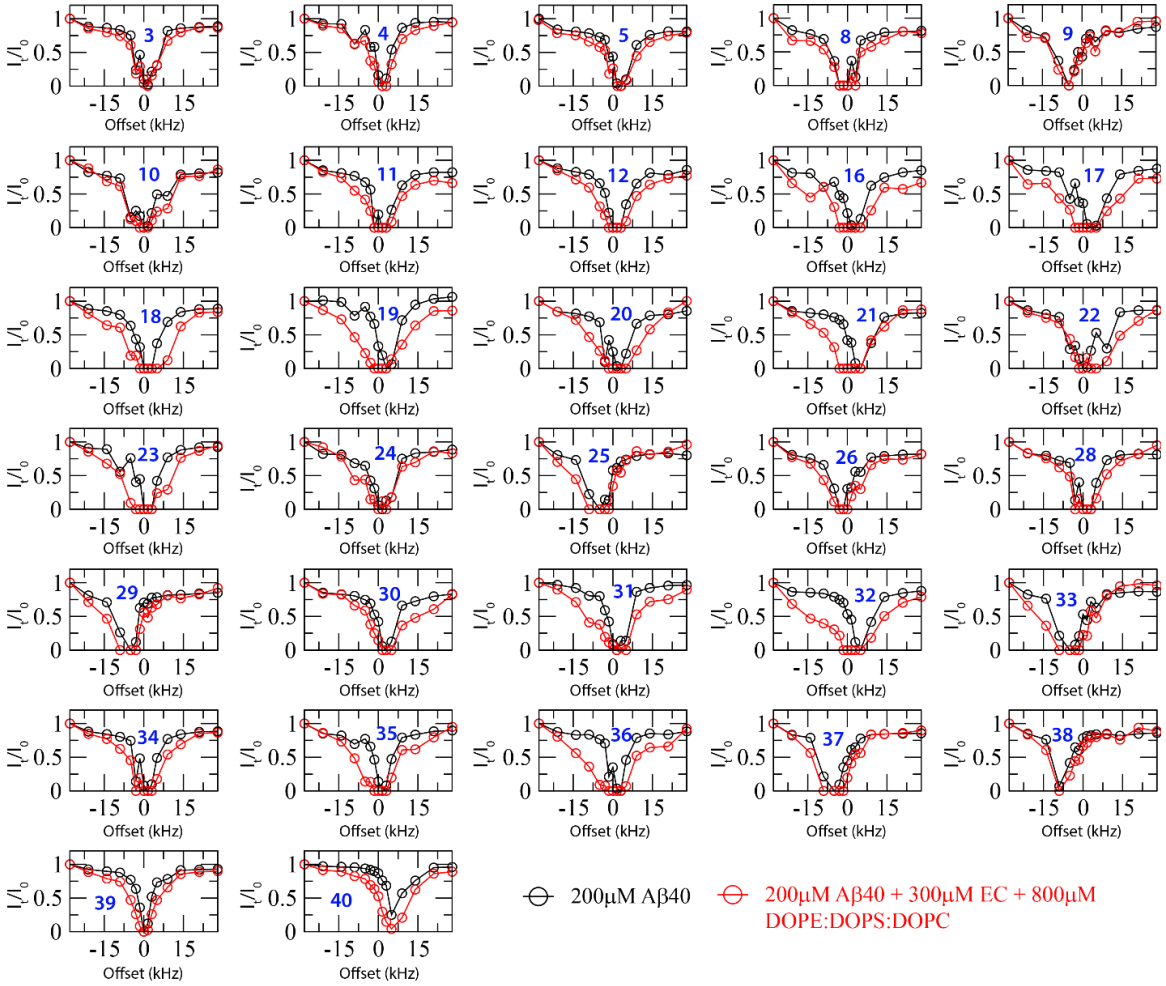

Figure S4. – Residue-specific ^{15}N –DEST profiles of canonical Aβ40 assemblies in the absence (black) and presence (red) of EC and DOPE:DOPS:DOPC SUVs.

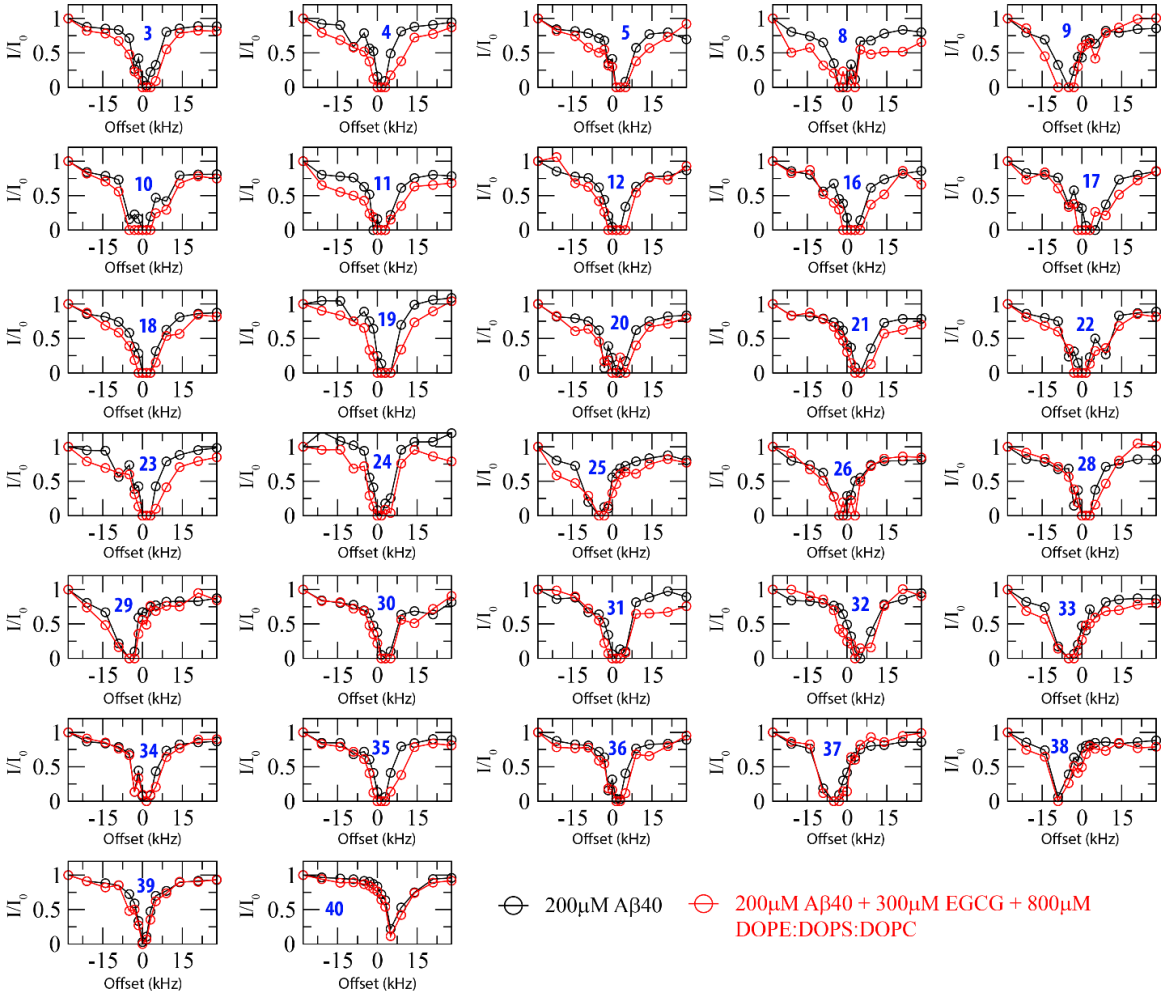

Figure S5. – Residue-specific ^{15}N –DEST profiles of canonical Aβ40 assemblies in the absence (black) and presence (red) of EGCG and DOPE:DOPS:DOPC SUVs.

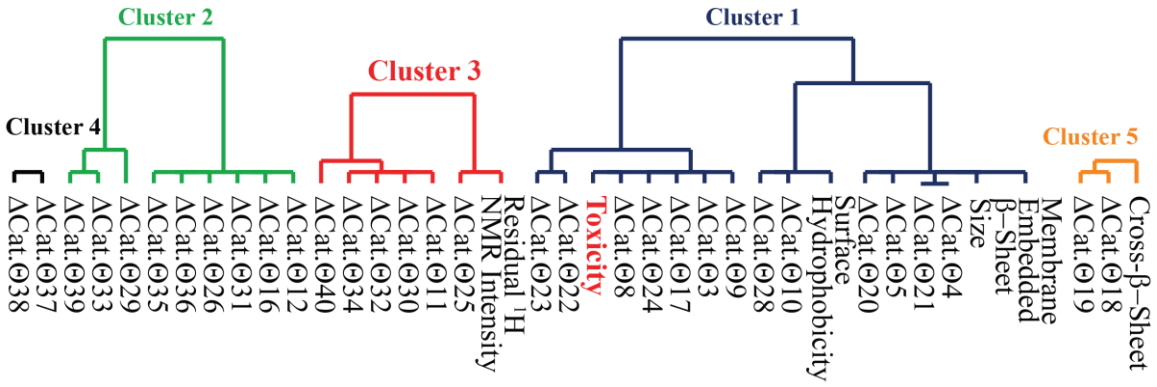

Figure S6 – Dendrogram displaying the clusters identified through agglomerative clustering of $A\beta_n$ observables, similarly to Fig. 4b, but including cellular viability/toxicity.

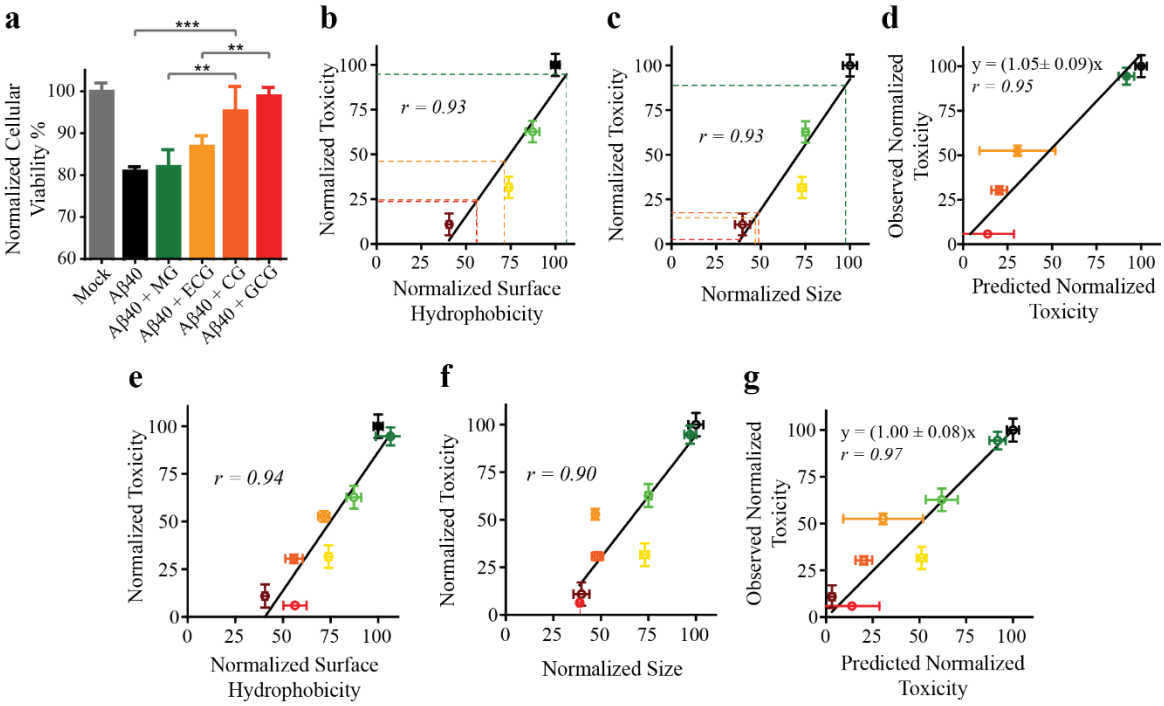

Figure S7. – *Validation of the predictive power of the Aβ$_n$ toxicity model.* (a) Cellular viability of the remaining catechin-remodeled Aβ$_n$ not included in Fig. 1a evaluated using the retinal pigment epithelial (RPE1) cell line and the PrestoBlue assay. One-way ANOVA and subsequent Tukey's post-hoc test was used to determine statistical significance between treatments and mock (1X PBS delivery solution), where *, ** and *** represent p values of 0.0423, 0.001 and 0.0005, respectively. The experiments were conducted independently of Fig. 1a using newly prepared Aβ assemblies. (b, c) The toxicities of the Aβ$_n$ evaluated in (a) were predicted using the two cluster 1 observables, size and surface hydrophobicity, for which data is available for all Aβ$_n$ in our library. (b) Relationship between surface hydrophobicity and cellular toxicity (solid black line) as determined using the observed toxicities in Fig. 1a for the canonical (black), EC- (light green), EGC- (yellow) and EGCG- (maroon) remodeled Aβ$_n$ as inputs. The surface hydrophobicity is normalized to the canonical Aβ$_n$, which is set to 100. The normalized toxicity is calculated as $(CV_x - CV_{Mock})/(CV_{Aβ} - CV_{Mock})$ where subscript x represents the cellular viability of the Aβ$_n$ for which the normalized toxicity is being calculated. Coloured dashed lines indicate the extrapolation of the Aβ$_n$ normalized toxicities based on their normalized surface hydrophobicity measured in Fig. 1g. (c) As (b)except using normalized size measurements from DLS experiments (Fig. 1e). (d) Relationship between the normalized toxicity predicted from (b) and (c) and the normalized toxicity observed in panel (a). The predicted normalized toxicity for each Aβ$_n$ is an average of the values shown in (b) and (c), and the error is derived from the standard deviation between the two values. The solid blackline indicates the linear regression of the data with y-intercept set to zero. (e) Relationship between normalized surface hydrophobicity and normalized toxicity using all Aβ$_n$ in our library as inputs. (f) As (e) except using normalized size. (g) As (d) except using all Aβ$_n$ in our library as inputs.

Table S1 – Pairwise statistical analyses of the RPE1 cellular viability in the absence and presence of the Aβ assembly library.

Species	P-value*
Mock *vs.* EC, EGC and EGCG	0.9947, 0.8692 and 0.8477
Mock *vs.* Aβ40	< 0.0001
Aβ40 *vs.* EC-remodeled Aβ40	0.0478
Aβ40 *vs.* EGC-remodeled Aβ40	0.0003
Aβ40 *vs.* EGCG-remodeled Aβ40	< 0.0001
EC-remodeled Aβ *vs.* EGCG-remodeled Aβ40	0.0097
Aβ40 *vs.* GCG-remodeled Aβ40	< 0.0001
Aβ40 *vs.* CG-remodeled Aβ40	0.0005
MG-remodeled Aβ40 *vs.* CG-remodeled Aβ40	0.001
ECG-remodeled Aβ40 *vs.* CG-remodeled Aβ40	0.0423
ECG-remodeled Aβ40 *vs.* GCG-remodeled Aβ40	0.0018

*The p-values are generated from the post-hoc Tukey test of the cellular viability data shown in Fig. 1a and Fig. S7a.

3.9.9 Table S2 – Average residue-specific solvent accessible surface area (SASA) ratios for the 2LMN Aβ40 fibril structure.

Residue #	Total		Edge		Non-Edge	
	Average SASA Ratio (%)	STDEV	Average SASA Ratio (%)	STDEV	Average SASA Ratio (%)	STDEV
9	98.3	4.4	100.0	0.0	97.9	4.7
10	83.5	14.4	99.3	0.6	80.3	13.7
11	43.0	18.1	66.4	0.7	38.3	15.9
12	41.9	11.4	43.0	3.3	41.6	12.5
13	44.4	18.0	79.4	13.1	37.4	7.2
14	45.5	25.0	66.8	6.9	41.2	25.2
15	35.7	20.5	74.8	8.5	27.9	9.8
16	51.3	14.8	64.9	6.8	48.6	14.6
17	33.6	19.7	55.1	3.8	29.3	18.7
18	40.0	15.4	49.2	4.2	38.2	16.3
19	25.4	27.9	23.4	11.5	25.8	30.6
20	44.5	14.6	62.6	14.4	40.9	12.3
21	25.5	19.3	21.0	14.7	26.4	20.6
22	38.8	16.0	50.5	24.1	36.5	14.6
23	23.8	27.2	14.1	0.1	25.7	29.7
24	67.3	24.3	95.1	5.7	61.7	22.7
25	71.4	20.9	87.2	4.5	68.3	21.5
26	38.5	32.3	38.7	8.6	38.5	35.6
27	62.7	30.8	97.7	3.3	55.7	28.9
28	38.1	44.8	100.0	0.0	25.8	37.9
29	36.0	15.2	46.3	14.7	34.0	15.1
30	19.1	12.1	30.4	8.3	16.9	11.7
31	18.8	10.7	38.5	3.9	14.9	6.0
32	28.5	18.2	63.2	0.9	21.6	9.1
33	14.5	9.6	33.8	4.2	10.7	3.3
34	20.8	26.9	71.1	8.6	10.8	14.4
35	6.2	8.5	22.9	1.3	2.9	3.8
36	30.1	22.6	67.9	13.9	22.5	14.8
37	9.8	11.8	11.5	4.1	9.5	12.9
38	45.4	10.0	49.5	1.1	44.5	10.8
39	55.1	16.6	75.8	20.0	51.0	13.3
40	96.5	9.2	100.0	0.0	95.8	10.0

The residue-specific solvent accessible surface areas were determined using the GETAREA software provided by the University of Texas Medical Branch.

Chapter 4. Molecular Mechanism for the Suppression of Alpha Synuclein Membrane Toxicity by an Unconventional Extracellular Chaperone

4.1 Author's Preface

The work presented in this chapter has previously been published and is reproduced here with permission from the Journal of the American Chemical Society. Full citation is as follows:

Ahmed, R.; Huang, J.; Weber, D. K.; Gopinath, T.; Veglia, G.; Akimoto, M.; Khondker, A.; Rheinstädter, M. C.; Huynh, V.; Wylie, R. G.; *et al.* Molecular Mechanism for the Suppression of Alpha Synuclein Membrane Toxicity by an Unconventional Extracellular Chaperone. *Journal of the American Chemical Society* [Online early access]. DOI: 10.1021/jacs.0c01894.

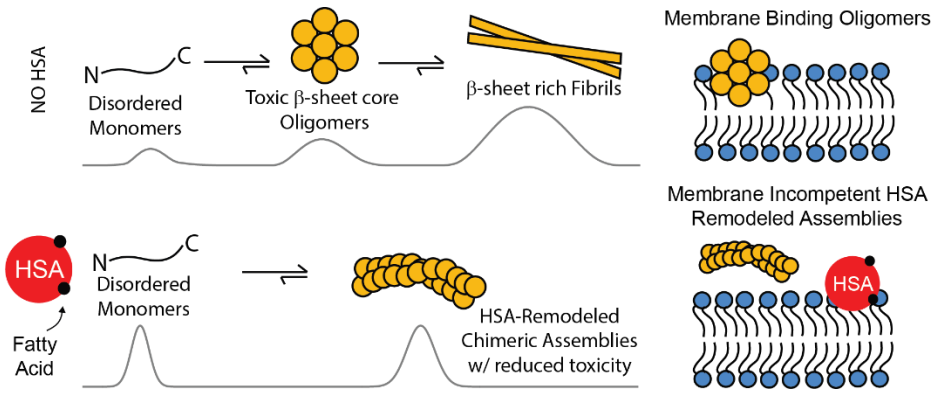

I conducted most of the experiments necessary for the manuscript and analyzed the data. Jinfeng Huang provided support in purifying alpha synuclein and conducting fluorescence experiments. Dr. Daniel Weber, Dr. Tata Gopinath and Dr. Gianluigi Veglia aided with the acquisition and analysis of solid-state NMR data. Dr. Madoka Akimoto acquired and analyzed the SEC-MALS data. Adree Khondker acquired and analyzed the Wide-Angle X-ray Diffraction (WAXD) data with support from Dr. Maikel Rheinstädter. Jose Carlos Bozelli Jr. made the liposomes and Dr. Richard Epand provided feedback regarding the membrane data. Vincent Huynh cultured the mammalian cell lines and provided feedback on the cell toxicity data with support from Dr. Ryan Wylie. I co-wrote the manuscript and designed the research with Dr. Giuseppe Melacini.

4.2 Abstract

Alpha synuclein (αS) oligomers are a key component of Lewy Bodies implicated in Parkinson's disease (PD). Although primarily intracellular, extracellular αS exocytosed from neurons also contributes to PD pathogenesis through a prion-like transmission mechanism. Here, we show at progressive degrees of resolution that the most abundantly expressed extracellular protein, Human Serum Albumin (HSA), inhibits αS oligomer (αS_n) toxicity through a three-pronged mechanism. First, endogenous HSA targets αS_n with sub μM affinity via solvent exposed hydrophobic sites, breaking the catalytic cycle that promotes αS self-association. Second, HSA remodels αS oligomers and high MW fibrils into chimeric intermediates with reduced toxicity. Third, HSA unexpectedly suppresses membrane interactions with the N-terminal and central αS regions. Overall, our findings suggest that the extracellular proteostasis network may regulate αS cell-to-cell transmission not only by reducing the populations of membrane-binding competent αS oligomers, but possibly also by shielding the membrane interface from residual toxic species.

4.3 Introduction

The aggregation of alpha synuclein (αS) into Lewy Bodies (LBs) is a clinical hallmark of Parkinson's disease (PD) [1]. It is widely accepted that β-sheet rich αS oligomers contribute to the neurodegeneration observed in PD [2]. Indeed, genetic mutations of familial PD are observed exclusively in the αS encoding gene (SNCA) and such mutations enhance the accumulation of toxic αS oligomers [3]. Moreover, sporadic forms of PD also result in αS accumulation [2].

While LBs observed in PD are intracellular, emerging evidence suggests that extracellular αS also exists and contributes to PD pathology via a prion-like cell-to-cell transmission mechanism [4,5]. LBs expand through anatomically connected regions of the brain from the peripheral tissues of the olfactory bulb to the cerebral cortex [6], suggesting a prion-like transmission hypothesis. Moreover, monomeric and oligomeric forms of αS have been detected in blood plasma [7] and cerebrospinal fluid (CSF) [8]. Notably, grafting fetal mesencephalic neurons in the neostriatum of PD patient brains caused the development of intracellular LBs in the exogenously introduced cells [9,10]. Similar observations have also been reported in cell culture and mouse model studies [11], which collectively showed that αS is secreted from cells via an unconventional exocytosis pathway independent of the endoplasmic reticulum and Golgi apparatus [12]. The extracellular αS is able to subsequently enter into recipient cells, with αS aggregates exhibiting enhanced propensity to internalize compared to monomeric forms [13,14].

While a substantial body of evidence now points to the presence of extracellular αS species, the specific interactions of such species with the extracellular proteome and its role in regulating αS internalization into cells is poorly understood. The extracellular milieu thus remains an untapped potential that could be harnessed for therapeutic interventions in PD. As a first step towards tapping the translational potential of the extracellular milieu, here we focus on the most abundantly expressed protein in human blood plasma and CSF [15], *i.e.* Human Serum Albumin (HSA). HSA is not only the endogenous transporter for a broad range of serum solutes, such as fatty acids and exogenous ligands, but it is also the most potent plasma inhibitor of self-association for numerous unstructured polypeptides prone to form cytotoxic oligomers, such as the prototypical amyloidogenic peptide Aβ [16–22] and more recently αS [23–25]. Hence, the extracellular chaperone HSA[26] serves as an ideal candidate to explore the regulatory capacity of the extracellular proteome in the context of cell-to-cell transmission in PD.

Several open questions remain about the mechanism through which HSA regulates the conformations of extracellular αS species and their capacity to internalize into cells. First, it is currently unclear whether HSA interacts with αS oligomers, which are the predominant internalized species and, if so, what are the determinants of such interactions. Second, it is unknown whether HSA perturbs the interactions and

subsequent internalization of αS into cells. Addressing these questions is critical to understanding the intercellular transmission of αS and the role of the extracellular proteome in this process.

Here, we have examined the interactions of defatted (rHSA) and non-defatted, endogenous (gHSA) HSA extracted from blood plasma with both monomeric and oligomeric αS. We also evaluated how such interactions influence the association of αS with membranes. By combining both solution and solid state NMR with extrinsic fluorescence, dynamic light scattering (DLS), size exclusion chromatography with multi-angle light scattering (SEC-MALS), transmission electron microscopy (TEM), biolayer interferometry (BLI) and wide-angle x-ray diffraction (WAXD) we show that HSA binds αS oligomers with sub μM affinity through multiple solvent-exposed hydrophobic surfaces. The αS oligomer - HSA interactions result not only in the inhibition of αS self-association, but also in the remodeling of existing low molecular weight (LMW) and high molecular weight (HMW) αS aggregates into chimeric intermediates that are thermodynamically stable and exhibit reduced toxicity. Unexpectedly, HSA also inhibits the interactions of the αS N-terminal and Non Amyloid-β Component (NAC) regions with lipid membranes, pointing to a role of HSA in suppressing membrane damage by αS. These two HSA-induced effects, *i.e.* the αS oligomer remodeling and the preservation of membrane integrity, provide a viable mechanism to explain how HSA, and possibly the extracellular proteome, suppresses cell-to-cell transmission of αS.

4.4 Results

4.4.1 Both Defatted and Non-Defatted HSA Reduce the Cytotoxicity of αS Oligomers and Bind αS Oligomers with Sub μM Affinity.

Our working definition of "oligomer" refers to any pre-fibrillar species with diameters less than 1000 nm and aggregate MW <1M Da[27]. Three different oligomer preparation protocols are used in this work (Experimental Section), each of which is optimized for a different experimental technique. The size-distribution of the αS oligomers prepared according to these protocols were characterized by SEC-MALS (Table 1, Fig. 1a-c). Despite originating from different protocols, the size distribution of the αS species are similar for all three preparations (Table 1, Fig. 1a-c).

Table 1 – Molecular Weights (kDa) of αS Species as Determined by SEC-MALS.

Sample	Monomer	LMW Oligomer	Intermediate MW Oligomer	HMW Aggregates
100 μM 2d 37°C	14.1 ± 0.9	31.8 ± 6.9	122 ± 10	731 ± 12
800 μM 1d 37°C	15.1 ± 0.1	37.7 ± 0.5	112 ± 2	835 ± 1
800 μM 2d 37°C	14.1 ± 0.1	32.5 ± 0.9	132 ± 6	767 ± 2

We first analyzed whether HSA suppresses the cytotoxicity of αS oligomers and if this capacity is dependent on the fatty acid load of HSA. To this end, we used defatted and non-defatted HSA extracted from pooled blood plasma, denoted here as rHSA and gHSA, respectively. Under our conditions, the two

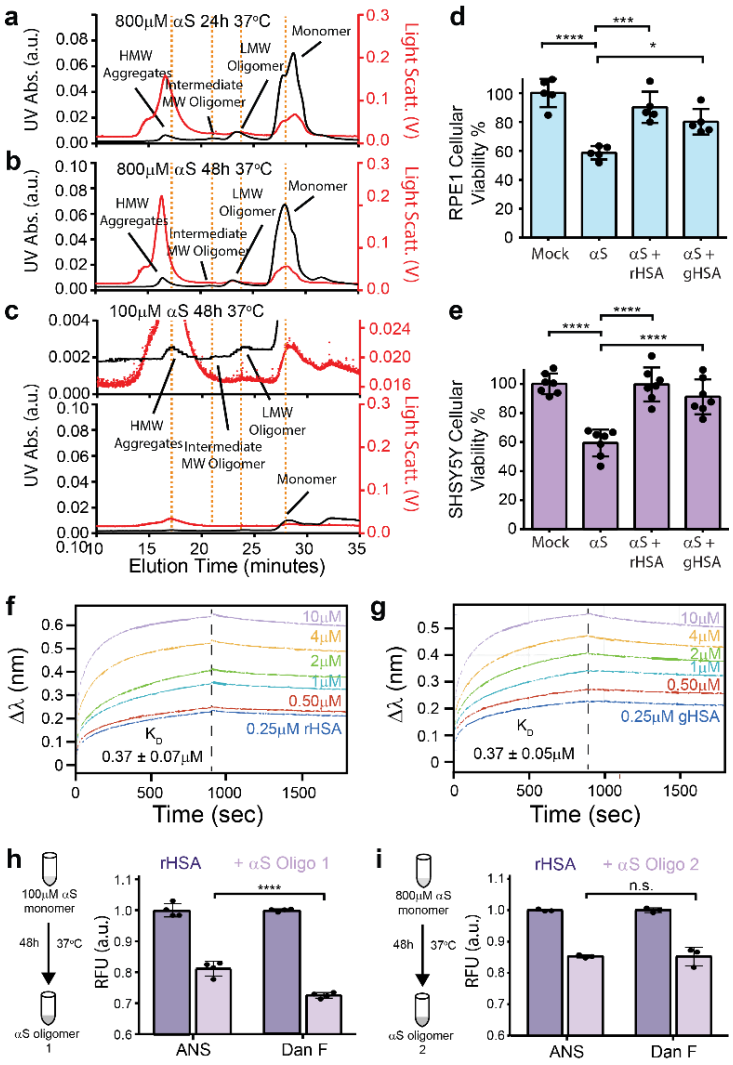

Figure 1. – *Both defatted and non-defatted HSA suppress αS oligomer cell toxicity and bind αS oligomers with sub-μM affinity*. (a)-(c) SEC-MALS characterization of the αS oligomers. A zoomed in chromatogram is shown in the upper panel of (c) to more clearly display lowly populated oligomers. (d) Cellular viability of retinal pigment epithelial (RPE1) cells after treatment with αS oligomers in the absence and presence of defatted (rHSA) and non-defatted (gHSA) HSA, as monitored by the reduction of Resazurin using the PrestoBlue assay. The data reported show the mean and standard deviation of technical replicates. One-way ANOVA and subsequent Tukey's post-hoc test was used to determine statistical significance between treatments and mock (PBS delivery solution), with *, *** and **** representing p-values of ≤0.05, ≤0.001 and ≤0.0001, respectively. (e) As (d) except measured for SHSY5Y neuroblastoma cells. (f)-(g) Biolayer interferometry (BLI) analysis of the (f) rHSA and (g) gHSA binding to αS oligomers, respectively. (h)-(i) Fluorescence intensities of ANS and Dan F bound to rHSA in the absence (dark purple) and presence (light purple) of two different αS oligomer preparations, normalized to the rHSA alone state. The data reported show the mean and standard deviation of technical replicates. Fluorescence contributions arising from ANS and Dan F binding each αS oligomer are accounted for. Two-way ANOVA and subsequent Sidak's multiple comparison tests were used to determine statistical significance between the rHSA or rHSA with αS oligomer samples in ANS vs. Dan F competition experiments. Cartoons in (h-i) depict the protocols for preparation of the αS oligomers.

highest-affinity sites of gHSA are occupied by long-chain fatty acids (FAs) (A and B, Fig. S1). We measured the αS oligomer cytotoxicity in the absence and presence of rHSA and gHSA using a Presto Blue assay. As seen in Fig. 1d-e, both albumins significantly recover the loss of cellular viability induced by αS oligomers to comparable levels. These effects are consistently observed in both retinal pigment epithelial (RPE1) (Fig. 1d, Table S1) and SHSY5Y neuroblastoma (Fig. 1e, Table S1) cell lines, pointing to a detoxification mechanism that appears to be largely independent of cell type and presence of fatty acid.

As a first step towards understanding the mechanism by which HSA detoxifies αS oligomers, we measured the affinity of αS oligomers for both rHSA and gHSA using Biolayer Interferometry (BLI). Our BLI analyses (Fig. 1f-g) reveal that both rHSA and gHSA bind to αS oligomers with comparable affinities of 0.37 ± 0.07 and 0.37 ± 0.05 μM, respectively, consistent with their equivalent detoxification capacities. While these results consistently point to similar efficacy of defatted and non-defatted HSA, they do not offer any insight on the drivers of the HSA - αS oligomer interactions. Hence, we relied on competitive binding experiments with well-known HSA binders, such as ^{13}C-Oleic Acid (OA) [28], 8-Anilinonaphthalene-1-sulfonic acid (ANS) and Dansyl-L-β-phenylalanine (Dan F) [29], to probe the determinants of HSA – αS oligomer interactions.

4.4.2 αS Oligomers Target Multiple Solvent-Exposed Hydrophobic Sites in HSA.

OA occupies nine binding sites scattered throughout the three domains of HSA, starting from the three high affinity sites at low FA:HSA stoichiometric ratios and progressing to lower affinity loci occupied at higher FA:HSA ratios (Fig. S1a) [28,30]. Of the six low affinity loci, two are commonly occupied by drugs, Sudlow sites I and II, located in domain 2 and 3, respectively (Fig. S1a). The ^{1}H – ^{13}C methyl HSQC spectra of ^{13}C – OA in the presence of HSA provide a comprehensive map of the occupancy of these HSA sites by long chain fatty acids (LCFAs) such as OA (Fig S1a,b). Moreover, both ANS and Dan F exhibit comparable affinities for HSA[31] and occupy HSA Sudlow sites I and II, as revealed by ^{1}H – ^{13}C HSQC spectra showing the competition between ANS/Dan F with ^{13}C-OA-bound to HSA at these sites (Fig. S1c-f). However, unlike Dan F, ANS binds to additional sites on HSA that do not overlap with ^{13}C-OA[29], consistent with the substantially smaller decrease in ANS fluorescence relative to Dan F in gHSA *vs*. rHSA (Fig. S1g). Overall, the combination of ^{13}C – OA, ANS and Dan F competition experiments provides an informative spectroscopic handle to probe the determinants of HSA – αS oligomer interactions.

In order to separate the contributions from αS monomers *vs*. αS oligomers to the ANS and Dan F fluorescence, we prepared two variations of αS oligomers with progressively larger populations of HMW aggregates and reduced populations of residual monomers (Fig. 1c *vs*. b, Table 1). Subsequently, we added these preformed αS oligomers to ANS or Dan F-bound rHSA and observed changes in the ANS or

Dan F fluorescence to assess the relative degree of competition. As the population of HMW species increases and monomer population decreases, a significantly larger decrease in ANS relative to Dan F fluorescence is observed (Fig. 1h-i). For example, αS oligomers prepared at a concentration of 100 μM through a two-day incubation at 37 °C lead to a substantially larger Dan F *vs.* ANS fluorescence reduction (Fig. 1h). However, when the population of αS oligomers is further promoted (monomer population further decreased) through higher αS concentrations, αS oligomer addition leads to comparable fluorescence losses for ANS and Dan F (Fig. 1i). These results are further confirmed for a substantially aggregated αS sample with no residual monomers (Fig. S2). Overall, these results show that αS oligomers preferentially bind to solvent exposed hydrophobic sites in HSA, which are distinct from the Sudlow Site I and II fatty-acid binding loci. Nevertheless, these results do not explain how the binding of HSA to αS oligomers lead to a reduction in cytotoxicity. To address this question, we monitored through ^{1}H NMR and TEM/DLS how HSA remodels the distribution of αS monomers and HMW species.

4.4.3 HSA Remodels αS Aggregates Into Thermodynamically Stable Chimeric Intermediates.

To understand how the αS oligomer – HSA interactions remodel αS oligomer species, we first recorded DLS data for αS oligomers prepared in the absence and presence of rHSA and gHSA (Fig. 2a). Figure 2a shows that albumin shifts the populations of low molecular weight (LMW, <10 nm) and HMW (>100 nm) αS species into intermediate assemblies with hydrodynamic radius of ~100 nm, resulting in a distribution more uniform in size compared to that in the absence of HSA. Such size remodeling effect is observed for both rHSA and gHSA to a comparable extent (Fig. 2a) and it is also largely independent of whether albumin is added prior to or after αS aggregation (Fig. 2a *vs.* 2b). These observations suggest that the albumin-induced remodeling of αS oligomers is independent of fatty acid binding to the high-affinity sites and is under thermodynamic rather than kinetic control. Further inspection of the albumin-induced remodeling of αS oligomers through TEM imaging corroborates that albumin converts LMW spherical oligomers and HMW αS fibrils into intermediate assemblies (Fig. 2c and S3a).

Residue-resolution insight into the structural changes occurring upon HSA-induced remodeling of αS oligomers was gained through ^{13}C – ^{13}C Dipolar Assisted Rotational Resonance (DARR) solid-state NMR (ssNMR) experiments (Fig. 2d). The ^{13}C – ^{13}C DARR spectra were assigned based on previous assignments of αS oligomers[32] and fibrils[33]. The DARR spectrum acquired in the absence of HSA (Fig. 2d, *dark purple*) shows good overlay with αS fibrils simulated using the chemical shifts reported by Comellas and colleagues[33] (Fig. 2d, *light violet*), confirming that our αS oligomers form a rigid β-sheet rich core centred around the NAC region, as previously shown[32]. However, relative to the fibrils far fewer DARR cross-peaks are observed for αS oligomers, indicating an overall less rigid structure. The αS oligomer – fibril continuum thus serves as an effective tool to evaluate the effect of HSA addition to αS oligomers. Notably, addition

of sub-stoichiometric amounts of gHSA shifts the populations of αS oligomers to more rigid fibril-like states, as evidenced by the appearance of new DARR cross-peaks that overlay with αS fibrils (Fig. 2d-f, *blue vs. light violet*). These observations are further supported by the loss of DARR resonances that are more unique to αS oligomers (Fig. 2d,g,h *blue vs. dark purple*), indicating a shift away from the oligomeric states. The high-resolution ssNMR experiments are in good agreement with our low-resolution DLS and TEM data, both of which suggest that HSA remodels preformed αS aggregates into chimeric structural assemblies that are reminiscent of both oligomers and fibrils.

4.4.4 HSA inhibits the Heat-induced Self-Assembly of αS Monomers by Binding Primarily to αS Oligomers.

In order to further explore how the albumin-induced αS oligomer remodeling affects the self-association of αS, we monitored how albumin perturbs the transition from NMR visible monomers to NMR invisible αS oligomers induced by heating. For this purpose, we measured how the NMR intensity of H_b and other side chain αS protons is reduced upon heating in the absence and presence of gHSA and rHSA (Fig. 2i,j and S3c,d). gHSA at concentrations two-orders of magnitude above the $K_{d,\,app}$ for αS oligomer binding, *i.e.* conditions under which αS oligomers are saturated with gHSA, is effective at reducing the heat-induced NMR intensity losses (Fig. 2i,j – orange bars), indicating that αS oligomer binding is sufficient to inhibit αS self-association. A similar pattern is observed for rHSA (Fig. S3c,d – orange bars), consistent with the αS oligomer – HSA interactions being largely independent of fatty acid binding to the first two high affinity sites. However, when the gHSA concentration is increased by an additional order of magnitude, further inhibition of αS self-association is detected (Fig. 2i,j – red bars), possibly arising from gHSA - αS monomer binding, which is expected to be weaker (*vide infra*) [20]. These concentration-dependent contributions are somewhat greater in the case of rHSA (Fig. S3c, d – red bars). While these results consistently show that the archetypal extracellular protein, HSA, remodels and suppresses the formation of toxic αS oligomers, they do not provide insight into whether these αS species retain the capacity to associate with and insert into the membrane, a process known to underlie the neurotoxicity of several amyloidogenic proteins [34–38]. Hence, we evaluated whether HSA perturbs the interactions of αS with membranes.

4.4.5 HSA Perturbs interactions of αS with Membranes Through a Dual Mechanism.

To probe how albumin modulates αS - membrane interactions, we measured the leakage of the aqueous internal compartment of large unilamellar vesicles (LUVs) in the absence and presence of αS oligomers with and without rHSA or gHSA (Fig. 3a). Interestingly, in the absence of αS oligomers, both rHSA and gHSA reduce membrane permeabilization, pointing to direct interactions of albumin with lipid membranes. Similarly, the protective effect of both albumins is preserved in the presence of αS oligomers, significantly reducing αS oligomer-induced membrane permeabilization. We complemented these

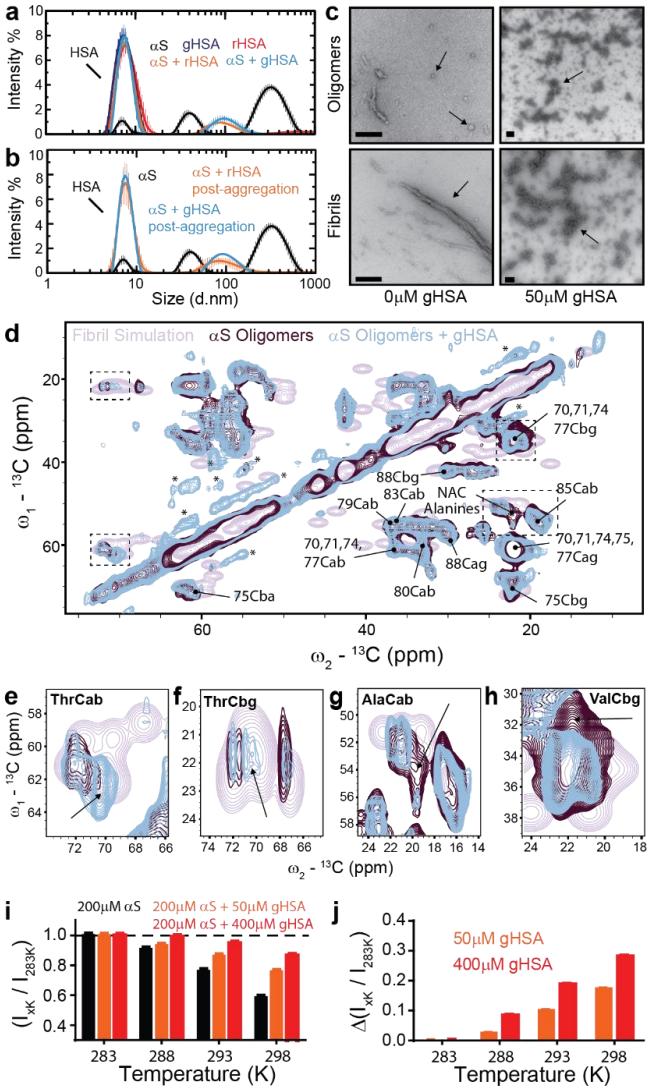

Figure 2. – *HSA remodels pre-existing αS oligomers, redirects aggregation pathways towards intermediate chimeric structures and inhibits the conversion of NMR visible αS species into NMR invisible αS oligomers.* (a) Dynamic light scattering (DLS) intensity measurements of αS oligomers prepared in the absence and presence of 50 μM rHSA and gHSA starting from an essentially monomeric state. Error bars are based on standard deviation of technical replicates. (b) As (a) except rHSA and gHSA were added to pre-aggregated aS oligomers. (c) Negative stain transmission electron microscopy images of the pre-formed αS aggregates without (*left*) and with (*right*) gHSA treatment shown in (b). All scale bars represent lengths of 100 nm. (d) ^{13}C – DARR spectrum of αS fibrils simulated using chemical shifts deposited in BMRB ID: 18207 (*light violet*) and αS oligomers in the absence (*dark purple*) and presence (*blue*) of sub-stoichiometric amounts of gHSA. Significant HSA-induced changes are indicated by black dashed squares. Spectral artefacts are indicated with asterisks (*). (e) – (h) Zoomed in regions of the spectra shown in (d). Black arrows indicate intensity changes observed upon HSA addition. (i) Average of three well-resolved αS H_b and other side chain proton intensities in the absence (*black*) and presence of 50 μM (*orange*) and 400 μM (*red*) gHSA at various temperatures, normalized to the intensities at 283 K. The H_b protons used for measurements are highlighted in Fig. S3b. (j) Differences in average αS intensities at each temperature between the gHSA bound *vs.* free state shown in (i).

membrane permeability results with Wide Angle X-ray Diffraction (WAXD) experiments, which probe the αS/HSA – membrane interactions from the perspective of the lipids (Fig. 3b-g). Stacks of membranes in the absence and presence of αS oligomers with and without rHSA or gHSA were subjected to WAXD measurements. Out of plane diffraction (q_z) is shown in Fig. 3b. The observed Bragg peaks are the result of multi-lamellar membranes stacking. A decrease in the number of peaks is indicative of a less well-ordered lamellar phase. Addition of r/gHSA preserves the number of observed Bragg peaks but reduces their intensities (Fig. 3b-d), once again pointing to the interaction of both defatted and non-defatted albumin with membranes.

Compared to albumin, a significantly greater loss of intensity and fewer Bragg peaks are observed upon addition of αS oligomers (Fig. 3b-d), suggesting a marked loss of membrane integrity. Interestingly, the effects of albumin and αS oligomers on the membrane are non-additive, with the presence of both species resulting in an effect intermediate to either protein alone (Fig. 3b-d). These results are consistent with the hypothesis that albumin alters the effect of αS oligomers on lipid membranes. In further support of these results is the effective lamellar spacing between membrane bilayers (Fig. 3e), which is enhanced in the presence of αS oligomers alone, consistent with αS being embedded or on the surface of the membranes, but reduced in the presence of r/gHSA (Fig. 3e). A similar effect is observed for the electron density profiles (Fig 3f-g), which are sensitive to the position of the molecules in the membrane. A shift towards the bilayer center is observed in the presence of αS oligomers, consistent with their partitioning in and interacting with the membrane (Fig. 3f-g). However, addition of both r/gHSA and αS oligomers results in an electron density profile more similar to the unperturbed membrane (Fig 3f-g), indicating a reduced interaction. Overall, Fig. 3 shows that both defatted and non-defatted HSA perturb the interactions of αS oligomers with membranes, either through directly interacting with the membrane and/or the αS oligomers themselves.

4.4.6 HSA inhibits the interactions of the αS N-terminal and NAC regions with Membranes.

To complement the WAXD and membrane permeability data and to gain residue-resolution information about the modulation of αS – membrane interactions by HSA, we acquired ^{15}N-Dark State Exchange Saturation Transfer (DEST) NMR experiments of ^{15}N-labeled αS prepared under four different conditions: αS alone or in the presence of unlabeled lipids, unlabeled gHSA or both lipids and gHSA (Fig. 4). The ^{15}N-DEST experiment probes the interaction of αS with HMW species, such as membranes, αS oligomers and their complexes, through the lens of NMR visible αS monomers [21,39–41]. As expected [32,34], addition of the lipids in the absence of albumin results in a major DEST reduction that is more pronounced for the N-terminal amphipathic and the NAC regions than the acidic C-terminus (Fig. 4f, black *vs.* blue traces).

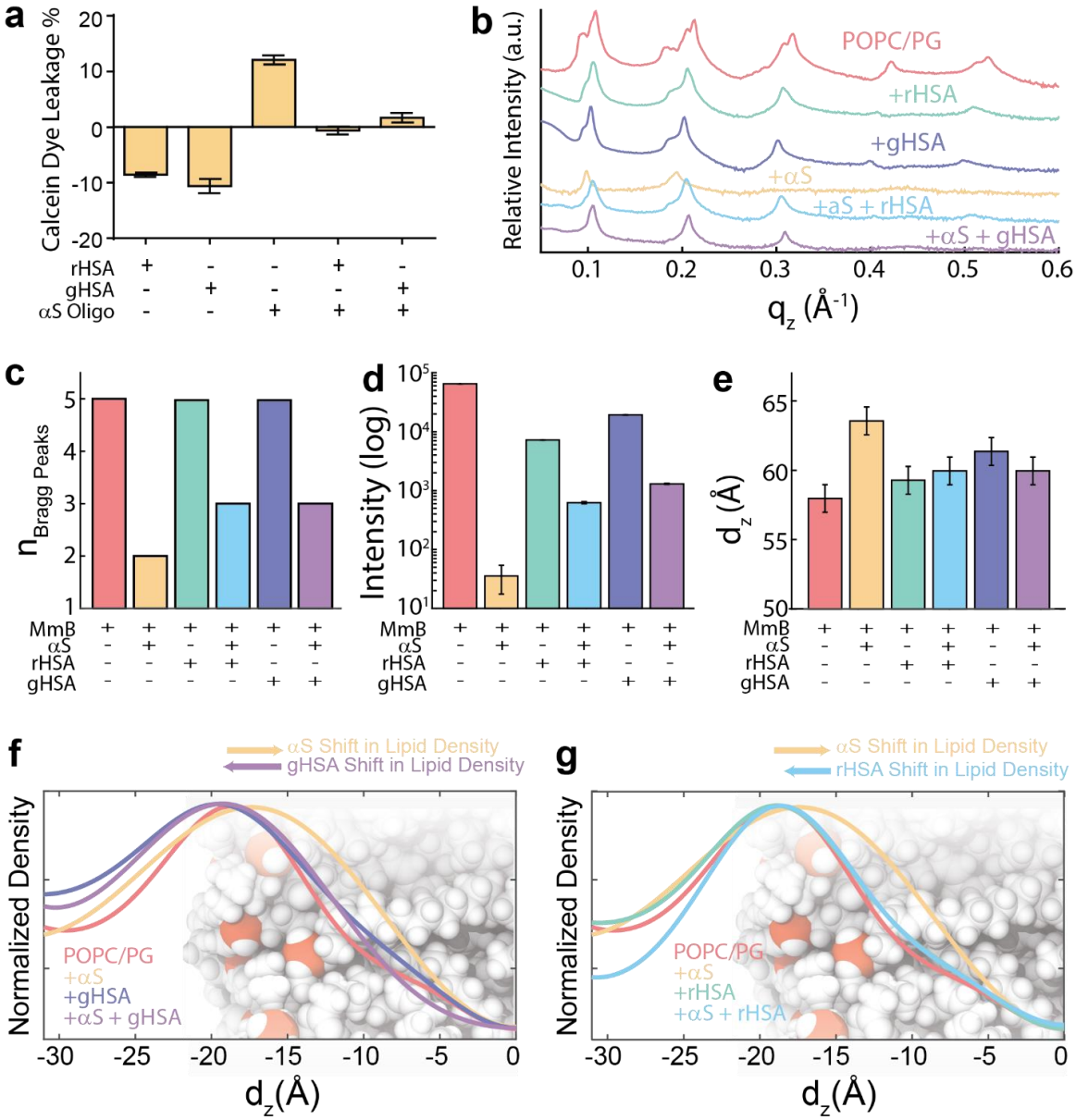

Figure 3. – *HSA perturbs αS – membrane interactions independent of the fatty-acid load.* (a) Normalized calcein dye leakage from LUVs composed of 5:3:2 DOPE:DOPS:DOPC lipids treated with αS oligomers in the absence and presence of rHSA and gHSA. Negative (positive) values indicate reduced (enhanced) leakage compared to buffer. (b) Absolute out-of-plane reflectivity of 1:1 POPC:POPG bilayers in the absence and presence of HSA, αS oligomers and HSA-remodeled αS oligomers. (c) Number of Bragg peaks for the samples shown in (b). (d) Peak intensity of the first Bragg peak for the samples shown in (b). (e) Calculated lamellar spacing (d_z) for the samples shown in (b). (f) Electron density maps for POPC:POPG bilayers in the absence and presence of gHSA, αS oligomers and αS oligomers in the presence of gHSA. Arrows indicate the shifts in the electron density maxima upon addition of αS oligomers (*yellow*) and gHSA (*violet*). (g) As (f), except with rHSA (*blue*) replacing gHSA.

Addition of gHSA in the absence of lipids also leads to a significant DEST reduction, but now the DEST losses are more uniform across the αS sequence (Fig. 4f, black *vs.* orange traces).

Interestingly, the DEST reduction observed upon addition of gHSA in the absence of lipids is not observed when gHSA is added in the presence of lipids (Fig. 4f, black – orange *vs.* blue – red; Fig. 4h green *vs.* pink), suggesting that the lipids interfere with the gHSA – αS interactions. Similarly, the marked DEST losses caused by the addition of lipids in the absence of gHSA (Fig. 4f, black *vs.* blue traces) are significantly reduced when lipids are added in the presence of gHSA (Fig. 4f, orange *vs.* red traces; Fig. 4g yellow *vs.* violet), revealing that gHSA weakens the lipid - αS interactions. These conclusions are independent of the DEST offsets utilized to monitor the binding of αS to lipids and gHSA (Fig. S5g) and are in agreement with changes in HSQC intensities (Fig. S6). Similar DEST variations are also observed when gHSA is replaced with rHSA (Fig S5a-f), corroborating that the inhibition of lipid - αS interactions by albumin is largely independent of fatty acids binding to the high-affinity sites of HSA.

Overall, our NMR data consistently point to albumin de-tuning the interactions of the αS N-terminal and NAC regions with lipids and vice versa (Fig. 4g,h), explaining how albumin counters the loss of membrane integrity caused by αS oligomers. However, in addition to the albumin – αS oligomer interactions, binding to αS monomers may further influence the formation and cytotoxicity of αS oligomers, as suggested by the further recovery of αS NMR signal in the presence of higher [HSA] in heating-induced aggregation assays (Fig. 2i,j and S3c,d, red *vs.* orange).

4.4.7 HSA Binds αS Monomers with mM – Sub mM Affinity Targeting Both the N- and C-termini of αS in a Fatty Acid Dependent Manner.

To measure the affinity of monomeric αS for both rHSA and gHSA, we titrated unlabeled rHSA and gHSA into ^{15}N-labeled αS monomers and monitored the titration through 1D-STD-HSQC NMR (Fig. S7a, b). The resulting binding isotherms are shown in Fig. 5a. Based on Hill-like fitting of the STD data (Fig. 5a), monomeric αS binds rHSA in the sub-mM range (K_D = 520 +/- 12 μM) and gHSA in the supra-mM range (K_D >> 1 mM), indicating that the affinity of monomeric αS for defatted albumin is comparable to the physiological concentration of albumin in plasma, but it is reduced when HSA binds fatty acids. These results are further confirmed through BLI (Fig. S8f, g). To map the binding sites for HSA within monomeric αS, we also acquired 2D-STD-HSQC spectra for ^{15}N-labeled αS monomers in the presence and absence of excess rHSA or gHSA (Fig. 5b; Fig. S7c-h). The 2D-STD-HSQC spectra show that rHSA targets not only the acidic C-terminal region of αS (residues > 110), but also select residues of the N-terminal amphipathic segment (Fig. 5b, grey highlights). The central NAC core and adjacent residues remain largely unaffected by saturation transfer from albumin. Interestingly, the interactions with the acidic C-terminus are almost

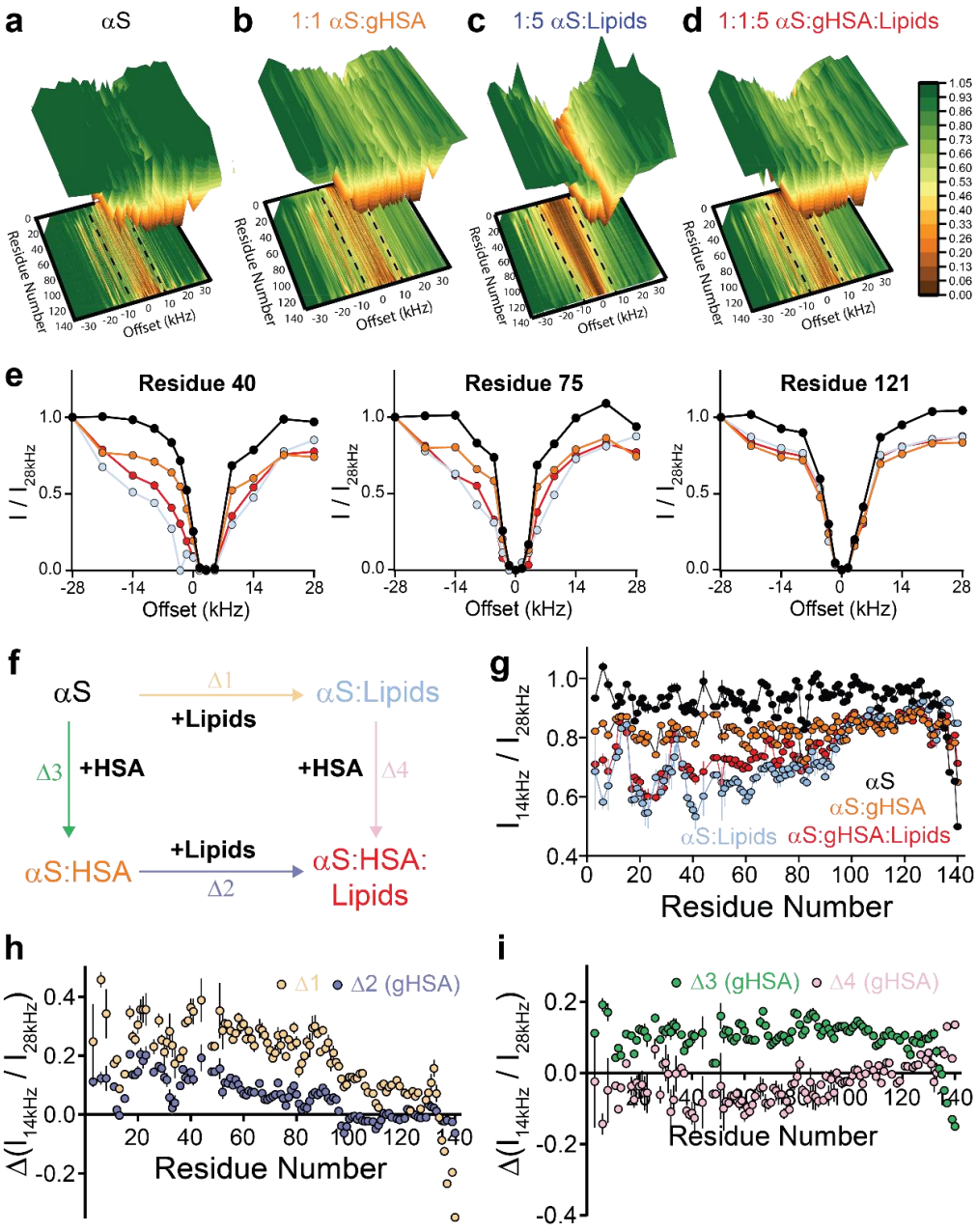

Figure. 4 – *Double-ligand DEST analyses reveal how HSA perturbs the αS NAC and N-terminal regions that interact with membranes.* (a)-(d) Normalized ^{15}N – DEST cross-peak intensities as a function of offset and residue number (see Experimental Section) measured for (a) 300μM αS, (b) 300 μM αS + 300 μM gHSA, (c) 300 μM αS + 1.5 mM DOPE:DOPS:DOPC and (d) 300μM αS + 300μM gHSA + 1.5 mM DOPE:DOPS:DOPC. (e) Double ligand cycle for the interaction of αS with HSA and lipids. Colour coding is preserved in the following panels. (f) Residue-specific ^{15}N – DEST profiles computed using off-resonance and far off-resonance saturation frequencies of 14 kHz and 28 kHz, respectively, from the ^{15}N – DEST profiles shown in (a)-(d). The DEST profile was smoothed by averaging the I_{14kHz}/I_{28kHz} values for each residue and the two residues directly adjacent to it, when available. (g)-(h) Differences between the residue-specific ^{15}N – DEST profiles shown in (f) according to the double ligand cycle shown in (e).

completely suppressed in going from the defatted rHSA to the non-defatted gHSA (Fig. 5b, red *vs.* black circles), while binding to the N-terminal amphipathic regions is more resilient to the replacement of rHSA with gHSA (Fig. 5b, red *vs.* black circles). These results are independent corroborated by the relative HSQC intensity profiles (Fig. S8), which indicate significant albumin-induced intensity losses at both C- and N-termini, with the C-terminal intensity reduction more pronounced than the N-terminal but also more dramatically suppressed by the fatty acids bound to gHSA (Fig. S8c).

Moreover, the interaction of the αS C-terminus with HSA is electrostatically driven, as addition of 150 mM NaCl completely recovers HSQC signal losses at the C-terminus but not the N-terminus (Fig. S8d-e). Overall, the HSQC intensity, BLI and STD-HSQC data consistently indicate that the interactions of monomeric αS with HSA are partially compromised in gHSA *vs.* rHSA, wherein binding of ~two fatty acid equivalents is sufficient to perturb the electrostatic interactions at the C-terminus.

4.4.8 αS Monomers Target Multiple Fatty Acid Dependent Sites Within HSA.

The fatty acid dependence of the αS monomer – albumin affinity suggests that monomeric αS competes with fatty acid binding at high-affinity sites. In order to test this hypothesis, we acquired methyl ^{1}H – ^{13}C HSQC spectra of ^{13}C-labeled oleic acid (OA) bound to albumin in the presence and absence of excess monomeric αS (Fig. 5c). This spectrum reveals that αS monomer binding displaces OA from the two highest-affinity sites (*i.e.* A and B, Fig. 5c,d), causing the displaced OA to relocate to other albumin loci and result in increased HSQC intensities (*i.e.* Fig. 5c-e). As a further means to probe the competition between αS monomers and fatty acids, we also acquired fluorescence spectra for the ANS and Dan F fluorophores. Interestingly, when αS monomers bind rHSA a loss of both ANS and Dan F fluorescence is observed (Fig. 5f), revealing that monomeric αS competes with binding of fatty acids at multiple albumin loci including not only high-affinity sites, but also the lower-affinity Sudlow sites I and II.

4.5 Discussion

We have investigated how the prototypical extracellular protein, HSA, interacts with αS monomers and oligomers and how these interactions modulate the association and insertion of αS into the membrane. Our results are summarized in Fig. 6 and provide a foundation to explain the mechanism by which HSA inhibits the cell-to-cell transmission of extracellular αS species. HSA binds αS oligomers with an affinity ~three orders of magnitude greater than monomers ($K_{D, app\ oligomer}$ < ~0.4 μM *vs.* $K_{D, monomer}$ ~500 μM; Fig. 1f, g, 5a, 6a, b). Whereas the binding of αS monomers to the C-terminus is electrostatically driven and fatty-acid dependent, the N-terminal binding is more resilient to the presence of salt and present in both rHSA and gHSA (Fig. 5a, 6a, S8d, e). These results suggest that the αS monomer N- and C-termini serve as two distinct HSA binding sites. However, it is also possible that transient interactions between the N- and C-

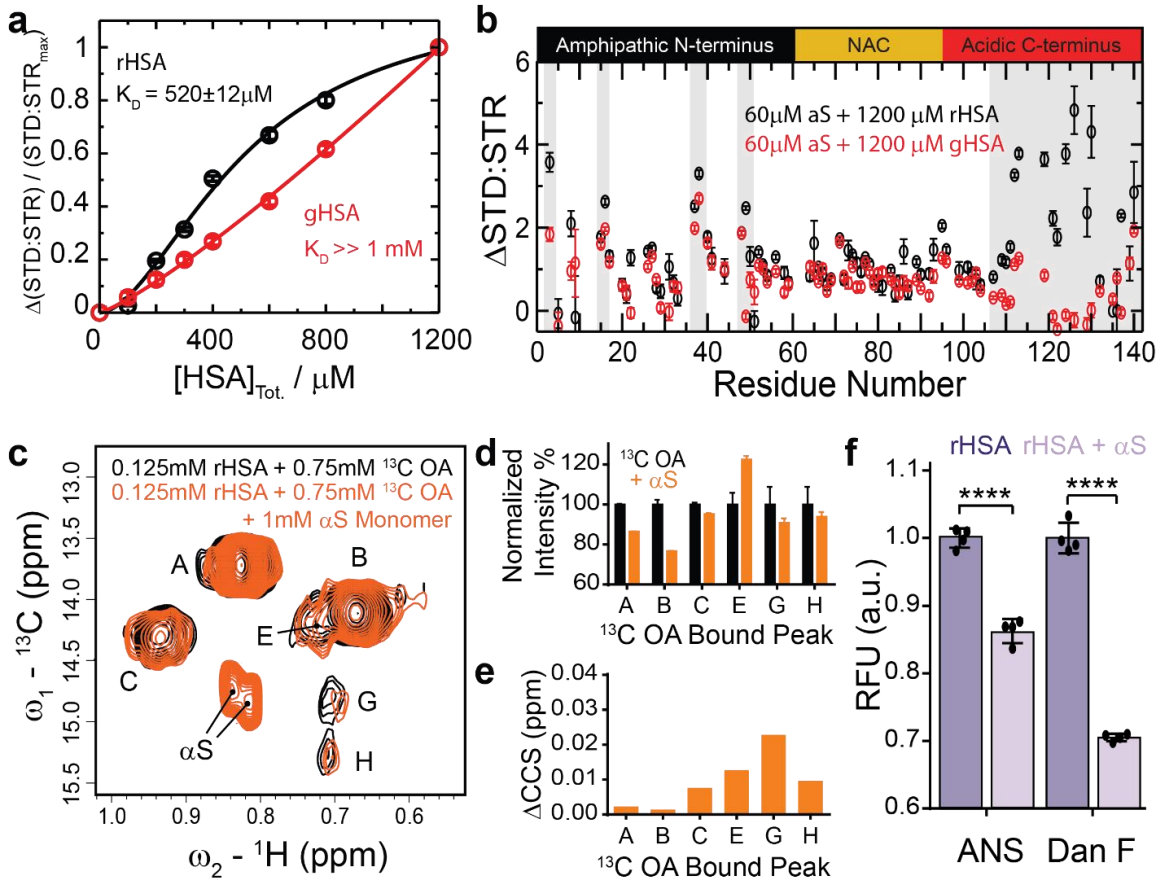

Figure. 5 – *HSA binds αS monomers at the N- and C-termini with sub mM – mM affinity in a fatty acid dependent manner.* (a) Normalized 1D Methyl STDHSQC-based binding isotherms for the interaction of αS monomers with defatted rHSA (*black*) and non-defatted gHSA (*red*). Experimental points were fit to a Hill-like (*solid line*) binding model to derive the K_D for rHSA and gHSA. (b) Residue-specific map of the interaction of αS monomers with rHSA (*black*) and gHSA (*red*) as probed by the 2D Methyl STDHSQC. Saturation transfer arising from αS monomers alone is accounted for in the data shown in both panels (a) and (b). (c) ^{1}H – ^{13}C HSQC spectral overlay of 1:6 rHSA:^{13}C Oleic Acid (OA) in the absence (*black*) and presence of 1 mM freshly-dissolved αS monomers (*orange*). (d) Intensity of ^{13}C OA bound peaks shown in (c) normalized to the state in the absence of αS monomers (*black* in panel c). (e) Combined chemical shift changes (ΔCCS) between the two states shown in (c). (f) Fluorescence intensities of ANS and Dan F bound to rHSA in the absence (*dark purple*) and presence (*light purple*) of 500μM αS monomers, normalized to the rHSA alone state. Fluorescence contributions arising from ANS and Dan F binding αS monomers is accounted for. Two-way ANOVA and subsequent Sidak's multiple comparison tests were used to determine the statistical significance for the rHSA *vs.* rHSA with αS monomer comparison in the ANS and Dan F competition experiments, with **** representing p-values <0.0001.

terminal regions of αS monomers[42] may be relevant for HSA binding. Unlike the fatty-acid dependent interaction with αS monomers, the defatted rHSA and the endogenous gHSA exhibit similar affinities for

the αS oligomers (Fig. 1f *vs.* g). Hence, the HSA - αS oligomer interactions are physiologically relevant not only in plasma, but also in CSF where HSA is diluted to ~3 μM[15].

The binding of HSA to αS oligomers is sufficient to suppress αS-associated toxicity (Fig. 1d-e). A viable explanation of the detoxifying effect of albumin is that HSA functions through three distinct but concurrent mechanisms (Fig. 6c, d, e). First, HSA remodels the distribution of LMW oligomers and HMW fibrils into intermediate MW chimeric assemblies (Fig. 2a-h, S3a, 6c) by binding to αS oligomers through interactions that are largely hydrophobically driven (Fig. 1h, i). These results are observed irrespective of whether HSA is added prior to or after aggregation (Figure 2a *vs.* b), suggesting that the HSA-induced remodeling of αS oligomers is primarily under thermodynamic, rather than kinetic control. Moreover, these results suggest that HSA may serve as a viable late-stage intervention strategy when toxic αS oligomers have already formed.

Second, the αS oligomer – HSA interactions also inhibit the conversion of NMR visible αS monomers into NMR invisible αS oligomers (Fig. 2i, j and S3c, d *orange vs. black*, Fig. 6d). This result is consistent with the reduced αS aggregation kinetics observed in ThT fluorescence experiments in the presence of HSA [23,25]. However, here we unambiguously show that the αS oligomer – HSA interactions are the primary driver of inhibition, whereas previously it was unclear whether such inhibition arose from monomer *vs.* oligomer binding. Moreover, here we show that such inhibitory effect is largely independent of the fatty-acid load of HSA (Fig. 2j *orange* vs. S3d *orange*), consistent with the similar αS oligomer affinities of rHSA and gHSA. These findings are also in agreement with HSA perturbing the catalytic cycle that generates toxic oligomers, which has been shown previously for another molecular chaperone, Brichos [43].

Third, HSA suppresses the association of αS oligomers with membranes, which has been implicated in the pathogenesis of PD [44]. The loss of membrane integrity caused by αS oligomers is remarkably reduced in the presence of either defatted and non-defatted HSA (Fig. 3), which substantially weakens the binding of the αS N-terminal and NAC regions with membranes (Fig. 4, Fig. 6e). Our findings are consistent with previous reports on clusterin and α_2-microglobulin, two other extracellular chaperones, which reduce the ability of αS oligomers to permeabilize lipid membranes[45]. However, unlike clusterin and α_2-microglobulin, which were shown to sequester αS oligomers from the membrane, here we show that the HSA interference may arise from HSA – αS and/or HSA – membrane interactions. The latter is ruled in based on the combination of our WAXD and membrane permeability experiments, which consistently reveal HSA-induced changes in lipid membrane structure (Fig. 3). Moreover, similar observations have been reported for HSA in the context of liposomal trafficking, wherein the direct interactions of HSA with liposomes interfere with the delivery of solutes into cell membranes [46,47]. Taken together, we show that the ameliorative effect of HSA is multi-faceted, operating not only at the level of remodeling the αS

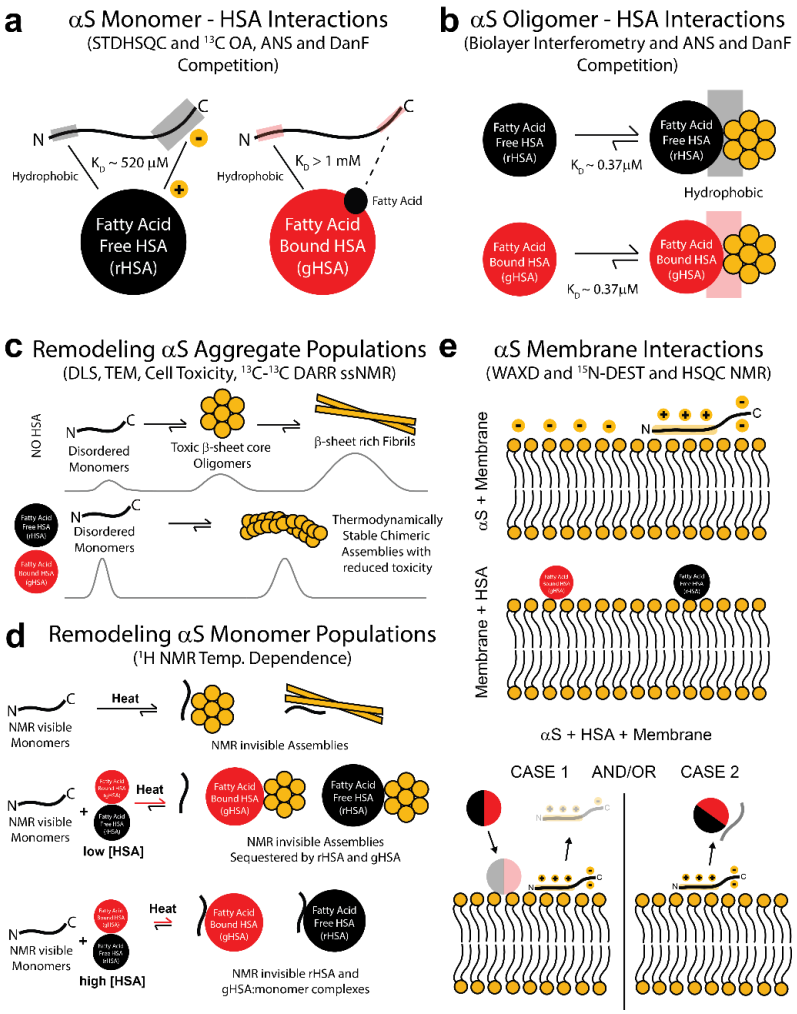

Figure. 6 – *Proposed mechanism for the inhibition of αS self-association and toxicity by human serum albumin.* (a) HSA binds αS monomers at the N- and C-termini through hydrophobic and electrostatic interactions, respectively. (b) HSA binds αS oligomers with an affinity several orders of magnitude greater than monomers. The binding is largely hydrophobically driven and is independent of the fatty acid load of HSA. (c) HSA binding of αS oligomers results in a shift in the morphology of toxic low MW β-sheet core oligomers and high MW β-sheet rich fibrils into less toxic intermediate MW, thermodynamically stable chimeric assemblies stabilized by HSA. (d) HSA perturbs the conversion of NMR visible αS monomers into NMR invisible αS oligomers. Addition of low [HSA], wherein HSA binding of αS monomers is negligible, shields the αS oligomers from monomers resulting in reduced incorporation of monomers into NMR invisible species. Such inhibition effect is largely independent of the fatty-acid load of HSA. Addition of high [HSA], wherein HSA binding of αS monomers is significant under our conditions, a further reduction in monomer conversion into NMR invisible species is observed relative to low [HSA]. The effect is dependent on the fatty acid load of HSA, as expected given the rHSA *vs.* gHSA differences in K_D values for αS monomer binding. (e) Both rHSA and gHSA perturb the interactions of the αS N-terminal and NAC regions with negatively charged membranes. The inhibition may arise from either the direct binding of HSA to the membrane, displacing the bound αS and/or binding of HSA to αS, competing out membrane interactions. This inhibitory effect is also independent of the fatty-acid content of HSA. αS in this panel denotes either monomeric and/or oligomeric species.

oligomer distribution, but also directly at the membrane.

Overall, our comparative analyses of the αS – HSA interactions at progressive degrees of resolution uncover an unprecedented mechanism by which a model extracellular chaperone inhibits the toxicity of PD-associated αS oligomers. On the same grounds, our results point to the notion that the extracellular proteostasis network may play a critical role in regulating the cell-to-cell transmission of αS. Our work thus underscores the importance of evaluating how these control mechanisms are dysregulated in diseased states. Unexpectedly, the data obtained here lend support to the idea that chaperones not only assist in the folding and assembly of a protein into non-toxic species but also prevent the interactions of toxic oligomers with membranes. The latter are known to promote the formation of toxic intermediates and enhance neuronal dysfunction [32]. Lastly, the results presented here illustrate the effectiveness of our integrated experimental strategy to comprehensively probe at multiple length-scales protein-protein interactions involving a heterogeneous and transient amyloidogenic system.

4.6 Experimental Section

Alpha Synuclein Expression and Purification

Alpha synuclein (αS) was expressed in *E. Coli BL21(DE3)* cells using the pT7-7 plasmid harboring the αS sequence, as described previously[48]. Briefly, the bacteria were grown at 37 °C in isotope-enriched M9 minimal media containing 1g/L of ^{15}N – ammonium chloride, 3g/L of ^{13}C – glucose and 100 µg/mL of ampicillin. At OD_{600} of ~ 0.6 – 0.8, αS was overexpressed with 100 µM of isopropyl β-D-1-thiogalactopyranoside (IPTG) at 37 °C for 4 h, and the cells were subsequently harvested by centrifugation at 9,800g. The cell pellets were resuspended in lysis buffer (10mM Tris-HCl pH 8, 1 mM EDTA and 1 mM AEBSF protease inhibitor) and lysed by three cycles of freeze thawing followed by sonication. The cell lysate was heated for 20 min at >100°C and centrifuged at 19,500g for 1 hour. Subsequently, streptomycin sulfate was added to the supernatant to a final concentration of 10 mg/mL. The mixture was stirred for 15 min at 4 °C followed by further centrifugation at 19,500g. Next, ammonium sulfate was added to the supernatant to a concentration of 360 mg/mL in order to precipitate the protein. The solution was stirred for 30 min at 4 °C and centrifuged again at 19,500g. The resulting pellet was resuspended in 25 mM Tris-HCl, pH 7.7 and loaded onto an anion exchange column (HiTrap Q Sepharose high performance, GE Healthcare) and eluted with a 0-600 mM NaCl step gradient. The eluted fraction (~300 mM NaCl) containing purified αS was dialyzed into ddH_2O, filtered through a 50 kDa Amicon filter and lyophilized to obtain essentially monomeric αS.

The N-terminal α-amino acids of αS was biotinylated by dissolving 5 mg of αS in 50 mM Phosphate Buffer pH 6.5 and subsequently mixing with a 5-fold molar excess of freshly dissolved 10mM NHS-LC-biotin (Thermofisher) in DMSO. The reaction mixture was incubated at 4 °C for 24 hours and subsequently injected into a HiLoad 16/600 Superdex 200pg Size Exclusion Chromatography column. The biotinylated αS was separated from the free NHS biotin. Buffer exchange was achieved in the SEC column by using PBS pH 7.4 as the running buffer. The biotinylated αS in PBS pH 7.4 was then concentrated and aggregated for BLI analysis (as discussed in the BLI section below).

Alpha Synuclein Monomer and Oligomer Preparation

Monomeric αS was prepared by resuspending the lyophilized powder in PBS pH 7.4, 100% H_2O or 50mM HEPES pH 7.4, 10% D_2O for non-NMR or NMR experiments, respectively. The samples were immediately analyzed to reduce sample drift. The final αS concentrations varied depending on the experiment and is detailed below in the specific experimental sections. Oligomeric αS for DLS and TEM were prepared by dissolving lyophilized αS powder in PBS pH 7.4, 100% H_2O to a final concentration of 100μM, followed by incubation at 37°C for 48h. αS oligomers for cell toxicity, membrane permeability and wide-angle x-ray diffraction (WAXD) experiments was prepared by dissolving lyophilized αS powder in PBS pH 7.4, 100% H_2O to a final concentration of 800μM, followed by incubation at 37°C for 24h. For ANS and DanF fluorescence competition experiments, oligomers were prepared using the two protocols above as well as by incubating 800μM αS in PBS pH 7.4, 100% H_2O at 37°C for 10 days to create a HMW aggregate sample. For solid state NMR experiments, αS oligomers were prepared by dissolving ~20 mg of lyophilized αS powder into PBS pH 7.4 to a final concentration of 12 mg/mL. The solution was incubated for 48 h at 37 °C, filtered extensively through a 30 kDa Amicon filter to remove monomers and subsequently split into two equal aliquots. To one solution gHSA was added to a molar ratio of 10:1 (αS:gHSA) and to the other an equivalent volume of PBS. The mixtures were incubated for a further 2 hours at 37 °C to allow gHSA remodeling of αS oligomers, subsequently loaded into a 3.2 mm rotor and flash frozen using liquid nitrogen. A 200 μL aliquot of each sample was loaded onto a Superdex 200 Increase 10/300 GL SEC Column for characterization of their relative size distributions (Fig. S4a). The concentration of αS (monomer equivalent) was determined by A_{275} measurements using an extinction coefficient of 5,600 $M^{-1} \cdot cm^{-1}$ [32].

Human Serum Albumin (HSA) Stock Preparation

Fatty acid and globulin free human serum albumin (rHSA; Sigma Aldrich A3782) and globulin free human serum albumin (gHSA; Sigma Aldrich A8763) were purchased from Sigma Aldrich as lyophilized powders. The lyophilized powders were resuspended in PBS pH 7.4 or 50 mM HEPES pH 7.4 to match alpha synuclein conditions. The concentration of HSA was determined through A_{280} measurements.

Cellular Viability Probed through Presto Blue Assay

SHSY5Y cells in 1:1 Dulbecco's modified eagle medium (DMEM): F12 medium supplemented with 10% fetal bovine serum (FBS) and RPE-1 cells in 1:1 DMEM: F12 medium, 10% FBS and 0.01 mg/mL hygromycin were seeded onto a 96 well plate (10 000 cells in 180 μL) and incubated for 24 h at 37°C, 5% CO_2. The media was then aspirated, and cells were treated with pre-formed αS oligomers (5 μM final concentration), mock (PBS delivery solution) and αS oligomers in the presence of rHSA/gHSA (10 μM final concentration) dissolved in fresh media. The cells were then incubated for 48 hours at 37°C and 5% CO_2. The media was aspirated, replaced with fresh media containing the presto blue reagent (resazurin) and the plate was incubated for a further two hours at 37°C, 5% CO_2. Fluorescence measurements were acquired using excitation and emission wavelengths of 560 and 590 nm, respectively, using a Biotek Cytation 5 plate reader. The error on these measurements was estimated through the standard error of five and seven technical replicates for RPE1 and SHSY5Y cells, respectively.

Biolayer Interferometry (BLI) for the Assessment of HSA Binding Affinities to αS Monomers and Oligomers

The binding affinities of αS monomers and oligomers for rHSA and gHSA were assessed by biolayer interferometry measurements (Octet Red 96, ForteBio). Biotinylation of αS significantly perturbs αS

aggregation[49], and hence prolonged incubation at 37°C was used to form αS oligomers. Specifically, 800 μM biotinylated αS monomers in PBS pH 7.4 was incubated at 37°C for 1 month to form oligomers. In contrast, freshly prepared biotinylated αS was used for monomer binding experiments. The αS monomers and oligomers were immobilized on Streptavidin (SA) biosensors (ForteBio) by dipping the sensor into a solution of 100 μM biotinylated αS (monomers or oligomers) for 300 s. Excess non-immobilized αS was washed off by dipping the sensor into PBS pH 7.4 for 120 s. The SA biosensor was subsequently dipped into solutions of rHSA or gHSA in PBS pH 7.4 at varying concentrations ranging from 0.25μM – 600μM for αS monomers and 0.25μM – 10μM for αS oligomers for 900 s to allow for association. Dissociation was subsequently monitored by dipping the biosensor in PBS pH 7.4 for 900 s. The association and dissociation curves were fit against a heterogenous ligand binding model, assuming multiple independent ligand binding sites, as found in the Octet analysis program provided by ForteBio to derive the effective K_{Dapp} values of the complexes formed by the αS (monomer and oligomers) with rHSA and gHSA.

^{13}C Oleic Acid (OA) Competition

^{13}C-methyl labeled oleic acid (OA) was purchased from Cambridge Isotope Laboratories as lyophilized powder and resuspended in 100% DMSO-d_6 to a final concentration of 100 mM. The 100 mM ^{13}C OA stock was incubated at 50 °C for 5 minutes prior to co-incubation with rHSA. Similarly, the rHSA was pre-incubated for 30 minutes at 37°C. Following this pre-incubation period, the ^{13}C OA and rHSA solutions were mixed to a final concentration of 250 μM rHSA and 1.5 mM ^{13}C OA and further incubated for 2 hours at 37 °C. To probe the competition of ANS and DanF with ^{13}C OA, the two fluorophores were added from their DMSO-d_6 stocks to two separate ^{13}C OA-rHSA mixtures to a final concentration of 500 μM prior to the 2-hour incubation period at 37 °C. At the end of the 2-hour incubation period, ^{1}H-^{13}C HSQC NMR spectra were acquired for the three samples, *i.e.* rHSA:^{13}C-OA, rHSA:^{13}C-OA:ANS and rHSA:^{13}C-OA:DanF, to assess the degree and sites of competition (further details in the NMR section below).

To probe the competition of αS monomers with ^{13}C – OA, a similar protocol to the ANS and DanF fluorescence was used with a few exceptions, which are detailed below. Given that the affinity of αS monomers is significantly weaker compared to ANS and DanF, a reduced concentration of rHSA and ^{13}C OA was used, while keeping the molar ratio of rHSA:^{13}C OA constant at 1:6, *i.e.* 125 μM rHSA and 750 μM ^{13}C OA. The alpha synuclein monomer was then added as lyophilized powder to the rHSA:^{13}C OA sample to a final concentration of 1 mM and incubated further for 2 hours at 37°C prior to NMR data acquisition. Importantly, a ^{1}H-^{13}C HSQC was acquired for the rHSA:^{13}C OA sample prior to αS monomer addition to serve as the reference spectrum for the competition.

^{13}C-Oleic Acid for the NMR-Based Assessment of Albumin-Bound LCFA Concentration (CONFA)

Similar to above, the 100 mM ^{13}C OA stock was incubated at 50 °C for 5 minutes prior to co-incubation with gHSA. Similarly, the gHSA was pre-incubated for 30 minutes at 37°C. Following this pre-incubation period, the ^{13}C OA and gHSA samples were mixed to a final concentration of 500 μM gHSA and 500 μM ^{13}C OA and further incubated for 2 hours at 37°C. The $[^{12}\text{C-FA}]_{\text{Tot.}}/[\text{gHSA}]_{\text{Tot.}}$ ratio (*r*) was determined according to equation 1:

$$r = (\alpha - \Delta\nu_{AB})/\beta \qquad (1)$$

where α =71.287 ± 0.235 and β = 1.8697 ± 0.1057 and $\Delta\nu_{AB}$ is the ^{13}C-chemical shift difference in Hz between ^{13}C-OA HSA-bound peaks A and B scaled to 700 MHz (*i.e.* $\Delta\nu_{AB,700MHz} = \Delta\nu_{AB,850MHz} * 700/850$). Further details of the CONFA method have been described previously[30].

1-Anilino-8-Napthalene Sulfonate (ANS) and Dansyl Phenylalanine (DanF) Fluorescence Competition

ANS and DanF were diluted from their DMSO stock solutions into 50 µM rHSA in PBS pH 7.4 to a final concentration of 50 µM. These concentrations are greater than the K_D of each fluorophore for rHSA and hence a significant fraction is expected to be bound[29]. The final concentrations of DMSO in the samples were less than 0.1% and had no appreciable effect on the measurements (data not shown). Fluorescence measurements were taken using a Biotek Cytation 5 plate-reader using excitation and emission wavelengths of 400, 465 and 370, 480 nm for ANS and DanF, respectively. Fluorescence competition was assessed by the relative reduction in fluorescence intensity upon addition of either freshly dissolved αS monomer or pre-formed αS oligomers. The final concentration of αS monomers was 500 µM and the concentration of αS oligomers (monomer equivalent) was 50 µM for Type I (100 µM αS, 48h at 37°C) and 200 µM for Type II (800µM αS, 24 h at 37°C). The final concentration of aggregated αS (800 µM αS, 240 h at 37°C) was 200 µM. Fluorescence reduction arising from the direct binding of ANS or DanF to αS monomers or oligomers is accounted for by subtracting the fluorescence intensity in concentration-matched αS monomer or oligomer samples in the presence of ANS or DanF.

Dynamic Light Scattering (DLS)

he samples used for DLS were prepared using two protocols. First, lyophilized αS powder was resuspended in buffer or in the presence of 50 µM rHSA or gHSA to a final concentration of 100 µM. The resulting mixtures were then incubated for 48 h at 37 °C to initiate oligomer formation. In the second protocol, the 100 µM αS was pre-incubated for 48 h at 37 °C to form the oligomers. rHSA, gHSA or equivalent volume of buffer to account for dilution by HSA were then added to three aliquots of this pre-incubated oligomer sample and allowed to further incubate for 24 h at 4 °C. The αS alone, αS:rHSA and αS:gHSA samples prepared from the two protocols were then subjected to DLS measurements. DLS was performed using a Zetasizer Nano ZS Instrument (Malvern Instruments, Malvern UK). Autocorrelation functions were accumulated for two minutes at 10 °C with an angle θ of 173° and a 4 mW He-Ne laser operating at a wavelength of 633 nm. All measurements were performed using a 40 µL (ZEN0040) plastic cuvette. The particle diameter detection limit was 0.6 – 6 µm. The viscosity value for water was used in the analysis of all measurements. All the samples were centrifuged for 10 min at 13,000 rpm prior to DLS measurements.

Negative Stain Transmission Electron Microscopy (TEM)

he samples used for TEM matched those used for the post-aggregation DLS protocol above. The DLS reaction mixtures were diluted 100-folds with ddH_2O. Copper EM grids (400-mesh), which had been freshly coated with a continuous layer of amorphous carbon, were glow discharged with 5 mA current for 15 seconds and shortly afterward the grids were floated on 3 µL drops of the diluted assembly reaction mixtures for two 2 min. Excess of sample was blotted with filter paper and the grids were stained with 1 % uranyl acetate for 30 seconds. Grids were loaded in a room temperature holder and introduced into a JEOL 1200-EX electron microscope operated at 80 kV. All images were acquired with an AMT XR-41 Side-Mount Cooled 4 megapixel format CCD camera.

Preparation of DOPE:DOPS:DOPC Lipid Films

SUVs were prepared as described before[39]. Briefly, 1,2-dioleoyl-sn-glycero-3-phosphoethanolamine (DOPE), 1,2-dioleoyl-sn-glycero-3-phospho-L-serine (DOPS), and 1,2-dioleoyl-sn-glycero-3-phosphocholine (DOPC) were purchased from Avanti Polar Lipids. The lipids were stored at -20 °C, under Argon. Solutions in chloroform were prepared from the lipids and were mixed to result in a 5:3:2 lipid

molar ratio. The solvent was then evaporated under a stream of nitrogen gas and the sample was dried thoroughly under vacuum to yield a thin lipid film on the wall of a glass test tube.

Preparation of DOPE:DOPS:DOPC Small Unilamellar Vesicles (SUVs)

The thin film was rehydrated with 50 mM HEPES, 1.5 mM Tris pH 6.8 and 10% D_2O at a concentration of 15 mg/mL and subjected to vortex mixing at room temperature to form multilamellar vesicles (MLVs). The MLVs were subsequently sonicated in a Cole-Palmer bath type ultrasonic cleaner until a clear solution was obtained indicating the formation of SUVs. The concentration of total phospholipids was confirmed by measuring the amount of inorganic phosphate released after digestion[50].

Membrane Permeabilization Measurements

Lipid films were suspended in a calcein solution (50 mM calcein, 20 mM HEPES, pH 7.4) by vigorous vortexing to yield MLVs. In order to form large unilamellar vesicles (LUVs), the MLVs were then extruded by 11 passages through two stacked polycarbonate membranes (100 nm pore size; Nucleopore Filtration Products, Pleasanton, CA) in a barrel extruder (Lipex Biomembranes, Vancouver, BC). External calcein was removed in a CL-2B Sepharose column by elution with 20 mM HEPES, pH 7.4 and 370 mM NaCl, which had the osmolarity matching the calcein solution as measured by a cryo-osmometer (Advanced Model 3 Plus Micro-Osmometer, Advanced Instruments Inc., Norwood, MA). The calcein-loaded LUVs were collected in the column void volume, had their concentration determined as above and were kept at 4 °C until use. Alpha synuclein oligomer-induced calcein dye leakage was measured in a Biotek Cytation 5 plate-reader at 37°C using Calcein fluorescence excitation and emission wavelengths of 490 and 525 nm, respectively. Lipid concentration of calcein-containing LUVs was kept constant at 20 μM. Mock (PBS pH 7.4) and 1% (v/v) Triton X-100 were used as negative and positive controls, respectively. The liposomes were treated with 40 μM rHSA, 40 μM gHSA, αS oligomers (20 μM final concentration) and αS oligomers in the presence of rHSA/gHSA (20 μM αS oligomers and 40 μM HSA final concentration).

Liposome permeabilization was quantified using equation 2:

$$Permeabilization\ (\%) = \frac{(F_x - F_B)}{(F_T - F_B)}\ x\ 100 \qquad (2)$$

where F_x, F_B, and F_T are, respectively, the fluorescence intensity after addition of treatment, buffer negative control, and triton X-100 positive control.

Wide-Angle X-ray Diffraction (WAXD)

Solutions of 800 μM αS were aggregated in PBS buffer pH 7.4 in the absence or presence of 1600 μM rHSA or gHSA over 48 hours. Membranes were prepared with 1-palmitoyl-2-oleoyl-sn-glycero-3-phosphocholine (POPC) and 1-palmitoyl-2-oleoyl-sn-glycero-3-phospho-(-(1'-rac-glycerol) (POPG) at a 1:1 molar ratio, ensuring a net negative membrane charge while retaining a fluid structure. The αS and αS:HSA solutions were then mixed with the membranes to ensure a protein:lipid ratio of 1:50.

Polished silicon wafers (1 × 1 cm^2) were incubated in piranha solution, H_2SO_4/H_2O_2 (7/3, vol/vol %), to prepare a hydrophilic silicon surface. The solutions were then deposited on the wafers and annealed at 37 °C for 2 hours in an orbital shaker to ensure full coverage of the wafers and formation of highly-oriented membranes on the surface. The samples were then hydrated at 97% RH in a humidity chamber for 48 hours prior to acquisition of the X-ray diffraction data at temperatures of 30 °C.

Out-of-plane X-ray scattering data was obtained using BLADE at McMaster University. BLADE uses a 9kW (45 kV, 200 mA) CuKα rotating anode at a wavelength of 1.5418Å. Both source and detector are mounted on moveable arms such that the membranes stay horizontal during measurements. Focusing, multi-layer optics provide a high intensity collimated, 200 µm sized beam with monochromatic X-ray intensities up to 108 counts/s. Scattering was detected using a Rigaku HyPix-3000 2D semiconductor detector with an area of 3,000 mm^2 and 100 µm pixel size[51].

Electron density profiles were determined from specular reflectivity. The relative electron density was calculated as previously described[52]. The membrane electron densities were then normalized to the peak phosphate density, while holding the density of the bilayer center fixed, as previously described[53].

Size Exclusion Chromatography coupled with Multi-Angle Light Scattering (SEC-MALS)

SEC-MALS measurements were conducted on a Wyatt miniDAWN MALS detector coupled to a Wyatt Optilab rEX online refractive index detector. αS samples (100 µL injection volume), prepared as described above, were resolved using a Superdex 200 increase 10/300 analytical gel filtration column (GE Healthcare) running at 0.5 ml/min in PBS buffer before passing through the light scattering and refractive index detectors in a standard SEC-MALS format.

Protein concentration was determined from the excess differential refractive index (RI) based on 0.185×10^{-3} RI increment for protein solution. The concentration and the observed scattered intensity at each point in the chromatograms were used to calculate the absolute molecular mass from the intercept of the Debye plot using Zimm's model as implemented in Wyatt's ASTRA software.

^{13}C – ^{13}C Dipolar Assisted Rotational Resonance (DARR) Solid State NMR

Solid-state NMR experiments were performed on a 700 MHz Varian spectrometer equipped with a low-*E* Black Fox 3.2mm HXY MAS probe. Two-dimensional DARR and NCA spectra were acquired simultaneously using a DUMAS experiment[54] at -18°C under 12.5 kHz MAS rate. The 2D spectra were acquired with 15 ms acquisition time, and 3 s recycle delay using 440 to 2048 scans per each t1 increment. The t1 or indirect spectral width for ^{13}C and ^{15}N were set to 33.33 and 3.33 kHz, respectively. In the DUMAS experiment, during the SIM-CP (simultaneous cross polarization) preparation period, ^{13}C and ^{15}N RF amplitudes were set to 35 kHz, whereas 60 kHz ^{1}H RF was applied with 90 to 100% linear ramp. The spectra were processed in NMRpipe and analyzed using Sparky. Spectral resolution of DARR spectrum was improved by using TIDE (T2*Weighted Deconvolution) covariance processing with customized MATLAB scripts[55], and the spectra are shown in Fig. S4b-g. NCA spectra were not reported due to poor resolution. Spectra were externally referenced to the most downfield CH resonance (29.46 ppm) of adamantane at 25°C[56]. The fibril DARR spectrum was simulated from chemical shifts deposited in BMRB (ID: 18207) using an in-house python tool, sim-sparky, freely available at https://github.com/weberdak/sim-sparky. The spectrum was simulated using artificial linewidths of 200Hz and 1k points in the direct and indirect dimension.

General Solution NMR Spectroscopy

All solution NMR spectra were recorded using either a Bruker AV 700 spectrometer equipped with a TCI cryo-probe or a Bruker 850 HD spectrometer equipped with a TXI room temperature probe. All spectra were analyzed with TopSpin 3.2.1, NMRpipe and Sparky using Gaussian line-fitting. Additional details are discussed below.

^{1}H NMR to Probe Alpha Synuclein Self-association

αS was freshly dissolved in 50mM HEPES pH 7.4, 10% D_2O to a final concentration of 200μM in the absence and presence of 50 or 400μM rHSA and gHSA. The samples were then subjected to a temperature gradient ranging from 10 °C to 30 °C at 5 °C intervals with a 30-hour incubation at each temperature. ^{1}H NMR spectra were acquired both at the beginning and end of the 30 hours incubation period. ^{1}H NMR spectra were recorded with 128 scans, 64K points and a spectral width of 20.00 ppm. A 30 ms spinlock was introduced to minimize contributions arising from HSA. The normalized average intensities of three protons in the H_b region (shown in Fig. S3b) were used to evaluate the monomer population at each temperature relative to the starting temperature of 10°C. We selected the NMR signals arising from H_b protons, because for the NH protons the intensity losses at increasing temperatures are amplified by the exchange with water, while for the methyls the intensity losses upon heating are minimized by increased dynamics (Fig. S3b).

^{1}H-^{13}C HSQC to Probe Competition with ^{13}C – OA Binding Sites in HSA

The samples for the ^{13}C – OA competition experiments, prepared as described above, were monitored by ^{1}H-^{13}C HSQC NMR. Two-dimensional NMR spectra were recorded with a recycle delay of 1.4s, 32 scans, 2K (t_2) and 200 (t_1) complex points for spectral widths of 13.9 ppm (^{1}H) and 31.8 ppm (^{13}C), respectively. NMR experiments were acquired at 298K. Chemical shift and intensity changes were measured through Gaussian fitting of the peaks in Sparky.

^{1}H-^{15}N HSQC to Probe HSA and Membrane Binding Sites in Alpha Synuclein

HSA and membrane binding to αS was probed by losses in ^{1}H – ^{15}N HSQC intensities upon addition of HSA or membrane relative to a sample of αS alone. ^{1}H – ^{15}N HSQC experiments were recorded at 283K with a recycle delay of 1.0s, 16 scans, 2K (t_2) and 300 (t_1) complex points for spectral widths of 14.05ppm (^{1}H) and 31.82ppm (^{15}N), respectively.

Methyl STDHSQC to Probe the HSA Binding Sites in Alpha Synuclein Monomers and the Binding Affinity of HSA – Alpha Synuclein Monomer Interactions

Methyl STDHSQC (MeSTDHSQC) spectra were acquired for alpha synuclein monomers with and without rHSA or gHSA. Briefly, saturation was introduced through methyl irradiation (MeSTD, 50 ms Gaussian pulses at a carrier frequency of 417 Hz at 700 MHz) and recorded with a sensitivity enhanced ^{15}N,^{1}H-(HSQC) read out block. Hence, the MeSTDHSQC pulse sequence probes the saturation transferred to the amides of ^{15}N-labeled NMR visible solutes (*i.e.* αS monomers). The spectra were recorded with 64 scans, 2K (t_2) and 200 (t_1) complex points for spectral widths of 14.1 ppm (^{1}H) and 31.8 ppm (^{15}N), respectively. Reference (STRHSQC) spectra with far off-resonance saturation (21,000 Hz at 700 MHz) were also recorded but with only 16 scans. The residue-specific STD *vs.* STR ratios were then computed to map the HSA binding sites in αS monomers. Residual contributions arising from the direct saturation of the αS monomers was accounted for by subtracting from the αS:HSA MeSTDHSQC : STRHSQC intensity ratios the corresponding MeSTDHSQC : STRHSQC intensity ratios for a sample containing αS alone.

^{15}N – DEST to Probe the Interaction of αS with Membranes, HSA and Their Complexes

The ^{15}N-DEST experiment was implemented as described previously[39]. Briefly, a 900 ms ^{15}N continuous wave (CW) saturation pulse was applied at 16 different radiofrequency offsets (no saturation, -28, -21, -14, -9, -5, -3, -1.5, 0, 1.5, 3, 5, 9, 14, 21 and 28 KHz) with a field strength of 170 Hz. The experiment was recorded in interleaved mode with 16 scans, 128 dummy scans, a recycle delay of 1.20 s, 200 (t1) and 2K (t2) complex

points and spectral widths of 14.28 ppm (^{1}H) and 31.82 ppm (^{15}N). All spectral processing was implemented in TopSpin 3.2.1. and transferred to Sparky for peak intensity measurements. The Gaussian line fitting function in Sparky was used to determine the fitted peak heights and the signal-to-noise ratio was used as a measure of error for the fitted peak heights. The residue-specific ^{15}N – DEST ratio was calculated as $(I_{-v} + I_{+v})/(I_{-28kHz} + I_{+28kHz})$ where I_v denotes the peak height measured for a given residue at the ^{15}N CW offset of v kHz.

4.7 References

(1) Spillantini, M. G.; Schmidt, M. L.; Lee, V. M.-Y.; Trojanowski, J. Q.; Jakes, R.; Goedert, M. α-Synuclein in Lewy bodies. *Nature* **1997**, *388*, 839–840.

(2) Zhang, G.; Xia, Y.; Wan, F.; Ma, K.; Guo, X.; Kou, L.; Yin, S.; Han, C.; Liu, L.; Huang, J.; Xiong, N.; Wang, T. New Perspectives on Roles of Alpha-Synuclein in Parkinson's Disease. *Frontiers in Aging Neuroscience* **2018**, *10*, 370.

(3) Conway, K. A.; Lee, S. J.; Rochet, J. C.; Ding, T. T.; Williamson, R. E.; Lansbury, P. T. Acceleration of oligomerization, not fibrillization, is a shared property of both alpha-synuclein mutations linked to early-onset Parkinson's disease: implications for pathogenesis and therapy. *Proceedings of the National Academy of Sciences of the United States of America* **2000**, *97*, 571–576.

(4) Lee, H.-J.; Bae, E.-J.; Lee, S.-J. Extracellular α--synuclein-a novel and crucial factor in Lewy body diseases. *Nature Reviews. Neurology* **2014**, *10*, 92–98.

(5) Ma, J.; Gao, J.; Wang, J.; Xie, A. Prion-Like Mechanisms in Parkinson's Disease. *Frontiers in Neuroscience* **2019**, *13*, 552.

(6) Braak, H.; Tredici, K. D.; Rüb, U.; Vos, R. A.I. de; Jansen Steur, E. N.H.; Braak, E. Staging of brain pathology related to sporadic Parkinson's disease. *Neurobiology of Aging* **2003**, *24*, 197–211.

(7) El-Agnaf, O. M. A.; Salem, S. A.; Paleologou, K. E.; Curran, M. D.; Gibson, M. J.; Court, J. A.; Schlossmacher, M. G.; Allsop, D. Detection of oligomeric forms of alpha-synuclein protein in human plasma as a potential biomarker for Parkinson's disease. *FASEB Journal : Official Publication of the Federation of American Societies for Experimental Biology* **2006**, *20*, 419–425.

(8) Borghi, R.; Marchese, R.; Negro, A.; Marinelli, L.; Forloni, G.; Zaccheo, D.; Abbruzzese, G.; Tabaton, M. Full length α-synuclein is present in cerebrospinal fluid from Parkinson's disease and normal subjects. *Neuroscience Letters* **2000**, *287*, 65–67.

(9) Kordower, J. H.; Chu, Y.; Hauser, R. A.; Olanow, C. W.; Freeman, T. B. Transplanted dopaminergic neurons develop PD pathologic changes: a second case report. *Movement Disorders : Official Journal of the Movement Disorder Society* **2008**, *23*, 2303–2306.

(10) Li, J.-Y.; Englund, E.; Holton, J. L.; Soulet, D.; Hagell, P.; Lees, A. J.; Lashley, T.; Quinn, N. P.; Rehncrona, S.; Björklund, A.; Widner, H.; Revesz, T.; Lindvall, O.; Brundin, P. Lewy bodies in grafted neurons in subjects with Parkinson's disease suggest host-to-graft disease propagation. *Nature Medicine* **2008**, *14*, 501–503.

(11) Hansen, C.; Angot, E.; Bergström, A.-L.; Steiner, J. A.; Pieri, L.; Paul, G.; Outeiro, T. F.; Melki, R.; Kallunki, P.; Fog, K.; Li, J.; Brundin, P. α-Synuclein propagates from mouse brain to grafted dopaminergic neurons and seeds aggregation in cultured human cells. *The Journal of Clinical Investigation* **2011**, *121*, 715–725.

(12) Lee, H.-J.; Patel, S.; Lee, S.-J. Intravesicular localization and exocytosis of alpha-synuclein and its aggregates. *The Journal of Neuroscience : The Official Journal of the Society for Neuroscience* **2005**, *25*, 6016–6024.

(13) Danzer, K. M.; Kranich, L. R.; Ruf, W. P.; Cagsal-Getkin, O.; Winslow, A. R.; Zhu, L.; Vanderburg, C. R.; McLean, P. J. Exosomal cell-to-cell transmission of alpha synuclein oligomers. *Molecular Neurodegeneration* **2012**, *7*, 42.

(14) Hoffmann, A.-C.; Minakaki, G.; Menges, S.; Salvi, R.; Savitskiy, S.; Kazman, A.; Miranda, H. V.; Mielenz, D.; Klucken, J.; Winkler, J.; *et al*. Extracellular aggregated alpha synuclein primarily triggers lysosomal dysfunction in neural cells prevented by trehalose. *Scientific Reports* **2019**, *9*, 1–18.

(15) Bohrmann, B.; Tjernberg, L.; Kuner, P.; Poli, S.; Levet-Trafit, B.; Näslund, J.; Richards, G.; Huber, W.; Döbeli, H.; Nordstedt, C. Endogenous proteins controlling amyloid beta-peptide polymerization. Possible implications for beta-amyloid formation in the central nervous system and in peripheral tissues. *The Journal of Biological Chemistry* **1999**, *274*, 15990–15995.
(16) Milojevic, J.; Raditsis, A.; Melacini, G. Human Serum Albumin Inhibits Aβ Fibrillization through a "Monomer-Competitor" Mechanism. *Biophysical Journal* **2009**, *97*, 2585–2594.
(17) Milojevic, J.; Esposito, V.; Das, R.; Melacini, G. Understanding the molecular basis for the inhibition of the Alzheimer's Abeta-peptide oligomerization by human serum albumin using saturation transfer difference and off-resonance relaxation NMR spectroscopy. *Journal of the American Chemical Society* **2007**, *129*, 4282–4290.
(18) Milojevic, J.; Melacini, G. Stoichiometry and Affinity of the Human Serum Albumin-Alzheimer's Aβ Peptide Interactions. *Biophysical Journal* **2011**, *100*, 183–192.
(19) Algamal, M.; Milojevic, J.; Jafari, N.; Zhang, W.; Melacini, G. Mapping the Interactions between the Alzheimer's Aβ-Peptide and Human Serum Albumin beyond Domain Resolution. *Biophysical Journal* **2013**, *105*, 1700–1709.
(20) Algamal, M.; Ahmed, R.; Jafari, N.; Ahsan, B.; Ortega, J.; Melacini, G. Atomic-resolution map of the interactions between an amyloid inhibitor protein and amyloid β (Aβ) peptides in the monomer and protofibril states. *The Journal of Biological Chemistry* **2017**, *292*, 17158–17168.
(21) Ahmed, R.; Melacini, G. A solution NMR toolset to probe the molecular mechanisms of amyloid inhibitors. *Chemical Communications (Cambridge, England)* **2018**, *54*, 4644–4652.
(22) Choi, T. S.; Lee, H. J.; Han, J. Y.; Lim, M. H.; Kim, H. I. Molecular Insights into Human Serum Albumin as a Receptor of Amyloid-β in the Extracellular Region. *Journal of the American Chemical Society* **2017**, *139*, 15437–15445.
(23) Bellomo, G.; Bologna, S.; Cerofolini, L.; Paciotti, S.; Gatticchi, L.; Ravera, E.; Parnetti, L.; Fragai, M.; Luchinat, C. Dissecting the Interactions between Human Serum Albumin and α-Synuclein: New Insights on the Factors Influencing α-Synuclein Aggregation in Biological Fluids. *The Journal of Physical Chemistry. B* **2019**, *123*, 4380–4386.
(24) Theillet, F.-X.; Binolfi, A.; Bekei, B.; Martorana, A.; Rose, H. M.; Stuiver, M.; Verzini, S.; Lorenz, D.; van Rossum, M.; Goldfarb, D.; Selenko, P. Structural disorder of monomeric α-synuclein persists in mammalian cells. *Nature* **2016**, *530*, 45–50.
(25) Kakinen, A.; Javed, I.; Faridi, A.; Davis, T. P.; Ke, P. C. Serum albumin impedes the amyloid aggregation and hemolysis of human islet amyloid polypeptide and alpha synuclein. *Biochimica et Biophysica Acta (BBA) - Biomembranes* **2018**, *1860*, 1803–1809.
(26) Finn, T. E.; Nunez, A. C.; Sunde, M.; Easterbrook-Smith, S. B. Serum albumin prevents protein aggregation and amyloid formation and retains chaperone-like activity in the presence of physiological ligands. *The Journal of Biological Chemistry* **2012**, *287*, 21530–21540.
(27) Chen, S. W.; Drakulic, S.; Deas, E.; Ouberai, M.; Aprile, F. A.; Arranz, R.; Ness, S.; Roodveldt, C.; Guilliams, T.; De-Genst, E. J.; *et al*. Structural characterization of toxic oligomers that are kinetically trapped during α-synuclein fibril formation. *Proceedings of the National Academy of Sciences of the United States of America* **2015**, *112*, E1994-2003.
(28) Krenzel, E. S.; Chen, Z.; Hamilton, J. A. Correspondence of fatty acid and drug binding sites on human serum albumin: a two-dimensional nuclear magnetic resonance study. *Biochemistry* **2013**, *52*, 1559–1567.
(29) Sudlow, G.; Birkett, D. J.; Wade, D. N. The characterization of two specific drug binding sites on human serum albumin. *Molecular pharmacology* **1975**, *11*, 824–832.
(30) Jafari, N.; Ahmed, R.; Gloyd, M.; Bloomfield, J.; Britz-McKibbin, P.; Melacini, G. Allosteric Sensing of Fatty Acid Binding by NMR: Application to Human Serum Albumin. *Journal of Medicinal Chemistry* **2016**, *59*, 7457–7465.
(31) Boulton, S.; Selvaratnam, R.; Ahmed, R.; Van, K.; Cheng, X.; Melacini, G. Mechanisms of Specific versus Nonspecific Interactions of Aggregation-Prone Inhibitors and Attenuators. *Journal of Medicinal Chemistry* **2019**, *62*, 5063–5079.

(32) Fusco, G.; Chen, S. W.; Williamson, P. T. F.; Cascella, R.; Perni, M.; Jarvis, J. A.; Cecchi, C.; Vendruscolo, M.; Chiti, F.; Cremades, N.; Ying, L.; Dobson, C. M.; De Simone, A. Structural basis of membrane disruption and cellular toxicity by α-synuclein oligomers. *Science (New York, N.Y.)* **2017**, *358*, 1440–1443.
(33) Comellas, G.; Lemkau, L. R.; Zhou, D. H.; George, J. M.; Rienstra, C. M. Structural intermediates during α-synuclein fibrillogenesis on phospholipid vesicles. *Journal of the American Chemical Society* **2012**, *134*, 5090–5099.
(34) Fusco, G.; Simone, A. de; Gopinath, T.; Vostrikov, V.; Vendruscolo, M.; Dobson, C. M.; Veglia, G. Direct observation of the three regions in α-synuclein that determine its membrane-bound behaviour. *Nature Communications* **2014**, *5*, 3827.
(35) Kotler, S. A.; Walsh, P.; Brender, J. R.; Ramamoorthy, A. Differences between amyloid-β aggregation in solution and on the membrane: insights into elucidation of the mechanistic details of Alzheimer's disease. *Chemical Society Reviews* **2014**, *43*, 6692–6700.
(36) Sciacca, M. F.M.; Kotler, S. A.; Brender, J. R.; Chen, J.; Lee, D.-k.; Ramamoorthy, A. Two-Step Mechanism of Membrane Disruption by Aβ through Membrane Fragmentation and Pore Formation. *Biophysical Journal* **2012**, *103*, 702–710.
(37) Lee, S. J. C.; Nam, E.; Lee, H. J.; Savelieff, M. G.; Lim, M. H. Towards an understanding of amyloid-β oligomers: characterization, toxicity mechanisms, and inhibitors. *Chemical Society Reviews* **2017**, *46*, 310–323.
(38) Fusco, G.; Pape, T.; Stephens, A. D.; Mahou, P.; Costa, A. R.; Kaminski, C. F.; Schierle, G. S. K.; Vendruscolo, M.; Veglia, G.; Dobson, C. M.; *et al.* Structural basis of synaptic vesicle assembly promoted by α-synuclein. *Nat Communications* **2016**, *7*, 1–12.
(39) Ahmed, R.; Akcan, M.; Khondker, A.; Rheinstädter, M. C.; Bozelli, J. C.; Epand, R. M.; Huynh, V.; Wylie, R. G.; Boulton, S.; Huang, J.; Verschoor, C. P.; Melacini, G. Atomic resolution map of the soluble amyloid beta assembly toxic surfaces. *Chemical science* **2019**, *10*, 6072–6082.
(40) Ahmed, R.; VanSchouwen, B.; Jafari, N.; Ni, X.; Ortega, J.; Melacini, G. Molecular Mechanism for the (-)-Epigallocatechin Gallate-Induced Toxic to Nontoxic Remodeling of Aβ Oligomers. *Journal of the American Chemical Society* **2017**, *139*, 13720–13734.
(41) Fawzi, N. L.; Ying, J.; Ghirlando, R.; Torchia, D. A.; Clore, G. M. Atomic-resolution dynamics on the surface of amyloid-β protofibrils probed by solution NMR. *Nature* **2011**, *480*, 268–272.
(42) Dedmon, M. M.; Lindorff-Larsen, K.; Christodoulou, J.; Vendruscolo, M.; Dobson, C. M. Mapping long-range interactions in alpha-synuclein using spin-label NMR and ensemble molecular dynamics simulations. *Journal of the American Chemical Society* **2005**, *127*, 476–477.
(43) Cohen, S. I. A.; Arosio, P.; Presto, J.; Kurudenkandy, F. R.; Biverstal, H.; Dolfe, L.; Dunning, C.; Yang, X.; Frohm, B.; Vendruscolo, M.; Johansson J.; Dobson, C. M.; Fisahn, A.; Knowles, T. P. J.; Linse, S. The molecular chaperone Brichos breaks the catalytic cycle that generates toxic Aβ oligomers. *Nature Structural & Molecular Biology* **2015**, *22*, 207–213.
(44) Auluck, P. K.; Caraveo, G.; Lindquist, S. α-Synuclein: membrane interactions and toxicity in Parkinson's disease. *Annual Review of Cell and Developmental Biology* **2010**, *26*, 211–233.
(45) Whiten, D. R.; Cox, D.; Horrocks, M. H.; Taylor, C. G.; De, S.; Flagmeier, P.; Tosatto, L.; Kumita, J. R.; Ecroyd, H.; Dobson, C. M.; Klenerman, D.; Wilson, M. R. Single-Molecule Characterization of the Interactions between Extracellular Chaperones and Toxic α-Synuclein Oligomers. *Cell Reports* **2018**, *23*, 3492–3500.
(46) Galántai, R.; Bárdos-Nagy, I. The interaction of human serum albumin and model membranes. *International Journal of Pharmaceutics* **2000**, *195*, 207–218.
(47) Thakur, R.; Das, A.; Chakraborty, A. Interaction of human serum albumin with liposomes of saturated and unsaturated lipids with different phase transition temperatures: a spectroscopic investigation by membrane probe PRODAN. *RSC Advances* **2014**, *4*, 14335–14347.
(48) Hoyer, W.; Antony, T.; Cherny, D.; Heim, G.; Jovin, T. M.; Subramaniam, V. Dependence of alpha-synuclein aggregate morphology on solution conditions. *Journal of Molecular Biology* **2002**, *322*, 383–393.
(49) Povilonienė, S.; Časaitė, V.; Bukauskas, V.; Šetkus, A.; Staniulis, J.; Meškys, R. Functionalization of α-synuclein fibrils. *Beilstein Journal of Nanotechnology* **2015**, *6*, 124–133.

(50) Ames, B. N. Assay of inorganic phosphate, total phosphate and phosphatases. Neufeld E. F., Ginsburg F. Complex Carbohydrates; Methods in Enzymology; Elsevier, 1966; pp 115–118.
(51) Khondker, A.; Malenfant, D. J.; Dhaliwal, A. K.; Rheinstadter, M. C. Carbapenems and Lipid Bilayers: Localization, Partitioning, and Energetics. *ACS Infectious Diseases* **2018**, *4*, 926–935.
(52) Khondker, A.; Dhaliwal, A. K.; Saem, S.; Mahmood, A.; Fradin, C.; Moran-Mirabal, J.; Rheinstadter, M. C. Membrane charge and lipid packing determine polymyxin-induced membrane damage. *Communications Biology* **2019**, *2*, 67.
(53) Kucerka, N.; Tristram-Nagle, S.; Nagle, J. F. Structure of fully hydrated fluid phase lipid bilayers with monounsaturated chains. *The Journal of Membrane Biology* **2005**, *208*, 193–202.
(54) Gopinath, T.; Veglia, G. Dual acquisition magic-angle spinning solid-state NMR-spectroscopy: simultaneous acquisition of multidimensional spectra of biomacromolecules. *Angewandte Chemie (International ed. in English)* **2012**, *51*, 2731–2735.
(55) S., M. V.; Gopinath, T.; Wang, S.; Veglia, G. T 2 * weighted Deconvolution of NMR Spectra: Application to 2D Homonuclear MAS Solid-State NMR of Membrane Proteins. *Scientific Reports* **2019**, *9*, 1–8.
(56) Morcombe, C. R.; Zilm, K. W. Chemical shift referencing in MAS solid state NMR. *Journal of Magnetic Resonance* **2003**, *162*, 479–486.

4.8 Supplementary Information

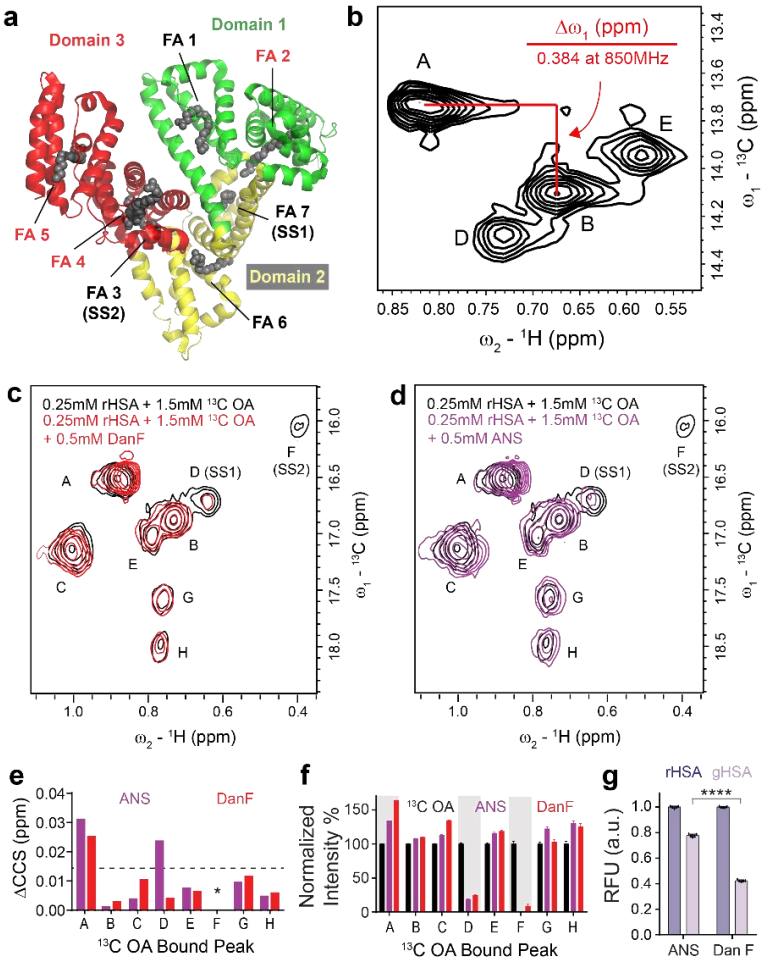

Figure. S1 – *Binding sites of 1-anilino-8-napthalene sulfonate (ANS) and dansyl phenylalanine (DanF) in human serum albumin as probed through ^{13}C oleic acid competition.* (a) Crystal structure of OA-bound to HSA (PDB code: 1GNI). Domains one, two, and three are shown in green, yellow and red, respectively. High affinity fatty-acid binding sites (FA 2, FA 4 and FA 5) are labeled in red, whereas low affinity sites are labeled in black. Two low affinity sites are not reported in this structure. (b) Red horizontal and vertical lines indicate the separation between peaks A and B, corresponding to two high affinity fatty acid binding sites in HSA, in the ^{1}H and ^{13}C dimensions, respectively. The separation in the ^{13}C dimension is 0.384 ppm measured at 850MHz, corresponding to 67.2 Hz at 700 MHz. (c) Overlay of the ^{1}H-^{13}C HSQC spectra of HSA-bound ^{13}C-oleic acid in the absence (*black*) and presence (*red*) of DanF. (d) As (c), except in the presence (*purple*) of ANS. (e) Combined chemical shift changes in HSA-bound ^{13}C-oleic acid peaks in the presence of ANS (*purple*) or DanF (*red*). The * indicates that the peak intensity was too low to accurately measure chemical shift changes. (f) Intensity of HSA-bound ^{13}C-oleic acid peaks in the absence (*black*) and presence of ANS (*purple*) or DanF (*red*). All peak intensities are normalized to the values in the absence of fluorophore (*black*) which is set to 100%. (g) Normalized fluorescence intensity of ANS or DanF in the presence of rHSA (*dark purple*) or gHSA (*light purple*). Fluorescence intensities are normalized to the state in the presence of rHSA, which is set to 1.0. Two-way ANOVA and subsequent Sidak's multiple comparison tests were used to determine the statistical significance between the rHSA or gHSA samples in ANS *vs.* Dan F competition experiments.

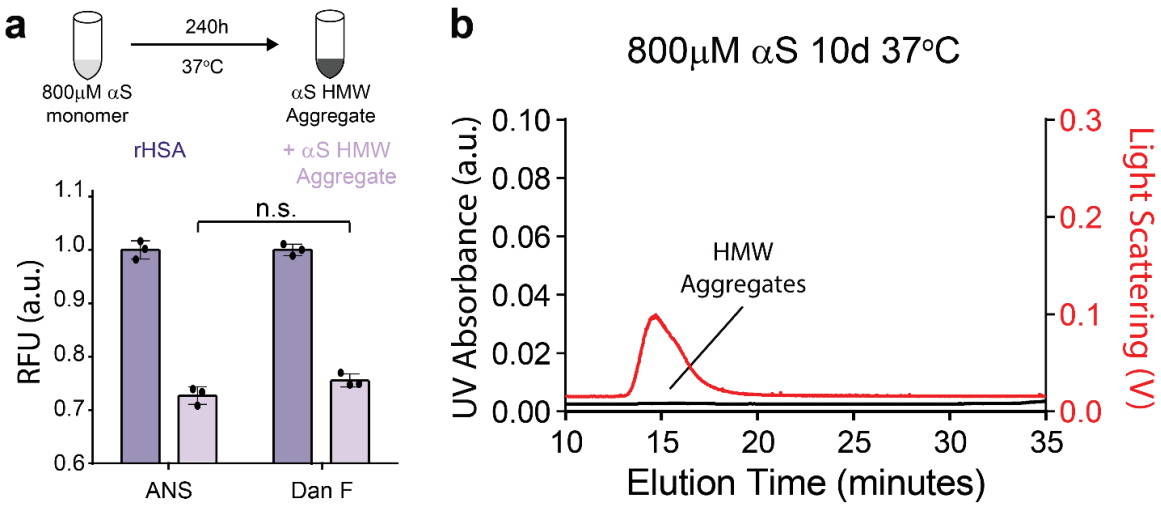

Figure. S2 – *HMW αS aggregates compete out ANS and Dan F from the surface of HSA to comparable extents.* (a) Fluorescence intensities of ANS and Dan F bound to rHSA in the absence (dark purple) and presence (light purple) of HMW αS aggregates, normalized to the rHSA alone state. The data reported show the mean and standard deviation of technical replicates. Fluorescence contributions arising from ANS and Dan F binding αS aggregates are accounted for. Two-way ANOVA and subsequent Sidak's multiple comparison tests were used to determine statistical significance between the rHSA or rHSA with αS aggregate samples in ANS vs. Dan F competition experiments. (b) SEC MALS characterization of a 800μM αS in PBS pH 7.4 sample incubated for 10 days at 37°C.

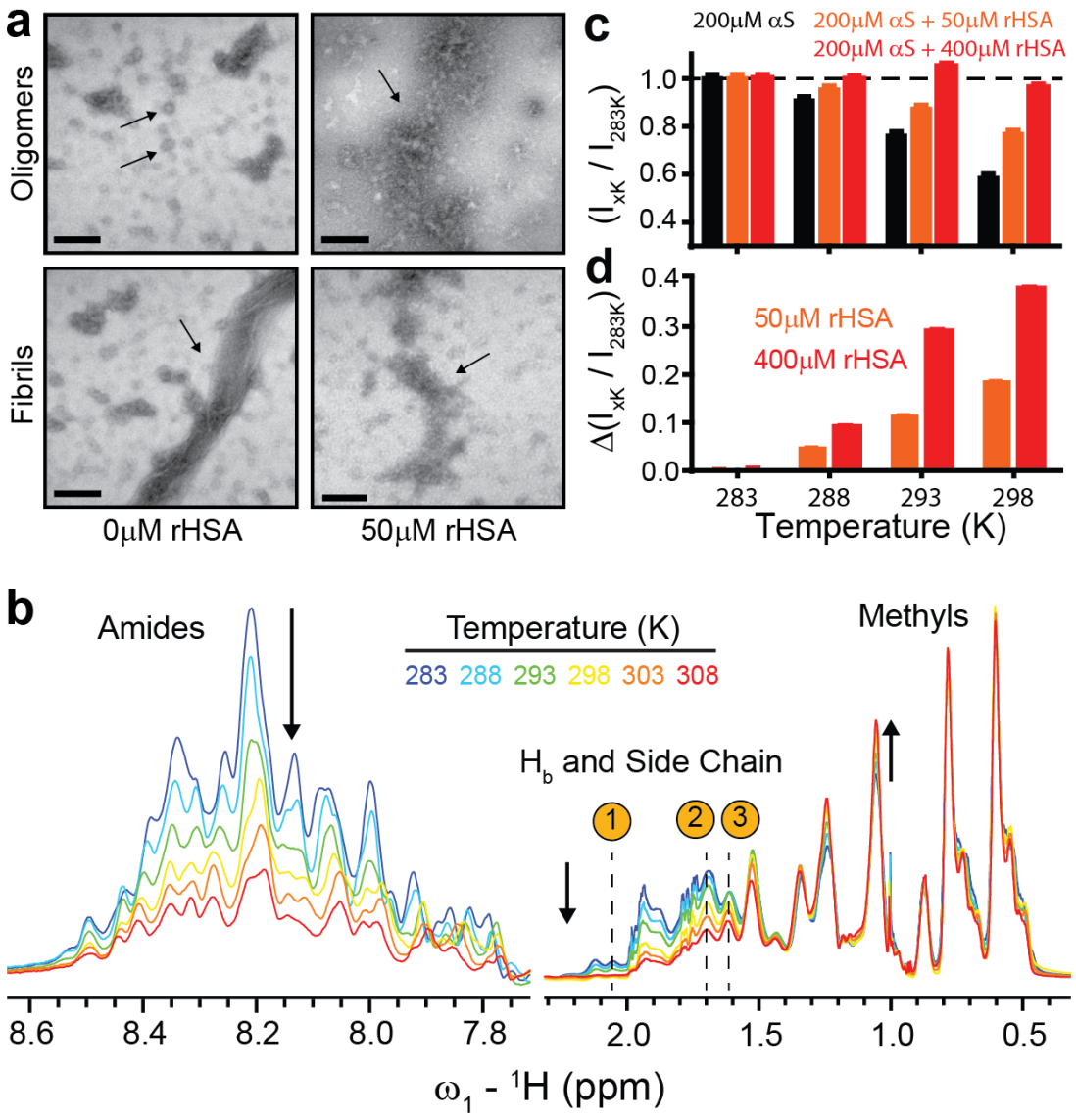

Figure. S3 – rHSA remodels pre-existing αS oligomers into intermediate structures and inhibits the conversion of NMR visible αS species into NMR invisible αS aggregates. (a) Negative stain transmission electron microscopy images of the pre-formed αS oligomers and fibrils without (*left*) and with (*right*) rHSA treatment. All scale bars represent lengths of 100 nm. (b) Representative ^{1}H NMR spectra of αS highlighting the temperature-dependent conversion of NMR visible αS species into NMR invisible assemblies. A spin lock was incorporated into the ^{1}H NMR pulse sequence to effectively remove contributions arising from HMW species such as HSA. Black arrows indicate the direction of intensity changes at increasing temperatures for the three groups of protons *i.e.* amides, H_b and other side chains and methyls. Dashed vertical lines and associated numbers indicate the well-resolved protons for which the data heights were measured and averaged to monitor relative changes in NMR visible αS population. (c) Average of three well-resolved αS H_b and other side chain proton intensities in the absence (*black*) and presence of 50 μM (*orange*) and 400 μM (*red*) rHSA at various temperatures, normalized to the intensities at 283 K. The H_b protons used for measurements are highlighted in (b). (d) Differences in average αS intensities at each temperature between the rHSA bound *vs.* free state shown in (c).

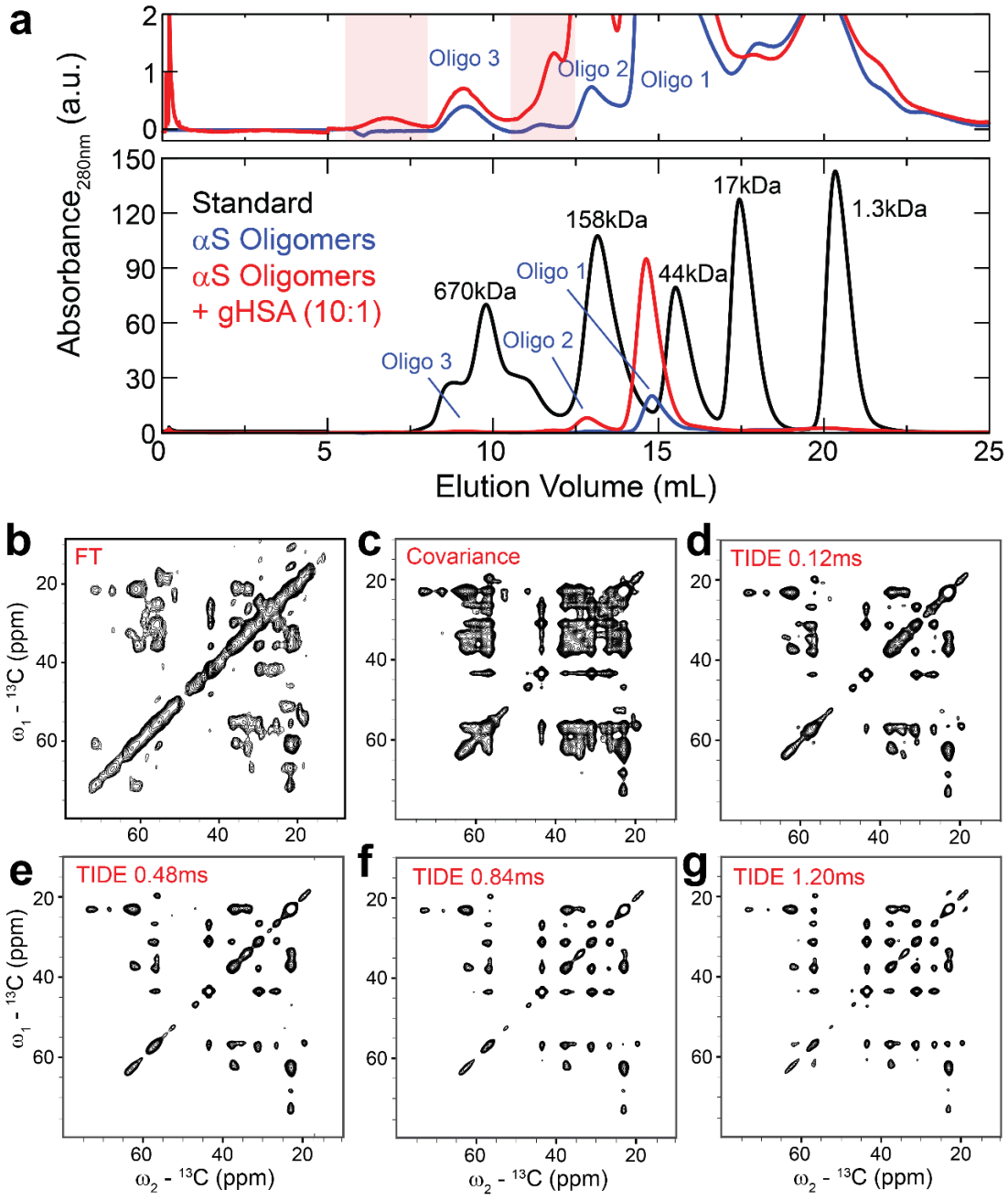

Figure. S4 – *Size distribution of αS oligomer samples for ^{13}C – ^{13}C DARR ssNMR and post processing of DARR spectra.* (a) Size Exclusion Chromatography (SEC) profiles of αS oligomers created in the absence (*blue*) and presence (*red*) of sub-stoichiometric (10:1 αS:gHSA) amounts of gHSA. Sizes are estimated relative to a standard shown in black. A zoomed in chromatogram is shown in the upper panel to more clearly display lowly populated oligomers. Pink shaded regions indicate changes in size distribution of lowly populated oligomers due to gHSA remodeling. (b)-(g) Comparison of the [^{13}C,^{13}C]-DARR spectra of αS oligomers processed using Fourier Transform (FT) (b), Covariance NMR (c) and T2* welghted DEconvolution (TIDE) of NMR using gaussian averaging of FIDs in the indirect dimension centred around 0.12ms (d), 0.48ms (e), 0.84ms (f) and 1.20ms (g) with 10% variance.

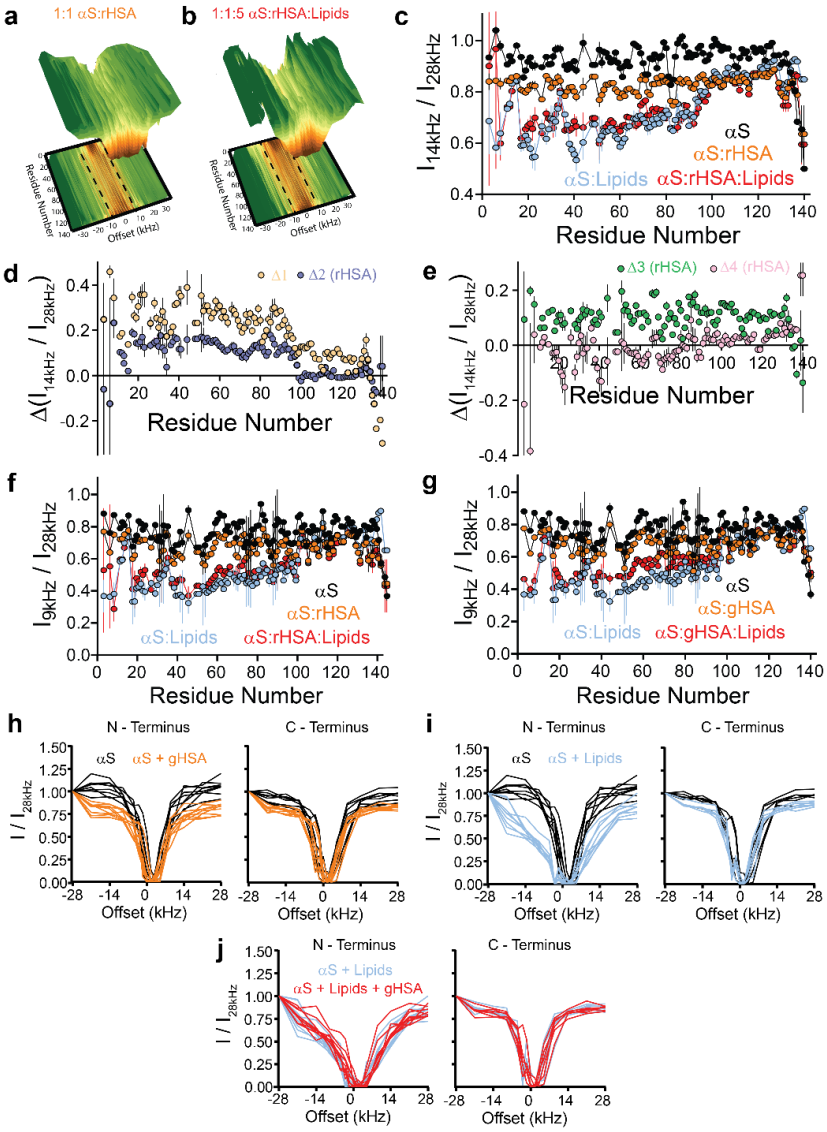

Figure. S5 – *^{15}N – DEST profiles for rHSA-containing samples measured using 14kHz off-resonance saturation offset and both rHSA and gHSA- containing samples measured at 9 kHz offset.* Normalized ^{15}N – DEST cross-peak intensities as a function of offset and residue number (see Methods) measured for (a) 300 μM αS + 300 μM rHSA and (b) 300 μM αS + 300 μM rHSA + 1.5 mM DOPE:DOPS:DOPC. (c) Residue-specific ^{15}N – DEST profiles computed using off-resonance and far off-resonance saturation frequencies of 14 kHz and 28 kHz, respectively, from the ^{15}N – DEST profiles shown in (a)-(b) and Fig. 4a,c. The DEST profile was smoothed by averaging the I_{14kHz}/ I_{28kHz} values for each residue and the two residues directly adjacent to it, when available. (d)-(e) Differences between the residue-specific ^{15}N – DEST profiles shown in (c) according to the double ligand cycle shown in Fig. 4e. (f)-(g) Residue-specific ^{15}N – DEST profiles computed using off-resonance and far off-resonance saturation frequencies of 9 kHz and 28 kHz, respectively, for (f) rHSA- and (g) gHSA-containing samples. (h) Representative ^{15}N - DEST cross-peak intensities as a function of offset for select residues in the N- and C-Termini of αS in the absence (*black*) and presence (*orange*) of gHSA. (i) As (h), except in the presence (*blue*) of lipids. (j) Representative ^{15}N - DEST cross-peak intensities as a function of offset for select residues in the N- and C-Termini of lipid-bound αS in the absence (*blue*) and presence (*red*) of gHSA.

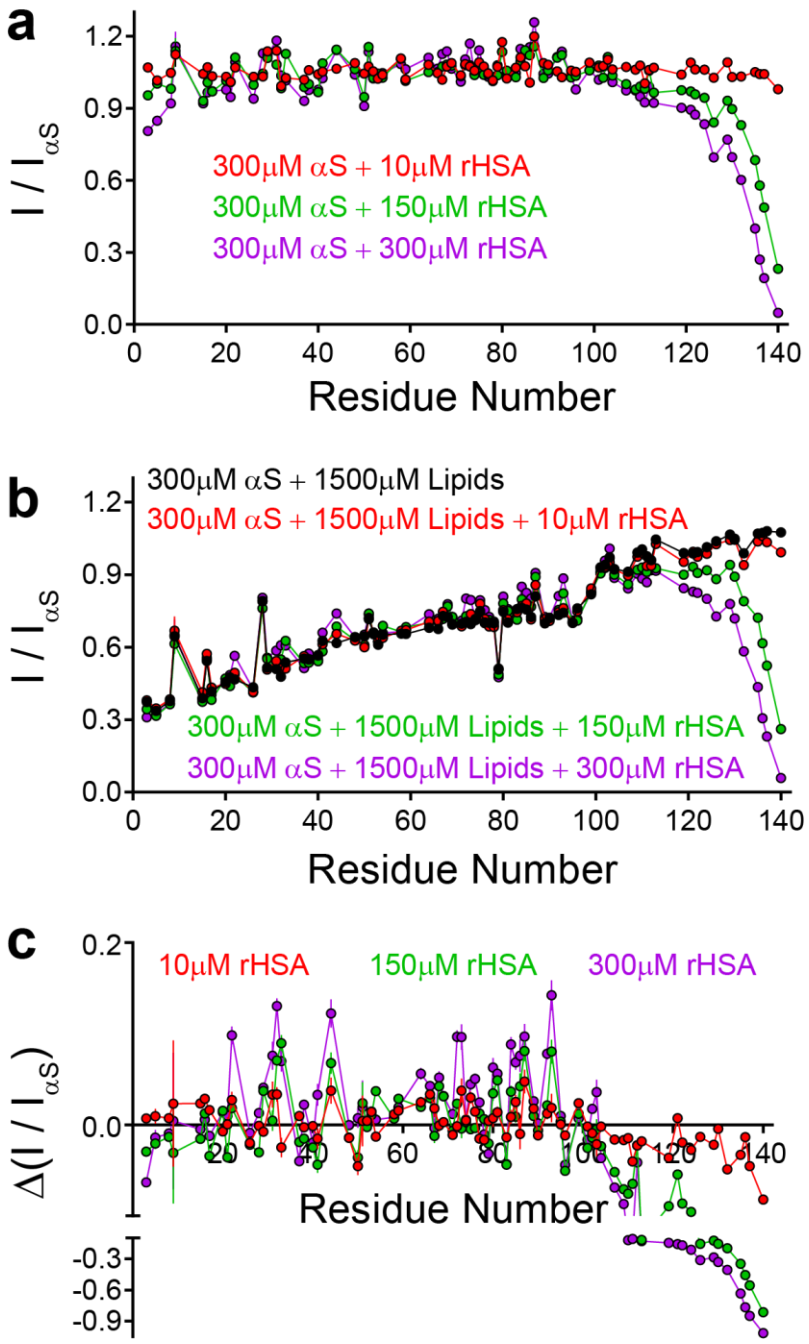

Figure. S6 – *Effect of rHSA on αS – membrane interactions, as probed by ^{1}H – ^{15}N HSQC intensity losses.* (a) Normalized HSQC cross-peak intensities of 300 μM αS in the presence of 10 μM (*red*), 150 μM (*green*) and 300 μM (*purple*) rHSA. All intensities are normalized to αS in the absence of rHSA, which is arbitrarily set to 1.0. (b) Normalized HSQC cross-peak intensities of 300 μM αS + 1500 μM DOPE:DOPS:DOPC lipids in the absence (*black*) and presence of 10 μM (*red*), 150 μM (*green*) and 300 μM (*purple*) rHSA. All intensities are normalized to αS in the absence of rHSA and DOPE:DOPS:DOPC lipids, which is arbitrarily set to 1.0. (c) Differences in the normalized HSQC cross-peak intensities between the αS+lipids+rHSA measurements and αS+lipids shown in (b).

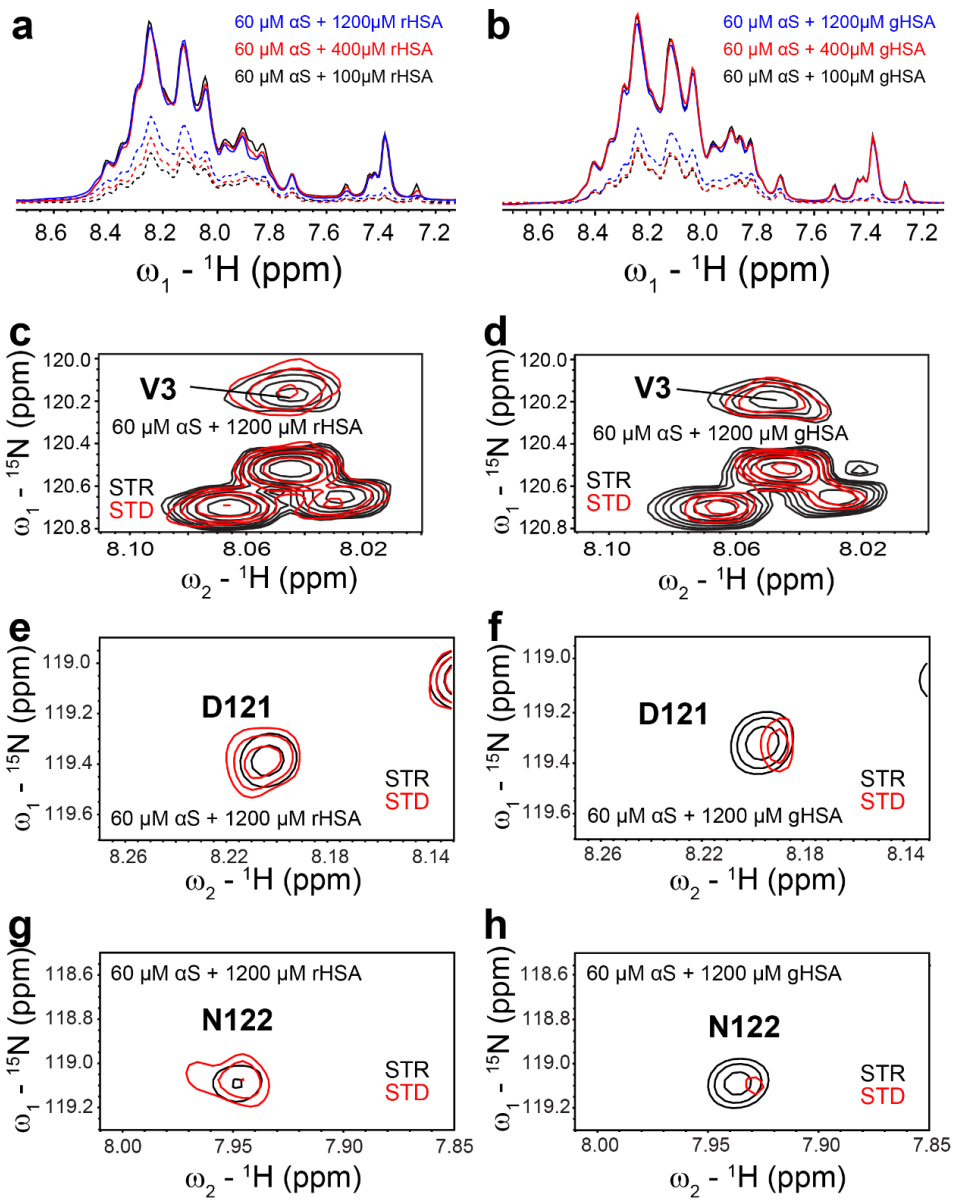

Figure. S7 – *1D and 2D STDHSQC NMR spectra showing the extent of rHSA and gHSA binding to αS monomers.* (a) 1D STDHSQC (*dashed lines*) and STRHSQC (*solid lines*) spectra of 60μM αS in the presence of 100μM (*black*), 400μM (*red*) and 1200μM (*blue*) rHSA. The STD:STR relative intensities at each concentration is arbitrary and is dependent on the # of scans acquired for the STD and STR spectra. The spectra have been normalized to account for differences in the # of scans, and hence the changes in STD:STR ratios reflect differences in binding. (b) As (a) except with gHSA in place of rHSA. (c) Overlay of 2D STDHSQC (*red*) and STRHSQC (*black*) spectra highlighting Valine 3 (V3) cross-peak intensities for 60 μM αS in the presence of 1200 μM rHSA. (d) As (c) except with gHSA replacing rHSA. (e) As (c) except highlighting Aspartate 121 (D121). (f) As (d) except highlighting Aspartate 121 (D121). (g) As (c) except highlighting Asparagine 122 (N122). (h) As (d) except highlighting Asparagine 122 (N122).

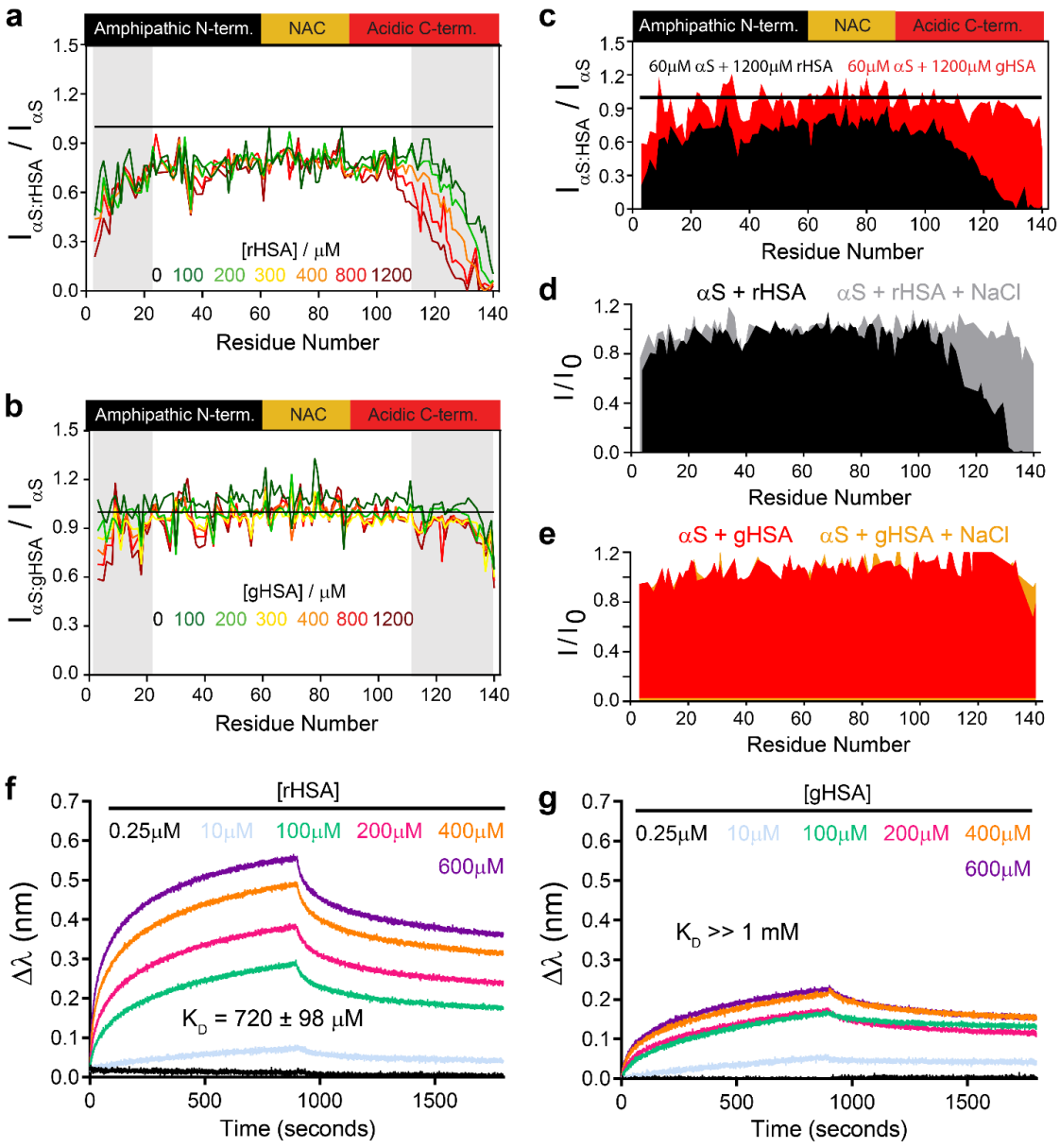

Figure. S8 – *Binding sites of rHSA and gHSA in αS monomers as probed by $^{1}H - ^{15}N$ HSQC NMR intensity losses.* (a) Normalized HSQC cross-peak intensities as a function of residue number for 60 μM αS in the presence of increasing concentrations of rHSA. Intensities are normalized relative to αS in the absence of rHSA. Colour coding is as per the legend in figure inset. Grey boxes highlight regions of significant intensity losses. (b) As (a) except for gHSA. (c) Overlay of the normalized HSQC intensity profiles of αS at the end of the titration with rHSA and gHSA shown in (a) and (b), respectively. The data is reproduced here for the convenience of comparison. (d) Normalized HSQC cross-peak intensities for 60 μM αS in the presence of 600 μM rHSA without (*black*) and with (*grey*) 150 mM sodium chloride. (e) Normalized HSQC cross-peak intensities for 60 μM αS in the presence of 600 μM gHSA without (*red*) and with (*gold*) 150 mM sodium chloride. (f) – (g) Biolayer interferometry (BLI) analysis of the (f) rHSA and (g) gHSA binding to αS monomers, respectively.

Table S1 – Pairwise statistical analyses of the RPE1 cellular viability in the absence and presence of the αS oligomers.

Species	RPE1 P Values*	SHSY5Y P Values*
Mock *vs.* rHSA (data not shown)	0.3055 (ns)	0.9994 (ns)
Mock *vs.* gHSA (data not shown)	0.0875 (ns)	0.9519 (ns)
Mock *vs.* αS	<0.0001	<0.0001
Mock *vs.* αS + rHSA	0.6709 (ns)	>0.9999 (ns)
Mock *vs.* αS + gHSA	0.0586 (ns)	0.4628 (ns)
αS *vs.* αS + rHSA	0.0009	<0.0001
αS *vs.* αS + gHSA	0.0358	<0.0001

*The p values are generated from the post-hock Tuckey test of the cellular viability data shown in Figure 1a-b.

Chapter 5. Mapping Self-Association by Temperature-Induced Relaxation Enhancement (SATIRE)

5.1 Author's Preface

The work presented in this chapter is based on the data that is currently available and is not the final version of this study.

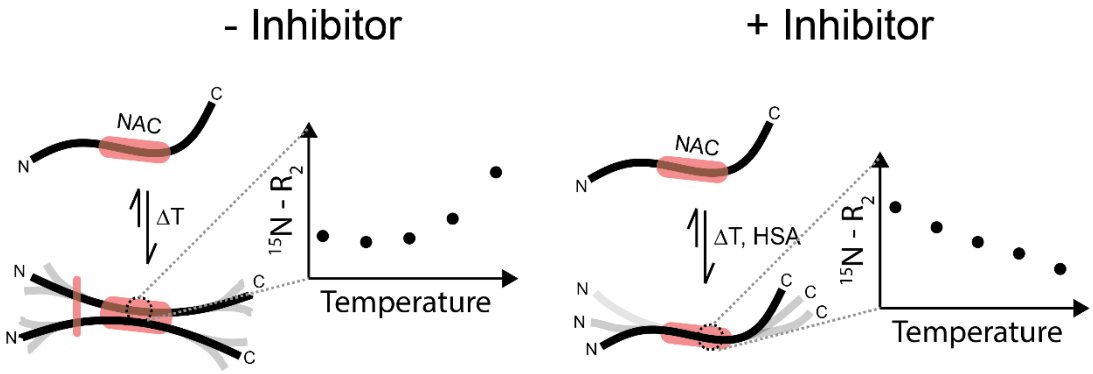

I conducted most of the experiments necessary for the manuscript and analyzed the data. Jinfeng Huang provided support in purifying alpha synuclein, computing the SASA and mapping the SATIRE-identified self-association sites on αS fibrils. I co-wrote the manuscript and designed the research with Dr. Giuseppe Melacini.

5.2 Abstract

Soluble oligomers formed by amyloidogenic intrinsically disorder proteins are some of the most cytotoxic species linked to neurodegeneration. Due to the transient nature of such oligomeric intermediates, the underlying self-association events often remain elusive. NMR relaxation measurements sensitive to zero-frequency spectral densities (J(0)), such as the $^{15}N - R_2$ rates, are ideally suited to map sites of self-association at atomic resolution and without the need of exogenous labels, by exploiting the dynamic exchange between NMR visible monomer and slowly tumbling oligomers. However, $^{15}N - R_2$ rates are also sensitive to intrinsic monomers dynamics, and it is often difficult to discern these contributions from those arising from exchange with oligomers. Here, using the archetypical amyloidogenic protein alpha synuclein (αS), we show that the temperature-dependence of $^{15}N - R_2$, effectively identifies self-association sites with minimal bias from internal dynamics. The key signature of residues involved in self-association is a non-linear temperature-dependence of $^{15}N - R2$ with a positive $\Delta R_2/\Delta T$ slope. These two hallmarks are systematically probed through a thermal R_2 correlation matrix, from which the network of residues involved in self-association is extracted through agglomerative clustering. The resulting self-association maps help dissect the determinants of toxic oligomers and are expected to reveal how amyloid inhibitors affects oligomer formation.

5.3 Introduction

The accumulation of insoluble inclusions composed of misfolded proteins is the hallmark of a plethora of neurodegenerative and non-neuropathic systemic disorders.[1] On-pathway soluble oligomers that precede the formation of mature amyloid fibrils are often the primary pathogenic species.[2] However, the transient and heterogeneous nature of these oligomeric intermediates has hindered the characterization of such species and consequently the elucidation of the underlying self-association drivers.

Solution NMR techniques offer a means to probe at atomic resolution lowly populated oligomeric species by taking advantage of the dynamic exchange of NMR-invisible oligomers with NMR-visible monomers. For example, one noteworthy solution NMR experiment that has thus far been pivotal to map oligomerization sites is based on intermolecular paramagnetic relaxation enhancement (PRE).[3] Nonetheless, a reliable residue-specific map of early self-association based uniquely on PREs often requires multiple spin-labels at different positions throughout the protein sequence. Moreover, the introduction of such spin-labels may perturb the structural and aggregation properties of the wildtype protein. Hence, it is essential to map self-association events also through additional methods that do not require covalent modifications, but preserve the residue-resolution typical of PRE experiments.

Label-free approaches commonly used to map self-association are typically based on relaxation NMR measurements[4,5], such as ^{15}N - dark state exchange saturation transfer (^{15}N - DEST)[6] and ^{15}N – transverse relaxation rates (^{15}N - R_2)[7]. Notably, ^{15}N – R_2 measurements are sensitive to zero-frequency spectral densities (J(0)) which are amplified in slow-tumbling, high molecular weight (MW) assemblies,[8–11] and therefore are ideally suited to sense even minor populations of soluble oligomers in dynamic exchange with NMR visible monomers of intrinsically disordered proteins (IDPs)[4–7,12–15]. However, J(0) also senses contributions arising from the complex intrinsic dynamics of the monomeric protein, an effect that frequently dominates residue-dependent variation of relaxation rates[7,16]. Motions of monomeric IDPs typically span the ps-to-tens of ns time scale, ranging from < 50 ps for librational dynamics, to ~ns for local backbone sampling of Ramachandran substates and ~tens of ns for segmental chain dynamics.[17–20] These protein motions are effectively detected by conventional ^{15}N transverse relaxation measurements and need to be reliably separated from contributions arising from high MW assemblies in order to obtain accurate self-association maps.

Here, we propose a simple but effective approach to circumvent this challenge by monitoring temperature-dependent changes in ^{15}N – R_2, *i.e.* $\Delta R_2/\Delta T$, as opposed to just R_2. We refer to this approach as Self-Association by Temperature-Induced Relaxation Enhancement, or SATIRE in short. We validated the SATIRE method by applying it to an archetypical amyloidogenic protein, the 140 amino acid

intrinsically disordered alpha synuclein (αS), for which self-association sites have been previously characterized by extensive mutations[21–29], DEST[15] and intermolecular PREs[3]. These investigations have shown the self-association sites to be primarily localized to the central NAC region spanning residues 61-95, as well as sites of familial Parkinson's disease mutations *i.e.* residues ~30-53. The N- and C-terminal segments, in contrast, are not directly involved in self-association[15] but may play an ancillary role, possibly through allosteric regulation[30–33].

Our data illustrate that a reliable self-association map is obtained based on the switch from negative-to-positive $\Delta R_2/\Delta T$ slopes and the non-linearity of the R_2 *vs.* temperature dependence (Fig. 1a). These two hallmarks are systematically probed through a so-called thermal R_2 correlation matrix, from which the network of residues involved in self-association is extracted through agglomerative clustering. Notably, when the αS concentration is increased, the transition temperature ($T_{transition}$) for the switch in $\Delta R_2/\Delta T$ slope from negative to positive, significantly decreases. Moreover, when the $\Delta R_2/\Delta T$ analyses are repeated in the presence of an aggregation inhibitor, Human Serum Albumin (HSA), a linear R_2 *vs.* temperature dependence with negative slope is observed for nearly all residues, consistent with a monomeric IDP pattern. Importantly, the oligomerization sites mapped here are in agreement with previous mutagenesis studies which identified these regions to be critical for toxicity and aggregation.[15,26,28] Overall, the SATIRE method proposed here emerges as a robust, tag-free and sensitive approach to map at atomic resolution sites involved in early oligomerization as well as to probe the effect of aggregation inhibitors, such as small molecules or biologics.

5.4 Results

5.4.1 Positive *vs.* Negative Temperature-Dependent Changes in ^{15}N-R_2 ($\Delta R_2/\Delta T$) Report on Sites of Oligomer Formation *vs.* intrinsic Monomer Dynamics.

Conventional techniques to probe IDP self-association, such as the measurement of ^{15}N – transverse relaxation rates, are often confounded by contributions arising from intrinsic monomer dynamics[16]. Adaptations of current ^{15}N – R_2 experiments, that can effectively discern these two contributions are therefore of significant interest. One parameter that can be taken advantage of is temperature. Heat is expected to not only accelerate the intrinsic dynamics of IDPs but also promote IDP self-association[34], which is often initially mediated by hydrophobic interactions, an entropically driven effect. Enhanced monomer dynamics and self-association lead to opposite effects on the measured ^{15}N – R_2 rates. The heat-induced acceleration of the motional regimes typical of monomeric IDPs, *i.e.* the fast ($\tau \leq 50$ ps), intermediate ($\tau \sim 1$ ns) and slow segmental dynamics ($\tau = 5 – 25$ ns), is expected to decrease the ^{15}N – R_2 rates [20]. MD simulations of the monomeric C-terminal segment of αS reveal that such ^{15}N – R_2 decrease is linear with temperature in first approximation (Fig. S1). In contrast, as oligomers start to form upon

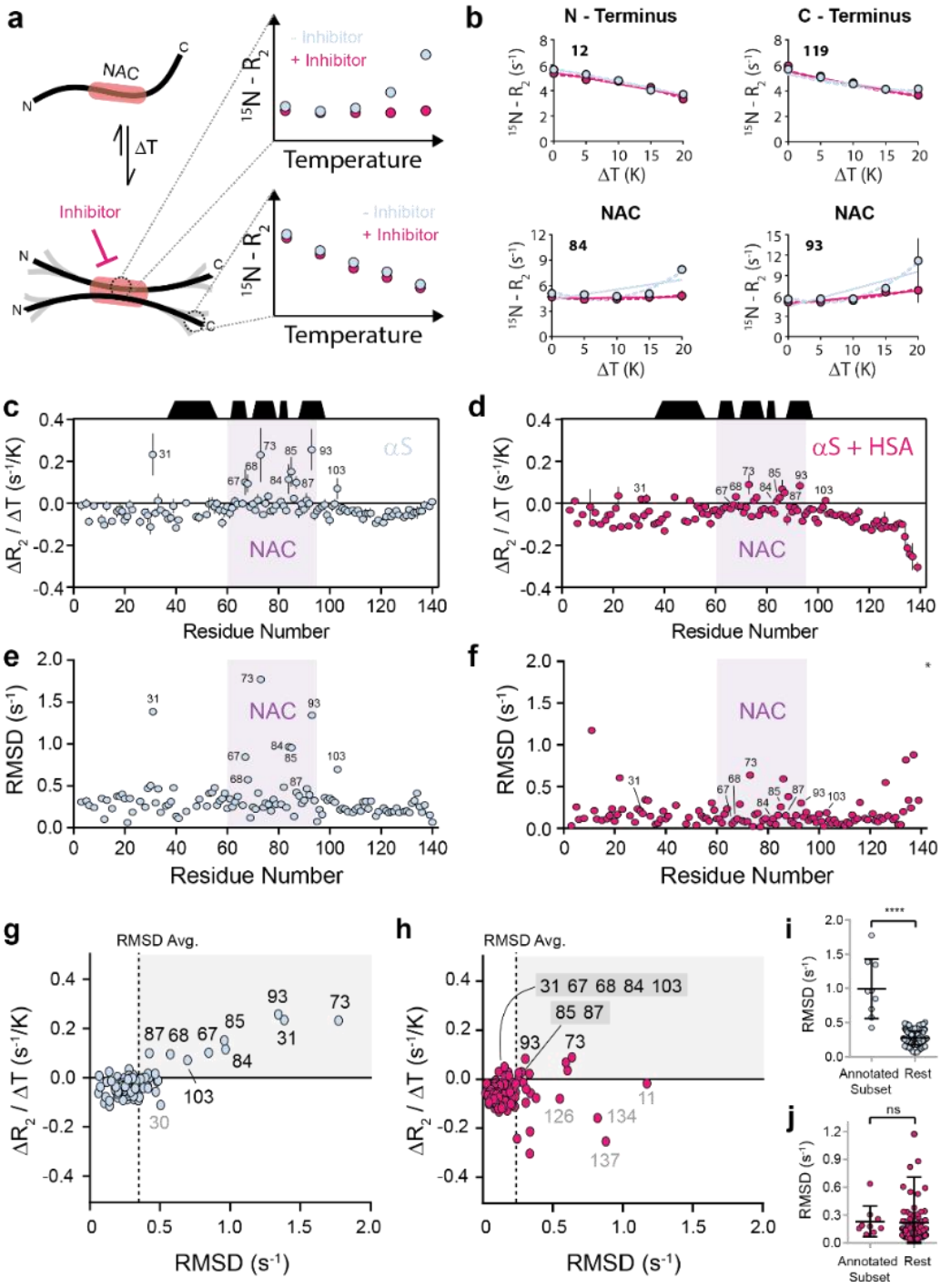

Figure 1. *The temperature-dependence of amide nitrogen transverse relaxation rates is sensitive to oligomer formation.* (a) Schematic diagram illustrating the expected $^{15}N - R_2$ *vs.* temperature dependencies for residues at oligomerization sites or other regions in the absence (*light blue*) and presence of an aggregation inhibitor (*magenta*). (b) Representative temperature-dependent $^{15}N - R_2$ profiles for select residues in the N-terminus, NAC and C-terminus for αS in the absence (*light blue*) and presence (*magenta*) of sub-stoichiometric amounts of HSA. Linear (quadratic) fittings of the experimental points are shown in

solid (dashed) lines. (c) Residue-specific slopes from the linear fitting of the temperature-dependent $^{15}N - R_2$ profiles of 200 μM αS. Black trapezoids indicate the positions of β-strands in the fibril structure (PDB ID: 2N0A), the purple highlight indicates the NAC region and annotations indicate residues with large positive slopes. (d) As (c) except in the presence of 50 μM rHSA. Residues annotated in (c) are shown here for purpose of comparison. (e) Residue-specific Root Mean Squared Deviation (RMSD) between the experimental $^{15}N - R_2$ and the calculated values from the linear fitting of the experimental points. Purple highlight indicates the NAC region and annotations indicate residues with large RMSD. (f) As (e) except in the presence of 50μM rHSA. Residues annotated in (e) are shown here for the purpose of comparison. The asterisk (*) indicates an off-scale value. (g) Relationship between slope and RMSD of the αS $^{15}N - R_2$ *vs.* temperature plots. The dashed line indicates the average RMSD. Residues with RMSD above average and positive slope are annotated in black and selected residues with high RMSD but negative slope are annotated in grey. (h) As (g), except in the presence of 50 μM HSA. (i) Unpaired parametric T-Test of annotated residues *vs.* rest in (g). **** indicates a p value <0.0001. (j) As (i) except in the presence of HSA, based on data shown in (h).

heating, sites involved in self-association are expected to exhibit locally enhanced $^{15}N - R_2$ rates and thus are anticipated to display deviations from the linear decrease pattern typical of αS monomers (Fig. 1a). Therefore, we hypothesized that temperature-dependent changes in $^{15}N - R_2$, *i.e.* the $\Delta R_2/\Delta T$ slopes, may provide a map of oligomerization sites.

To test our hypothesis, we measured residue-specific $\Delta R_2/\Delta T$ slopes starting from essentially monomeric αS (Fig. S2b). We heated the αS sample from 278K to 303K in incremental steps of 5K and measured $^{15}N - R_2$ rates at each step (Fig. S2a). The sample stability over the course of the temperature-dependent R_2 protocol were monitored through $^{1}H - ^{15}N$ HSQCs (Fig. S2a, c). Notably, the samples were stable over the course of $^{15}N - R_2$ acquisition, as indicated by negligible changes in HSQC intensities prior to and after R_2 experiments (Fig. S2c). The $^{15}N - R_2$ *vs.* temperature plots were then constructed for each residue and fitted against the simplest possible model *i.e.* linear temperature-dependency (Fig. S3-S7, *light blue circles and solid line*). For most residues at the N- and C-termini, a linear relationship with negative slope is observed for the $^{15}N - R_2$ *vs.* temperature plots (Fig. 1b,c *light blue*). However, for several residues especially in the NAC region, significant deviations from this pattern are observed (Fig. 1b, lower panels, *light blue* and Fig. 1c, *light blue circles with purple highlights*). Considering that the NAC region is the primary site of αS aggregation, the data of Fig. 1b, c provide an initial confirmation of our hypothesis on positive $\Delta R_2/\Delta T$ slopes as local reporters of self-association, as opposed to alternative sources of $^{15}N - R_2$ enhancement (Supplementary text).

As further control of our hypothesis, we also measured the $\Delta R_2/\Delta T$ slopes in the presence of sub-stoichiometric amounts of a potent aggregation inhibitor, Human Serum Albumin (HSA), which shields αS monomers from oligomers.[12] As expected, a switch from positive to non-positive $\Delta R_2/\Delta T$ slopes is observed for several NAC residues, while the $\Delta R_2/\Delta T$ values for the N- and C-termini remain negative (Fig. 1b, *light blue vs. magenta* and Fig. 1d). While the sign of the $\Delta R_2/\Delta T$ can effectively discern between self-

association and intrinsic monomer dynamics, it relies on the assumption that the linear model is a good fit. Hence, we also examined another hallmark of self-association, which is the non-linearity of the R_2 *vs.* temperature dependency (*vida infra*).

5.4.2 Non-linear ^{15}N-R_2 Temperature-Dependence is a Hallmark of Oligomer Formation.

Besides the positive $\Delta R_2/\Delta T$ slope, another distinctive feature of residues sensing self-association is the non-linearity of the $^{15}N - R_2$ temperature-dependence (Fig. 1b, lower panel, *light blue dashed line*). To quantify such non-linearity, we computed the residue-specific root mean squared deviations (RMSDs) of the experimental R_2 values from the fitted linear model. The RMSD values clearly identify a main cluster of residues localized at the NAC region with significant deviations from linearity (Fig. 1e). It is notable that deviation from linearity is significantly diminished in the presence of the HSA inhibitor, which suppresses most observed RMSD values to baseline (Fig. 1f), further supporting the notion that the non-linearity of the $^{15}N - R_2$ *vs.* T plots is a hallmark of self-association. We also complemented the non-linearity RMSD analysis with quadratic fits of the experimental $^{15}N - R_2$ *vs.* T plots, *i.e.* the simplest possible non-linear model. The quadratic fits substantially reduce the RMSDs for residues with the greatest non-linear dependencies (Fig. S8 and supplementary text).

However, loss of linearity may also arise simply due to R_2 rates with large error margins and from binding of inhibitors to monomers. Hence, a more robust self-association map is obtained by filtering the residues with elevated RMSD for positive $\Delta R_2/\Delta T$ values. For this purpose, we plotted the $\Delta R_2/\Delta T$ *vs.* RMSD values and focused on residues with positive slopes and RMSD > average (Fig. 1g, h *upper right quadrant with purple highlights*). This $\Delta R_2/\Delta T$ *vs.* RMSD quadrant captures residues involved in self-association in the absence of HSA (Fig. 1g) and, as expected, is significantly less populated in the presence of HSA (Fig. 1h). The filtering intrinsic to the $\Delta R_2/\Delta T$ *vs.* RMSD plot removes false positives arising from measurement error, such as for example residue 30 for αS alone (Fig. 1g, *grey annotation* and Fig. S3) and residues 11, 126, 134 and 137 for αS + HSA (Fig. 1h, *grey annotation* and Fig. S3, S6, S7). The C-terminal residues fall within the HSA binding site in αS monomers[12] and lead to substantial enhancements in 15N – R2 (Fig. S7, red), resulting in the poor linear fits observed. Notably, residues identified through the $\Delta R_2/\Delta T$ *vs.* RMSD plots exhibit statistically higher deviation from linearity compared to the remaining residues not identified (Fig. 1i). Such deviation is lost in the presence of HSA (Fig. 1j). Overall, these results suggest that positive $\Delta R_2/\Delta T$ slopes and the R_2 *vs.* T non-linearity are two complementary distinguishing signatures of self-association sites, which are effectively identified through $\Delta R_2/\Delta T$ *vs.* RMSD plots.

5.4.3 αS Concentration-Dependence Further Validates $\Delta R_2/\Delta T$ Approach as a Method to Identify Self-Association Sites.

To further validate the $\Delta R_2/\Delta T$ approach for the identification of self-association sites, we repeated the temperature-dependent R_2 protocol using a two-fold higher concentration of αS[7,16], *i.e.* 400 μM. Increased concentration is expected to promote the nucleation and growth of αS oligomers[35] and in turn a more pronounced non-linear and positive R_2 *vs.* temperature dependency is anticipated to occur. Indeed, a larger set of residues within the NAC region exhibit high $\Delta R_2/\Delta T$ and RMSD from linear values as the concentration is increased (Fig. 2a-c). Moreover, the change in sign of the $\Delta R_2/\Delta T$ slopes from negative to positive occurs at earlier temperatures (Fig. 2d, e). These observations are consistent with the $\Delta R_2/\Delta T$ being exquisitely sensitive to changes in the population of oligomers in dynamic exchange with monomers, leading to a characteristic positive and non-linear R_2 *vs.* temperature dependency, as represented by the $\Delta R_2/\Delta T$ *vs.* RMSD plots (Fig. 1g,h; Fig. 2c). Nonetheless, an effective approach to capture both conditions simultaneously, without relying on possibly ill-defined slopes of non-linear plots and without any assumption on the nature of deviation from non-linearity *e.g.* the quadratic assumption, is through thermal-R_2 clustering analyses.

5.4.4 Thermal R_2 Clustering Analyses Systematically Partition Residues involved in Self-association *vs.* internal Dynamics.

Given that residues involved in self-association exhibit positive $\Delta R_2/\Delta T$ values, whereas residues experiencing intrinsic monomer dynamics show negative $\Delta R_2/\Delta T$ slopes, R_2 correlations between pairs of residues are expected to offer unique signatures depending on the nature of the two correlated residues. The simplest case is for pairwise R_2 correlations between αS residues not significantly involved in self-association (*e.g.* residues in the N- or C-termini; Fig. 3a-c). Fig. 3a-c show that, when two residues experience primarily internal monomer dynamics, a positive slope and Pearson's correlation coefficient (*r*) is observed for the pairwise R_2 correlations. This is expected because R_2 depends linearly on the temperature for both residues and for both residues the $\Delta R_2/\Delta T$ slopes are negative (Fig. 3a-c). In contrast, when a residue involved in internal dynamics (linear, negative $\Delta R_2/\Delta T$) is correlated with a residue experiencing self-association (non-linear, positive $\Delta R_2/\Delta T$), such as in the NAC region, the result is a negative Pearson's correlation coefficient (Fig. 3d, e). In this case, the correlation coefficient is also weakened due to the non-linearity of the R_2 *vs.* temperature dependency for the residue involved in self-association (Fig. 3d, e). In the final scenario, when two residues involved in self-association (positive $\Delta R_2/\Delta T$) are correlated, a positive Pearson's correlation coefficient is observed (Fig. 3f). Therefore, homotypic residue pairs result in strong, positive linear pairwise R_2 correlations (Fig. 3a-c, f), while heterotypic residue pairs lead to weak, negative pairwise R_2 correlations (Fig. 3d,e).

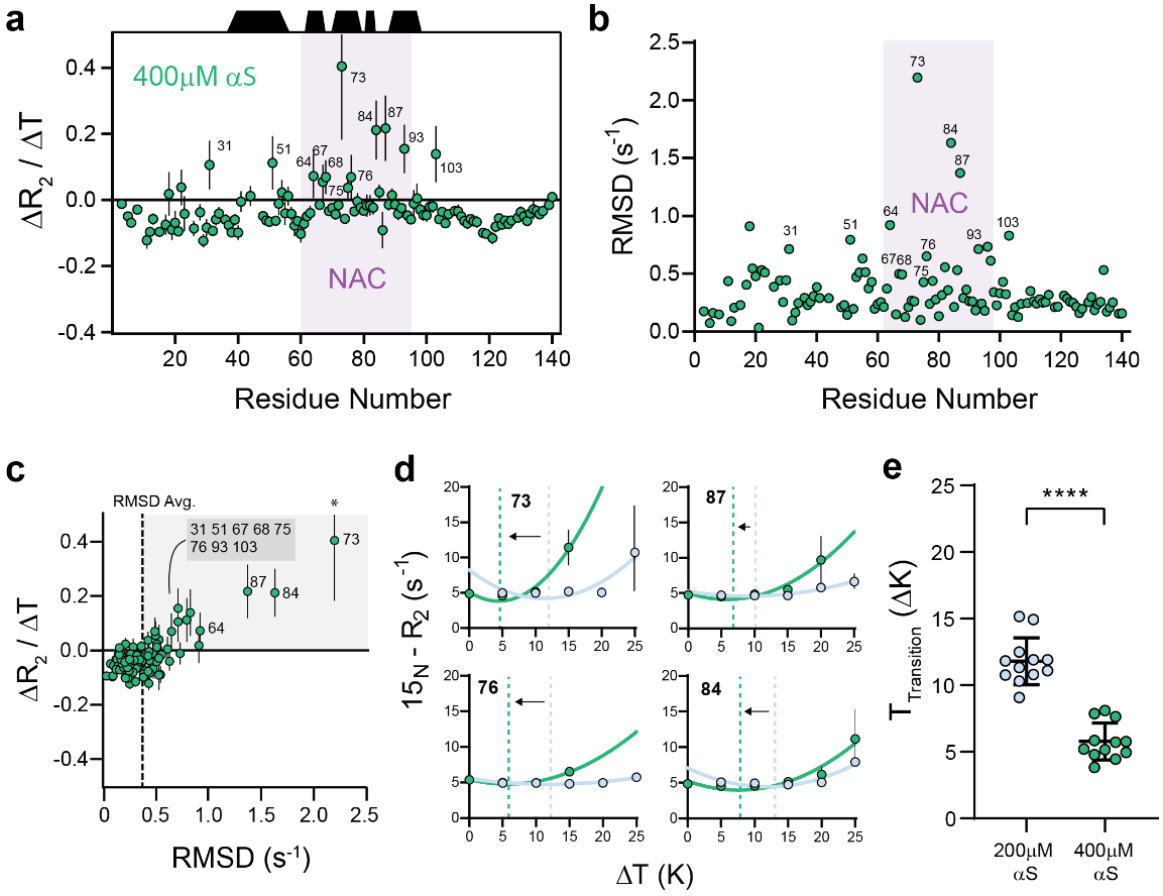

Figure 2. *αS concentration-dependence of $\Delta R_2/\Delta T$.* (a) Residue-specific slopes from the linear fittings of the temperature-dependent $^{15}N - R_2$ profiles of 400 μM αS. Annotations are as in Fig. 1c. (b) Residue-specific RMSD computed as for Fig. 1e. (c) Relationship between slope and RMSD of αS $^{15}N - R_2$ *vs.* temperature. Annotations are as in Fig. 1g. The asterisk (*) indicates off-scale extension of the error bar. (d) Representative R_2 *vs.* T profiles for select residues identified in the purple quadrant in (c) for 200 μM αS (*blue*) and 400μM αS (*green*). Dashed lines indicate the temperature at which the transition from negative to positive slope *i.e.* $T_{transition}$ occur. (e) Unpaired parametric T-Test for the comparison of $T_{transition}$ between the 200 μM (*blue*) and 400 μM (*green*) αS samples. Annotated residues identified through the RMSD *vs.* $\Delta R_2/\Delta T$ comparison in (c) were used as inputs for the T-test. **** indicates a p value <0.0001.

Based on the distinct unique homo- *vs.* hetero-typic R_2 correlation signatures, systematically performing R_2 pairwise correlations for every residue pair, *i.e.* creating an R_2 correlation matrix, allows for the identification of distinct clusters of residues involved in self-association and internal dynamics. Notably, residues involved in self-association correlate positively with one another. Similarly, residues involved in internal dynamics will also correlate positively. However, the two sets will correlate negatively and, on that basis, the internal dynamics *vs.* self-association clusters can be partitioned. An effective method to quantitatively extract distinct clusters based on the magnitude and direction (positive *vs.* negative) of pairwise correlations is single-linkage agglomerative clustering analysis. When applied to αS, five distinct

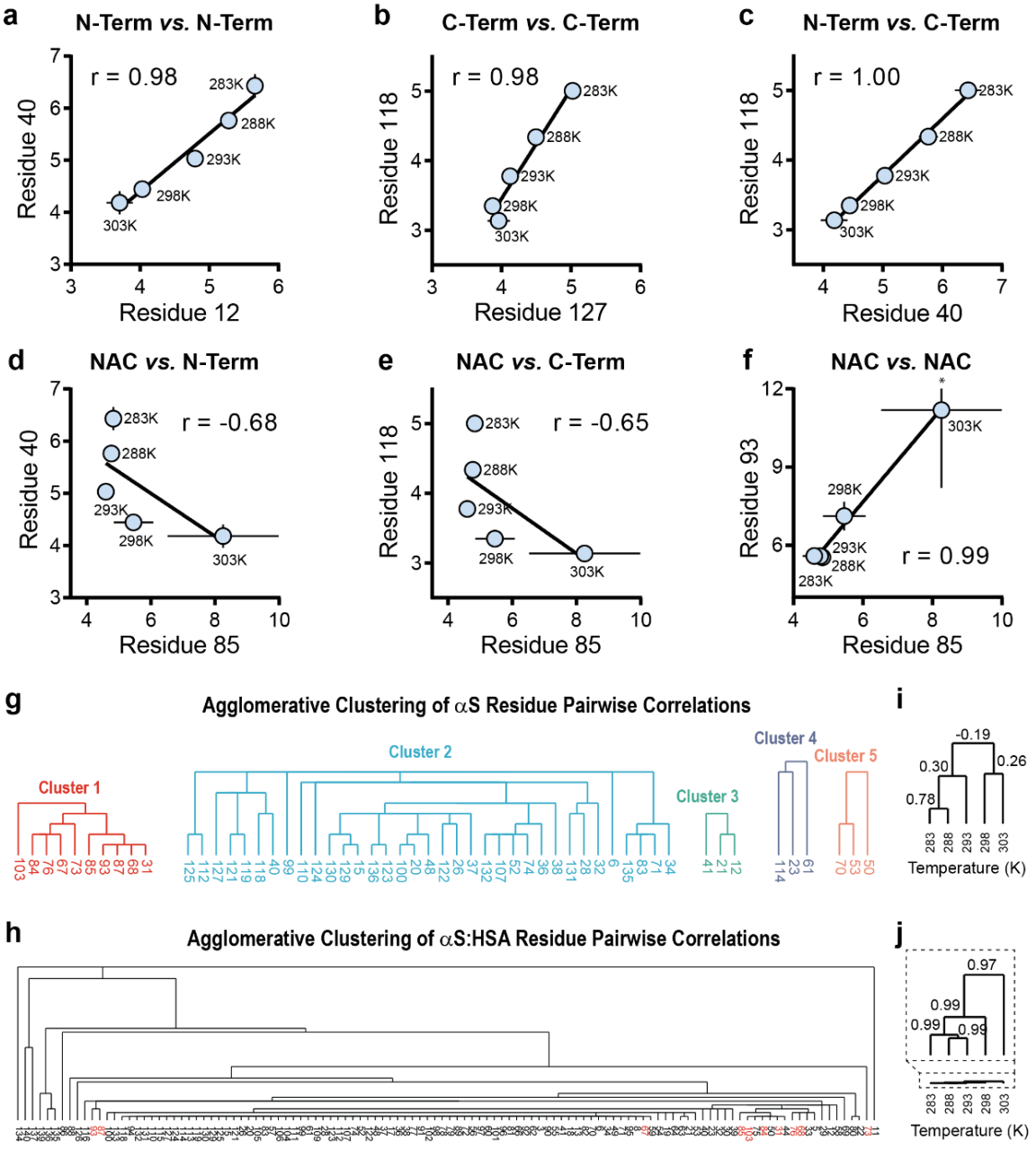

Figure 3. *Thermal* R_2 clustering analysis partitions residues primarily involved in oligomerization *vs.* internal dynamics. (a – f) Representative pairwise ^{15}N-R_2 correlations illustrating whether a pair of residues exhibits a concerted change in R_2 as a function of temperature. Homotypic correlations are shown in panel a-c and f. The other two correlations (d, e) are heterotypic. The asterisk (*) indicates the off-scale extension of the error bar. (g) Dendrograms identifying clusters of αS residues with concerted changes in R_2 *vs.* temperature. Each cluster is comprised of residues with Pearson correlation coefficients (r) ≥ 0.99. (h) As (g) except for αS in the presence of HSA. (i) Dendrogram showing how the αS residues partition the five temperatures used in the SATIRE analysis. (j) As (i) except in the presence of HSA. A zoomed in dendrogram is shown in the dashed box to highlight the negligible partitioning of the temperatures.

clusters with Pearson's correlation coefficient ≥ 0.99 are observed (Fig. 3g). Notably, cluster 1 contains all the residues identified through the RMSD *vs.* $\Delta R_2/\Delta T$ analysis (Fig. 1g), indicating that this cluster uniquely maps to sites of self-association. In stark contrast, addition of HSA generates one major single-linkage cluster with $r \geq 0.99$ (Fig. 3h), as expected given that HSA stabilizes αS monomers, which results in linear R_2 *vs.* T plots with negative $\Delta R_2/\Delta T$ slopes for most residues (homotypic correlations). These findings are in agreement with the RMSD *vs.* $\Delta R_2/\Delta T$ analysis, which shows that, in the presence of HSA, most αS residues cluster together with negative $\Delta R_2/\Delta T$ and low RMSD values (Fig. 1h). The $\Delta R_2/\Delta T$ vs. RMSD and the thermal R_2 clustering analyses therefore validate each other.

An effective means to further substantiate the combined $\Delta R_2/\Delta T$ *vs.* RMSD and thermal R_2 clustering analyses, is to perform the clustering analysis in reverse, essentially transposing the residue x temperature R_2 matrix. In this case, the correlations are now between pairs of temperatures (as opposed to residues) and the R_2 values for the residues (as opposed to temperatures) are used as points to build the correlation. This analysis evaluates how the residues partition the different temperatures. If the residues are involved in self-association, the temperatures will not be evenly partitioned due to the non-linear dependency of R_2 *vs.* T. Indeed, for αS alone the highest two temperatures are effectively separated from the remaining lower temperatures (Fig. 3i), consistent with the dramatic enhancement in R_2 at high temperatures. In contrast, no significant temperature partitioning is observed in the presence of HSA (Fig. 3j), consistent with a linear R_2 *vs.* temperature dependency. Notably, given the molecular weight of the oligomer species, chemical shifts are largely insensitive to the formation of the soluble oligomers formed through the temperature ramp (Fig. S9). Moreover, the temperature-dependent solvent exchange of αS amide protons precludes the identification of self-association sites through $^{1}H - {}^{15}N$ HSQC intensities (Fig. S2d, e)

5.5 Discussion

Our results show that the temperature dependent changes in $^{15}N - R_2$ provide a residue-resolution map of the early self-association sites in amyloidogenic proteins, with minimal bias from intrinsic monomer dynamics, an effect often confounding the interpretation of conventional $^{15}N - R_2$ measurements[16]. These two contributions *i.e.* self-association and monomer dynamics are effectively separated based on two key discerning features. First, residues sensing self-association exhibit enhancements in $^{15}N - R_2$ upon heating (positive $\Delta R_2/\Delta T$), while other residues show a characteristic decrease (negative $\Delta R_2/\Delta T$), typical of purely monomeric IDPs. Second, for residues involved in self-association the R_2 *vs.* temperature dependence is non-linear, whereas other sites display a linear R_2 *vs.* temperature dependence, as expected for monomeric species. These two dichotomous temperature-induced signatures are effectively assessed through the analysis of the $\Delta R_2/\Delta T$ *vs.* RMSD plots, wherein self-association residues with high RMSD from

linear values and positive $\Delta R_2/\Delta T$ are distinctively found in the upper right quadrant (Fig. 1g and 2c). Notably, the intersection of residues with high RMSD and positive $\Delta R_2/\Delta T$ values largely removes false positives arising from experimental errors and monomer binding by inhibitors (Fig. 1g, h, *bottom right quadrant*). These temperature-dependent features linked to self-association are further validated by experiments at higher protein concentrations and in the presence of potent aggregation inhibitors, which serve as positive and negative controls, as they exhibit more (Fig. 2) or less pronounced R_2 *vs.* T effects (Fig. 1, *red*), respectively.

Here, we also propose a more systematic approach to analyze the R_2 vs. T data that does not rely on *a priori* assumptions regarding the nature of R_2 *vs.* T dependency, *i.e.* linear *vs.* quadratic. This approach is the thermal R_2 clustering analysis (Fig. 3), wherein the Pearson's correlation coefficient (*r*) for the pairwise residue *vs.* residue R_2 plots is used to discern sites involved in self-association *vs.* primarily monomer dynamics. Homotypic residue correlations *i.e.* correlations between two residues both involved in either self-association or monomer dynamics, result in strong, positive *r* values (Fig. 3a-c, f), while heterotypic correlations result in weak, negative *r* values (Fig. 3d, e). Notably, the strength of the heterotypic correlations determines the degree to which the two sets of homotypic correlations are segregated. Based on these different patterns for homo- *vs.* heterotypic correlations, the single-linkage agglomerative clustering of the thermal R_2 correlation matrix effectively separates out distinct clusters of residues involved in self-association. When applied to αS, this approach reveals a unique cluster of aggregation prone residues (Fig. 3g) that overlap with those determined through the RMSD *vs.* $\Delta R_2/\Delta T$ analysis (Fig. 1h).

The residues involved in self-association, as identified through the combined RMSD *vs.* $\Delta R_2/\Delta T$ and thermal R_2 clustering analyses at both low and high αS concentrations, include: G31, G51, T64, G67, G68, G73, T75, A76, G84, A85, S87, G93 and N103 (Fig. 4a). Most of these residues are glycines or other amino acids with small side chains, possibly owing to the conformational flexibility of the oligomers[36,37] and the plasticity of these amino acids. Nonetheless, other residues containing small side chains within these segments are not identified (Fig. 4a). Notably, a large subset of the residues identified fall within the NAC region and its subsection, the NACore (residues 71-82), which has been shown previously to be sufficient to form amyloids[28]. Moreover, synthetic mutations G67P, A76P, A85P (Fig. 4a), as well as deletions Δ71-82 and Δ85-94 have been shown to strongly perturb the aggregation kinetics of αS.[38] Furthermore, O-GlcNAcylation of T75 and both phosphorylation and O-GlcNAcylation of S87 significantly inhibit the aggregation propensity and toxicity of αS (Fig. 4a).[26,39] Interestingly, the SATIRE also identifies residues outside of the NAC region *i.e.* G31 and G51 which fall within the αS N-terminal segment susceptible to familial mutations *e.g.* A30P, E46K, H50Q, G51D and A53T (Fig. 4a). These mutations alter the propensity

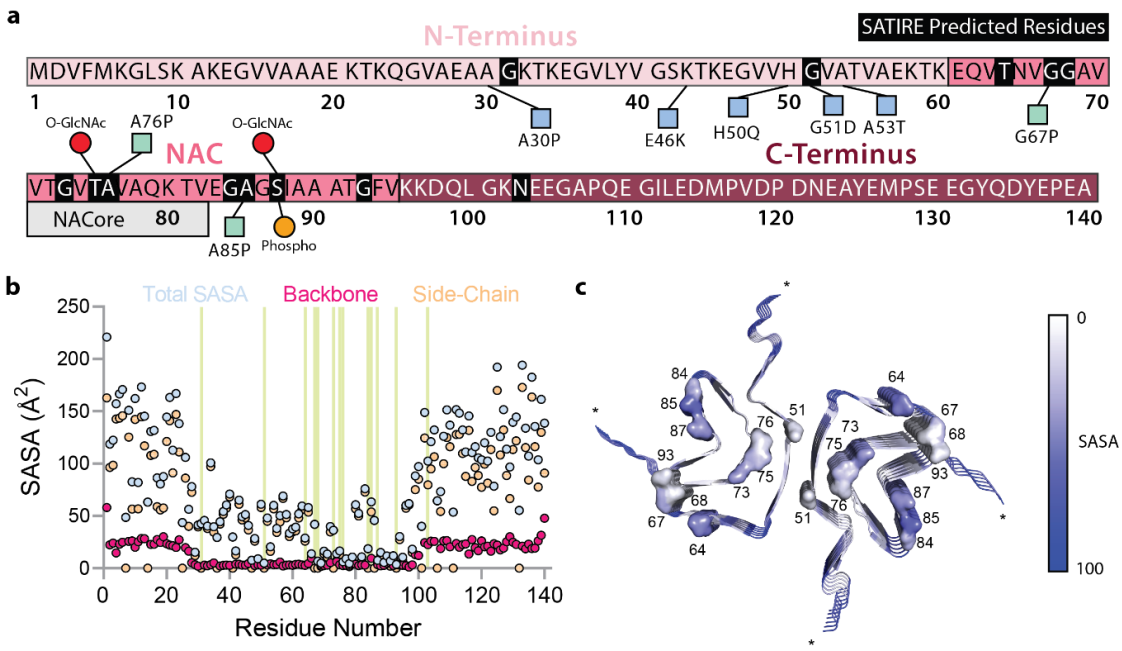

Figure 4. *Map of αS self-association sites identified through SATIRE.* (a) Map of the post-translational modifications and mutations of αS that alter kinetics of aggregation and their overlay with SATIRE predicted self-association sites. SATIRE predicted sites are shown in black highlights. Familial and synthetic mutations are indicated in blue and green boxes, respectively. O-GlcNAcylation and phosphorylation modifications are shown in red and orange circles, respectively. The NACore spanning residues 71-82 is indicated by a grey box. (b) Backbone (*red*), side-chain (*yellow*) and total (*blue*) solvent accessible surface areas (SASA) computed for αS fibrils (PDB ID: 2N0A). Residues identified through SATIRE are shown here in green highlight for comparison. (c) Residues identified through thermal R_2 clustering analysis (Cluster 1) are mapped on the αS fibril (PDB ID: 6A6B) structure. Asterisks (*) indicate disordered regions for which coordinates are not available. Residues 31 and 103 identified through the thermal R_2 clustering analysis fall within these disordered regions and are not shown.

of αS to aggregate and induce toxicity in mammalian cells[23–25,27,29]. Overall, mutagenesis studies provide compelling evidence in support of the role of the self-association sites identified through SATIRE.

Intriguingly, the self-association sites mapped here fall within the least solvent exposed sites of mature αS fibrils (Fig. 4b). This finding is consistent with a hierarchical assembly of amyloid fibrils, which starts from the most shielded sites.[40] Accordingly, when the SATIRE-identified self-association sites are mapped onto the structure of αS fibrils[41], they cluster within the interior of the fibril (Fig. 4c). Notably, although the SATIRE residues are not always contiguous in the primary sequence, they appear to form clusters of residues in close spatial proximity within the fibril structure (Fig. 4c). Moreover, residues at the interface between two protofilaments, which are involved in the supramolecular assembly of mature fibrils, are identified by the SATIRE as only marginally involved in self-association leading to soluble oligomers. This observation suggests that interfilament interactions are dispensable for formation of soluble oligomeric species.[42]

Overall, the SATIRE method presented here emerges as a robust NMR toolset to map at atomic resolution the self-association sites within IDPs prone to form cytotoxic oligomers. Given that αS is a prototype for a broad range of amyloidogenic proteins, it is anticipated that the SATIRE can be extended to other amyloidogenic systems amenable to be prepared in largely monomeric form at NMR detectable concentrations and low temperature. In fact, SATIRE relies on the thermally-induced transition from monomeric to oligomeric species, which manifests itself in the non-linear temperature-dependence of ^{15}N-R_2 rates and the positive $\Delta R_2/\Delta T$ slopes. One of the distinct advantages of methods starting from monomers is that they are typically more reproducible than other techniques requiring concentrated samples with pre-existing oligomers. Lastly, the results herein indicate the strength of the SATIRE approach to map the effect of aggregation inhibitors, for which HSA serves as a model system.

5.6 Experimental Section

Alpha Synuclein Expression and Purification, Monomer Preparation and Temperature Dependent ^{15}N – R_2 Protocols

Alpha synuclein (αS) was expressed in *E. Coli BL21(DE3)* cells using the pT7-7 plasmid harboring the αS sequence and purified as described previously[12]. Purified αS was buffer exchanged into ultrapure ddH_2O on a 10kDa amicon filter, injected into a Superdex 200 increase 10/300 analytical gel filtration column (GE healthcare) and the monomeric fraction was extracted and lyophilized for storage at -20°C. For preparation of the αS sample for temperature-dependent ^{15}N – R_2 data acquisition, lyophilized αS powder was resuspended in 50 mM HEPES pH 7.4, 0.05% NaN_3 and 5% D_2O to a final concentration of 200 µM. The total αS concentration was determined by A_{280} measurements using an extinction coefficient of 5,600 $M^{-1}\cdot cm^{-1}$ [15]. As an internal reference standard, 50 µM ^{15}N – Acetyl – Glycine was spiked into the sample.

The 200 µM (or 400 µM) αS sample was subsequently placed into the NMR spectrometer or a temperature-controlled water bath and subjected to a temperature gradient from 278K – 303K at increments of 5K. Incubation at each temperature lasted for approximately 48 hours, with six hours dedicated to acquisition of four HSQC spectra at the onset of temperature changes, 40 hours dedicated to ^{15}N – R_2 data acquisition and an additional 1.5 hours to acquire an HSQC spectrum to monitor sample stability post ^{15}N – R_2 acquisition. A schematic diagram detailing the temperature-dependent ^{15}N – R_2 protocol is shown in Figure S1a. Calibration of the NMR spectrometer temperature was performed as described previously[44].

Human Serum Albumin (HSA) Stock Preparation

Defatted, globulin free Human Serum Albumin (rHSA; Sigma Aldrich A3782) was purchased from Sigma Aldrich as lyophilized powder. The lyophilized powder was resuspended in 50 mM HEPES pH 7.4 to match alpha synuclein conditions and added to the αS sample to a final concentration of 50 µM. The concentration of HSA was determined through A_{280} measurements using an extinction coefficient of 30,810 $M^{-1}\cdot cm^{-1}$.

Analytical Size Exclusion Chromatography

200 µM αS (100 µL injection volume), prepared as described above, was resolved using a Superdex 200 increase 10/300 analytical gel filtration column (GE Healthcare) coupled to an AKTA FPLC running at 0.5 mL/min in 50mM HEPES pH 7.4 buffer.

General NMR Spectroscopy

All NMR data were acquired on a Bruker AV700 spectrometer equipped with a TCI Cryoprobe. All spectra were analyzed with TopSpin 4.0.6 and NMRFAM Sparky using Gaussian line-fitting. Additional details are discussed below.

$^{1}H - ^{15}N$ HSQC vs. HMQC chemical shift analysis to probe intermediate exchange

HSQC and HMQC spectra were acquired for a freshly dissolved 200 µM αS sample at both 283K and 303K. Both $^{1}H - ^{15}N$ HSQC and HMQC experiments were recorded with a recycle delay of 1.0s, 8 scans, 4K (t_2) and 200 (t_1) complex points for spectral widths of 16.23 ppm (^{1}H) and 35.00 ppm (^{15}N), respectively. Intermediate exchange contributions, or lack thereof, were determined by measuring chemical shift changes for αS resonances in HMQC *vs*. HSQC spectra[45].

$^{1}H - ^{15}N$ HSQC Intensity and chemical shift analysis to monitor αS self-association

$^{1}H - ^{15}N$ HSQC spectra were recorded at each temperature with a recycle delay of 1.0s, 16 scans, 4K (t_2) and 300 (t_1) complex points for spectral widths of 16.23 ppm (^{1}H) and 35.00 ppm (^{15}N), respectively. Chemical shift and intensity changes were measured through Gaussian fitting of the αS peaks in NMRFAM Sparky. Chemical shifts were externally referenced to DSS. To check for possible departures of the ^{1}H temperature-dependent chemical shifts from linearity, an F-test was conducted through the Curvalyzer tool, as implemented in the Shift Track software (University of Waterloo, Meiering Lab).[46]

Amide nitrogen transverse relaxation rates ($^{15}N - R_2$) to probe αS early self-association

^{15}N transverse relaxation rates were measured using a Bruker pseudo-3D pulse sequence with water flip back and sensitivity enhancement. The experiment was recorded with 16 scans, 16 dummy scans, a recycle delay of 1.30 s, 2K complex points for a spectral width of 13.73 ppm in the t_2 dimension and 300 complex points for a spectral width of 38.00 ppm in the t_1 dimension. The total CPMG lengths were 31.36, 62.72, 94.08, 125.44, 156.88 and 188.16 ms using a τ delay of 900 µs. The pseudo-3D spectra were processed with TopSpin 4.0.6 and the peak height decays were fitted to single exponentials in NMRFAM Sparky[47].

Agglomerative Clustering of ^{15}N-R_2 Pairwise Correlations

The $^{15}N - R_2$ measurements for each αS residue (rows) measured at five different temperatures (columns) were used to create a data matrix (**D**). The Pearson's correlation coefficients (r) were computed between each pair of residues in **D** using the $^{15}N - R_2$ measurements at five temperatures as points to build the correlation. Subsequent agglomerative clustering of the data using single linkage was performed through the Cluster 3.0 program (http://bonsai.hgc.jp/~mdehoon/software/cluster/) and the dendrogram trees were generated using JavaTreeview (http://jtreeview.sourceforge.net/). The clusters in Fig. 3g-h were identified using a cut-off value of 0.99 for the Pearson's correlation coefficient.

Solvent Accessible Surface Area (SASA) of αS Fibrils

The SASA of αS fibrils was computed through the Getarea software (http://curie.utmb.edu/getarea.html) based on the PDB ID: 6A6B αS fibril structure reported by Li and colleagues[41] and the PDB ID: 2N0A fibril structure by Tuttle et al.[48].

MD Simulation of amide nitrogen transverse relaxation rates ($^{15}N - R_2$) at increasing temperatures

The C-terminus (Residues 96 – 140) of αS was extracted from the micelle-bound structure (PDB ID: 1XQ8) and minimized using the AMBER ff99sbnmr force field.[49] The system was subsequently solvated in a rectangular box of the TIP4P-D water model[50] with a minimum distance of 23 Å from the edge of the solute to the wall of solvent. Twelve Na^+ ions were added to neutralize the system. All MD simulations

were performed at five temperatures *i.e.* 283, 288, 293, 298 and 303K, using the AMBER 18 software[8] on the Shared Hierarchical Academic Research Computing Network (SHARCNET). The αS C-terminal construct was simulated at each temperature for 1 μs using the GPU version pmemd.cuda implemented in the AMBER 18 software. Briefly, the system was energy minimized and an equilibration simulation was performed for 40 ps from 0 to 100K in the constant volume and temperature ensemble. Subsequently, a 120 ps equilibration from 100K to the desired temperature in the constant pressure and temperature (NPT) ensemble was conducted in intervals of 50K, when possible, with a restraint of 3 kcal/mol*Å^2 on the main chain atoms. Additional equilibrations were conducted for 200 ps with a restraint on the main chain atoms of 1 kcal/mol*Å^2 and 400 ps without any restraints. Lastly, a 1 μs simulation was performed at the desired temperature in the NPT ensemble with isotropic position scaling and a weak-coupling algorithm. During the simulations, the nonbonded cut-off was set to 12 Å with Particle Mesh Ewald implementation. A constant pressure of 1 atm was maintained using the Berendsen method. Structures were saved every 10000-time steps *i.e.* every 20 ps, for subsequent analyses. NMR ^{15}N R_2 transverse relaxations were calculated using the iRED approach[9] as implemented in the Amber 18 software.

5.7 References

(1) Chiti, F.; Dobson, C. M. Protein misfolding, functional amyloid, and human disease. *Annual review of biochemistry* **2006**, *75*, 333–366.

(2) Benilova, I.; Karran, E.; Strooper, B. de. The toxic Aβ oligomer and Alzheimer's disease: an emperor in need of clothes. *Nat Neurosci* **2012**, *15*, 349–357.

(3) Janowska, M. K.; Wu, K.-P.; Baum, J. Unveiling transient protein-protein interactions that modulate inhibition of alpha-synuclein aggregation by beta-synuclein, a pre-synaptic protein that co-localizes with alpha-synuclein. *Scientific reports* **2015**, *5*, 15164.

(4) Milojevic, J.; Esposito, V.; Das, R.; Melacini, G. Understanding the molecular basis for the inhibition of the Alzheimer's Abeta-peptide oligomerization by human serum albumin using saturation transfer difference and off-resonance relaxation NMR spectroscopy. *J. Am. Chem. Soc.* **2007**, *129*, 4282–4290.

(5) Milojevic, J.; Esposito, V.; Das, R.; Melacini, G. Analysis and parametric optimization of 1H off-resonance relaxation NMR experiments designed to map polypeptide self-recognition and other noncovalent interactions. *The journal of physical chemistry. B* **2006**, *110*, 20664–20670.

(6) Fawzi, N. L.; Ying, J.; Ghirlando, R.; Torchia, D. A.; Clore, G. M. Atomic-resolution dynamics on the surface of amyloid-β protofibrils probed by solution NMR. *Nature* **2011**, *480*, 268–272.

(7) Fawzi, N. L.; Ying, J.; Torchia, D. A.; Clore, G. M. Kinetics of amyloid beta monomer-to-oligomer exchange by NMR relaxation. *Journal of the American Chemical Society* **2010**, *132*, 9948–9951.

(8) Palmer, A. G. NMR characterization of the dynamics of biomacromolecules. *Chemical reviews* **2004**, *104*, 3623–3640.

(9) Kay, L. E. Protein dynamics from NMR. *Biochemistry and cell biology = Biochimie et biologie cellulaire* **1998**, *76*, 145–152.

(10) Hajduk, P. J.; Sheppard, G.; Nettesheim, D. G.; Olejniczak, E. T.; Shuker, S. B.; Meadows, R. P.; Steinman, D. H.; Carrera, G. M.; Marcotte, P. A.; Severin, J.; *et al.* Discovery of Potent Nonpeptide Inhibitors of Stromelysin Using SAR by NMR. *J. Am. Chem. Soc.* **1997**, *119*, 5818–5827.

(11) Esposito, V.; Das, R.; Melacini, G. Mapping polypeptide self-recognition through (1)H off-resonance relaxation. *J. Am. Chem. Soc.* **2005**, *127*, 9358–9359.

(12) Ahmed, R.; Huang, J.; Weber, D. K.; Gopinath, T.; Veglia, G.; Akimoto, M.; Khondker, A.; Rheinstädter, M. C.; Huynh, V.; Wylie, R. G.; *et al.* Molecular Mechanism for the Suppression of Alpha Synuclein Membrane Toxicity by an Unconventional Extracellular Chaperone. *Journal of the American Chemical Society* [Online early access]. DOI: 10.1021/jacs.0c01894.

(13) Ahmed, R.; VanSchouwen, B.; Jafari, N.; Ni, X.; Ortega, J.; Melacini, G. Molecular Mechanism for the (-)-Epigallocatechin Gallate-Induced Toxic to Nontoxic Remodeling of Aβ Oligomers. *J. Am. Chem. Soc.* **2017**, *139*, 13720–13734.

(14) Ahmed, R.; Akcan, M.; Khondker, A.; Rheinstädter, M. C.; Bozelli, J. C.; Epand, R. M.; Huynh, V.; Wylie, R. G.; Boulton, S.; Huang, J.; *et al.* Atomic resolution map of the soluble amyloid beta assembly toxic surfaces. *Chemical science* **2019**, *10*, 6072–6082.
(15) Fusco, G.; Chen, S. W.; Williamson, P. T. F.; Cascella, R.; Perni, M.; Jarvis, J. A.; Cecchi, C.; Vendruscolo, M.; Chiti, F.; Cremades, N.; *et al.* Structural basis of membrane disruption and cellular toxicity by α-synuclein oligomers. *Science (New York, N.Y.)* **2017**, *358*, 1440–1443.
(16) Anthis, N. J.; Clore, G. M. Visualizing transient dark states by NMR spectroscopy. *Quarterly reviews of biophysics* **2015**, *48*, 35–116.
(17) Lewandowski, J. R.; Halse, M. E.; Blackledge, M.; Emsley, L. Protein dynamics. Direct observation of hierarchical protein dynamics. *Science (New York, N.Y.)* **2015**, *348*, 578–581.
(18) Busi, B.; Yarava, J. R.; Hofstetter, A.; Salvi, N.; Cala-De Paepe, D.; Lewandowski, J. R.; Blackledge, M.; Emsley, L. Probing Protein Dynamics Using Multifield Variable Temperature NMR Relaxation and Molecular Dynamics Simulation. *The journal of physical chemistry. B* **2018**, *122*, 9697–9702.
(19) Nicola Salvi; Anton Abyzov; Martin Blackledge. Solvent-dependent segmental dynamics in intrinsically disordered proteins. *Science Advances* **2019**, *5*, eaax2348.
(20) Abyzov, A.; Salvi, N.; Schneider, R.; Maurin, D.; Ruigrok, R. W. H.; Jensen, M. R.; Blackledge, M. Identification of Dynamic Modes in an Intrinsically Disordered Protein Using Temperature-Dependent NMR Relaxation. *J. Am. Chem. Soc.* **2016**, *138*, 6240–6251.
(21) Xiang, W.; Menges, S.; Schlachetzki, J. C.; Meixner, H.; Hoffmann, A.-C.; Schlötzer-Schrehardt, U.; Becker, C.-M.; Winkler, J.; Klucken, J. Posttranslational modification and mutation of histidine 50 trigger alpha synuclein aggregation and toxicity. *Molecular neurodegeneration* **2015**, *10*, 8.
(22) Burré, J.; Sharma, M.; Südhof, T. C. Systematic mutagenesis of α-synuclein reveals distinct sequence requirements for physiological and pathological activities. *J. Neurosci.* **2012**, *32*, 15227–15242.
(23) Flagmeier, P.; Meisl, G.; Vendruscolo, M.; Knowles, T. P. J.; Dobson, C. M.; Buell, A. K.; Galvagnion, C. Mutations associated with familial Parkinson's disease alter the initiation and amplification steps of α-synuclein aggregation. *Proceedings of the National Academy of Sciences of the United States of America* **2016**, *113*, 10328–10333.
(24) Khalaf, O.; Fauvet, B.; Oueslati, A.; Dikiy, I.; Mahul-Mellier, A.-L.; Ruggeri, F. S.; Mbefo, M. K.; Vercruysse, F.; Dietler, G.; Lee, S.-J.; *et al.* The H50Q mutation enhances α-synuclein aggregation, secretion, and toxicity. *The Journal of biological chemistry* **2014**, *289*, 21856–21876.
(25) Ostrerova-Golts, N.; Petrucelli, L.; Hardy, J.; Lee, J. M.; Farer, M.; Wolozin, B. The A53T α-Synuclein Mutation Increases Iron-Dependent Aggregation and Toxicity. *J. Neurosci.* **2000**, *20*, 6048–6054.
(26) Oueslati, A.; Paleologou, K. E.; Schneider, B. L.; Aebischer, P.; Lashuel, H. A. Mimicking phosphorylation at serine 87 inhibits the aggregation of human α-synuclein and protects against its toxicity in a rat model of Parkinson's disease. *The Journal of neuroscience : the official journal of the Society for Neuroscience* **2012**, *32*, 1536–1544.
(27) Pandey, N.; Schmidt, R. E.; Galvin, J. E. The alpha-synuclein mutation E46K promotes aggregation in cultured cells. *Experimental neurology* **2006**, *197*, 515–520.
(28) Rodriguez, J. A.; Ivanova, M. I.; Sawaya, M. R.; Cascio, D.; Reyes, F. E.; Shi, D.; Sangwan, S.; Guenther, E. L.; Johnson, L. M.; Zhang, M.; *et al.* Structure of the toxic core of α-synuclein from invisible crystals. *Nature* **2015**, *525*, 486–490.
(29) Rutherford, N. J.; Moore, B. D.; Golde, T. E.; Giasson, B. I. Divergent effects of the H50Q and G51D SNCA mutations on the aggregation of α-synuclein. *Journal of neurochemistry* **2014**, *131*, 859–867.
(30) Esteban-Martín, S.; Silvestre-Ryan, J.; Bertoncini, C. W.; Salvatella, X. Identification of fibril-like tertiary contacts in soluble monomeric α-synuclein. *Biophysical journal* **2013**, *105*, 1192–1198.
(31) Wu, K.-P.; Baum, J. Detection of transient interchain interactions in the intrinsically disordered protein alpha-synuclein by NMR paramagnetic relaxation enhancement. *J. Am. Chem. Soc.* **2010**, *132*, 5546–5547.
(32) Cho, M.-K.; Nodet, G.; Kim, H.-Y.; Jensen, M. R.; Bernado, P.; Fernandez, C. O.; Becker, S.; Blackledge, M.; Zweckstetter, M. Structural characterization of alpha-synuclein in an aggregation prone state. *Protein science : a publication of the Protein Society* **2009**, *18*, 1840–1846.

(33) Dedmon, M. M.; Lindorff-Larsen, K.; Christodoulou, J.; Vendruscolo, M.; Dobson, C. M. Mapping long-range interactions in alpha-synuclein using spin-label NMR and ensemble molecular dynamics simulations. *J. Am. Chem. Soc.* **2005**, *127*, 476–477.
(34) Chi, E. Y.; Krishnan, S.; Randolph, T. W.; Carpenter, J. F. Physical stability of proteins in aqueous solution: mechanism and driving forces in nonnative protein aggregation. *Pharmaceutical research* **2003**, *20*, 1325–1336.
(35) Thanh, N. T. K.; Maclean, N.; Mahiddine, S. Mechanisms of nucleation and growth of nanoparticles in solution. *Chemical reviews* **2014**, *114*, 7610–7630.
(36) Glabe, C. G. Structural classification of toxic amyloid oligomers. *The Journal of biological chemistry* **2008**, *283*, 29639–29643.
(37) Campioni, S.; Mannini, B.; Zampagni, M.; Pensalfini, A.; Parrini, C.; Evangelisti, E.; Relini, A.; Stefani, M.; Dobson, C. M.; Cecchi, C.*; et al.* A causative link between the structure of aberrant protein oligomers and their toxicity. *Nature chemical biology* **2010**, *6*, 140–147.
(38) Waxman, E. A.; Mazzulli, J. R.; Giasson, B. I. Characterization of hydrophobic residue requirements for alpha-synuclein fibrillization. *Biochemistry* **2009**, *48*, 9427–9436.
(39) Levine, P. M.; Galesic, A.; Balana, A. T.; Mahul-Mellier, A.-L.; Navarro, M. X.; Leon, C. A. de; Lashuel, H. A.; Pratt, M. R. α-Synuclein O-GlcNAcylation alters aggregation and toxicity, revealing certain residues as potential inhibitors of Parkinson's disease. *Proceedings of the National Academy of Sciences of the United States of America* **2019**, *116*, 1511–1519.
(40) Fitzpatrick, A. W. P.; Debelouchina, G. T.; Bayro, M. J.; Clare, D. K.; Caporini, M. A.; Bajaj, V. S.; Jaroniec, C. P.; Wang, L.; Ladizhansky, V.; Müller, S. A.*; et al.* Atomic structure and hierarchical assembly of a cross-β amyloid fibril. *Proceedings of the National Academy of Sciences of the United States of America* **2013**, *110*, 5468–5473.
(41) Li, Y.; Zhao, C.; Luo, F.; Liu, Z.; Gui, X.; Luo, Z.; Zhang, X.; Li, D.; Liu, C.; Li, X. Amyloid fibril structure of α-synuclein determined by cryo-electron microscopy. *Cell research* **2018**, *28*, 897–903.
(42) Schmit, J. D.; Ghosh, K.; Dill, K. What drives amyloid molecules to assemble into oligomers and fibrils? *Biophysical journal* **2011**, *100*, 450–458.
(43) Kumari, P.; Frey, L.; Sobol, A.; Lakomek, N.-A.; Riek, R. 15N transverse relaxation measurements for the characterization of µs-ms dynamics are deteriorated by the deuterium isotope effect on 15N resulting from solvent exchange. *Journal of biomolecular NMR* **2018**, *72*, 125–137.
(44) Findeisen, M.; Brand, T.; Berger, S. A 1H-NMR thermometer suitable for cryoprobes. *Magnetic resonance in chemistry : MRC* **2007**, *45*, 175–178.
(45) Skrynnikov, N. R.; Dahlquist, F. W.; Kay, L. E. Reconstructing NMR spectra of "invisible" excited protein states using HSQC and HMQC experiments. *J. Am. Chem. Soc.* **2002**, *124*, 12352–12360.
(46) Trainor, K.; Palumbo, J. A.; MacKenzie, D. W. S.; Meiering, E. M. Temperature dependence of NMR chemical shifts: Tracking and statistical analysis. *Protein science : a publication of the Protein Society* **2020**, *29*, 306–314.
(47) Lee, W.; Tonelli, M.; Markley, J. L. NMRFAM-SPARKY: enhanced software for biomolecular NMR spectroscopy. *Bioinformatics (Oxford, England)* **2015**, *31*, 1325–1327.
(48) Tuttle, M. D.; Comellas, G.; Nieuwkoop, A. J.; Covell, D. J.; Berthold, D. A.; Kloepper, K. D.; Courtney, J. M.; Kim, J. K.; Schwieters, C. D.; Lee, V. M.*; et al. Atomic-resolution structure of alpha-synuclein fibrils*, 2016.
(49) Ulmer, T. S.; Bax, A.; Cole, N. B.; Nussbaum, R. L. Structure and dynamics of micelle-bound human alpha-synuclein. *The Journal of biological chemistry* **2005**, *280*, 9595–9603.
(50) Piana, S.; Donchev, A. G.; Robustelli, P.; Shaw, D. E. Water dispersion interactions strongly influence simulated structural properties of disordered protein states. *The journal of physical chemistry. B* **2015**, *119*, 5113–5123.

5.8 Supplementary Information

Discussion of other modes of $^{15}N - R_2$ enhancement besides self-association

It has previously been shown that the solvent exchange of amide protons with deuterium contributes to the apparent ^{15}N relaxation decay and results in an enhancement of the $^{15}N - R_2$ rates. This effect is amplified at higher temperatures[43]. However, the temperature-dependent enhancements in $^{15}N - R_2$ observed under our conditions are not expected to arise from the solvent exchange-induced deuterium isotope effect, as a low D_2O content of 5% was used for NMR experiments. Moreover, the deuterium isotope effect for αS is localized to both the N-terminus and the NAC region[43], yet we observe opposing temperature-dependent effects for these two segments under our conditions. Furthermore, it is unlikely that the enhancement in $^{15}N - R_2$ is due to intrinsic conformational exchange between multiple monomeric states in the intermediate exchange regime, as ruled out through HSQC *vs*. HMQC chemical shift comparisons at a single magnetic field for both low and high T measurements (Fig. S10).

Residues with high RMSD from linear fits aptly conform to a quadratic model

The simplest possible non-linear model *i.e.* quadratic fit was used to rule in the possibility of non-linear R_2 vs. temperature dependency. The quadratic fits identify αS residues with positive $\Delta R_2/\Delta T$ and high RMSD from linear values, as those with the most marked quadratic dependency (Fig. S8a, *annotated residues*). Notably, the quadratic model aptly fits the residues that do not conform to a linear relationship (Fig. 1e *vs*. Fig. S8b). Negligible improvements in fitting is observed for αS in the presence of HSA, in further support of HSA restoring for almost all residues the R_2 vs. T dependence to the linear pattern observed for monomers (Fig. S8c, d *vs*. Fig. 1d, f).

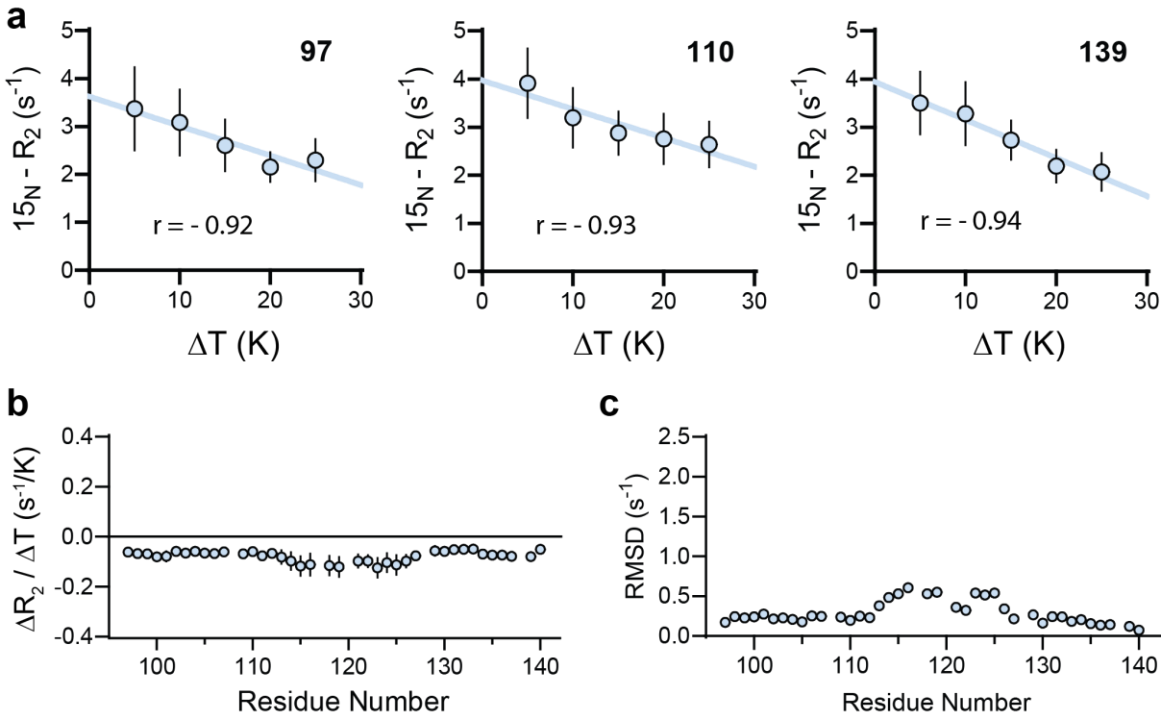

Figure S1. *MD simulations of the R_2 vs. temperature dependence for the C-terminal αS fragment (96-140) reveals a linear R_2 vs. T pattern with negative $\Delta R_2/\Delta T$ slope.* (a – c) Representative $^{15}N - R_2$ *vs.* temperature plots of select residues at the αS C-terminus. (b) Computed $\Delta R_2/\Delta T$ slopes from the linear fit of the simulated $^{15}N - R_2$ values at multiple temperatures in the 283K – 303K range. (c) Root mean squared deviation between the simulated $^{15}N - R_2$ values and the modeled values from the linear fits.

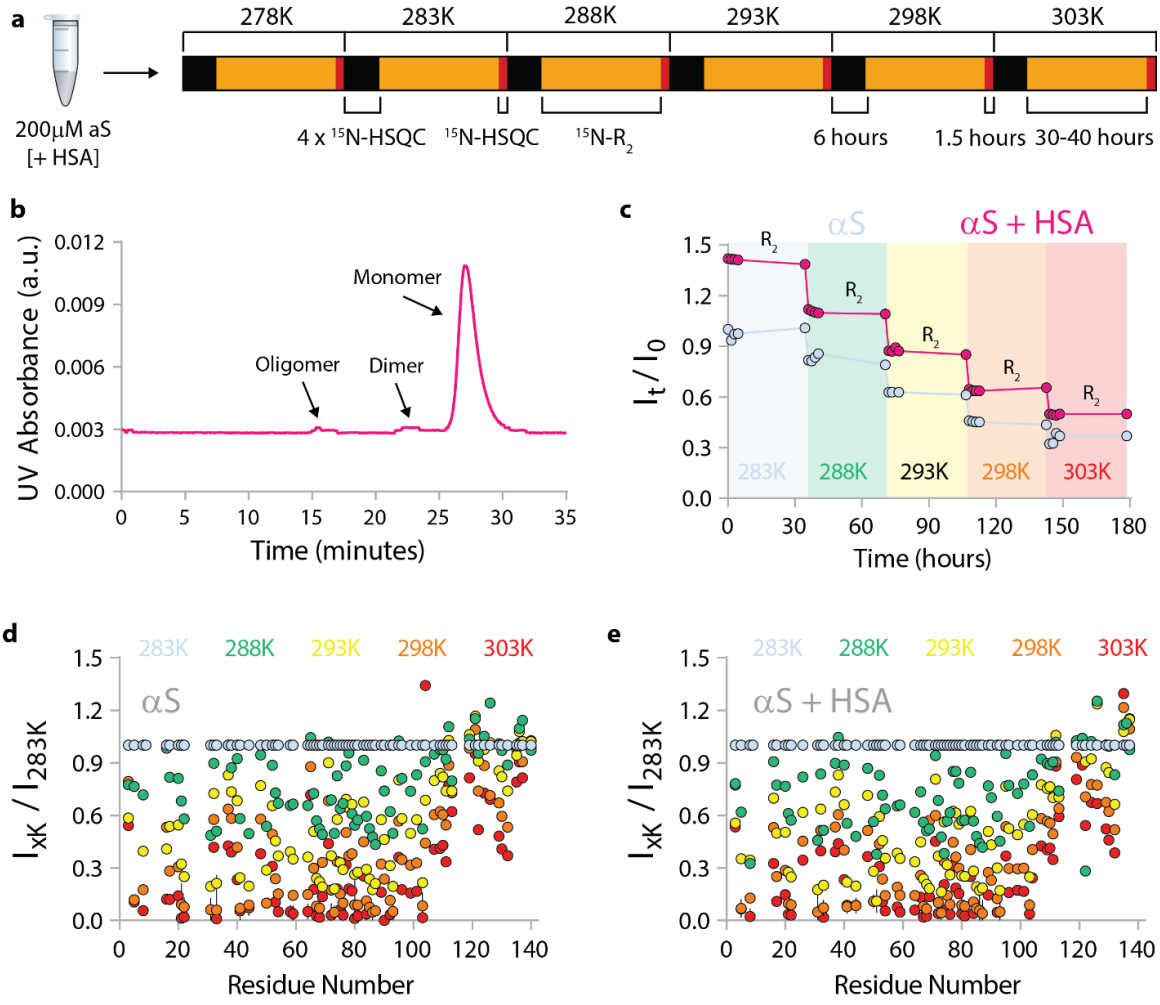

Figure S2. *Time-dependent temperature ramp protocol.* (a) Schematic depiction of the time-dependent temperature ramp protocol. (b) Analytical SEC chromatogram of the initial αS sample subjected to the temperature ramp. (c) Average HSQC intensities of αS at each temperature normalized to the starting temperature of 278K both in the absence (*blue*) and presence (*red*) of HSA. The HSQC intensities of αS + HSA sample were also normalized to the intensities of αS alone at 278K. (d) Residue-specific HSQC intensities of αS at each temperature normalized to the starting temperature of 278K. (e) As (d) except in the presence of HSA.

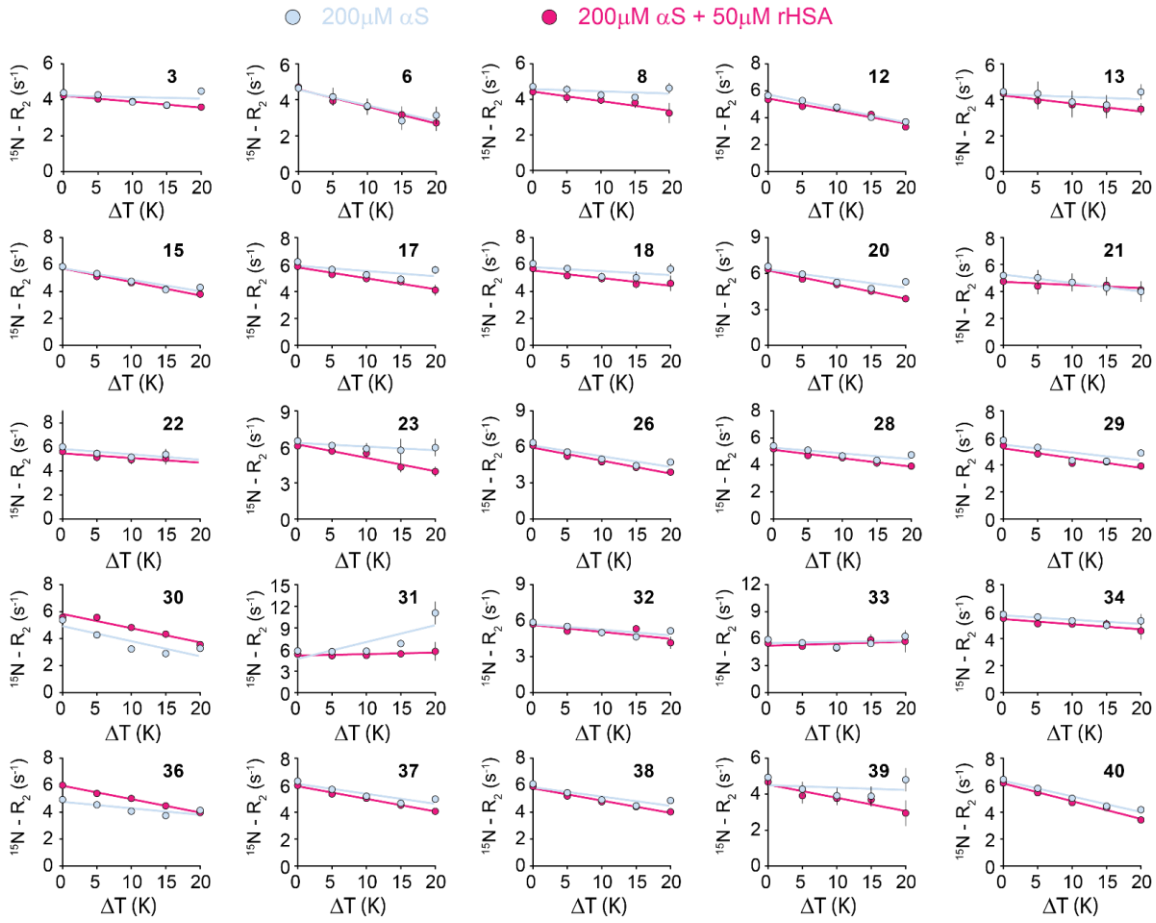

Figure S3. *^{15}N – R_2 vs. Temperature dependence for αS residues 3-40 in samples containing 200μM αS (blue) and 200μM αS + 50μM HSA (magenta).*

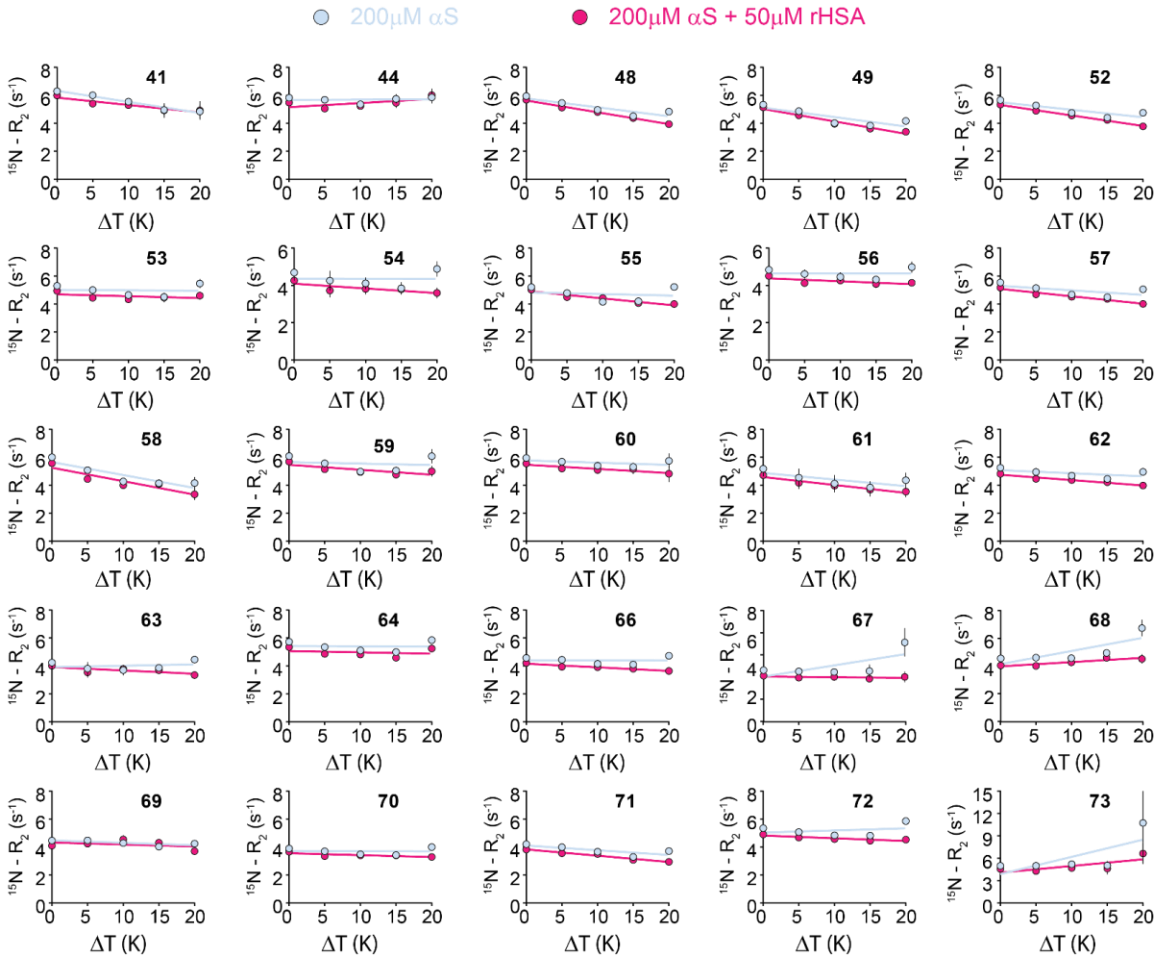

Figure S4. *$^{15}N - R_2$ vs. Temperature dependence for αS residues 41-73 in samples containing 200μM αS (blue) and 200μM αS + 50μM HSA (magenta).*

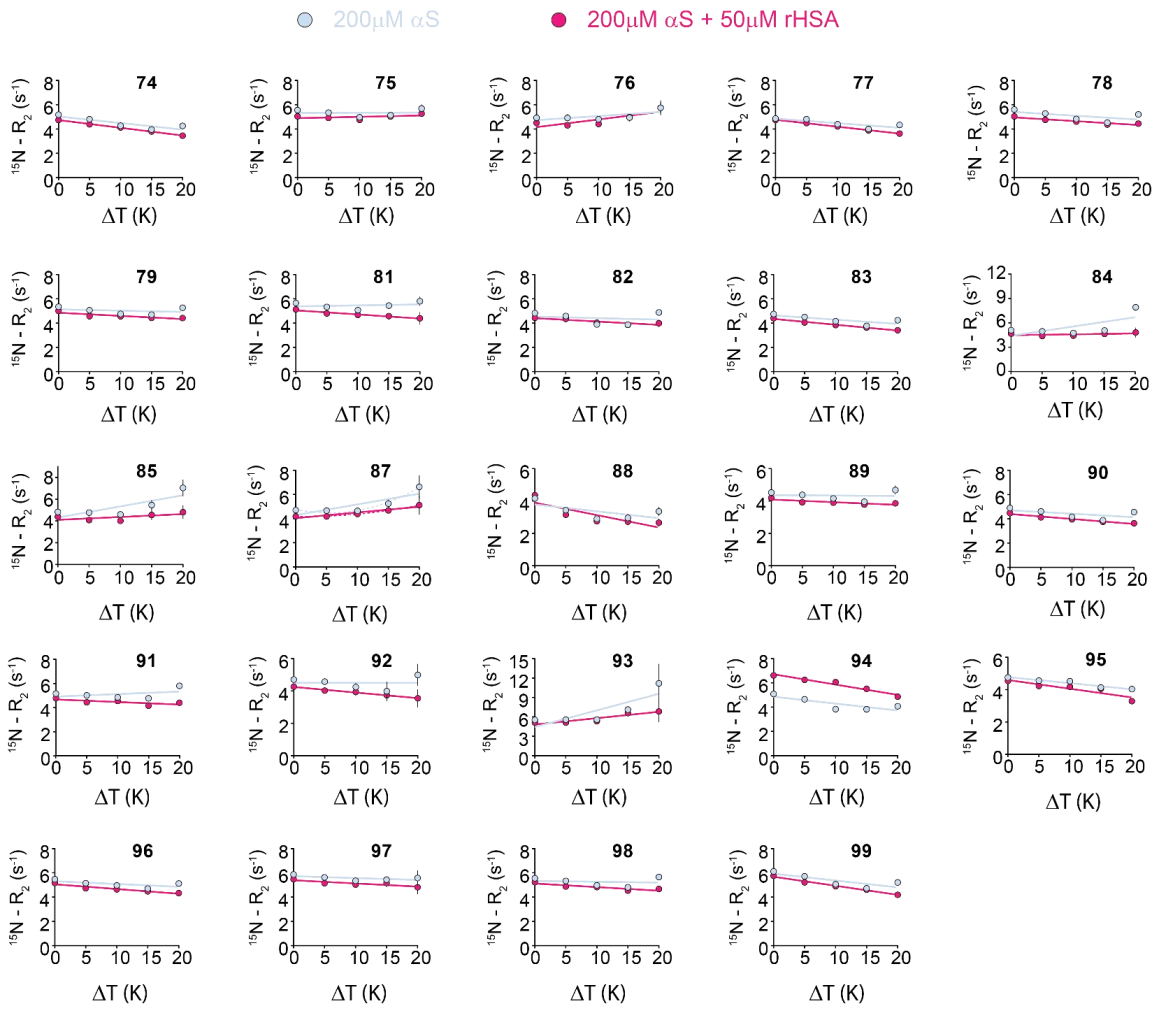

Figure S5. *$^{15}N - R_2$ vs. Temperature dependence for αS residues 74-99 in samples containing 200 μM αS (blue) and 200 μM αS + 50μM HSA (magenta).*

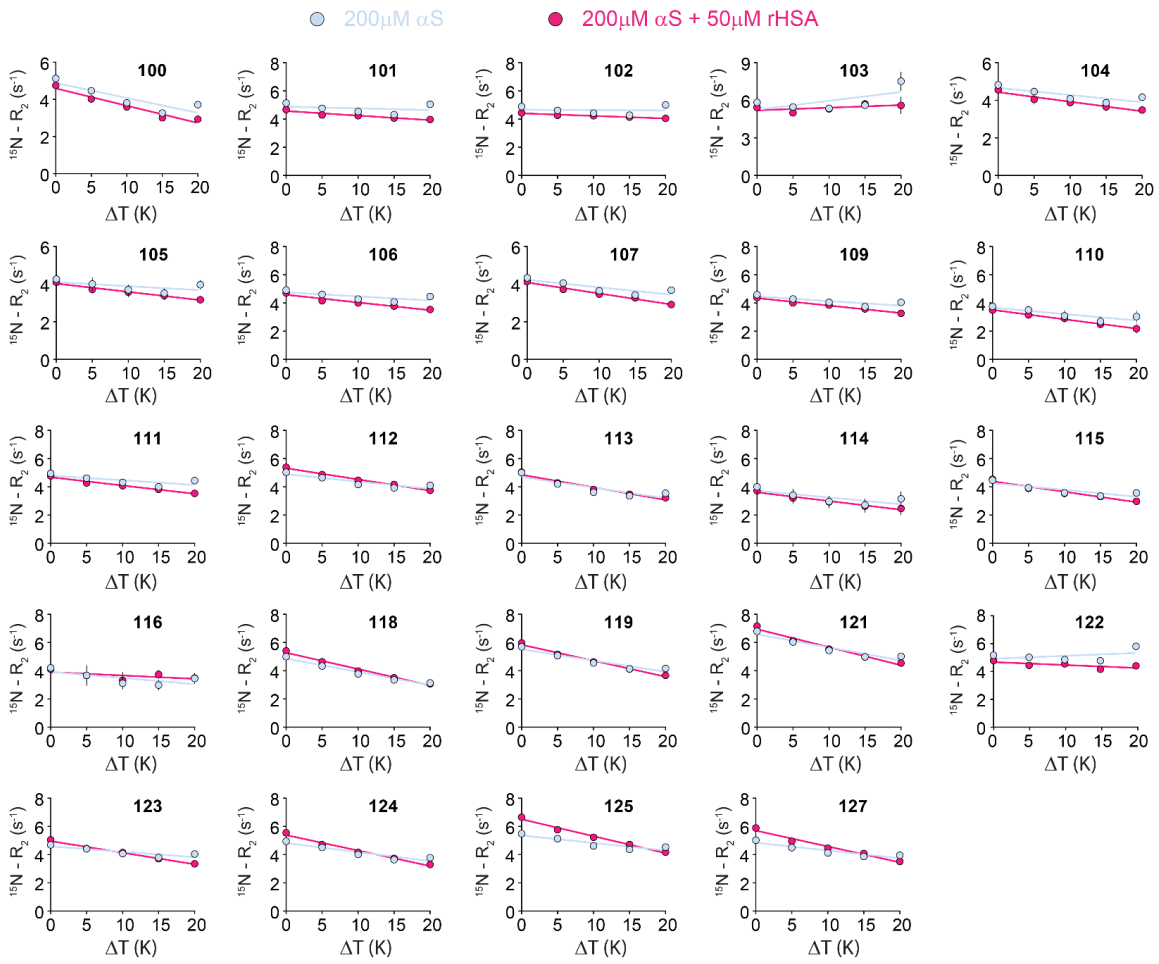

Figure S6. *$^{15}N - R_2$ vs. Temperature dependence for αS residues 100-127 in samples containing 200 μM αS (blue) and 200 μM αS + 50μM HSA (magenta).*

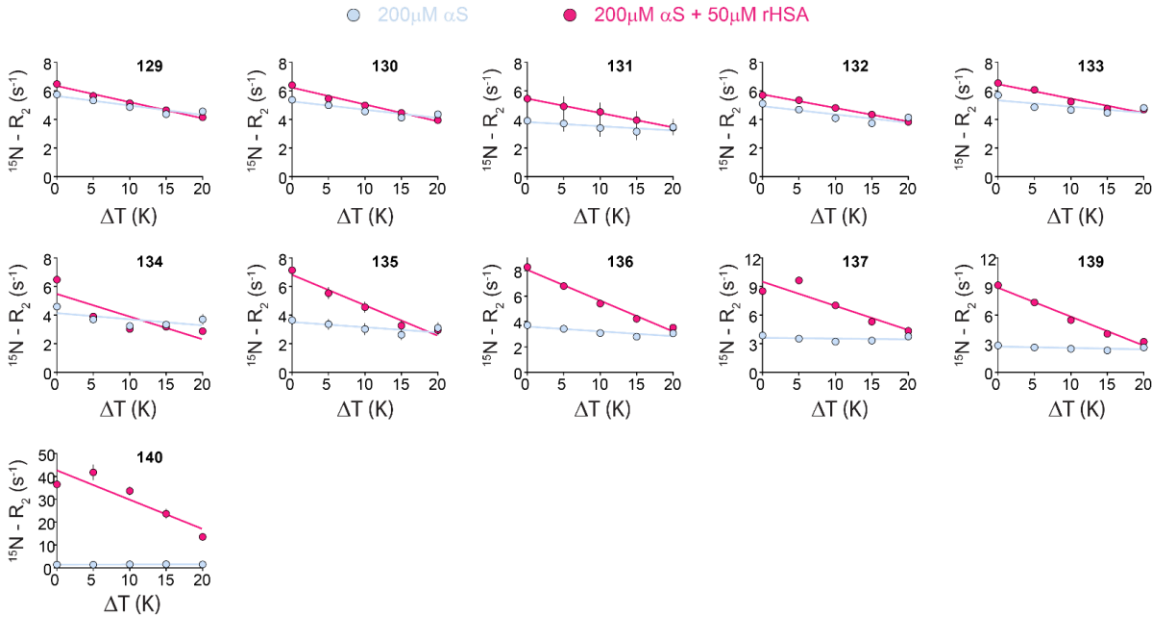

Figure S7. *$^{15}N - R_2$ vs. Temperature dependence for αS residues 129-140 in samples containing 200 μM αS (blue) and 200 μM αS + 50μM HSA (magenta).*

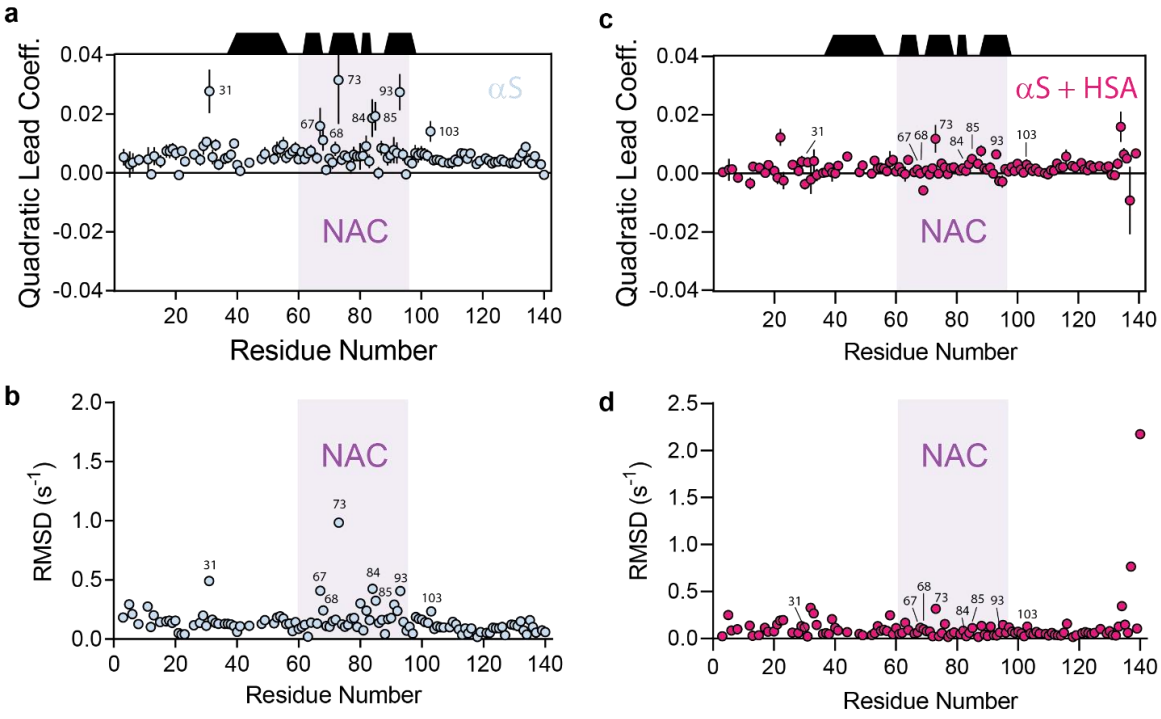

Figure S8. *Quadratic fitting of temperature-dependent ^{15}N-R_2 rates.* (a) Residue-specific quadratic leading coefficient from the quadratic fitting of the temperature-dependent ^{15}N – R_2 profiles of 200 μM αS. Black trapezoids indicate the positions of β-strands in the fibril structure (PDB ID: 2N0A), purple highlight indicates the NAC region and annotations indicate residues with a large positive slope. (b) As (a) except in the presence of 50 μM rHSA. Residues annotated in (a) are shown here for the purpose of comparison. (c) Residue-specific Root Mean Squared Deviation (RMSD) between the experimentally determined ^{15}N – R_2 values and the calculated values from the quadratic fitting of the experimental points. Purple highlight indicates the NAC region and annotations indicate residues with large RMSD. (d) As (c) except in the presence of 50μM rHSA. Residues annotated in (c) are shown here for the purpose of comparison.

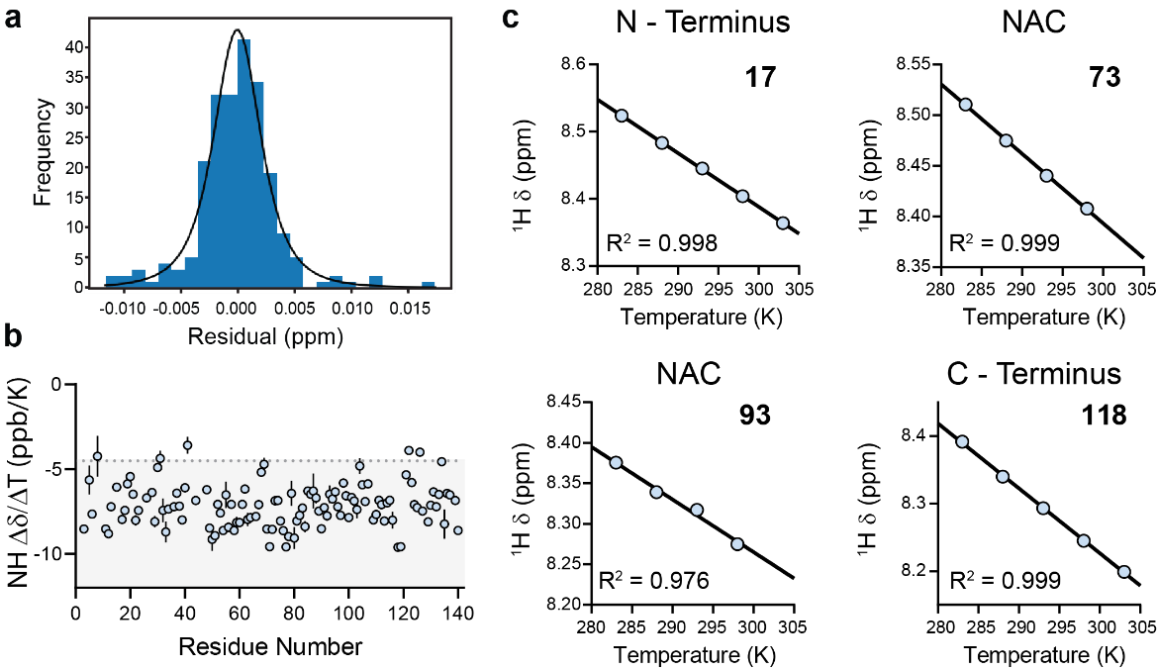

Figure S9. *Amide proton chemical shifts depend linearly on temperature.* (a) Frequency distribution of residuals from linear fitting of amide proton chemical shifts as a function of temperature. (b) Residue-specific amide proton temperature coefficients. Grey area indicates residues that are fully exposed. (c) Representative ^{1}H temperature dependent chemical shift plots for select residues at the N-terminus, NAC and C-terminus of αS. Chemical shifts were externally referenced to DSS.

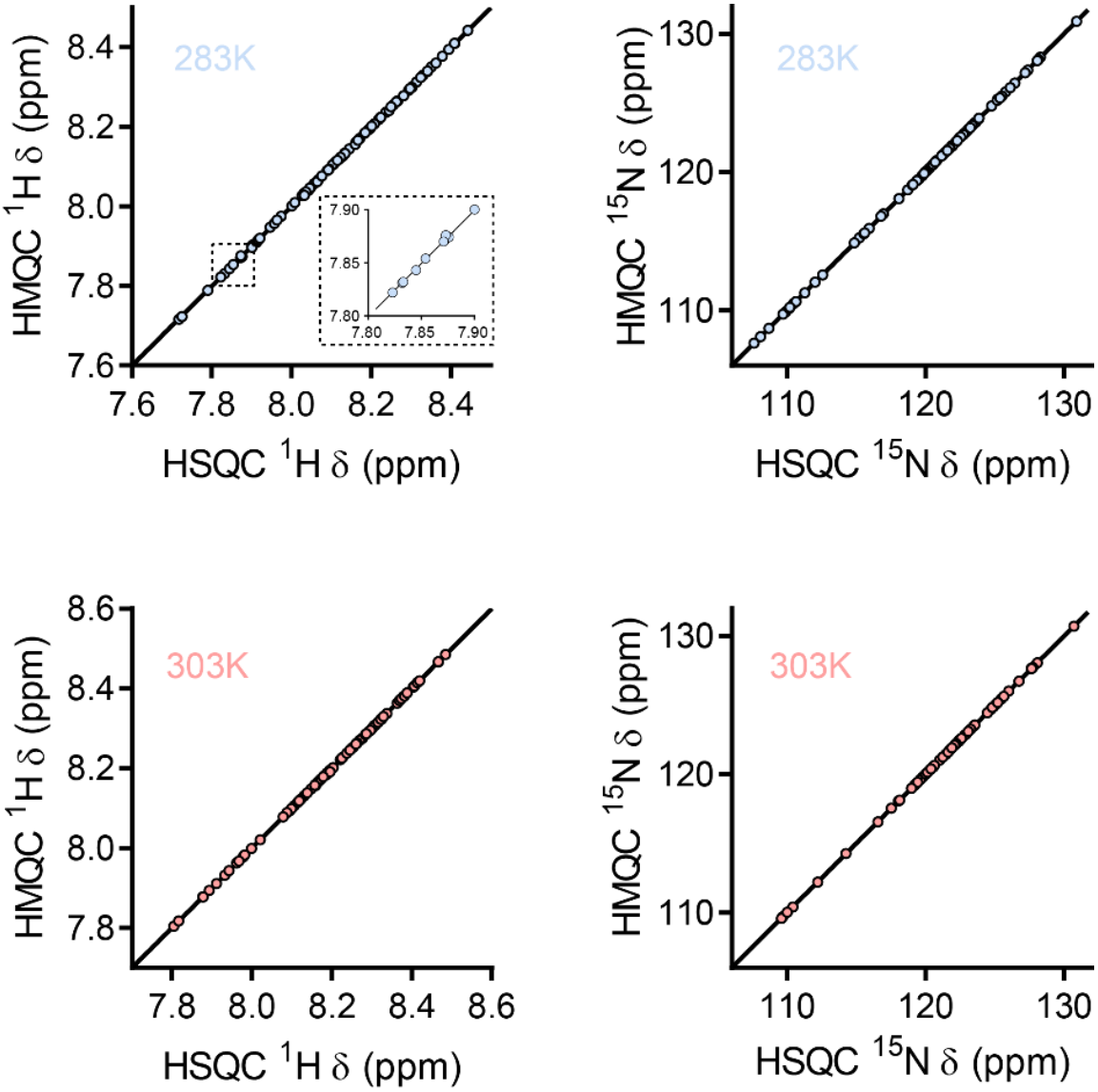

Figure S10. *HMQC vs. HSQC Chemical shift correlations indicate negligible intermediate exchange contributions to ^{15}N-R_2 enhancements.* Zoomed-in inset is shown to highlight the strength of the correlation.

Chapter 6. Concluding Remarks and Future Direction

6.1 Structural Determinants of Aβ Oligomer Toxicity

The presence of soluble Aβ oligomer species is linked to the early pathogenesis of AD[1]. The notoriety of soluble oligomers is associated with the presence of toxic surfaces, which facilitate maladaptive interactions with multiple cellular components, including cell surface receptors and membranes. Chapters two and three of this thesis aimed at identifying these toxic surfaces through comparative structural analyses of toxic *vs.* non-toxic oligomers. Specifically, green tea catechins were used as a chemical toolset to remodel toxic Aβ oligomers into Aβ assemblies with reduced toxicity. Interrogation of the resulting oligomer library through a combination of biophysical experiments probing structure and interactions at progressive degrees of resolution, and subsequent covariance analyses of the resulting data matrix revealed key structural differences between toxic *vs.* non-toxic oligomers and the underlying mechanism of oligomer toxicity. These include the exposure of a hydrophobic surface spanning residues 17 – 28 and the concomitant occlusion of the highly charged N-terminus. These structural transitions promote the colocalization, interaction and subsequent embedding of β-sheet rich Aβ assemblies into membranes, resulting in the loss of membrane integrity. Notably, the model proposed here can predict the relative toxicities of Aβ oligomers based on easily quantifiable low-resolution measurements such as surface hydrophobicity and hydrodynamic radius. Moreover, since Aβ is an archetypical amyloidogenic protein, and given that soluble oligomers of amyloid proteins have been suggested to share common structural motives, the structure – toxicity relationship established here may be relevant for other amyloidogenic systems.

6.2 Suppression of αS Oligomer Membrane Toxicity by Human Serum Albumin

The Aβ peptide is not the only extracellular amyloidogenic species. Other amyloidogenic IDPs previously thought to be exclusively intracellular have been discovered extracellularly as well. For example, emerging evidence implicating the extracellular release and cell-to-cell trafficking of αS raises questions regarding the specific interactions of such species with the extracellular proteome, and its role in regulating αS internalization into cells. In chapter five, we describe the mechanism by which the most abundant extracellular protein, Human Serum Albumin (HSA), selectively binds and modifies the structural properties of toxic αS oligomers. We show that HSA preferentially binds αS oligomers with an affinity an order of magnitude greater than monomers (*i.e.* 0.37μM *vs.* 510μM) and that the αS oligomer – HSA interactions elicit two main effects. First, they remodel toxic αS oligomers into chimeric intermediates that exhibit both rigid "fibril-like" and dynamic "monomer-like" regions with an overall reduction in toxicity. Second, HSA remodeling of αS oligomers prevents the incorporation of monomers, inhibiting the

seeding-induced growth of aggregates. Unexpectedly, our data indicate that HSA inhibits the interactions of the αS N-terminal and NAC regions with lipid membranes, revealing at multiple length scales from μm to Å an unanticipated mechanism for how an extracellular chaperone suppresses membrane damage by a neurotoxic amyloidogenic protein. Overall, these results point to molecular chaperones serving functions well beyond their established ability to interact directly with aggregation prone species in solution, and that they are able to suppress the toxicity associated with misfolded oligomers by remodeling such oligomers into membrane-binding incompetent species and/or by shielding the membrane interface from residual toxic species.

6.3 A Solution NMR Method to Map Early Oligomerization Sites in Amyloidogenic Proteins

The transient and heterogeneous nature of soluble amyloid oligomers presents significant challenges for high-resolution structural studies. In chapters two to four, we show how solution NMR techniques that takes advantage of the dynamic exchange of NMR visible monomers with lowly populated, NMR invisible oligomers can be utilized to report on structural characteristics of the oligomeric intermediates. However, one of the persisting challenges is that such techniques are often unable to separate contributions arising from intrinsic monomer dynamics and typically rely on experiments performed under both dilute and concentrated protein conditions, which are often unstable and/or poorly reproducible. In chapter six, we show that monitoring the temperature-dependent changes in $^{15}N - R_2$ *i.e.* $\Delta R_2/\Delta T$, for a single sample, uniquely differentiates residues involved in self-association from residues experiencing enhanced monomer dynamics. Such differentiation relies on two key characteristics. First, residues involved in aggregation exhibit an overall increase in $^{15}N - R_2$ as a function of temperature *i.e.* $\Delta R_2/\Delta T$ is positive. Second, the dependency of R_2 with respect to temperature is non-linear. In contrast, a linear and negative $\Delta R_2/\Delta T$ is observed for residues involved in monomer intrinsic dynamics. These two key features are systematically discerned through the thermal R_2 correlation matrix and subsequently extracted through agglomerative clustering analysis. When applied to the PD-associated αS protein, regions involved in early self-association are reliably mapped and coincide with highly hydrophobic segments and sites of familial PD mutations. Notably, the Self-Association by Temperature-Induced Relaxation Enhancement (SATIRE) method described herein, takes advantage of all the benefits of typical $^{15}N - R_2$ experiments, *i.e.* residue-resolution, high sensitivity, and label-free spectroscopy. Moreover, given that the monomers are used as the starting material for SATIRE, the method is expected to be less prone to irreproducibility than other techniques requiring a concentrated oligomeric sample.

6.4 Evaluation of the Amyloid Cascade Hypothesis: Pressing Need of Biomarkers for Early Detection

Despite the compelling genetic, animal model, and biochemical evidence supporting the revised amyloid cascade hypothesis, *i.e.* soluble oligomers as the primary driver of pathogenesis, the failure of clinical trials successfully reducing amyloid aggregate burden has raised questions regarding the role of amyloid deposition in AD. However, the extent to which such therapeutic interventions can serve to critically evaluate the amyloid cascade hypothesis is dependent on the posited role of Aβ in AD pathogenesis. Three possible scenarios can be considered: Aβ trigger, Aβ threshold and Aβ driver (Figure 1).[1]

If the Aβ trigger hypothesis is true, therapeutic interventions aimed at reducing the deposition of Aβ would be ineffective should they be introduced after amyloid deposition has already occurred, even if such interventions reduce Aβ load below the trigger point (Figure 1).[1] In the case of Aβ threshold, administering treatment before the Aβ threshold has been reached or after if the agent can resolubilize Aβ aggregates, can be used to evaluate the amyloid cascade hypothesis. If the post-threshold therapeutic agent is unsuccessful, it can be posited that such treatment did not have an appreciable effect on Aβ.

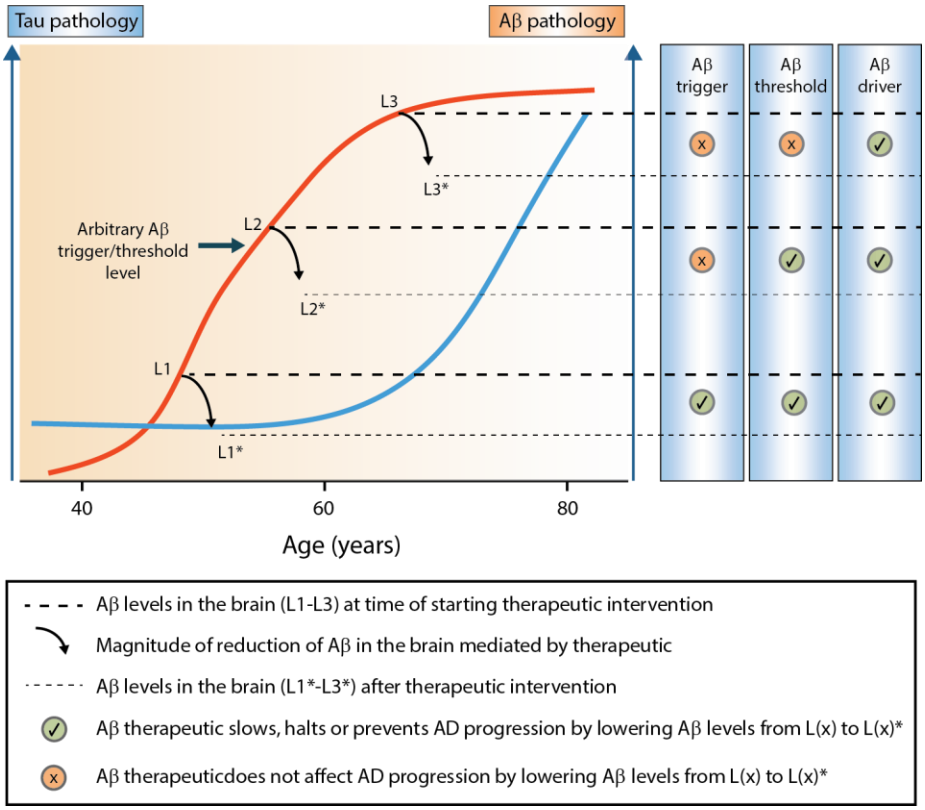

Figure 1. Potential roles of amyloid beta and the effects of treatments in each scenario. This figure is adapted from Karran et al., *Nature Reviews Drug Discovery*, **2011**.[1]

For the Aβ driver scenario, any therapeutic agent that can reduce the load of Aβ would demonstrate a proportional positive clinical response. However, given the lack of correlation between the spatiotemporal patterning of Aβ plaques in the brain and disease pathology as well as the absence of ameliorative cognitive effects after reduction of parenchymal Aβ plaque levels,[2] it appears likely that Aβ mediates its deleterious effects through another mechanism; such as by triggering tau pathology.

Indeed, mutations in the gene encoding tau cause frontotemporal lobe dementia, with clinical manifestations similar to AD pathology, but without the appearance of Aβ plaques.[3] Therefore, tau pathology alone is sufficient to cause neuronal loss. Moreover, unlike Aβ plaques, tau aggregates are anatomically connected to areas of severe neuronal loss in AD[2], placing emphasis on a direct role of tau in neurodegeneration. Nonetheless, cortical tau pathology in AD is solely observed in patients with coincident Aβ plaque deposition[4], pointing to an upstream role of Aβ aggregation in triggering tau pathology. Furthermore, mutations that lead to Aβ aggregation also exacerbate tau tangle formation, while the inverse is not observed.[5,6] Therefore, out of the various scenarios discussed, both preclinical and clinical findings are largely in support of the Aβ trigger and threshold hypotheses.

However, the clinical trials conducted to date have not been able to effectively assess these two scenarios due to interventions occurring already after the significant presentation of clinical symptoms. Indeed, if the Aβ trigger scenario is correct, testing the amyloid cascade hypothesis would require the selection of clinical trial cohorts with normal Pittsburgh compound B (PIB) scans and who are at risk of developing of AD. Such trial guidelines present significant challenges, not only in the selection of participants but also ethical considerations, trial duration and incurred costs. The development of biomarkers for early detection of amyloid pathology is therefore of crucial importance both for the rational selection of clinical trial populations and early intervention.

6.5 Alternative Hypotheses Proposed for the Etiology of Alzheimer's and Parkinson's Diseases

While familial forms of AD and PD substantiate a role of Aβ and αS as triggers of disease pathology, given that the mutations directly influence the production and aggregation propensities of these IDPs, in sporadic cases the initiator of pathogenesis is not entirely clear. This ambiguity in conjunction with the failure of clinical trials targeting sporadic forms of AD and PD has prompted efforts to explore other theories regarding the etiology of these age-related disorders. One of the prevalent alternative hypotheses postulates that the underlying stress that promotes the deposition of misfolded proteins is of energetic origin. Indeed, in cases of metabolic stress *e.g.* ischemia, hypoglycemia, and traumatic brain injury, an upregulation of APP and its mRNA is observed in cell culture and animal models.[7-9] Moreover,

depression of mitochondrial energy metabolism alters APP processing and the generation of amyloidogenic derivatives.[10] Similarly in PD, post-mortem studies of patient brains reveal the progressive accumulation of dysfunctional mitochondria.[11] Notably, the age-related decline in energy metabolism is consistent with the delayed onset of AD and PD, providing a compelling argument for an upstream initiator role of energy metabolism in neurodegenerative diseases.

Concordant with changes in energy metabolism, it is often noted that significant changes in the composition of gut microflora occurs with age[12] and such alterations often precedes the presentation of motor dysfunction in PD[13] and is concomitant with the development of AD pathology[14]. Indeed, the enteric nervous system serves as a direct route for the bi-directional communication between the gut and the brain[15] and the microflora plays a critical role in regulating the gut-brain axis[16]. The integrity and permeability of both the blood-brain and the gastrointestinal barriers have been shown to be dependent on the composition of microbiota in the gut, wherein age-related changes in microflora composition drives proinflammatory responses that weaken barrier function.[17,18] A seminal study comparing the microbiota of PD patients and aged-matched controls found correlations between microflora composition and the severity of gait difficulty and postural instability, although no temporal or causal relationship could be established between the two.[19] While the role of gut dysbiosis in AD and PD development remains exploratory, the associations discovered thus far provide an impetus for further elucidation of this link.

Despite the discordances between the promises initially offered by the amyloid cascade hypothesis and the lack of therapeutic success for AD and PD, and irrespective of the emergence of alternative hypotheses that appear to describe key observations that are germane to the disease processes, the association of Aβ and αS in AD and PD pathology remain indisputable. While they may not necessarily be efficacious targets for therapeutic intervention, their presence in early disease pathology renders them invaluable targets for biomarker development. In this context, the work presented in this dissertation provides valuable high-resolution information for the cogent diagnostic exploitation of these biomarkers. Given that the oligomers precede the formation of mature fibrils, the oligomer surface epitopes identified here to be critical for toxicity may guide the development of biomarkers for early detection.

6.6 Future Directions

While the structural determinants of amyloid oligomer toxicity and mechanisms of action of potent oligomer inhibitors described in this dissertation are validated through *ex vivo* cell-based experiments, it remains unclear whether such principles are fully translatable to *in situ* biofluids. Notably, the cytosol and blood plasma contain ~200-400 g protein/L and ~80 g protein/L[20], respectively. These cytosolic and

plasma matrix protein concentrations are sufficient to elicit significant molecular crowding arising primarily from steric repulsion (Fig. 2a) and weak binding.[20,21] Steric crowding favors dynamic changes that reduce the volume excluded by proteins, such as folding and conformational transitions from extended to more compact structures (Fig. 2b *vs.* c).[20] The compaction exerted by steric crowding agents is most apparent for intrinsically disordered proteins (IDPs), as their inherent dynamics make them highly susceptible to crowding effects (Fig. 2a). For example, a seminal study by Theillet et al., shows that αS adopts more compact conformations in the crowded environment of the cell, wherein the N- and C-termini exhibit transient long-range interactions that occlude the aggregation prone NAC region from interprotomer recognition.[22] Hence, a significant proportion of αS remains monomeric and intrinsically disordered *in cells* in stark contrast to observations *in vitro*.

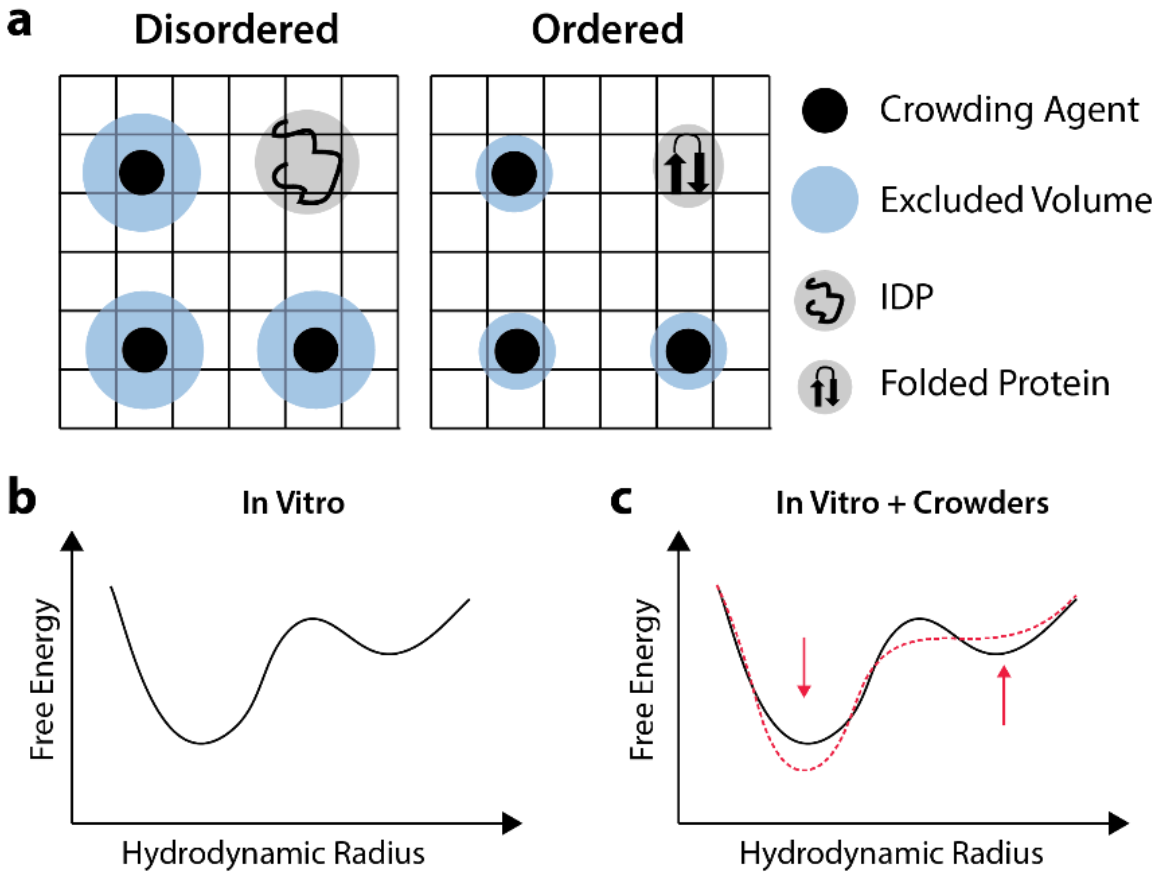

Figure 2. Schematic representation of macromolecular crowding. (a) Volume exclusion (*blue*) by crowding agents (*black*) for IDPs with extended conformations (*left*) and folded proteins with compact conformations (*right*). The accessible volume (*white*) is less on the left *vs.* right. Free energy *vs.* hydrodynamic radius plots for proteins *in vitro* in the absence (b) and presence (c) of crowding agents. The red dashed line indicates changes upon addition of crowders and arrows indicate direction of change.

Follow-up investigations, however, show that the ensemble of αS conformations observed *in cells* is tightly regulated by post-translational modifications.[23] Age-related PTMs in αS, such as phosphorylation and oxidation, are sufficient to interfere with transient binding of αS to the intracellular proteome, *e.g.* chaperones, and result in re-localization of αS to the mitochondrial membrane, and consequent formation of aggregates. However, the structures of αS oligomers *in cells* remain unknown. Moreover, to date there has been no high-resolution structural investigation of IDPs in blood plasma. Given the plasma *vs.* cytoplasm differences in ion, metabolite, protein and lipid compositions, the crowding effects elicited by the plasma environment are likely to be new and clearly distinct from those previously reported for intracellular proteins.[20,24] Moreover, given that the large majority of Aβ in the interstitial fluid is transported via the blood-brain barrier into peripheral circulation[25], understanding the conformation space of amyloidogenic proteins *in plasma* may offer new structural insight into disease pathology.

Taken together, future studies should aim to investigate IDP interactions, structure, and dynamics and the effect of PTMs on these characteristics in their native physiological environment. Such investigations will reveal how the plasma and cellular milieu shapes the conformational ensemble of IDPs, providing a better understanding of the structural determinants of oligomer toxicity *in situ*. These principles will facilitate the development of a new framework for the early detection of neurodegenerative disorders, such as AD and PD, and inhibitors of amyloidogenic proteins.

6.7 References

(1) Karran, E.; Mercken, M.; Strooper, B. de. The amyloid cascade hypothesis for Alzheimer's disease: an appraisal for the development of therapeutics. *Nature reviews. Drug discovery* **2011**, *10*, 698–712.
(2) Serrano-Pozo, A.; William, C. M.; Ferrer, I.; Uro-Coste, E.; Delisle, M.-B.; Maurage, C.-A.; Hock, C.; Nitsch, R. M.; Masliah, E.; Growdon, J. H.; *et al.* Beneficial effect of human anti-amyloid-beta active immunization on neurite morphology and tau pathology. *Brain* **2010**, *133*, 1312–1327.
(3) Hutton, M.; Lendon, C. L.; Rizzu, P.; Baker, M.; Froelich, S.; Houlden, H.; Pickering-Brown, S.; Chakraverty, S.; Isaacs, A.; Grover, A.; *et al.* Association of missense and 5'-splice-site mutations in tau with the inherited dementia FTDP-17. *Nature* **1998**, *393*, 702–705.
(4) Price, J. L.; Morris, J. C. Tangles and plaques in nondemented aging and "preclinical" Alzheimer's disease. *Ann Neurol.* **1999**, *45*, 358–368.
(5) Reed, L. A.; Grabowski, T. J.; Schmidt, M. L.; Morris, J. C.; Goate, A.; Solodkin, A.; van Hoesen, G. W.; Schelper, R. L.; Talbot, C. J.; Wragg, M. A.; *et al.* Autosomal dominant dementia with widespread neurofibrillary tangles. *Annals of neurology* **1997**, *42*, 564–572.
(6) Lindquist, S. G.; Holm, I. E.; Schwartz, M.; Law, I.; Stokholm, J.; Batbayli, M.; Waldemar, G.; Nielsen, J. E. Alzheimer disease-like clinical phenotype in a family with FTDP-17 caused by a MAPT R406W mutation. *European journal of neurology* **2008**, *15*, 377–385.
(7) Hall, E. D.; Oostveen, J. A.; Dunn, E.; Carter, D. B. Increased amyloid protein precursor and apolipoprotein E immunoreactivity in the selectively vulnerable hippocampus following transient forebrain ischemia in gerbils. *Experimental neurology* **1995**, *135*, 17–27.

(8) Jendroska, K.; Poewe, W.; Daniel, S. E.; Pluess, J.; Iwerssen-Schmidt, H.; Paulsen, J.; Barthel, S.; Schelosky, L.; Cervós-Navarro, J.; DeArmond, S. J. Ischemic stress induces deposition of amyloid beta immunoreactivity in human brain. *Acta neuropathologica* **1995**, *90*, 461–466.
(9) Yokota, M.; Saido, T. C.; Tani, E.; Yamaura, I.; Minami, N. Cytotoxic fragment of amyloid precursor protein accumulates in hippocampus after global forebrain ischemia. *Journal of cerebral blood flow and metabolism : official journal of the International Society of Cerebral Blood Flow and Metabolism* **1996**, *16*, 1219–1223.
(10) Mattson, M. P.; Pedersen, W. A. Effects of amyloid precursor protein derivatives and oxidative stress on basal forebrain cholinergic systems in Alzheimer's disease. *International journal of developmental neuroscience : the official journal of the International Society for Developmental Neuroscience* **1998**, *16*.
(11) Park, J.-S.; Davis, R. L.; Sue, C. M. Mitochondrial Dysfunction in Parkinson's Disease: New Mechanistic Insights and Therapeutic Perspectives. *Current neurology and neuroscience reports* **2018**, *18*, 21.
(12) Dinan, T. G.; Cryan, J. F. Gut instincts: microbiota as a key regulator of brain development, ageing and neurodegeneration. *The Journal of physiology* **2017**, *595*, 489–503.
(13) Nair, A. T.; Ramachandran, V.; Joghee, N. M.; Antony, S.; Ramalingam, G. Gut Microbiota Dysfunction as Reliable Non-invasive Early Diagnostic Biomarkers in the Pathophysiology of Parkinson's Disease: A Critical Review. *Journal of neurogastroenterology and motility* **2018**, *24*, 30–42.
(14) Kowalski, K.; Mulak, A. Brain-Gut-Microbiota Axis in Alzheimer's Disease. *Journal of neurogastroenterology and motility* **2019**, *25*, 48–60.
(15) Aziz, Q.; Thompson, D. G. Brain-gut axis in health and disease. *Gastroenterology* **1998**, *114*, 559–578.
(16) Foster, J. A.; Lyte, M.; Meyer, E.; Cryan, J. F. Gut Microbiota and Brain Function: An Evolving Field in Neuroscience. *The international journal of neuropsychopharmacology* **2016**, *19*.
(17) Kelly, J. R.; Kennedy, P. J.; Cryan, J. F.; Dinan, T. G.; Clarke, G.; Hyland, N. P. Breaking down the barriers: the gut microbiome, intestinal permeability and stress-related psychiatric disorders. *Frontiers in Cellular Neuroscience* **2015**, *9*.
(18) Montagne, A.; Barnes, S. R.; Sweeney, M. D.; Halliday, M. R.; Sagare, A. P.; Zhao, Z.; Toga, A. W.; Jacobs, R. E.; Liu, C. Y.; Amezcua, L.; *et al.* Blood-brain barrier breakdown in the aging human hippocampus. *Neuron* **2015**, *85*, 296–302.
(19) Scheperjans, F.; Aho, V.; Pereira, P. A. B.; Koskinen, K.; Paulin, L.; Pekkonen, E.; Haapaniemi, E.; Kaakkola, S.; Eerola-Rautio, J.; Pohja, M.; *et al.* Gut microbiota are related to Parkinson's disease and clinical phenotype. *Movement disorders : official journal of the Movement Disorder Society* **2015**, *30*, 350–358.
(20) Ellis, R.J. Macromolecular crowding: obvious but underappreciated. *Trends in Biochemical Sciences* **2001**, *26*, 597–604.
(21) Rivas, G.; Fernandez, J. A.; Minton, A. P. Direct observation of the self-association of dilute proteins in the presence of inert macromolecules at high concentration via tracer sedimentation equilibrium: theory, experiment, and biological significance. *Biochemistry* **1999**, *38*, 9379–9388.
(22) Francois-Xavier Theillet; Andres Binolfi; Beata Bekei; Andrea Martorana; Honor May Rose; Marchel Stuiver; Silvia Verzini; Dorothea Lorenz; Marleen van Rossum; Daniella Goldfarb; *et al.* Structural disorder of monomeric α-synuclein persists in mammalian cells. *Nature* **2016**, *530*, 45–50.
(23) Burmann, B. M.; Gerez, J. A.; Matečko-Burmann, I.; Campioni, S.; Kumari, P.; Ghosh, D.; Mazur, A.; Aspholm, E. E.; Šulskis, D.; Wawrzyniuk, M.; *et al.* Regulation of α-synuclein by chaperones in mammalian cells. *Nature* **2020**, *577*, 127–132.
(24) Smith, A. E.; Zhang, Z.; Pielak, G. J.; Li, C. NMR studies of protein folding and binding in cells and cell-like environments. *Current opinion in structural biology* **2015**, *30*, 7–16.
(25) Shibata, M.; Yamada, S.; Kumar, S. R.; Calero, M.; Bading, J.; Frangione, B.; Holtzman, D. M.; Miller, C. A.; Strickland, D. K.; Ghiso, J.; *et al.* Clearance of Alzheimer's amyloid-ss(1-40) peptide from brain by LDL

receptor-related protein-1 at the blood-brain barrier. *The Journal of clinical investigation* **2000**, *106*, 1489–1499.